Understanding oxygen photochemistry in CO_2-dominated planetary atmospheres

by

Marie-Ève Gagné

A thesis submitted in conformity with the requirements
for the degree of Doctor of Philosophy
Graduate Department of Physics
University of Toronto

Abstract

Understanding oxygen photochemistry in CO_2-dominated planetary atmospheres

Marie-Ève Gagné

Doctor of Philosophy

Graduate Department of Physics

University of Toronto

2012

The motivation for this work is the weak level of confidence in forecasting the temperature profile for the Martian atmosphere over the aerobraking region. This limitation comes mainly because of a misrepresentation of the atomic oxygen distribution in atmospheric models, which is a result of lack of measurements. One effective way to observe atomic oxygen and temperature remotely in the 50 to 100 km altitude region is through airglow measurements.

The first part of the thesis involves the development of an airglow model to simulate four O_2 emissions: the Herzberg I, Herzberg II, and Chamberlain band systems, as well as the Infrared Atmospheric emission at 1.27 μm. The model predictions are compared with available observations from both the Mars and Venus atmospheres to exploit the consistency in the photochemistry of these two CO_2-dominated atmospheres. Using composition from 3-D global circulation models of the Mars and Venus atmospheres, simulations are performed with realistic dynamical variations. Previous studies used 1-D photochemical models only. Hence, this novel approach allows in-depth investigation of the influence of dynamics and circulation on the airglow behaviour. A sensitivity study is conducted to understand the impact of the different photochemical parameters available in the literature and to recommend a set of parameters to be used in future model predictions. This approach also provides an understanding of the impact of atmospheric conditions, like temperature, dust load, water concentrations, etc., on the vertical

structure of the emissions.

A retrieval algorithm is also developed to perform a partial inversion of the recorded signal to extract the NO airglow emission in the Mars atmosphere from the SPICAM instrument. The method is tested with one year of stellar occultation measurements and validated with observations from SPICAM in a limb-viewing geometry and with airglow model predictions. This work identified and quantified, for the first time, localised variations in the NO nightglow, providing insights into the factors influencing the distribution of the oxygen species other than the general circulation and the photochemistry. The method proved to be a useful tool to build a climatology of the NO emission in the Mars atmosphere.

Dedication

This thesis is dedicated to my father André for his inspiration and to my mother Carole for her support. Merci pour tout!

Acknowledgements

I first want to express how thankful I am to my two supervisors, Prof. Kimberly Strong and Dr. Stella Melo, for making the last five years a positive graduate experience for me. They are both models of strength and dedication, and being surrounded by passionate women like they are was truly inspiring and motivating. I am now convinced that the synergy between this co-supervision added an extra flavour to the course of a regular Ph.D. degree. Moreover, the contribution of Prof. James Donaldson to the success of my Ph.D. degree is important. He has cared about my progress more than it is required as a member of my supervisory committee. I really feel that I had three supervisors!

Thank you Kim for not having forgotten about me after our first meeting and for successfully trying to find a research project on the atmosphere of Mars. I was told by your students at the beginning of my Ph.D. that you are an excellent supervisor; now I can confirm that it was not an overstatement! I do not think I could have found a better example of organisation and discipline in a supervisor. Also, you have been overly patient with my written English, I really appreciate it.

The first four years of my Ph.D. degree were spent in Toronto, working from my office in the Department of Physics at the University of Toronto. A special acknowledgement to Krystyna Biel for being so dedicated to the graduate students. I am grateful to the availability of the extraordinary professors in the Atmospheric Physics group to the students, particularly Kaley Walker for our collaboration within the Noble fund committee. I have to thank William for believing in my capacity to meet the Ph.D. challenge. I will not forget the first office crew composed of Felicia, Melissa and Cristen. It was so entertaining to listen to Melissa's stories. Also, the girls were always willing for a coffee break at Starbucks. Felicia, my time in Toronto favoured the development of a strong friendship and that is a plus on the interpersonal side!

I am grateful to Stella to have made possible for me to work from the Canadian Space Agency. I really enjoyed working with like-minded space enthusiasts. While speaking

about the Canadian Space Agency, I cannot pass the opportunity to thank everybody there who has impacted my education. First, Dr. Victoria Hipkin, who was my supervisor for my first internship back in 2006 while I was still an undergraduate student at McGill University. She is the one who inspired me to do research about the atmosphere of Mars. I thank Marilyn Steinberg and Jason Clement who made available absolutely amazing opportunities for students through the Space Learning Program. Marilyn, I will keep in mind our lunches outside the CSA and our workouts sessions abroad! Thank you for all your good advice, you are a mentor to me! I thank Nathalie Cassidy for all her hard work that ease the duties of the research scientists. I thank Daniel Provençal for the ever so interesting discussions during the many hours spent commuting to work.

Adding the many trips to France, I spent over three months in total working at LATMOS. I am very grateful to Dr. Jean-Loup Bertaux to have offered me this incredible opportunity. I also thank Dr. Franck Montmessin for being available for constructive discussions during my visits there. I have many good memories from the LATMOS, thanks to the warm welcome from the graduate students. In particular, I had good times with the girls: Anni, Kristell, Jennyfer, Maude, and most importantly, Emilie. Thank you Emilie for your mentorship on the SPICAV work, and above all, for the good times spent outside the lab. The next crazy adventure will take place in America: tornado chasing!

I cannot skip a mention to all the people at Crossfit CapOp with whom I crushed intense workouts after a day at work. My motivation and discipline for my research during the last year came from my strong desire to show up at the box to see my friends and hit a WoD to sweat it out! It is not overstating to say that I would not have made it with all my sanity if I would not have had the CapOp community. A special thanks to Vince who transmitted to me his passion for the sport. Sean, you are a model of discipline; I tried to transpose the consistency in your training to my research. And Math, your drive and ambition is truly inspiring; thank you for your support and your

trust.

Finally, I thank my two best friends, Marie-Josée et Marie-Hélène, for your support throughout my exile to Toronto. I would probably not have had the courage to pursue this Ph.D. if I have not made the monthly trips to Montreal to reunite like *back in the days*!

Contents

List of Tables

List of Figures

Chapter 1

Introduction

The aim of this chapter is to give the reader an explanation of the reasons that motivated this research and the current gaps in the knowledge of the chosen field of study, as well as stating the problem we attempted to solve and the way we addressed it.

1.1 Motivation

Understanding the physical and dynamical processes that control the temperature distribution is fundamental to explain the structure, composition, and circulation of the atmosphere of a planet. Our limited understanding of the processes that govern the thermal structure of the middle atmosphere of Mars prevents atmospheric scientists from properly forecasting the atmospheric conditions during the aerobraking phase of landing missions to the planet. This is a major obstacle that delays the possibility of manned missions to Mars. This gap in our knowledge illustrates how challenging and complex it is to capture all the processes that control the energetic budgets of the terrestrial planets.

The temperature structure in the atmospheric region between 50 and 100 km on Mars is poorly characterized. Measurements of temperature in this altitude range are scarce, both spatially and temporally; only a few missions to Mars have attempted to infer the temperature over this altitude range. The Viking Landers 1 and 2 (1975-1977)

and the entry accelerometer on board the Mars Pathfinder (1996) provided single entry profiles (Nier and McElroy, 1977; Seiff and Kirk, 1977; Magalhaes et al., 1999). The Mars Global Surveyor (MGS) Thermal Emission Spectrometer (TES) obtained profiles of temperature from the ground to 35 km on average for over 10 years (1996-2006), and only a few profiles extended up to 65 km with the limb-viewing mode (Conrath et al., 2000; Smith, 2004). Since 2003, the Spectroscopy for the Investigation of the Characteristics of the Atmosphere of Mars (SPICAM) experiment on the Mars Express (MEx) spacecraft has been monitoring the atmosphere between 80 and 130 km. The temperature data covers this altitude range with a temperature error varying between 7 to 15 K and 70 km (Forget et al., 2009). Lastly, the Mars Climate Sounder (MCS) on board the Mars Reconnaissance Orbiter (MRO) has completed more than two Martian years of observations of the lower and middle atmosphere, providing temperature profiles from the surface to as high as 80 km (McCleese et al., 2010). The error associated with these temperature measurements is about $\pm$10 K at 70 km. Indeed, the current and past exploration missions to Mars have not delivered a complete and precise coverage of the thermal structure over the middle atmospheric region. On the other hand, global circulation models (GCMs) fail to reproduce accurately the few available observations. So far, the GCMs, which are state-of-the-art representations of our understanding of the atmospheric system, overestimate the temperature in the middle atmosphere at all time scales when compared to observations (González-Galindo et al., 2009; Forget et al., 2009; McDunn et al., 2010). As a matter of fact, numerical results are model dependent and only a few observations are available for their validation (Bertaux et al., 2006; González-Galindo et al., 2009).

Similarly, little is known about the precise distribution of atomic oxygen (O) in the middle atmosphere of Mars, and the available datasets show a significant variability. Undoubtedly, the role of atomic oxygen in the photochemistry of the Martian atmosphere is important since it controls the energetic budget in the 70 to 130 km altitude range

(Slanger et al., 2007; González-Galindo et al., 2009). Atomic oxygen has an important effect on the carbon dioxide (CO_2) 15-μm cooling: the collisions with atomic oxygen excite the vibrational states of the CO_2 molecule, enhancing the emission rate and thus the cooling (Huestis et al., 2007). The variations can be up to a factor of five in the cooling due to changes in the atomic oxygen profile (López-Puertas and López-Valverde, 1995). Therefore, without proper validation of Mars GCMs, an underestimation of the atomic oxygen content would yield an overestimation of the temperatures because of the role of CO_2 15-μm cooling in the thermal balance (González-Galindo et al., 2009).

The objectives of this thesis are therefore to increase our knowledge of: (1) the photochemical reactions that involve atomic oxygen, (2) the mechanisms that control the atomic oxygen distribution, and (3) the impacts of variations in the atomic oxygen concentration on the thermal structure and the energetic budget of CO_2-dominated atmospheres. Studying the processes responsible for the oxygen-related emissions provides a powerful way to constrain the behaviour of GCMs above 50 km.

1.2 Methodology

A novel approach for remote sensing the temperature in the middle atmosphere of terrestrial planets is to study airglow. Airglow arises from the emission of energy due to photochemical reactions that occur in the atmosphere, usually at high altitudes where the atmospheric density is relatively low. Airglow measurements provide a highly promising approach for the determination of temperature over the Mars middle atmosphere given the strong heritage of this technique for Earth observations. On Earth, airglow emissions in the visible and infrared (IR) spectral regions from hydroxyl (OH) and from both atomic and molecular oxygen have been used as a proxy for mesospheric temperature and atomic oxygen for over a decade (She and Lowe, 1998; Melo et al., 2000, 2001).

The temperature can be monitored via airglow measurements, which provides the

possibility of obtaining a temperature climatology. Additionally, airglow can be simulated in GCMs and the results used to validate the airglow scheme via a comparison with observations. Airglow used in this way enables an assessment of the dynamics of the atmosphere by tracing the transport of the species that come into play. Modeling of airglow from oxygen-related emissions is a promising technique to validate the temperature field in GCMs with observations.

A modeling perspective is chosen to investigate the physical and chemical processes that govern the distribution of the oxygen concentration in the atmosphere of Mars between 50 and 100 km in altitude. Specifically, we investigated the use of airglow emissions resulting from the production of oxygen-related excited species after recombination of oxygen atoms during nighttime to retrieve temperature and atomic oxygen density profiles. The kinetics of the oxygen reactions in CO_2-dominated atmospheres remain poorly known to this day. There are large uncertainties in the reaction rates of the excited species of O_2 with CO_2. Even the lifetimes of these excited states are not well-quantified. Furthermore, the pathways of production of the excited states have yet to be characterized. Hence, accurate modeling of molecular oxygen airglow emissions has proven to be challenging.

To overcome this challenge, one can exploit the similarity between the composition of the Mars and Venus atmospheres at the altitude of the airglow layer, i.e., at about 65 km on Mars and 95 km on Venus, to provide constraints on the kinetics of the reactions. By forcing model simulations to match the observations, the range of uncertainty of these parameters can be narrowed, which helps to improve the parametrization of the oxygen photochemistry. Given the comparability between these two CO_2-dominated atmospheres, i.e., both are comprised of 95% CO_2, we expect that the chemistry will be similar for both planets. However, the oxygen photochemistry occurring on Earth is significantly different given the lower concentration of CO_2 on Earth at the airglow altitude, i.e., at about 95 km. This work is therefore a good example of the value of a

comparative atmosphere approach.

Increasing the knowledge of the oxygen photochemistry through modeling of specific airglow features and sensitivity testing of the kinetics of the reactions producing the features can be improved by comparing the simulations with available observations of the emissions. This exercise provides further constraints on the reaction rates and efficiencies. Moreover, the chosen airglow emission features are directly proportional to the distribution of atomic oxygen, such that it is possible to constrain the atomic oxygen density assuming that the model results of O_2 airglow reproduce the observations within the measurements uncertainties. Lastly, from the emission intensities, the atmospheric temperature can be inferred given that the excited states are thermalized before deactivation.

To this date, the oxygen airglow emissions at nighttime have not been measured systematically in the Mars and Venus atmospheres, which limits the number of datasets available for comparison with model simulations. Hence, a data processing segment has been incorporated in this thesis. After trying unsuccessfully to isolate a signal from O_2 emissions from measurements made with the SPICAM UV channel, it was recognized that the NO emissions that are present in these spectra could be retrieved to give supplementary information to the modeling work. Airglow emissions from nitric oxide (NO) are a prominent feature of the nighttime atmosphere of these planets; this emission also depends on the atomic oxygen density. Since the NO emission is produced from a different mechanism than the O_2 emissions, it is useful to consider it to further constrain the atomic oxygen and temperature structures in the Mars atmosphere. The unique dataset of SPICAM stellar occultation sequences provides extensive spatial and temporal coverage of the NO emission and enables study of its distribution at nighttime, thus providing more information to constrain the parametrization of temperature in current GCMs. An inversion algorithm was developed to allow for retrievals of the NO spatial distribution in the SPICAM observations.

By investigating the airglow emissions of excited NO and O_2 in the Mars and Venus atmospheres with both modeling and data processing approaches, this thesis improves our understanding of oxygen photochemistry in CO_2-dominated atmospheres. By achieving a realistic atomic oxygen density distribution, current GCMs can predict the temperature structure in the Martian middle atmosphere with better accuracy, which can be validated with current measurements of temperature. Furthermore, the airglow model developed within the context of this thesis constitute an important tool for the development of an instrument to measure airglow in CO_2-dominated atmospheres, as it allows for a clear definition of instrument requirements.

1.3 Contributions

The results presented in this thesis are essentially the outcomes of my own work efforts. However, the results from the modeling and the data processing could not have been obtained without the contribution of many scientists in the Mars and Venus atmospheric science community.

I am responsible for the development of the airglow model to calculate the O_2 and NO emissions in a CO_2 atmosphere. However, this airglow model requires profiles of temperature and of density of the species involved in the chemical reactions. These profiles for the atmosphere of Mars were obtained from simulations using the Laboratoire de Météorologie Dynamique (LMD) Mars GCM, herein referred to as LMD-MGCM, that were provided by Dr. Franck Lefèvre from the Laboratoire Atmosphères, Milieux, Observations Spatiales (LATMOS) in France, as well as from Dr. Francisco González-Galindo, from the Instituto de Astrofísica de Andalucía in Spain. Regarding the results using Venus atmospheric conditions, I obtained the profiles from Dr. Stephen W. Bougher from the University of Michigan in the United States of America (USA) and from Dr. Amanda S. Brecht, who graduated under the supervision of Dr. Bougher and now works

at NASA Ames (USA); she ran the Venus Thermospheric GCM (VTGCM). The results from the model simulations of O_2-related emissions in the Mars and Venus atmospheres have been published in the *Journal of Geophysical Research - Planets* in two separate articles (Gagné et al., 2012a,b).

As for handling the measurements from SPICAM, I was first helped by Dr. Emilie Royer, a former doctoral student at LATMOS and now at the Jet Propulsion Laboratory (USA), to understand the characteristics of this spectrometer and the routine to process the raw data and extract the airglow signal with the routine developed by her Ph.D. supervisor, Dr. Franck Montmessin. I also used the forward model that she developed to analyse the NO emission in the Venus atmosphere with the analogue instrument on Venus Express (VEx), SPICAV, to retrieve the signal in the Mars atmosphere as measured by SPICAM.

Lastly, I worked closely with Dr. Jean-Loup Bertaux, also at LATMOS, who is the Principal Investigator of SPICAM, to derive an inversion method to retrieve the brightness and location of the NO emission from the SPICAM measurements. His knowledge of the instrument and the observational mode was essential for the development of a reliable retrieval method. The outcomes from data processing the first three years of SPICAM observations of the NO airglow are highlighted in a letter submitted to *Geophysical Research Letters* (Gagné et al., 2012c).

1.4 Outline

This thesis is divided into three parts:

- *Part 1*: The first few chapters of the thesis provide the background information to facilitate the understanding of the results and the analyses to be presented in this thesis. There is a general overview of the planetary atmospheres of Mars and Venus, and a summary of the observations of airglow in these atmospheres.

There are also basic discussions about spectroscopy, photochemistry, and kinetics of chemical reactions that are necessary to explain the phenomena of airglow.

- *Part 2*: The following part contains the modeled simulations of O_2 airglow from several band emissions in the Mars and Venus atmospheres. The model developed within the context of this thesis is described, and the results from these simulations are presented.

- *Part 3*: Then, the next part starts with a description of the Mars Express' SPICAM instrument and the inversion algorithm developed to retrieve the NO observations from the stellar occultation sequences. The results from one year of NO retrievals are presented.

Note that Appendix A lists all the abbreviations used in this thesis for easy reference.

Part I

Background knowledge

The core of this thesis is the presentation and analysis of results from airglow simulations and retrievals of nighttime oxygen-related emissions in CO_2-dominated atmospheres. This part gives some background material to facilitate the understanding of the thesis work. First, in Chapter 2, we provide a general overview of the characteristics of the atmospheres of Mars and Venus to inform the discussions related to the results presented in this thesis. Chapter 3 is a general introduction to the phenomenom of airglow and its applications. The spectroscopy of the O_2 and NO emissions considered in this study is described in Chapter 4. Then, Chapter 5 explains the mechanisms responsible for the O_2 and NO nightglow in the Mars and Venus atmospheres, and the chemical kinetics of the relevant reactions is detailed in Chapter 6. Finally, Chapter 7 is a review of the measurements of these emissions in the Mars and Venus atmospheres.

Chapter 2

The atmospheres of Mars and Venus

A terrestrial planet is a planet that is composed primarily of silicate rocks or metals. The term terrestrial is derived from Latin words for Earth, e.g., Terra and Tellus, as these planets are, in a certain way, "Earth-like". Within the Solar System, the terrestrial planets are the inner planets closest to the Sun: Mercury, Venus, Earth, and Mars.

In some ways, Mars is much like Earth. It has a similar rotation period of 24 hours 39 minutes, defined as a sol, and its revolution period is 668.6 sols, about twice that of Earth. Moreover, its axis tilt is 25.19°, slightly more inclined than the Earth with respect to the ecliptic plane. Therefore, the global atmospheric circulation resembles that of Earth. However, the Mars atmosphere is mainly composed of CO_2, like that of Venus. These two CO_2-dominated atmospheres are therefore subjected to carbon- and oxygen-related photochemistry, which dictates the energetic budget in their middle atmospheres.

This chapter provides a brief and general description of the main characteristics of Mars and Venus that are related to the atmospheric structure and composition of these planets. This description is intended to help understand the discussion of the results to be presented at the core of this thesis. Table 2.1 gives the main characteristics of Mars and Venus that are pertinent to this study. The parameters for Earth are also listed as a reference.

Table 2.1: Orbital, physical, and atmospheric characteristics and composition of Mars, Earth and Venus. Parameters obtained from the JPL HORIZONS on-line Solar System data (http://ssd.jpl.nasa.gov/horizons.cgi).

	Mars	**Earth**	**Venus**
Orbital			
Mean distance from the Sun (AU)	1.52	1	0.72
Eccentricity	0.0934	0.0167	0.0068
Revolution (years)	1.88	1	0.615
Solar day (days)	1.02	1	116.75
Rotation (hours)	24.62	23.93	5,832.24
Solar constant (kW m^{-2})	0.594	1.376	2.613
Physical			
Obliquity (°)	25.19	23.45	177.36
Gravitational acceleration (m s^{-2})	3.71	9.81	8.87
Radius (km)	3,396	6,371	6,052
Density (g cm^{-3})	3.96	5.51	5.24
Atmospheric			
Molecular weight (g)	43.49	28.98	43.44
Surface temperature (K)	220	288	730
Surface pressure (bar)	0.007	1	92
Density (kg m^{-3})	0.02	1.2	∼65
Composition (mixing ratio)			
CO_2	0.95	0.0003	0.96
N_2	0.027	0.77	0.035
Ar	0.016	0.0093	0.00007
H_2O	∼0.0003	∼0.01	∼0.0001
O_2	0.0013	0.21	∼0
SO_2	∼0	0.2 ppb	150 ppm
CO	700 ppm	0.12 ppm	40 ppm
Ne	2.5 ppm	18 ppm	5 ppm

2.1 The atmosphere of Mars

Mars is the fourth planet of the Solar System, starting from the Sun, and it is often referred to as the red planet because of the rusty colour from iron oxide, commonly known as rust, that covers its surface. Phobos and Deimos, both names having their origin in Greek mythology, are the two satellites of Mars and were discovered in 1877. Mars bears the name of the Roman god of war.

Mars is a terrestrial planet with a thin atmosphere, having surface features reminiscent both of the impact craters of the Moon and the volcanoes, valleys, deserts, and polar ice caps of Earth. It has the highest mountain in the Solar System, Olympus Mons, which rises to a height of 27 km, as well as the deepest valley, Hellas Planitia, that reaches a depth of 11 km. Figure 2.1 is a topographic map of Mars showing the extreme variations in elevation and the dichotomy between the Northern and Southern hemispheres, whose origin is still an enigma.

2.1.1 Orbital and physical properties

The average distance between Mars and the Sun is roughly 230×10^6 km ($\sim$1.5 AU) and its orbital period is 687 (Earth) days. The solar day, or sol, on Mars is only slightly longer than a day on Earth: 24 hours, 39 minutes, and 35 seconds. A Martian year is equal to 1.88 (Earth) years, or 1 year, 320 days, and 18 hours[1].

The axial tilt of Mars is 25.19°, which is similar to the axial tilt of the Earth, i.e., 23.45°. As a result, Mars has seasons similar to that of Earth, though on Mars, they are nearly twice as long given its longer year. Mars has a relatively pronounced orbital eccentricity of about 0.09; of the seven other planets in the Solar System, only Mercury shows greater eccentricity.

[1]A Martian calendar was proposed by Clancy et al. (2000) that starts on date April 11, 1955, that is at L_S=0° of the first year of the Martian exploration era. In this convention, Mars Express arrived at Mars at the end of MY 26, MY standing for Martian Year, and Mars Curiosity landed on Mars in the middle of MY 31.

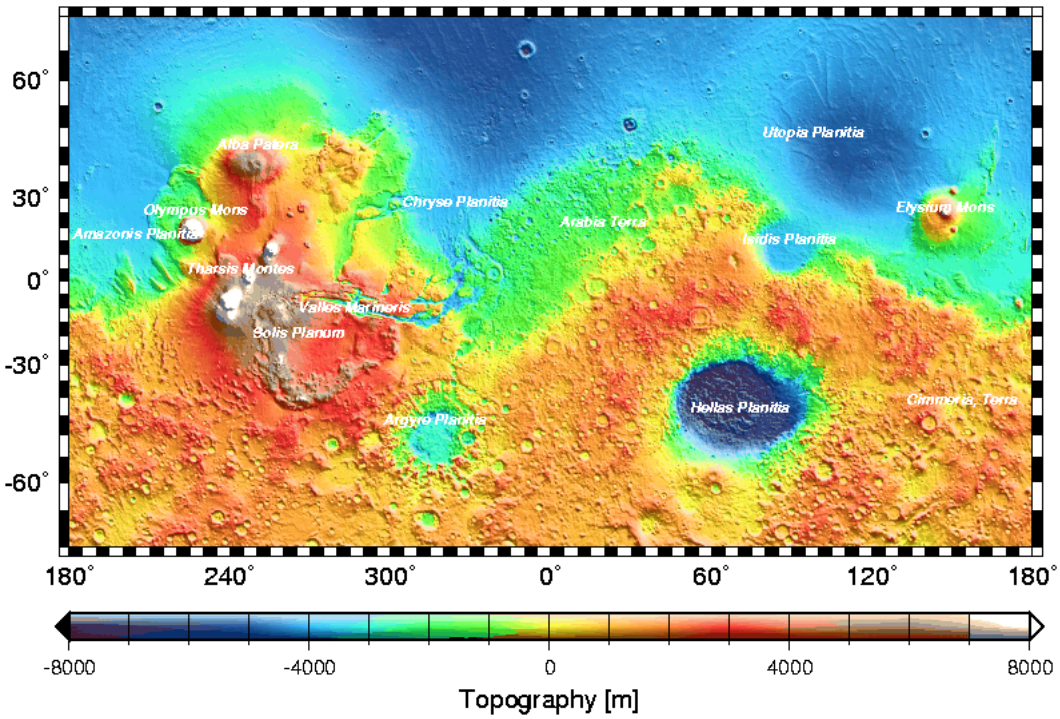

Figure 2.1: Global topographic map of Mars derived from the Mars Orbiter Laser Altimeter (MOLA) MGS that operated from 1996 to 2007. Some of the major surface features are labelled. Credit: MOLA Science Team.

Mars is approximately half the diameter of Earth, and with a density, i.e., mass per volume, lower than that of Earth; the gravitational field is weaker with an average gravitational acceleration of 3.72 m s^{-2}.

2.1.2 Composition

The atmosphere of Mars consists of about 95% CO_2, 3% nitrogen (N_2), 1.6% argon (Ar) and contains traces of O_2, and water (H_2O). The atmosphere is quite dusty, which gives the Martian sky a tawny color when seen from the surface. These particles, of sizes ranging from microns to millimetres, are in suspension in the Mars atmosphere; they cover the surface of Mars and become airborne by the strong Martian surface winds.

Although there is no liquid water on the surface of Mars in the present era, there is

a substantial amount in the atmosphere in the vapour phase, and a large concentration in the polar regions forming the polar ice caps. The total column concentration of H_2 varies with latitude and season, between 1 and 100 μm-atm (Clancy et al., 2000)[2]. This seasonal variability will further be explored in the next section. The presence of water vapour on Mars, despite its small abundance, renders the atmosphere in a state close to saturation and also influences the photochemistry of the lower atmosphere of Mars. H_2O is dissociated by photolysis into OH and H. The resulting chemical reactions are responsible for the rapid cycling of the HO_x species, e.g., H, OH and HO_2, from which is formed the radical OH that catalytically reacts with CO to replenish CO_2. The chemistry of the HO_x species is therefore responsible for the recycling and stability of CO_2.

Ozone (O_3) on Mars is formed through photo-dissociation of O_2 followed by recombination of O_2 with an oxygen atom. The average total column abundance is 15 μm-atm. O_3 can be rapidly photo-dissociated again into O_2. These species, O, O_2, and O_3, are referred as the O_x family because of the rapid cycling between them. This cycle is commonly known as the Chapman cycle and it is responsible for the large diurnal variations of the O_3 column abundance. The destruction of ozone is closely related to the HO_x radicals. In fact, there is a loose anti-correlation between the ozone and water vapour cycles (Lefèvre et al., 2004; Perrier, 2006). The largest amounts are found in the dry winter and spring seasons close to the polar caps in the latitude bands 50-70°, whereas the abundance is close to zero in summer.

2.1.3 Structure

Compared to Earth, the atmosphere of Mars is quite rarefied. Atmospheric pressure on the surface today ranges from a low of 0.3 mbar at the summit of Olympus Mons to over 11.55 mbar in the Hellas Planitia. The mean pressure at the surface level is 6.4 mbar, which is equal to the pressure found 35 km above the Earth's surface. The resulting

[2]The unit for total column abundance is 1 μm-atm = 2.69×10^{15} cm^{-2} on Mars.

maximum surface pressure is only 0.6% of that of the Earth (1,013.0 mbar). The scale height[3] of the atmosphere is about 10.8 km, which is higher than Earth's (6 km) because the surface gravity of Mars is only about 38% of Earth's, an effect offset by both the lower temperature and 50% higher average molecular weight of the atmosphere of Mars.

The average temperature at the surface of Mars is 220 K, which is below the triple-point of H_2O, meaning that liquid water is not possible on the surface of Mars at today's normal temperature and pressure conditions. The variations in temperature are pronounced: 145 K over the poles in wintertime versus 300 K at the equator in summertime. Contrary to Earth's atmosphere, the temperature profile shows a monotonically decreasing trend from the surface to about 45 km, where the temperature remains roughly constant until it reaches the exobase at about 250 km. Below 45 km, the temperature responds very rapidly to surface heating and to the global circulation. Between 45 and 120 km, there is a balance between CO_2-IR cooling from absorption of solar radiation and radiative heating. Above 120 km, which is the average height of the homobase that is the boundary between the neutral atmosphere, or homosphere, and the heterosphere where molecular diffusion dominates over eddy diffusion. The vertical profile of temperature in the Mars atmosphere is displayed in Figure 2.2.

As mentioned above, Mars experiences seasons in a similar fashion to Earth. To examine the seasonal variations, we will refer to the temperature distribution throughout a Martian year as measured by MCS on MRO, which is displayed in Figure 2.3. We observe that there is a symmetry in the structure during the equinoxes (L_S[4]=0 and 180°) with intense middle atmospheric polar warmings (above 10 Pa for latitudes poleward of

[3]For planetary atmospheres, the scale height is the vertical distance over which the pressure of the atmosphere decreases by a factor of e. The scale height remains constant for a particular temperature. It can be calculated by: $H = \frac{kT}{Mg}$ where k is the Boltzmann constant, (1.38×10^{23} J K^{-1}), T is the mean planetary surface temperature (in K), M is the mean molecular weight of dry air (in kg), and g is the acceleration due to gravity on planetary surface (in m s^{-2}).

[4]The apparent seasonal advance of the Sun at Mars is commonly measured in terms of the areocentric longitude L_S. As defined, L_S=0, 90, 180, and 270° indicate the Mars Northern hemisphere vernal equinox, summer solstice, autumnal equinox, and winter solstice, respectively.

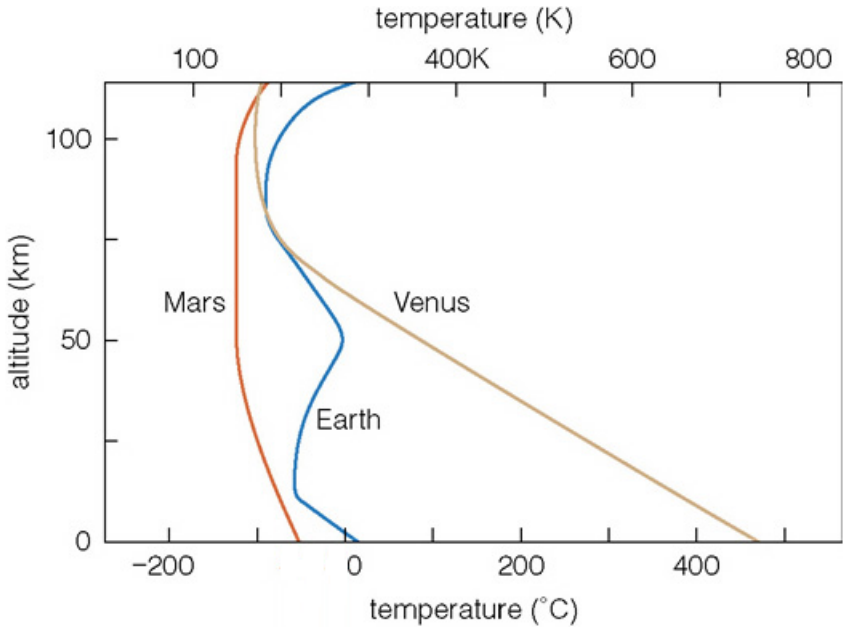

Figure 2.2: Schematic temperature profiles in the Mars, Earth, and Venus atmospheres for comparison. Figure copied from Nick Strobel's Astronomy Notes at [www.astronomynotes.com].

60°) overlying polar vortices of similar temperature. Conversely, the structure at the solstices (L_S=90 and 270°) shows a narrow winter middle atmospheric polar warming (above 40 km for latitudes poleward of 60°), a cold deep winter lower atmospheric polar vortex, and a summer low atmospheric polar warming (McCleese et al., 2010).

Related to the temperature distribution, MCS observed strong westerly jets in the extratropics, i.e., for latitudes between 30-60°, in both hemispheres during the equinoxes. During the solstices, there is one very strong jet in the extratropics of the winter hemisphere (McCleese et al., 2010). The annual variation of the wind structure is illustrated in Figure 2.4.

The presence of dust is responsible for variations in the opacity of the atmosphere, which induces strong temperature changes over the course of the seasons. When considering the dust cycle, as shown in Figure 2.5, the equinoxes are characterized by penetration of dust to high altitudes, up to 30 km, over the tropics and a lower height of penetration

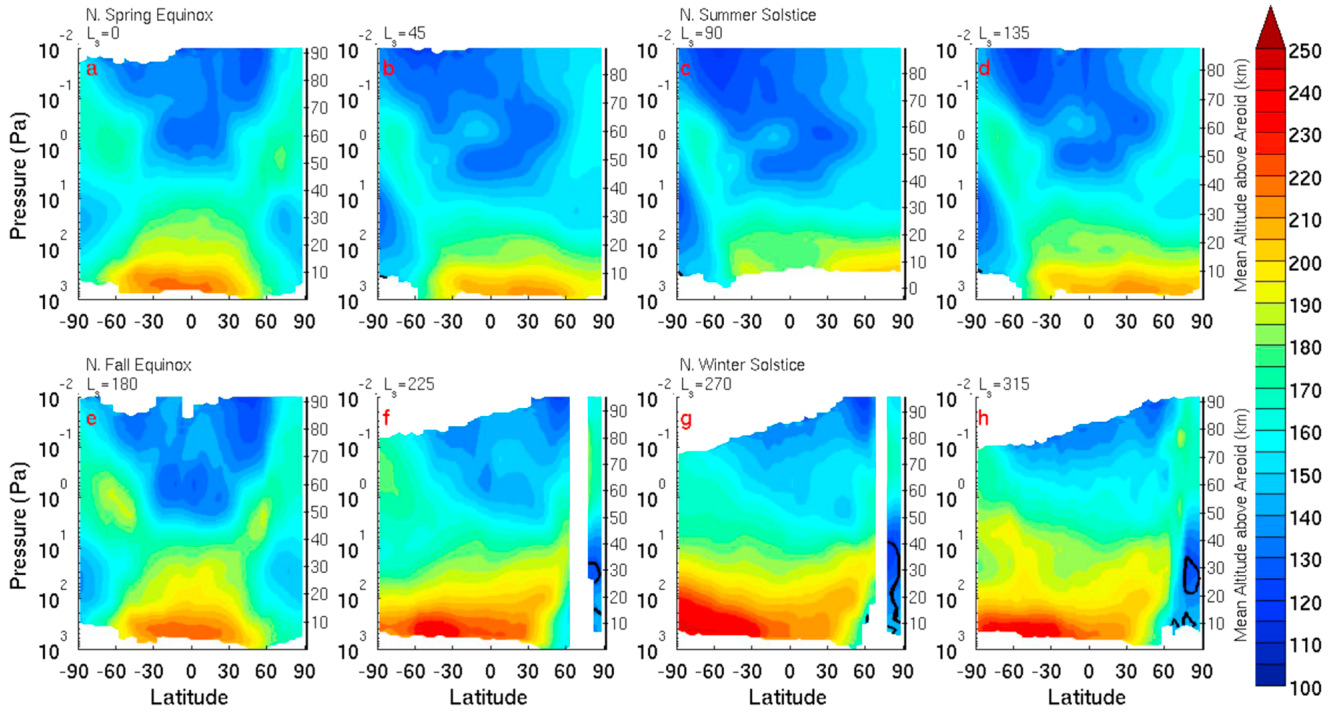

Figure 2.3: Zonal-average temperature (K) nightside retrievals of MY 29 for the L_S bins, i.e., average of 5° centered at L_S, labelled at the top of each panel. Contours are every 5 K. The black contour indicates the CO_2 condensation point. Figure taken from McCleese et al. (2010).

near the poles. During the solstices, there is also a penetration of dust to high altitudes over the tropics, but a clean atmosphere resides in the winter hemisphere over the mid-latitudes and extends to the pole, as well as a region of moderate dust load that starts in the tropics in the winter hemisphere and extends towards the summer pole (McCleese et al., 2010). The seasonal variability of the dust load is related to the water cycle and the peculiar dynamics that play around the polar caps. Importantly, an increase in dust loading causes an increase in CO_2 since the absorption of incoming solar radiation, or insolation for short, by dust reduces the O_3 loss mechanism.

Above 20 km, the annual altitude vs. latitude distribution of H_2O, shown in Figure 2.6, is clearly determined by the variations in temperature (see Figure 2.3), in response to

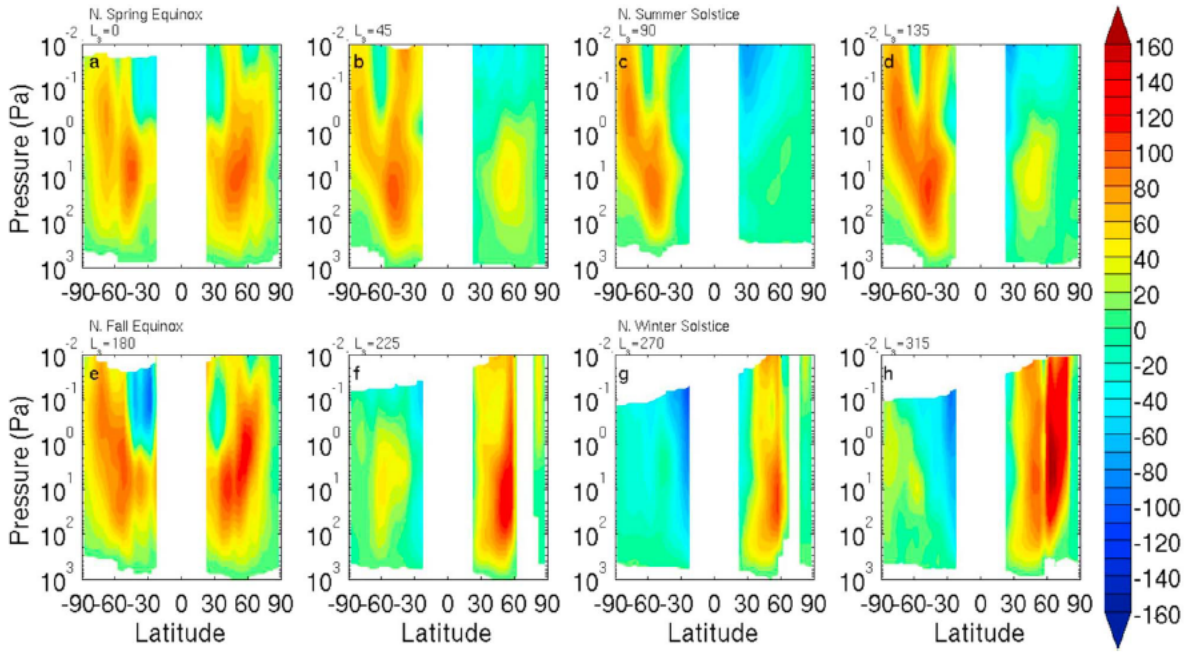

Figure 2.4: Wind velocity (m s^{-1}) nightside retrievals of MY 29 for the L_S bins labelled at the top of each panel. Contours are every 10 m s^{-1}. Figure taken from McCleese et al. (2010).

the evolution of dust (see Figure 2.5), and solar flux along the orbit. Around aphelion[5], the cold and dust-free atmosphere leads to a low saturation altitude for water vapour (at 10-15 km) with rapidly increasing mixing ratio above the hygropause[6]. After aphelion, the hygropause shows a steady increase until perihelion[7], where it is found above 40 km. In winter in both hemispheres, condensation suppresses most of the atmospheric H_2O-vapour, with an asymmetry between the Southern summer and northern summer, where there is less H_2O during the former, coinciding with aphelion, than the latter occuring during perihelion (Lefèvre et al., 2004).

[5]Aphelion occurs at L_S=71°.
[6]Altitude where the water vapour condenses.
[7]Perehelion occurs at L_S=251°.

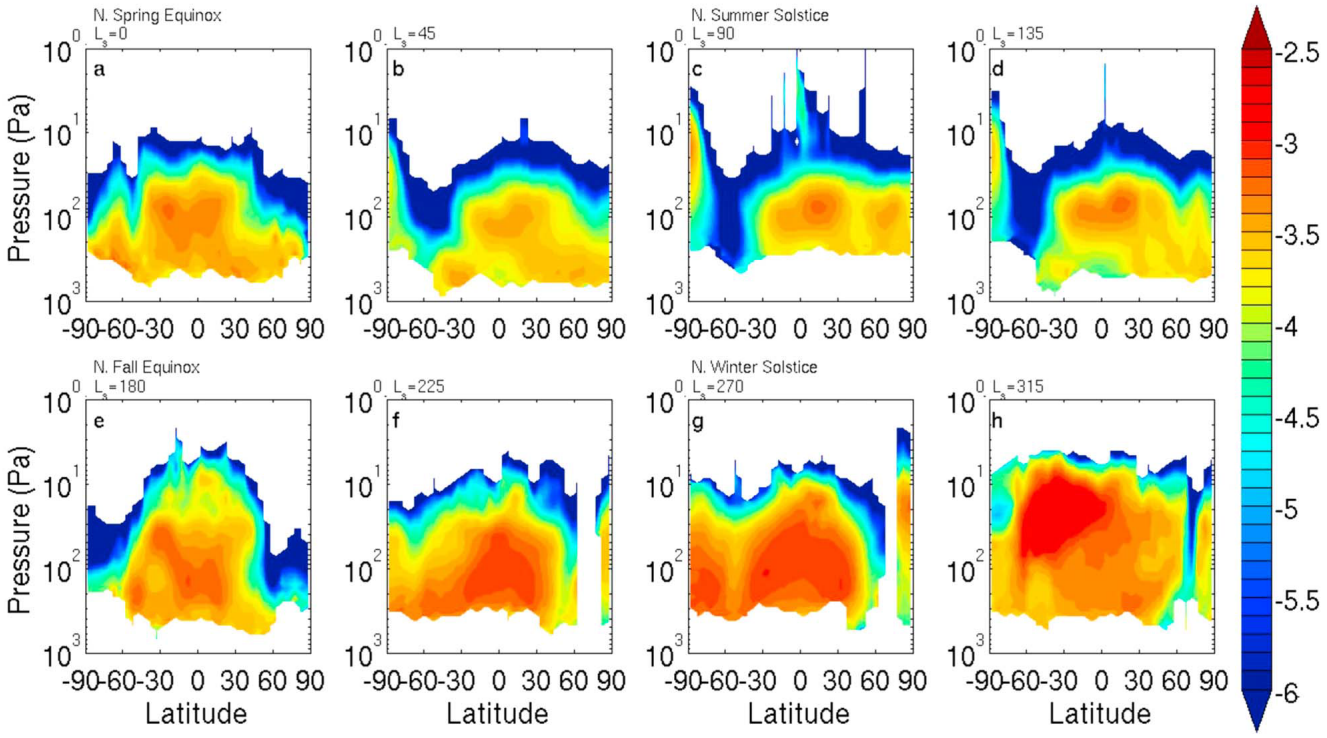

Figure 2.5: Log_{10} of the zonal average dust density-scaled opacity ($\mathrm{m}^2\ \mathrm{kg}^{-1}$) nightside retrievals of MY 29 for the L_S bins labelled at the top of each panel. Contours are shown every 0.1 log units. Note the pressure scale is between 1000 and 1 Pa. Figure taken from McCleese et al. (2010).

2.2 The atmosphere of Venus

Venus is the second planet of the Solar System, and its name refers to the Roman goddess of love and beauty. Venus is classified as a terrestrial planet and it is sometimes called Earth's "sister planet" owing to their similar size, gravity, and bulk composition. Venus is both the closest planet to Earth and the planet closest in size to Earth. It is covered with an opaque layer of highly reflective clouds of sulfuric acid, preventing its surface from being seen from space in visible light.

About 80% of the Venusian surface is covered by smooth, volcanic plains. Two highland "continent"-like features make up the rest of its surface area, one lying in the planet's Northern hemisphere and the other just south of the equator. Figure 2.7 presents

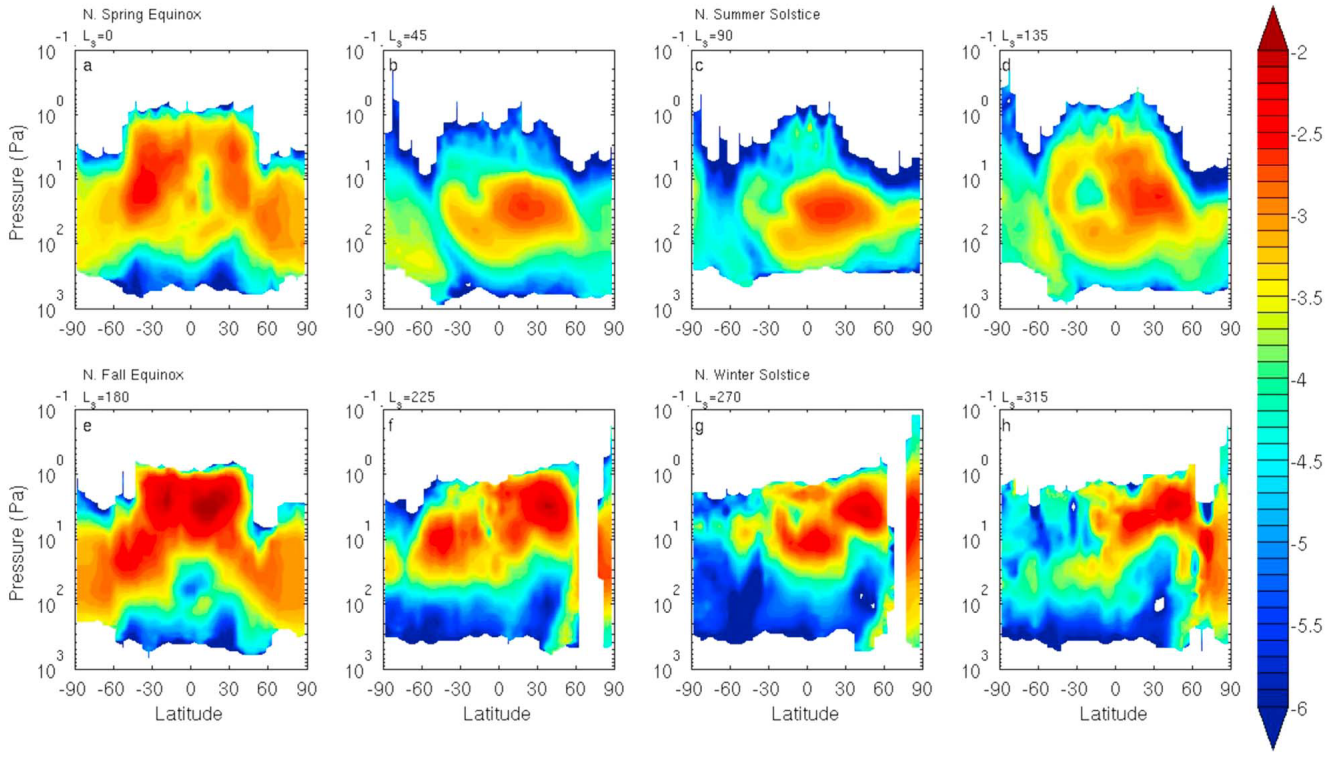

Figure 2.6: Log_{10} of the zonal-average water-ice density-scaled opacity ($\mathrm{m}^2\ \mathrm{kg}^{-1}$) night-side retrievals of MY 29 for the L_S bins labelled at the top of each panel. Contours are shown every 0.1 log units. Note the pressure scale is between 1000 and 1 Pa. Figure taken from McCleese et al. (2010).

the topography of Venus as provided by the Magellan mission.

2.2.1 Orbital and physical properties

Venus orbits the Sun at an average distance of about 108×10^6 km (0.72 AU), and completes an orbit every 224.65 (Earth) days. Although all planetary orbits are elliptical, Venus' orbit is the closest to circular, with an eccentricity of less than 0.01.

All the planets of the Solar System orbit the Sun in a counter-clockwise direction as viewed from above the Sun's North pole. Most planets also rotate on their axis in a counter-clockwise direction, but Venus rotates clockwise (called"retrograde" rotation) once every 243 (Earth) days, which is by far the slowest rotation period of any major

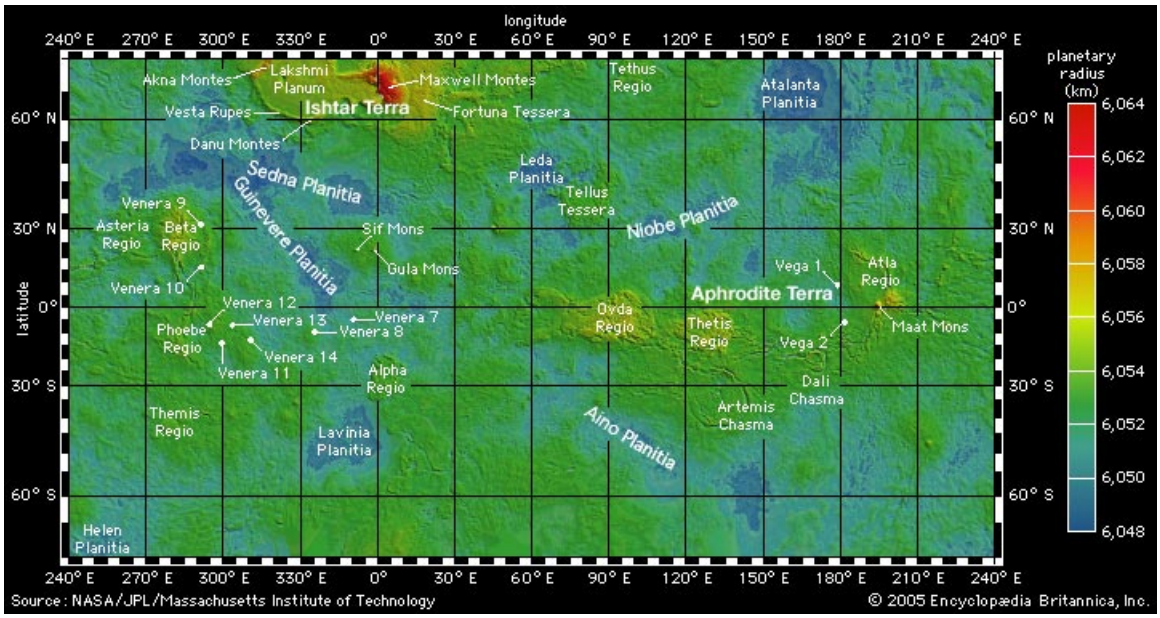

Figure 2.7: Global topographic map of Venus derived from laser altimetry data gathered by the Magellan spacecraft, which carried out observations from orbiting the planet between 1990 and 1994. Some of the major surface features are labelled. Credit: Magellan Science Team.

planet. Interestingly, Venus' rotation has slowed down by 6.5 minutes per day since the Magellan spacecraft visited it in 1996! A Venusian sidereal day[8] lasts longer than a Venusian year: 243 versus 224.7 (Earth) days. Because of the retrograde rotation, the length of a solar day on Venus is significantly shorter than the sidereal day. As a result of Venus's relatively long solar day, one Venusian year is about 1.92 Venusian days long! To an observer on the surface of Venus, the Sun would appear to rise in the west and set in the east and the time from one sunrise to the next would be 116.75 (Earth) days.

[8]A sidereal day is the length of time which passes between a given "fixed" star in the sky crossing a given projected meridian on the planet's surface. It is different than a solar day which is the length of time which elapses between the Sun reaching its highest point in the sky two consecutive times; we commonly refer to the latter as "the" day.

2.2.2 Composition

Venus has an extremely dense atmosphere, which consists mainly of CO_2 (95%) and a small amount of N_2 (3.5%). Above the dense CO_2 layer are thick clouds consisting mainly of sulfur dioxide (SO_2) and sulfuric acid (H_2SO_4) droplets. This cloud layer has its base around 40 km and extends to heights above 60 km. The planet-encircling cloud layer reflects and scatters back to space about 90% of the insolation. The permanent cloud cover means that although Venus is closer than Earth to the Sun, the Venusian surface receives less insolation.

2.2.3 Structure

The pressure at Venus's surface is about 92 times that at Earth's surface; this surface pressure is equivalent to that at a depth of nearly 1 km within Earth's oceans. The CO_2-rich atmosphere, along with thick clouds of SO_2, generates the strongest greenhouse effect in the Solar System, creating surface temperatures of over 760 K.

The vertical structure of Venus is characterized by three distinct layers. From the surface to the top of the cloud layer, between 0 and ∼60 km, the temperature steeply decreases; this region is referred as the troposphere. From the cloud layer top to the homopause, at ∼100 km, the region is mainly isothermal, and is called the mesosphere. Then, above 100 km up to the exobase, the thermosphere is characterized by rising temperature. Because of the cloud layer, there is a physical boundary between the atmospheric conditions above and below 60 km. Because of the difficulty in reconciling the physical and dynamical processes that govern these two atmospheric layers, it is very common to study the lower and upper atmospheric regions separately. The vertical structure of temperature in the Venus atmosphere is shown in Figure 2.2.

The main feature of the Venusian atmosphere is a convectively driven Hadley cell, which extends from the equatorial region up to about 60° latitude in each hemisphere,

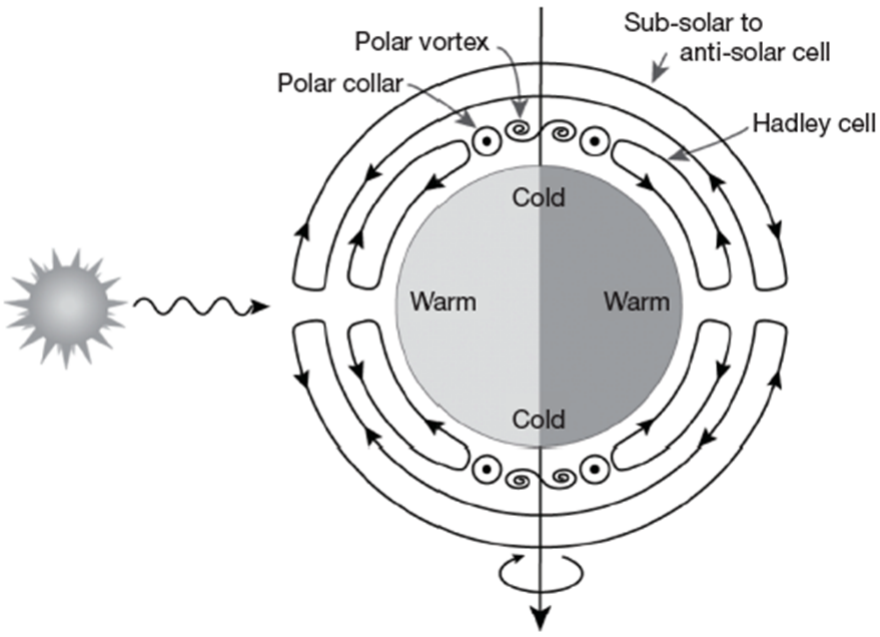

Figure 2.8: Schematic view of the general circulation of the atmosphere of Venus. Figure taken from Svedhem et al. (2007).

as depicted in Figure 2.8. The trend is polewards at all levels that can be observed by tracking the winds (at about 50–65 km altitude above the surface), so the return branch of the cell must be in the atmosphere below the clouds. The Hadley cell generates a mid-latitude jet at its poleward extreme, which forms a circumpolar belt characterized by remarkably low temperatures and dense, high clouds. This break in the Hadley cell and the slow Venusian rotation creates a cold "polar collar" around each pole at about 70° latitude. Inside the collar, a thinning of the upper cloud layer forms a complex and highly variable feature, called the "polar dipole" in earlier literature describing poorly resolved observations, which appears bright in the thermal IR region. In general, a thinner-than-average or lower-than-average cloud is often associated with a descending airmass, and vice versa, such that the vortex may represent a second, high-latitude circulation cell, resembling winter hemisphere behaviour on Earth.

Strong winds of 100 m s^{-1} at the cloud tops circle the planet about every four to five

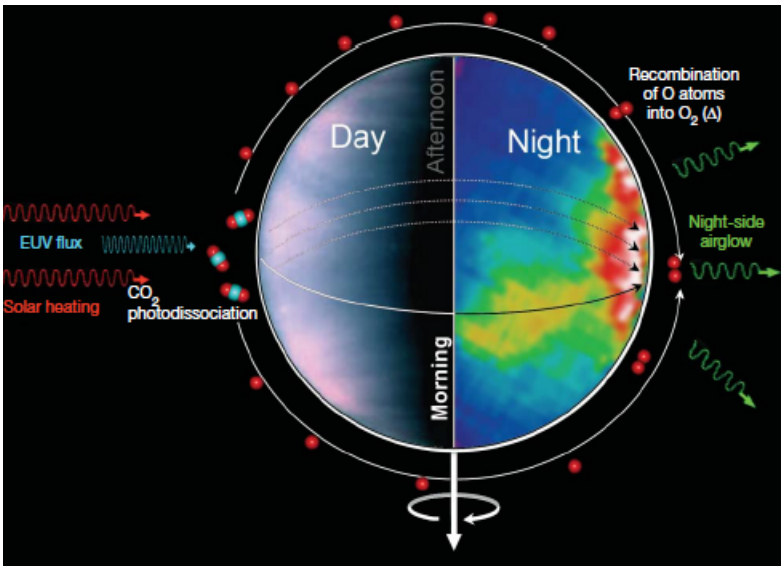

Figure 2.9: Schematic view of the transport of atoms from the dayside to the nightside of Venus. Figure taken from Svedhem et al. (2007).

(Earth) days; Venusian winds move at up to 60 times the speed of the planet's rotation. Above about 100 km, the circulation regime on Venus changes from the equatorial-to-polar circulation completely to a sub-solar to anti-solar pattern (SSAS). Oxygen airglow emission at 1.27 μm reveals the recombination of oxygen atoms into molecular oxygen while descending to lower altitudes in the anti-solar region (Svedhem et al., 2007). Additional evidence of this circulation is given by the upper-atmosphere temperature profiles, which show a pronounced temperature maximum on the night side that is due to compressional heating in the downward branch of the circulation cell. Figure 2.9 illustrates the transport of oxygen atoms from the sub-solar side to the anti-solar side where they recombine to generate O_2 airglow.

Chapter 3

The phenomenon of airglow

Airglow is a definition for emissions of photons that arise from electronic transitions of excited species in a planetary atmosphere (Slanger et al., 2008). This thesis focuses on the airglow features that result from the emission of photons following radiative deactivation of electronically excited molecules in the neutral atmosphere.

Airglow and aurorae, although both referring to emissions of light in planetary atmospheres, arise from different mechanisms. Slanger et al. (2008) define auroral emissions as "atmospheric photoemissions caused by the impact of energetic primary particles from the near-space environment, either directly or through the agency of the secondary particles produced by the impacts."

In this chapter, we discuss the mechanism producing the airglow emissions under investigation in this thesis. We also explain how airglow features can be used to investigate atmospheric properties.

3.1 Source of airglow emissions

At nighttime, the main source of the nightglow in the Martian and Venusian neutral atmospheres arise from a chemiluminescence mechanism:

$$X + Y \rightarrow XY* \rightarrow XY + h\nu \tag{3.1}$$

(Slanger et al., 2008). The atoms X and Y are formed on the dayside and transported to the nightside by the global circulation, where they recombine into a molecule XY, passing though an intermediate $XY^{\star}$. The energy released from this recombination, $h\nu$, is referred to as airglow and the exact frequency ν of the photon corresponds to a specific electronic transition of XY.

3.2 Airglow as a proxy for temperature measurements

In planetary atmospheres, airglow measurements have been used to derive the temperature at the exobase[1], which is often referred to as the exospheric temperature. From the airglow scale height, i.e., the height over which the airglow intensity decreases by a factor of e^{-1}, it is possible to extract the temperature following a simple expression detailed in Stewart (1972):

$$T = \frac{mg}{k} \frac{z_2 - z_1}{\ln n_2 - \ln n_1} \tag{3.2}$$

where m is the mass of the molecule, g and k are the gravitational acceleration and Boltzmann constant, respectively, and n_i is the number density at altitude z_i. The accuracy of this method is usually low because the vertical density distribution of the constituents varies greatly over the airglow layer. Moreover, there is no physical justification for the ratio of densities to be constant with altitude.

[1]The exobase defines the height above which there are negligible atomic collisions between the particles in a planetary atmosphere.

Another possibility using airglow detection is to measure the rotational temperature of the excited molecules, as was first proposed by Meinel (1951), assuming the targeted species is thermalized, i.e., the species has reached a thermal equilibrium with the environment, before de-excitation occurs by emission of light. According to Meinel, if we can resolve the ro-vibrational transition lines in the intensity spectra, the ratio between two nearby lines would give the rotational temperature of the emitting species, following the equation:

$$T = \frac{\frac{hc}{k}(F_b - F_a)}{\ln \frac{I_a}{I_b} \frac{A_b(2J_b+1)}{A_a(2J_a+1)}} \tag{3.3}$$

where h is the Planck constant, c is the speed of light, F is the rotational energy of the line, I is the intensity, A is the transition probability, and J is the quantum rotational number. This derivation follows the assumption of a Boltzmann distribution. This technique has strong heritage on Earth, where the O_2 and OH emissions have been used to derive temperature profiles in the mesosphere, She and Lowe (e.g., 1998); Melo et al. (e.g., 2001). However, current instruments flying on planetary missions do not have sufficient spectral resolution to separate the rotational lines, making it challenging to obtain an accurate rotational temperature.

Lastly, assuming an accurate modelling of specific airglow features using spectroscopic knowledge of the specific transitions and precise measurements of the kinetic parameters involved in the emission processes, spectra recorded with an airglow detector can be compared with simulated spectra. Given that the ratio between the intensity of ro-vibrational emission lines depends on the ambient temperature (assuming the molecules are thermalized before emission), the temperature profile can be derived with an iterative method that searches for the best match between the synthetic spectra produced for different temperatures and the observed spectrum using, for example, an optimal estimation method. A temperature profile can be derived over the airglow layer for each band system recorded, providing an estimate of the accuracy of the profiles. The technique is attractive because it also enables the derivation of the atomic oxygen density

profile from measurement of column-integrated intensity as first proposed by Sharp and McDade (1996) and later tested with emissions from Earth's mesosphere (Haley et al., 2000; Melo et al., 2001).

Chapter 4

Spectroscopy

Spectroscopy concerns the interaction of light with matter. More specifically, it is the study of the absorption, emission, and scattering of electromagnetic radiation. The use of spectroscopy is of particular importance for planetary atmospheric studies since it enables the remote investigation of the composition, structure, and circulation of the atmosphere of a planet. Spectroscopic information is quantitatively represented by a spectrum, which is a plot of the response of interest, e.g., intensity, as a function of wavelength or frequency.

To properly understand the physics of airglow, it is of fundamental importance to learn how the atoms and molecules manage their internal energy within their electronic configuration. The electron configuration is the distribution of electrons of an atom or molecule in atomic or molecular orbitals. Although a solid background in quantum physics is needed to fully describe the energy distribution in atoms and molecules, it is possible to simplify the subject matter and focus on explaining the symbols and nomenclature used in molecular spectroscopy needed to describe the aeronomical processes of interest in this thesis. This is the aim of the present chapter. However, in-depth discussions of the subject can be found in the literature, (e.g., Herzberg, 1950; Hollas, 1992; Bernath, 2005). Gombosi (1998) is a good reference for a discussion of spectroscopy

geared towards airglow applications.

4.1 Electronic configuration of atoms

4.1.1 Case for one electron

Following the Bohr model, we assume that the energy of the electron is quantized: $E_n \propto \frac{1}{n^2}$ where $n = 1, 2, 3, ...$ refers to the principal quantum number and defines the particular electron shell with energy E_n. Each value of the shell is assigned a specific capital letter, as is listed in Table 4.1.

Table 4.1: Designations associated with the quantum numbers n, l, and λ of an electron.

	0	1	2	3	4	5
n		K	L	M	N	O
l	s	p	d	f	g	h

The total angular momentum, $\vec{J}$, is the sum of the orbital, or azimuthal, angular momentum, $\vec{L}$, and the intrinsic, or electron spin, angular momentum, $\vec{S}$, of the electron: $\vec{J} = \vec{L} + \vec{S}$. Therefore, the total angular momentum quantum number, j, is the sum of the orbital, or azimuthal, quantum number, l, and the spin quantum number, s: $j = |l \pm s|$. The orbital quantum number defines the magnitude of the orbital angular momentum of an electron and can take any values: $l = 0, 1, 2, ..., n - 1$, each assigned a lowercase letter, as can be looked up in Table 4.1. Each value of l defines a subshell. So far, by knowing the values n and l, we know the position of the electron around the atomic nucleus. Lastly, the value of s is $s = \frac{1}{2}$.

In general physical terms, the total angular momentum vector is a vector precessing around an axis. In the case of the electron, the known component of $\vec{L}$ is quantized and can only take values $L = m_l\hbar$ where $m_l = 0, \pm1, \pm2, ..., \pm l$ is the magnetic quantum number, which corresponds to the projection of the orbital angular momentum along a

specified axis, i.e., the orientation of the subshell's shape. Therefore, for each subshell, there are $2l+1$ possible orbitals. Lastly, the projection of the intrinsic angular momentum along a specified axis is also quantized and is given by $S = m_s\hbar$, where $m_s = \pm s$ is the spin projection quantum number, i.e., the orientation of the spin. Hence, the projection of the total angular momentum along a specified axis is $J = m_j\hbar$, where m_j can take any values $m_j = 0, \pm 1, \pm 2, ..., \pm j = m_l + m_s$.

4.1.2 Atomic ground states

The Pauli Exclusion Principle states that no two electrons can take the same quantum numbers (n, l, m_l, m_S). Hence, each orbital on each subshell can accommodate two electrons. Given that each subshell has $2l + 1$ orbitals, then $2(2l + 1)$ electrons can be found on each subshell, such that the maximum number of electrons on each shell is $2n^2$. Table 4.2 is a visual representation of the way the electrons are arranged in their electronic configuration within an atom. We summarize the above discussion by computing the electronic configuration of the nitrogen and oxygen atoms that contain seven and eight electrons, respectively:

- nitrogen: $1s^2, 2s^2, 2p^3$
- oxygen: $1s^2, 2s^2, 2p^4$

given that $n = 2$ and $l = 1$, such that $\lambda = 0, \pm 1$, and that the nitrogen atom has three electrons on its outer shell, while the oxygen atom has four.

4.1.3 Atomic excited states

The above discussion referred to the ground state of atoms; describing atomic excited states turns out to be more challenging. In this case, we have to consider the Coulomb interactions between the electrons, interactions among the angular momentum and spin

Table 4.2: Configuration of the electrons in a given atom.

n	1	2		3		
shell	K	L		M		
l	0	0	1	0	1	2
subshell	1s	2s	2p	3s	3p	3d
m_l	0	0	0, 1	0	0, 1	0, 1, 2
s	$\frac{1}{2},-\frac{1}{2}$	$\frac{1}{2},-\frac{1}{2}$	$\frac{1}{2},-\frac{1}{2}$, $\frac{1}{2},-\frac{1}{2}$	$\frac{1}{2},-\frac{1}{2}$	$\frac{1}{2},-\frac{1}{2}$, $\frac{1}{2},-\frac{1}{2}$	$\frac{1}{2},-\frac{1}{2}$, $\frac{1}{2},-\frac{1}{2}$, $\frac{1}{2},-\frac{1}{2}$
spin	↑,↓	↑,↓	↑,↓, ↑,↓	↑,↓	↑,↓, ↑,↓	↑,↓, ↑,↓, ↑,↓
$2(2l+1)$	2	2	6	2	6	10
$2n^2$	2		8			18

vectors, and the interactions among the spin vectors of different electrons, on top of these between the electrons and the atomic nucleus.

To help with this description, a scheme called Russell-Saunders coupling was elaborated to provide a relatively simple recipe to understand one case of angular momentum coupling. In this scheme, the total orbital angular momentum and total spin vectors of the atom are the sums of the vectors of the individual electrons:

$$\vec{L} = \sum_i \vec{L_i} \text{ and } \vec{S} = \sum_i \vec{S_i} \text{ such that } \vec{J} = \vec{L} + \vec{S}.$$

Then, the quantum numbers associated with the projection of these three angular momentum vectors along a specified axis become:

$$M_L = \sum_i (m_l)_i \text{ and } M_S = \sum_i (m_s)_i \text{ such that } M_J = M_L + M_S.$$

These three quantum numbers can assume any value within the limits:

$$-L \leq M_L \geq L \text{ and } -S \leq M_S \geq S \text{ such that } \mid L - S \mid \leq M_J \geq L + S.$$

Therefore, there are $2L+1$ and $2S+1$ possible values for M_L and M_S, respectively. The energy level can be labelled as ^{2S+1}L, with L represented by its capital letter from Table 4.3, which gives the total degeneracy of a level J: $g = (2L+1)(2S+1)$.

Table 4.3: Designation associated with the quantum number L for the electronic configuration of an atom.

	0	1	2	3	4	5
L	S	P	D	F	G	H

On a filled subshell, the ensemble of electrons that comprise it yields a total angular momentum of zero since $\sum_i m_l = 0$ and $\sum_i m_s = 0$. Hence, the total angular momentum of the atom only depends on the contribution from the electrons on the outer unfilled subshell. These electrons determine the values of L and S that will yield the possible spectral emissions; hence, these parameters are referred to the spectral terms. From the above discussion, we can tentatively find the energy term that corresponds to the ground state of the nitrogen atom. Since nitrogen has three electrons in its outer unfilled shell that can each take the value $s = \frac{1}{2}$, then $S = \frac{1}{2}, \frac{3}{2}$ and $M_S = -\frac{3}{2}, -\frac{1}{2}, \frac{1}{2}, \frac{3}{2}$. Additionally, the value of l for each electron is $l = 1$, so $L = 0, 1, 2$ and $M_L = -2, -1, 0, 1, 2$. Therefore, there are 20 possible combinations (M_L, M_S) for the electronic configuration of the ground state of the nitrogen atom. Similarly for the oxygen atom which has four electrons in the outer unfilled shell, resulting in $S = 0, 1$ and again $L = 0, 1, 2$. Then, we arrive with the possible terms for the ground state of the nitrogen and the oxygen atoms:

- nitrogen: $1s^2, 2s^2, 2p^3 \Rightarrow {}^2\mathrm{P}$, ${}^2\mathrm{D}$, ${}^4\mathrm{S}$
- oxygen: $1s^2, 2s^2, 2p^4 \Rightarrow {}^1\mathrm{S}$, ${}^1\mathrm{D}$, ${}^3\mathrm{P}$

A set of empirical rules was developed to predict the lowest energy term arising from an electronic configuration. These rules are now referred to as Hund's Rules:

1. The term with the highest multiplicity, i.e., $2S + 1$, lies lowest in energy;
2. The term with the highest value of L lies lowest in energy for equal multiplicity;
3. The term with the lowest value of J lies lowest in energy within a similar manifold.

In a more simplified explanation, if two or more orbitals of equal energy are available, electrons will occupy them singly before filling them in pairs. We can therefore decide on the electronic configuration of the ground state of the nitrogen and oxygen atoms. For nitrogen, the highest multiplicity is $2S+1 = 4$, since $S = 3 \times s = \frac{3}{2}$, while for the oxygen atom, the highest multiplicity is $2S+1 = 2$ since $S = 3 \times s - s = 1$. Hence, the states ^{4}S and ^{3}P are the ground electronic states of the nitrogen and oxygen atoms, respectively, while the remaining states, i.e., ^{2}P, ^{2}D for nitrogen and ^{1}S, ^{1}D for oxygen, are possible excited states.

4.2 Electronic configuration of molecules

To explain the electronic configuration of molecules, we can extend the above discussion about the electronic configuration of many-electron interactions within atoms to many-electron interactions between different atoms. In the case of diatomic molecules, like molecular oxygen and nitrogen, we use the term Λ to describe the projection of the orbital angular momentum along the internuclear axis, which is the analogy of L in the case of atoms. However, here, we use the upper-case Greek letters to denote excited electronic states, following the convention in Table 4.4. Moreover, for diatomic molecules, there is a double degeneracy of the atomic orbital such that it is useful to define the orbitals with the quantum number $\lambda = \mid m_l \mid$, which we assigned a Greek lowercase letter, as shown in Table 4.4. The definition of the projection of the electron spin angular momentum onto the internuclear axis is similar to that for atoms, such that $\Sigma = 0, \pm 1, \pm 2, ..., \pm S$ is the analogy to M_S, and the multiplicity remains $2S + 1$. Hence, we express the excited electronic state as $^{2S+1}\Lambda$. Lastly, the projection of the total angular momentum onto the internuclear axis is now expressed by the Greek letter Ω and it is given by: $\Omega = \mid \Lambda + \Sigma \mid$. Figure 4.1 provides a visual representation of the different angular momenta in a diatomic molecule.

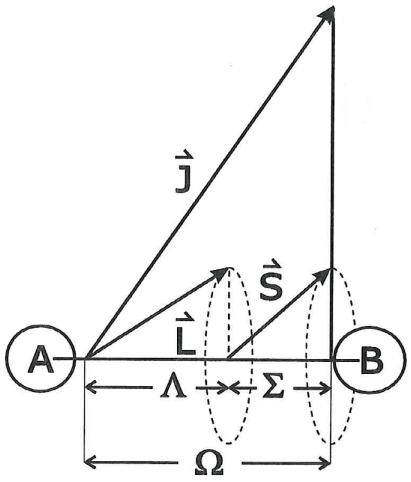

Figure 4.1: Schematic of the angular momenta in a diatomic molecule formed with atoms A and B. $\vec{J}$ is the total angular momentum with Ω being its projection on the internuclear axis, $\vec{L}$ is the orbital angular momentum with Λ being its projection on the internuclear axis, $\vec{S}$ is the spin angular momentum with Σ being its projection on the internuclear axis. Figure copied from Bernath (2005).

Table 4.4: Designation associated with the quantum number Λ for the electronic configuration of a molecule.

	0	1	2	3	4
Λ	Σ	Π	Δ	Φ	Γ
λ	σ	π	δ	ϕ	γ

Now, for diatomic molecules, there are additional parameters needed for the description of the electronic structure of the atoms. For homonuclear molecules, like O_2, there is a symmetry for reflection with respect to a plane perpendicular to the internuclear axis. The electronic configuration can remain unchanged, which is called "ungerade", or can change sign, which is called "gerade", following this reflection. We use the subscripts u and g, for "ungerade" and "gerade", respectively, when we write the state configuration. The other symmetry property applies to all diatomic molecules and it concerns the reflection with respect to any plane crossing the internuclear axis. If the reflection is

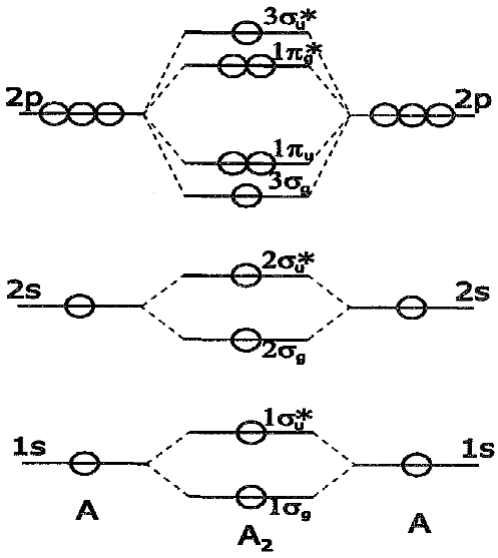

Figure 4.2: Molecular orbital diagram for diatomic molecules. Note that for N_2, the order of the $\pi_u 2p$ and $\sigma_g 2p$ states are switched. The asterisk implies antibonding character due to the nodal plane, perpendicular to the internuclear axis, of such orbitals (Hollas, 1992). Figure copied from Bernath (2005).

symmetric, it is labelled +, if not, we use the sign − as a superscript to the electronic state label. This last symbol is often used for Σ states, but usually not for the Π, Δ, Φ states. Hence, with the help of Figure 4.2 to place the electrons on the orbitals in order, we have the following electronic configuration and corresponding possible spectral terms for the ground states of NO and O_2:

- NO: $(\sigma_g 1s)^2(\sigma_u^\star 1s)^2(\sigma_g 2s)^2(\sigma_u^\star 2s)^2(\sigma_g 2p)^2(\pi_u 2p)^4(\pi_g^\star 2p)^1 \Rightarrow\ ^2\Pi, ^2\Sigma$
- O_2: $(\sigma_g 1s)^2(\sigma_u^\star 1s)^2(\sigma_g 2s)^2(\sigma_u^\star 2s)^2(\sigma_g 2p)^2(\pi_u 2p)^4(\pi_g^\star 2p)^2 \Rightarrow\ ^1\Sigma_g^+, ^3\Sigma_g^-, ^1\Delta_g$

since $\Lambda = 0, 1$ and $S = \frac{1}{2}$ for NO while $\Lambda = 0, 2$ and $S = 0, 1$ for O_2.

Finally, there is another convention when labelling electronic states. The ground state is labelled X, and the excited states with the same multiplicity as that of the ground state are named with upper-case letters in alphabetic order with increasing energy. For the excited states with a different multiplicity, we use the lower-case letters, a, b, c, ...,

in order of increasing energy. Again, Hund's Rules apply for deciding which of the states would be the ground state, such that:

- NO: $X^2\Pi$
- O_2: $X^3\Sigma_g^-$

are the states that lie lowest in energy. Hund's Rules are also used for ordering, e.g., for O_2: ${}^3\Sigma_g^- <^1 \Delta_g <^1 \Sigma_g^+$.

4.3 Electronic transitions in diatomic molecules

Electronic transitions occur within molecules for energies less than the energy difference between the ground state energy and the dissociation energy of that molecule. Transitions between electronic states are allowed given that they obey the electric-dipole selection rules:

1. projection of the orbital angular momentum: $\Delta\Lambda=0,\pm1$
2. multiplicity: $\Delta S=0$
3. projection of the electronic spin angular momentum: $\Delta\Sigma=0$
4. projection of the total angular momentum: $\Delta\Omega=0,\pm1$
5. +/- symmetry: + $\nleftrightarrow$ -
6. g/u parity: g $\leftrightarrow$ u .

The allowed transitions yield the strongest spectral features.

There are other transitions possible and they are called "forbidden" since they are not allowed by the first-order selection rules above. In special circumstances, the transitions follow the second-order selection rules, or magnetic-dipole rules:

1. projection of the orbital angular momentum: $\Delta\Lambda$=0,$\pm$1

2. multiplicity: ΔS=0

3. projection of the electronic spin angular momentum: $\Delta\Sigma$=0

4. projection of the total angular momentum: $\Delta\Omega$=0,$\pm$1

5. +/- symmetry: + $\leftrightarrow$ -

6. g/u parity: g $\nleftrightarrow$ u

Although the transitions allowed by these rules are nominally "forbidden", there is a small probability of their spontaneous occurrence, should an atom or molecule be raised to an excited state. More precisely, there is a certain probability that such an excited molecule will make a forbidden transition to a lower energy state per unit time; by definition this probability is much lower than that for any transition permitted by the electric-dipole selection rules. Therefore, if a state can de-excite via a permitted transition, or otherwise, e.g. via collisions, it will almost certainly do so rather than choosing the forbidden route. Nevertheless, "forbidden" transitions are only relatively unlikely: states that can only decay in this way are so-called meta-stable states. These excited states usually have lifetimes of order milliseconds to seconds, compared to less than a microsecond for decay via permitted transitions, e.g., $^1\Delta_g$ for O_2.

An electronic transition also comprises vibrational bands, as is illustrated in Figure 4.3. Each electronic level is made up of vibrational levels, which arise from vibrations in a periodic motion of the atoms in a molecule. A progression is a transition with a common upper v' or lower v'' vibrational level. Vibrational transitions that accompany electronic transitions are named vibronic transitions. The ensemble of vibronic transitions is a spectral band, while the spectral bands associated with a given electronic transition is an electronic band system.

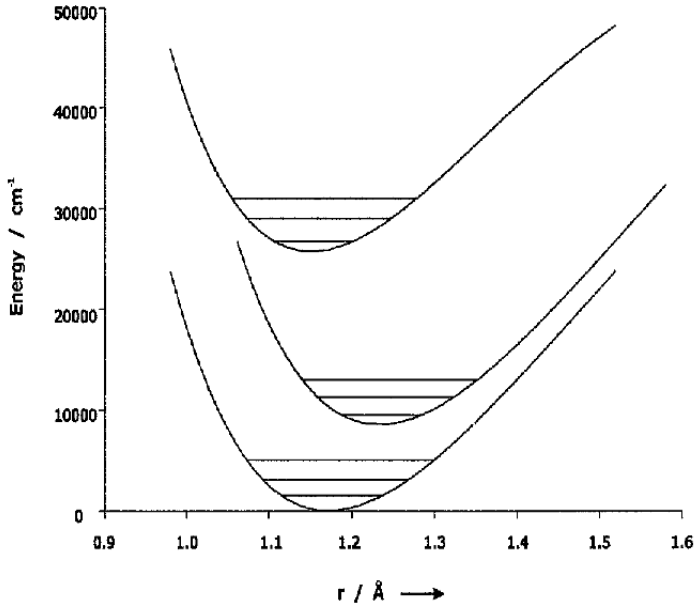

Figure 4.3: Schematic of the potential energy (cm^{-1}) vs. the internuclear distance ($\mathring{A}$) in a molecule showing the vibrational energy levels (horizontal lines) embedded in electronic energy levels (curves). Figure copied from Bernath (2005).

4.3.1 O_2 emissions

Figure 4.4 shows the seven meta-stable states of the bound oxygen molecule. The transitions between the three upper excited states and the ground state are named Herzberg, by whom they were discovered. The O_2 transitions of interest to this work are listed in Table 4.5. However, these electronic transitions are all forbidden by the selection rules listed above. The Herzberg I transition is forbidden because it breaks the Σ^+ symmetry selection rule, the Herzberg II and the Chamberlain transitions are not possible since a change of multiplicity is not allowed, and the IR Atmospheric transition is not allowed from rules 1, 2, and 6. These are then forbidden transitions, according to the definition above in Section 4.3, however, they are still possible by second-order approximation but the transitions will occur slowly, i.e., relatively long lifetime of the order of minutes.

Table 4.5: Electronic transitions of the selected O_2 and NO band systems studied in this work.

name	transition
Herzberg I	$A^3\Sigma_u^+$ - $X^3\Sigma_g^-$
Herzberg II	$c^1\Sigma_u^-$ - $X^3\Sigma_g^-$
Chamberlain	$A'^3\Delta_u$ - $a^1\Delta_g$
IR Atmospheric	$a^1\Delta_g$ - $X^3\Sigma_g^-$
NO δ	$C^2\Pi$ - $X^2\Pi$
NO γ	$A^2\Sigma$ - $X^2\Pi$

4.3.2 NO emissions

Figure 4.5 represents the potential energy curve of the electronic excited states of the molecule NO. As opposed to O_2 electronic transitions mentioned in the preceding section, the NO δ- and γ-transitions, which are listed in Table 4.5, are allowed following the selection rules enumerated above.

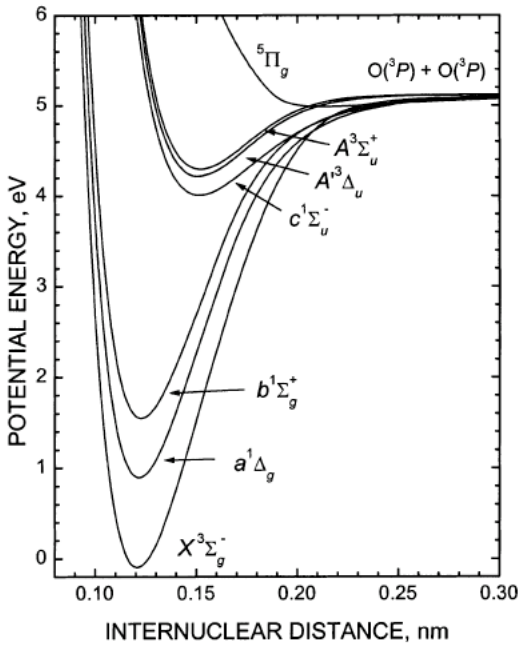

Figure 4.4: Potential energy curve of the low-lying states of molecular oxygen arising from ground states atoms. Figure taken from Slanger and Copeland (2003).

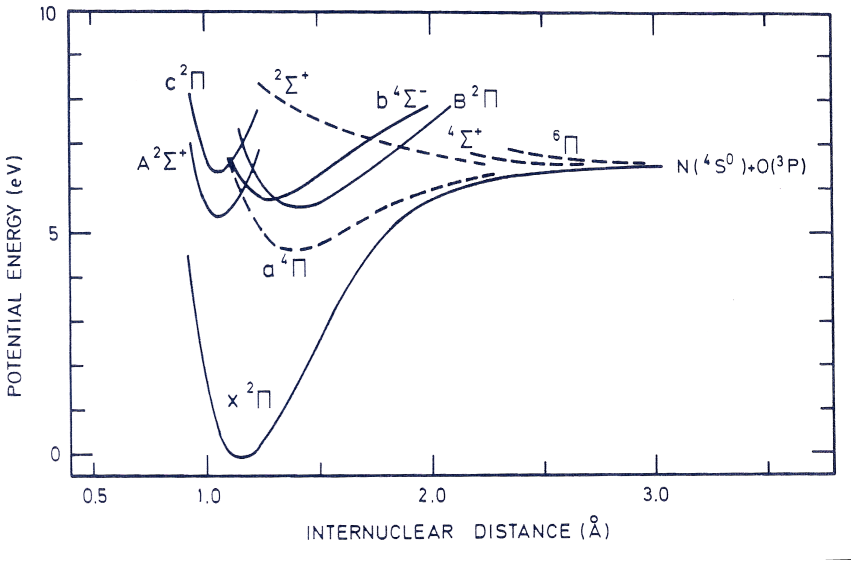

Figure 4.5: Potential energy curve of the electronic states of NO. Figure copied from Banks and Kockarts (1973).

Chapter 5

Photochemistry

Photochemistry is the study of chemical reactions that proceed with the absorption of light by atoms or molecules. Chemical reactions occur only when a molecule is provided with the necessary activation energy[1]. In the case of photochemical reactions, light provides the activation energy.

Although airglow has been studied for more than a century, the description of the physical chemistry producing the emissions remains a challenge (Slanger and Copeland, 2003). In this chapter, we explain the chain reactions that produce the O_2 and NO airglow emissions of interest to this study. For a more extensive overview, we will refer the reader to the review of photoemission phenomena in planetary atmospheres by Slanger et al. (2008).

5.1 O_2 emissions

At night, O_2 emissions arise from the recombination reaction of oxygen atoms that were produced during daytime from photodissociation of CO_2, CO, O_3, and O_2:

$$O(^3P) + O(^3P) + CO_2 \rightarrow O_2^\star + CO_2 \tag{5.1}$$

[1]The activation energy may be defined as the minimum energy required to start a chemical reaction.

which is referred to as the Barth mechanism after Barth and Hildebrandt (1961). This three-body reaction involving two oxygen atoms in a CO_2-dominated background produces O_2 in an excited state, denoted as $O_2^\star$, which can either emit a photon by radiative decay – Reaction 5.2 – or be quenched by collision with another molecule, M_i, resulting in the loss of the excited state – Reaction 5.3:

$$O_2^\star \rightarrow O_2 + h\nu \tag{5.2}$$

$$O_2^\star + M_i \rightarrow O_2 + M_i. \tag{5.3}$$

The energy released, $h\nu$, depends on the specific excited state, $O_2^\star$, produced following recombination in Reaction 5.1. In the atmospheres of Mars and Venus, the identity of M_i is most likely to be CO_2, but other species can play an important role, depending on their collisional cross-section and quenching rate.

During the day, the photolysis of ozone is an additional source of oxygen in its excited state $a^1\Delta_g$:

$$O_3 + h\nu \rightarrow O_2(a^1\Delta_g) + O(^1D) \tag{5.4}$$

for λ<310 nm. The contribution to the $a^1\Delta_g$ state formation from the three-body recombination reaction – Reaction 5.1 – is less important during daytime, but it is the major production mechanism at night.

In the atmosphere, relaxation of an excited state $O_2^\star$ to a less energetic excited state of O_2 through Reactions 5.2 and 5.3 occurs multiple times before the excited state formed directly from Reaction 5.1 loses all of its excess internal energy and reaches the O_2 ground state ($X^3\Sigma_g^-$). The distribution of the excited O_2 population is therefore complex and it is difficult to differentiate between the direct yield of $O_2^\star$ from the three-body recombination and the total yield resulting from both the recombination and the collisional and radiative relaxation processes. In the airglow model developed for this study, only the total yield for the excited state $O_2^\star$ is considered.

At photochemical steady state, the number density of $O_2^\star$ is the ratio between its production from reaction (5.1) and its loss by Reactions 5.2 and 5.3:

$$[O_2^\star] = \frac{\alpha k_{O_2}[O]^2[CO_2]}{1/\tau_{O_2} + \sum_i Q_{M_i}[M_i]} \tag{5.5}$$

where α is the total yield of $O_2^\star$ and k_{O_2} is the rate coefficient for the three-body recombination Reaction 5.1, Q_{M_i} is the quenching rate coefficient for the corresponding quenching species M_i in Reaction 5.3, and τ is the lifetime of the specific excited state $O_2^\star$.

5.2 NO emissions

At night, the NO emissions in the terrestrial atmospheres arise from the recombination reaction of oxygen and nitrogen atoms (Feldman and Takacs, 1974; Feldman et al., 1979; Bertaux et al., 2005). O atoms are produced during daytime from photodissociation of CO_2, CO, O_3, and O_2, while nitrogen atoms originate from photo- and electron-impact dissociation of N_2. The recombination reaction yields an excited state $C^2\Pi$:

$$N(^4S) + O(^3P) \rightarrow NO(C^2\Pi), \tag{5.6}$$

which can either decay directly to the ground state, $X^2\Pi$, or pass through an intermediate $A^2\Sigma$:

$$NO(C^2\Pi) \rightarrow NO(X^2\Pi) + \delta; \tag{5.7}$$

$$NO(C^2\Pi) \rightarrow NO(A^2\Sigma, \nu' = 0) + 1.22\ \mu m; \tag{5.8}$$

$$NO(A^2\Sigma, \nu' = 0) \rightarrow NO(X^2\Pi) + \gamma. \tag{5.9}$$

Here, δ and γ correspond to the exact energy released through Reactions 5.7 and 5.9, respectively, while the electronic cascade from the $C^2\Pi$ to the $A^2\Sigma$ yields photons with wavelengths of 1.22 μm. The emission from Reaction 5.8 is exactly as intense as the γ

band, Reaction 5.9, since it results from cascading from the $C^2\Pi$ state. From Reactions 5.7 through 5.9, the number density of the excited NO at equilibrium is:

$$[NO^\star] = \frac{k_{NO}[N][O]}{1/\tau_\delta + 1/\tau_\gamma} \tag{5.10}$$

where k_{NO} is the rate coefficient for the bimolecular recombination Reaction 5.6, and τ_δ and τ_γ are the lifetime of the $C^2\Pi$ and $A^2\Sigma$ excited species, respectively. We note that the total lifetime of $NO^\star$ is $\tau_{NO} = \frac{\tau_\delta \tau_\gamma}{\tau_\delta + \tau_\gamma}$.

Chapter 6

Reaction kinetics

Reaction kinetics is the study of rates of chemical processes and it deals with the experimental determination of reaction rates from which rate laws and rate constants are derived. Relatively simple rate laws exist for zero-order reactions for which reaction rates are independent of concentration, first-order reactions, and second-order reactions, and can be derived for others. In consecutive reactions, the rate-determining step often determines the kinetics. In consecutive first-order reactions, a steady-state approximation can simplify the rate law. The main factors that influence the reaction rate include: the physical state of the reactants, the concentrations of the reactants, the temperature at which the reaction occurs, and whether or not any catalysts are present in the reaction.

In this chapter, we give details about the reaction kinetics that are related to the O_2 and NO photochemical reactions that are investigated in this work.

6.1 O_2 emissions

The main path for electronic excitation of O_2 molecules during nighttime is the three-body recombination reaction (see Reaction 5.1) of atomic oxygen. Six bound electronic states of O_2 can be excited through this process: $a^1\Delta_g$, $b^1\Sigma_g^+$, $c^1\Sigma_u^-$, $A'^3\Delta_u$, $A^3\Sigma_u^+$, and $^5\Pi_g$. These states were all first observed in the laboratory, except for the state $O_2(^5\Pi_g)$,

which was postulated from theoretical studies and later observed in Resonance Enhanced Multi-Photon Ionization (REMPI) spectra. The review of Slanger and Copeland (2003) is an excellent compilation of laboratory and observational studies related to these states. The O_2 electronically excited states are all metastable with respect to radiation and have lifetimes ranging from 0.16 s ($A^3\Sigma_u^+$) to 4500 s ($a^1\Delta_g$), allowing for collisions to occur before radiation (Slanger and Copeland, 2003). Transitions between these states produce the emissions listed in Table 4.5. Figures 6.1 and 6.2 show the spectra of the IR and visible O_2 airglow emissions that are studied in this thesis.

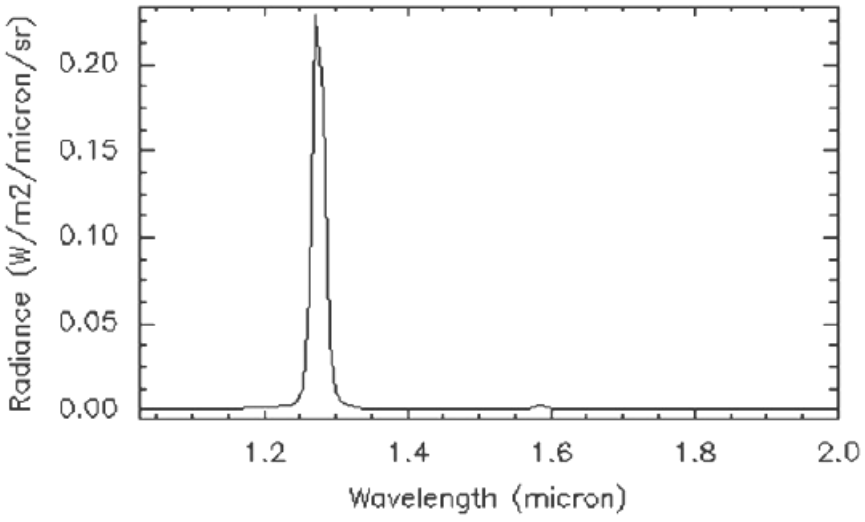

Figure 6.1: Spectrum of the Venusian O_2 IR nightglow obtained with VIRTIS. The main feature is from the $a^1\Delta_g(0)$-$X^3\Sigma_g^-(0)$ transition at 1.27 μm. Figure taken from Migliorini et al. (2011a).

For the Herzberg emissions, there are still uncertainties regarding the rate coefficients for removal of $A^3\Sigma_u^+$, $A'^3\Delta_u$, and $c^1\Sigma_u^-$ by Reaction 5.3, particularly in a CO_2 atmosphere. The rate coefficients previously measured in the laboratory in a flow discharge from the low vibrational levels (Kenner and Ogryzlo, 1980, 1983a,b, 1984) are orders of magnitudes smaller than those recently measured at high vibrational levels using REMPI (Copeland, 1994; Knutsen et al., 1994; Copeland et al., 1996; Hwang and Copeland, 1997; Mullen

et al., 2006). Furthermore, the complexity of the interplay between the metastable states of O_2 is not fully understood, and this renders laboratory measurements of quenching rates even more difficult.

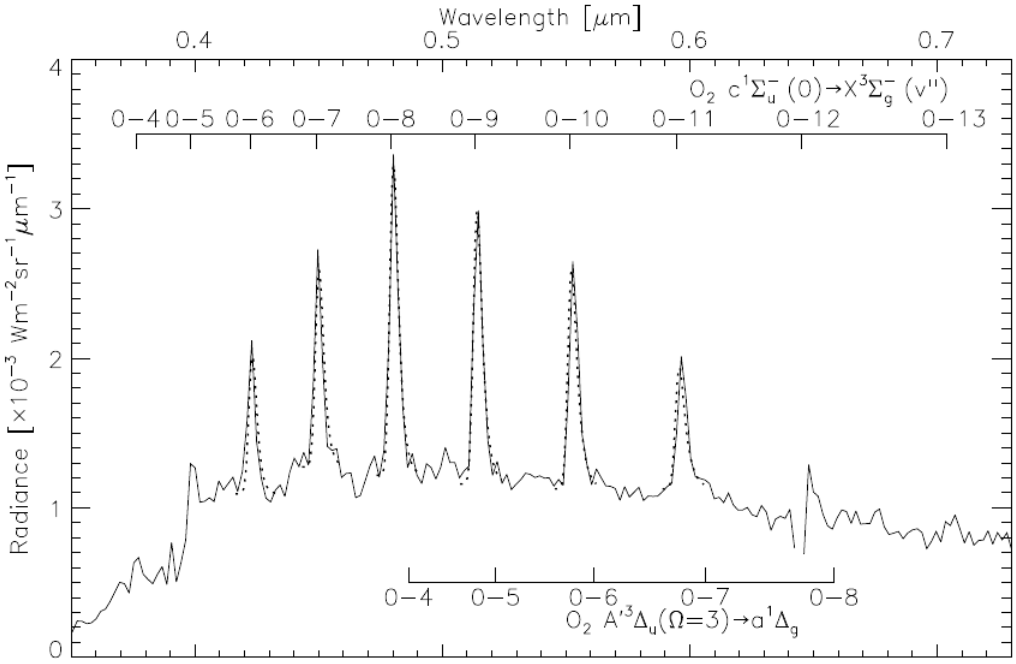

Figure 6.2: Spectrum of the Venusian O_2 visible nightglow obtained with VIRTIS. The bands v''=4-13 of the $c^1\Sigma_u^-(0)$-$X^3\Sigma_g^-(v'')$ progression are distinguishable. The positions of the bands v''=4-8 of the $A'^3\Delta_u(0)$-$X^3\Sigma_g^-(v'')$ progression are also present. Figure taken from García Muñoz et al. (2009b).

A review by Baulch et al. (1976) shows that the absolute rate coefficient for the recombination of oxygen atoms is poorly determined, as is the dependence on temperature and on the nature of the third-body (see Reaction 5.1). Until recently, the coefficient from Campbell and Thrush (1967) was used by the combustion community, while atmospheric scientists adopted the value of Campbell and Gray (1973). Pejaković et al. (2008) reported a new laboratory measurement of this rate coefficient, followed by a study by Smith and Robertson (2008) on its temperature dependence. These laboratory measurements were performed with N_2 as the third gas; it is generally accepted that the reaction

rate coefficient with CO_2 would be 2.5 times larger following the proposition of Nair et al. (1994). Recently, Krasnopolsky (2009) suggested increasing the multiplicative factor of the rate coefficient of the recombination with CO_2 from 2.5 to 3.5, but later Krasnopolsky (2011) mentioned that this latter ratio could indeed be too high. Jamieson et al. (2009) measured a value for the recombination in the presence of CO_2, as well as the yield of each excited state produced from this reaction. The value was measured at 200 K, and as expected, CO_2 is a more efficient third-body than is N_2. To first approximation, it seems appropriate to include the 2.5 multiplicative factor when using a rate coefficient measured with N_2 as the bath gas. In our simulations, we kept the rate used in each of the cited works for consistency with the kinetic parameters derived in those studies.

6.1.1 The O_2 Herzberg I transition

In the Earth's atmosphere, the vibrational distribution of the $O_2(A^3\Sigma_u^+\text{-}X^3\Sigma_g^-)$ emission band peaks at v=6. Laboratory experiments where CO_2 was added to the atomic oxygen flow in an argon carrier produced a vibrational distribution shifted towards the lower levels, i.e., v'=0-4 (Stott and Thrush, 1989; Steadman and Thrush, 1994). The laboratory experiments of Stott and Thrush (1989), Steadman and Thrush (1994), and Slanger and Copeland (2003) show that vibrational relaxation is more important than quenching of the electronic state for the interaction of the $O_2(A^3\Sigma_u^+)$ state with CO_2. Cascading from v=7 to v=6 of $A^3\Sigma_u^+$ has been shown to be the dominant process with CO_2 as the quencher (Slanger and Copeland, 2003). As mentioned above, Stott and Thrush (1989) concluded from their experiment that CO_2 causes collisional relaxation of $A^3\Sigma_u^+$ into the $c^1\Sigma_u^-$ state, which is also supported by the results of Slanger and Copeland (2003).

6.1.2 The O_2 Herzberg II transition

According to the laboratory results of Stott and Thrush (1989) and Steadman and Thrush (1994), the population of the O_2 ($c^1\Sigma_u^-$,v=0) state is greatly enhanced in the presence of

CO_2. This is in agreement with the airglow observations on Venus, where the Herzberg II band is strong, unlike on Earth where the Herzberg II band is relatively weak (see Table 7.1). Following their Earth-based observations of the Venus spectrum, Slanger et al. (2007) proposed that in a CO_2 atmosphere, the $O_2(A^3\Sigma_u^+, A'^3\Delta_u)$ states are quenched down to the $O_2(c^1\Sigma_u^-, v{=}0)$ state by CO_2 and CO. Steadman and Thrush (1994) advanced that collisional intersystem crossing of $A^3\Sigma_u^+$ and $A'^3\Delta_u$ cannot result in a vibrational distribution of the $c^1\Sigma_u^-$ state centered at the high vibrational levels. Therefore, there should be a mechanism for collisional relaxation of the more energetic states, $A^3\Sigma_u^+$, $A'^3\Delta_u$, and $c^1\Sigma_u^-$ ($v{>}0$), into O_2 ($c^1\Sigma_u^-$,$v{=}0$) to explain the Venus airglow observations. Three possibilities have been proposed to explain this state population:

1. The three-body recombination with CO_2 as the third molecule is largely populating the $c^1\Sigma_u^-$ state (Lawrence et al., 1977).

2. In the presence of CO_2, the quenching of $O_2(c^1\Sigma_u^-)$ would result in a vibrational cascade within the $c^1\Sigma_u^-$ state, hence enhancing the population of the $v{=}0$ level (Slanger and Copeland, 2003).

3. The presence of CO_2 would quench the $A^3\Sigma_u^+$ and $A'^3\Delta_u$ states down to the $c^1\Sigma_u^-$ state, while O_2 and O quench the $A^3\Sigma_u^+$ and $A'^3\Delta_u$ states to lower electronic levels $O_2(X^3\Sigma_g^-, a^1\Delta_g, b^1\Sigma_g^+)$ (Stott and Thrush, 1989).

Laboratory measurements favour options (2) and (3) to explain the enhanced population of the $c^1\Sigma_u^-(v{=}0)$ state in the presence of CO_2. A plausible scenario would be a combination of collisional relaxation of the $A^3\Sigma_u^+$ (v) and $A'^3\Delta_u$ (v) states into the $c^1\Sigma_u^-$ state and vibrational cascading within the $c^1\Sigma_u^-$ state. Unfortunately, the contribution of each mechanism for the production of $O_2(c^1\Sigma_u^-)$ has not been entirely quantified. Therefore, we use a total yield for the production of the desired excited state to account for the different pathways for production of the excited states.

6.1.3 The O_2 Chamberlain transition

Many uncertainties remain for the production of the emission resulting from the $O_2(A'^3\Delta_u$-$a^1\Delta_g)$ transition. The proximity of the $A'^3\Delta_u$ electronic potential to that of $A^3\Sigma_u^+$ renders laboratory measurements of this state very difficult and hence, to our knowledge, not a single removal rate coefficient of $A'^3\Delta_u$ by any species has been measured in the laboratory yet.

6.1.4 The O_2 IR transition

The expected yield of the $O_2(a^1\Delta_g, 0)$ state from the recombination reaction is approximately 0.7 as deduced from observations of the emission in the Venus and Mars atmospheres (Crisp et al., 1996; Krasnopolsky, 2003), which is much larger than the yield of 0.05 calculated from the direct excitation mechanism (Wraight, 1982; Smith, 1984). This simple fact highlights the need for an energy transfer via a precursor (Krasnopolsky, 2011).

There is experimental evidence from both laboratory studies and airglow observations that quenching of the upper electronic states of O_2 provides an efficient source of $O_2(a^1\Delta_g)$. Quenching of the Herzberg states, i.e., $A^3\Sigma_u^+$, $A'^3\Delta_u$, $c^1\Sigma_u^-$, by $O(^3P)$ is spin-allowed to $a^1\Delta_g$. Likewise for the quenching of $A^3\Sigma_u^+$ by O_2. Moreover, the $a^1\Delta_g$ state is the only allowed product of quenching of the $c^1\Sigma_u^-$ state by N_2 and CO_2. Huestis et al. (2000) proposed that the three-body reaction of oxygen atoms produces only $O_2(^5\Pi_g)$ molecules and then collision-induced intersystem crossing of this state populates the three Herzberg states with an efficiency of nearly 100%. Afterwards, quenching of the Herzberg states would generate the $b^1\Sigma_g^+$ and $a^1\Delta_g$ states. An effective yield for the $a^1\Delta_g$ state would then be the result of quenching of $^5\Pi_g$, $c^1\Sigma_u^-$, $b^1\Sigma_g^+$, and $a^1\Delta_g(v{>}1)$.

The $O_2(a^1\Delta_g,0)$ level is almost impervious to quenching (Slanger and Copeland, 2003) in spite of having a radiative lifetime of more than one hour (Badger et al., 1965; Lafferty

et al., 1998; Newman et al., 1999), whereas the vibrationally-excited levels of the $a^1\Delta_g$ state are rapidly removed to v'=0 by CO_2 collisions such that they are never observed in the atmosphere (Sander et al., 2006). Indeed, quenching of the $a^1\Delta_g$ state by CO_2 and N_2 is spin-forbidden such that the rate coefficients are very low. Moreover, the quenching factor due to $O(^3P)$ is weak even at the upper limit of the laboratory-measured rate coefficient given the low abundance of this species in the CO_2-dominated atmospheres (Krasnopolsky, 2011).

6.2 NO emissions

The major source for electronically excited NO molecules during nighttime is the recombination reaction of atomic oxygen with atomic nitrogen (see Reaction 5.6), which directly produces the $NO(a^4\Pi)$ state. Recombination in NO takes place primarily from atoms approaching on the $a^4\Pi$ potential. Interaction between this state and the $C^2\Pi$ state occurs just at the inner turning point of the vibrations in the $a^4\Pi$ state motion, which is coincidentally the position of the ($C^2\Pi$,v=0) level. The potential energy curve of the $a^4\Pi$ state crosses that of the $C^2\Pi$ state, hence inverse predissociation into the $C^2\Pi$ occurs although it is spin-forbidden, followed by spontaneous emission to the ground state $X^2\Pi$ (Sun and Dalgarno, 1992). This radiative decay gives the δ-band emission.

The $C^2\Pi$ state may also decay to the $A^2\Sigma$ state by IR cascade, and the resulting band emission from the deactivation of this state is referred as the γ-band. The branching ratio was calculated to be 0.7 for the δ emission and 0.3 for the γ emission (see Reactions 5.7 and 5.8). The transition probability[1] of the electronically excited levels is so high, 2.2×10^7 s^{-1} for the δ-band and 9.4×10^6 s^{-1} for the γ-band for a total $NO^\star$ emission rate of 3.1×10^7 sec^{-1} (Sun and Dalgarno, 1996), that collisional removal of $NO^\star$ is negligible. These transitions produce the spectral features displayed in Figure 6.3. The spectrum

[1]The transition probability, or Einstein coefficient, is the inverse of the lifetime $A = \frac{1}{\tau}$.

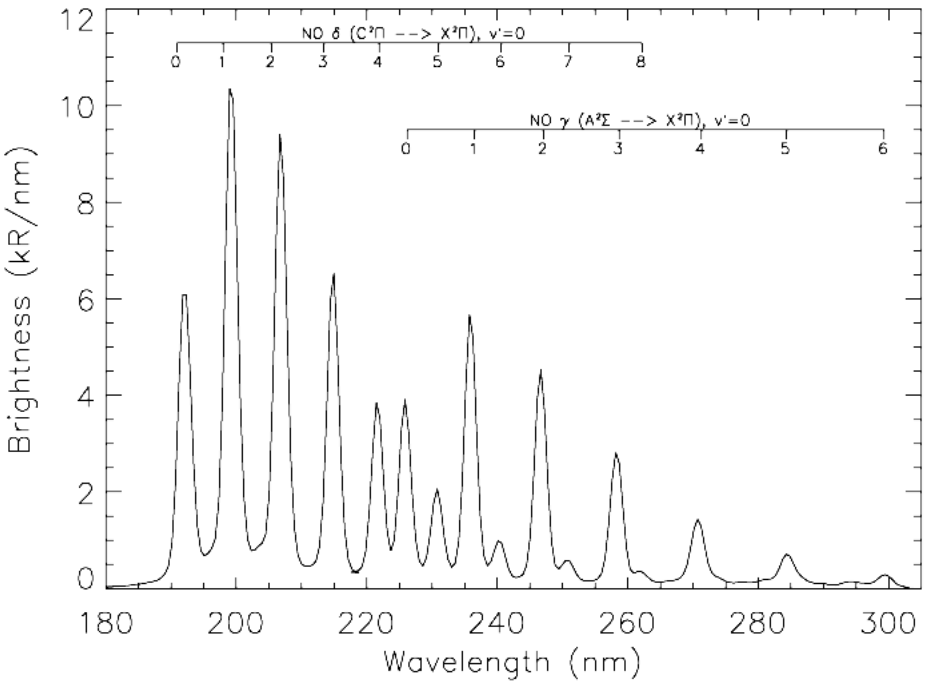

Figure 6.3: Spectrum of the Venusian NO UV nightglow obtained with SPICAV. The progression $(0,v'')$ of the δ- and γ-band systems are identified at their respective positions. Figure taken from Gérard et al. (2008a).

only contain features from the $(0,v'')$ transitions.

In planetary atmospheres, as well as in laboratory experiments, the $v'>0$ progressions of the δ and γ transitions of NO do not appear because the vibrational levels $v' \geq 1$ are energetically inaccessible at thermal energies. Indeed, since the $C^2\Pi$ and $A^2\Sigma$ states are Rydberg states[2], with similar spectroscopic parameters, radiation from $(C^2\Pi,0)$ to the $v''=0$ level of the $A^2\Sigma$ state is strongly favoured.

More on NO airglow can be found in the work of Tennyson et al. (1986).

[2]A Rydberg molecule is an electronically excited chemical species, for which the spectroscopic assignment of the electronic state follows the Rydberg formula that describes the wavelengths of spectral lines of many chemical elements (Herzberg, 1950).

Chapter 7

Observations of airglow in the Mars and Venus atmospheres

The first observations of airglow in the atmospheres of Mars date back to the Mariner spacecraft, i.e., Mariner 6, 7, and 9, in the late 1960s (Barth et al., 1967, 1971, 1972), followed by the Russian mission Mars 5 (Krasnopolsky and Krysko, 1976). Then, more than 30 years passed before other missions made dedicated airglow observations: MEx and MRO (Bertaux et al., 2005; Clancy et al., 2011b).

As for Venus, the very first detection of airglow is attributed to the Mariner 5 spacecraft (Barth et al., 1967). Then in the 1970s, the ultraviolet (UV) spectrometers on board the Venera 9 and 10 missions from Russia made further observations of the Venus atmospheric emissions (Krasnopolsky et al., 1976), followed by spectroscopic investigations by Pioneer Venus Orbiter (PVO) (Stewart et al., 1979). Again, three decades later interest in the Venus airglow was renewed and VEx dedicated some of its science operations to monitor it (Gérard et al., 2008c).

7.1 O_2 airglow

7.1.1 Mars atmosphere

The O_2 Infrared Atmospheric emission ($a^1\Delta_g,0 \rightarrow X^3\Sigma_g^-,0$), herein referred as the O_2 IR or 1.27-μm emission, was first detected in the Mars dayglow from Earth by Noxon et al. (1976), and later observed by other Earth-based observatories (Traub et al., 1979; Krasnopolsky and Bjoraker, 2000; Novak et al., 2002; Krasnopolsky, 2003, 2007; Farrel et al., 2005; Novak et al., 2005). The SPICAM and the Observatoire pour la Minéralogie, l'Eau, les Glaces et l'Activité (OMEGA) instruments, on board MEx, have been measuring the emission for the past few years (Fedorova et al., 2006a,b; Altieri et al., 2009, 2011). The typical intensity of the 1.27-μm feature varies between 1 and 30 megarayleigh[1] (MR) during daytime (Slanger et al., 2008). Figure 7.1 shows the latitudinal distribution of the emission over two Martian years of observations by OMEGA. One striking feature of the emission distribution is that the maxima of intensity are found along the terminator[2] during the polar nights in each hemisphere: between L_S=0-40° and L_S=180-360° in the Northern hemisphere and between L_S=0-180° and L_S=340-360° in the South hemisphere.

Recently, OMEGA observed for the first time the O_2 IR emission at nighttime (Gondet et al., 2010; Bertaux et al., 2011, 2012). OMEGA succeeded in detecting the O_2 IR emission on the nightside of the planet in three limb observations out of 40 (Bertaux et al., 2011, 2012). The intensity of the measurements is 0.24 MR at L_S=120° and 76.5°S, 0.15 MR at L_S=197° and 70°N, and 0.34 MR at L_S=3° and 85°S (Bertaux et al., 2012). The feature was also measured by the Compact Reconnaissance Imaging Spectromecter for Mars (CRISM) on MRO around the same period (McCleese and Kass, 2010; Clancy et al., 2011b, 2012). Observations from CRISM show that the peak altitude is within

[1] A rayleigh (R) is a typical measure of photon flux used to quantify airglow: 1 R=10^6photons cm^{-2} s^{-1}.

[2] The terminator is a moving line that separates the illuminated dayside and the dark nightside of a planetary body.

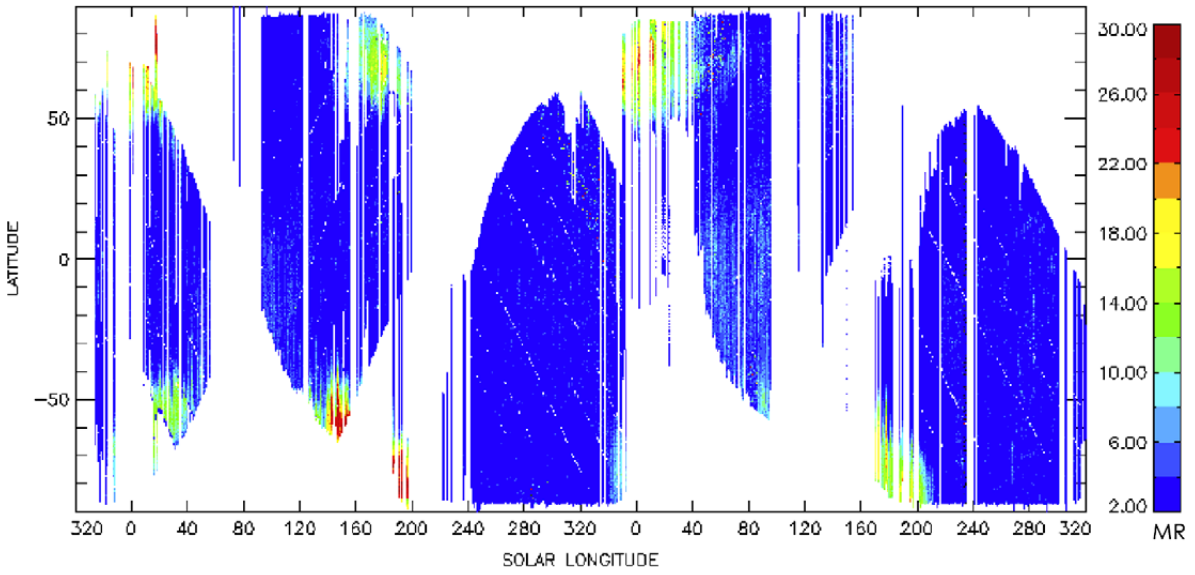

Figure 7.1: Latitudinal and seasonal distribution of O_2 IR dayglow intensity (in MR) as derived from the OMEGA datasets during two Martian years, i.e., MY 27 and 28, of acquisition. Figure taken from Altieri et al. (2009).

the 46-56 km altitude region for latitudes above 70°S and for the period L_S=50-137° (Clancy et al., 2011b, 2012). Interestingly, some profiles show a double-peaked vertical structure. Moreover, the measurements reveal a large diurnal variability in the emission rate, with values at the peak differing by a factor of two. More recently, Fedorova et al. (2011, 2012) reported measurements of the emission by SPICAM during nighttime, as displayed in Figure 7.2. There is only a limited number of observations in this dataset, but there is a clear tendency for the emission to occur in the polar regions where the O density is maximized.

Although not previously detected in the nighttime airglow of Mars, the O_2 visible emissions, comprising the Herzberg I, Herzberg II and Chamberlain band systems, are expected to be present since they are observed on Venus (Mullen et al., 2006; Migliorini et al., 2011a). The similarity between the composition of the Venus and Mars atmospheres at the peak altitude for O_2 airglow (see Table 2.1) supports the assumptions that these emissions can occur in the Martian atmosphere but have yet to be detected.

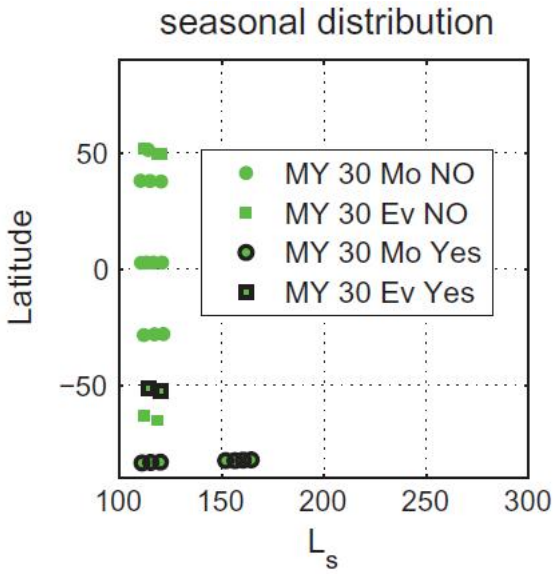

Figure 7.2: Latitudinal and seasonal distribution of O_2 IR nightglow intensity (in MR) as observed by SPICAM starting on MY 30. The black symbols show the observations with a successful detection of the emission; the green symbols correspond to no detection. The circles are for the observations towards the morning (Mo) terminator, i.e., after midnight; the squares are for the ones towards the evening (Ev) terminator, i.e., before midnight. Figure taken from Fedorova et al. (2012).

Possible explanations for the failure to detect O_2 visible emissions to date are the spectral sensitivity of previous instruments over the wavelength range of the emissions as noted by Krasnopolsky and Krysko (1976) and Migliorini et al. (2011a), and the fact that the observations were mostly made during daytime when the spectral region is dominated by emissions from the strong Fox-Duffendack-Barker band system of CO_2^+ as seen in the spectra reported by (Barth et al., 1971, 1972) and Leblanc et al. (2006). In the measurements of the nighttime UV spectra of Bertaux et al. (2005), there is possibly the presence of O_2 emissions but the signal-to-noise ratio (S/N) is not high enough in this spectral region to make a conclusive detection.

Table 7.1 gives the average intensity of the measured O_2 nightglow emissions in the planetary atmospheres of Earth, Venus, and Mars for comparison.

Table 7.1: Average nighttime emission intensity of selected O_2 and NO band systems in the planetary atmospheres. See Slanger et al. (2008) and references therein for more details on these numbers.

	wavelength (nm)	Earth	Venus	Mars
Herzberg I	240-440	600 R	140 R	
Herzberg II	260-450	50 R	3-6 kR	
Chamberlain	320-480	150 R	700 R	
IR Atmospheric	1,270	50 kR	0-1 MR	250 kR
NO $\delta + \gamma$	190–320	100 R	3 kR	85 R

7.1.2 Venus atmosphere

In the Venus nightglow, the O_2 emission at 1.27 μm is the strongest of all O_2 emissions, with an average maximum intensity of the order of a few MR (Connes et al., 1979; Bougher and Borucki, 1994; Crisp et al., 1996; Ohtsuki et al., 2005, 2008; Bailey et al., 2008; Hueso et al., 2008; Gérard et al., 2008c, 2009a,b, 2010; Piccioni et al., 2009; Krasnopolsky, 2010; Shakun et al., 2010; Soret et al., 2012; Migliorini et al., 2011a; Gérard et al., 2012). The nadir and limb observations of the O_2 1.27-μm emission by VIRTIS, the Visible and InfraRed Thermal Imaging Spectrometer on board the Venus Express (VEx) mission, show that the brightness typically peaks between 95 and 100 km, and there is a region of maximum emission intensity of 1.2 MR on the equator around midnight (Gérard et al., 2008c, 2009a, 2010, 2012; Hueso et al., 2008; García Muñoz et al., 2009b; Piccioni et al., 2009; Shakun et al., 2010; Migliorini et al., 2011a; Soret et al., 2012). Piccioni et al. (2009) reported on limb observations by VIRTIS and found that the total vertical emission rate decreases from 1.15 MR at the equator to 0.2 MR at 70°N. The peak altitude is rather constant, located between 97–99 km, from 0° to 55°N; then it starts to slowly decrease with increasing latitudes. Similarly, Soret et al. (2012) analysed the nadir measurements of VIRTIS and concluded that the emission has a maximum intensity of ∼1.6 MR near the antisolar point close to the midnight meridian, and

a mean hemispheric average of 0.47 MR. Figure 7.3 represents the spatial distribution of the emission as measured by VIRTIS. In this dataset, the intensity profiles derived from limb observations puts the peak altitude between 94 and 99 km. In many instances, the latitudinal variations of the O_2 IR emission intensity show some localized maxima at higher latitudes studied in Gérard et al. (2009a), Piccioni et al. (2009), and Shakun et al. (2010). For example, the nadir observations by VIRTIS as discussed in Hueso et al. (2008) exhibit an unexpected region of airglow brightness reaching 7 MR between 60–80°S. Also, the time of maximum brightness varies between 22h30 and 01h30 local time (LT) (Hueso et al., 2008; Shakun et al., 2010; Migliorini et al., 2011a).

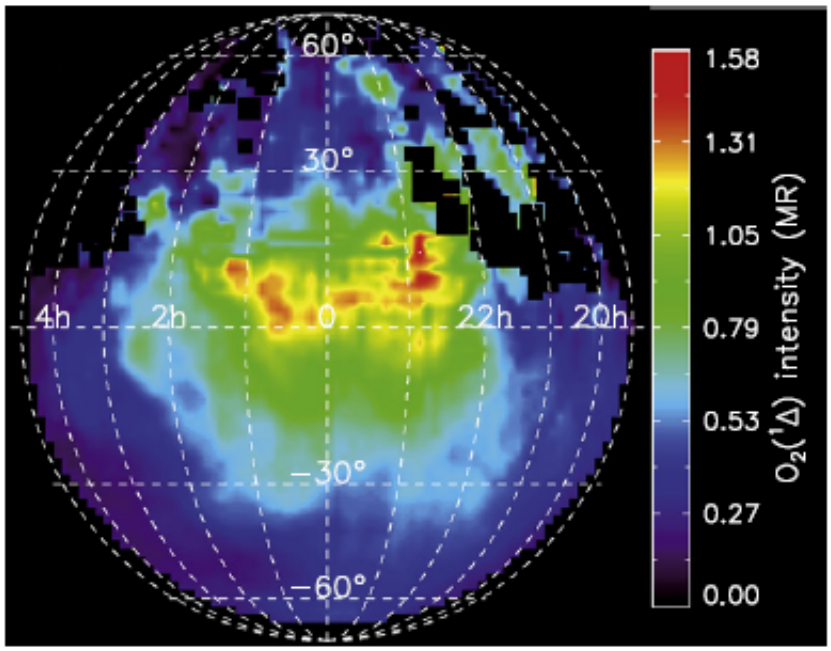

Figure 7.3: Global distribution of O_2 IR airglow intensity (in MR) as measured by VIRTIS. Figure taken from Soret et al. (2012).

The (0-v'') progression of the O_2 Herzberg II band ($c^1\Sigma_u^- \rightarrow X^3\Sigma_g^-$) is the most intense feature in the visible spectrum of Venus (Krasnopolsky et al., 1976; Lawrence et al., 1977; Slanger, 1978; Kenner et al., 1979; Krasnopolsky and Parshev, 1983; Bougher and Borucki, 1994; Slanger et al., 2001, 2006; García Muñoz et al., 2009b; Migliorini et al.,

2011b,c), with an average intensity of the total progression of 3–6 kR (Slanger et al., 2008). Migliorini et al. (2011c) reported a total vertically integrated intensity of 4 kR, with the vertical profiles having an average peak altitude of 95.5±1 km. Figure 7.4 demonstrates that the spatial distribution of the emission at nighttime is similar to that of the O_2 IR emission shown in Figure 7.3. At night, both the Herzberg II and the IR Atmospheric emissions arise from the same production mechanism and therefore their peak emission altitude and intensity are correlated (Bougher and Borucki, 1994; García Muñoz et al., 2009b; Migliorini et al., 2011c). The peak emission altitude varies between 95 and 105 km for both emissions and they are centred around the equator near midnight.

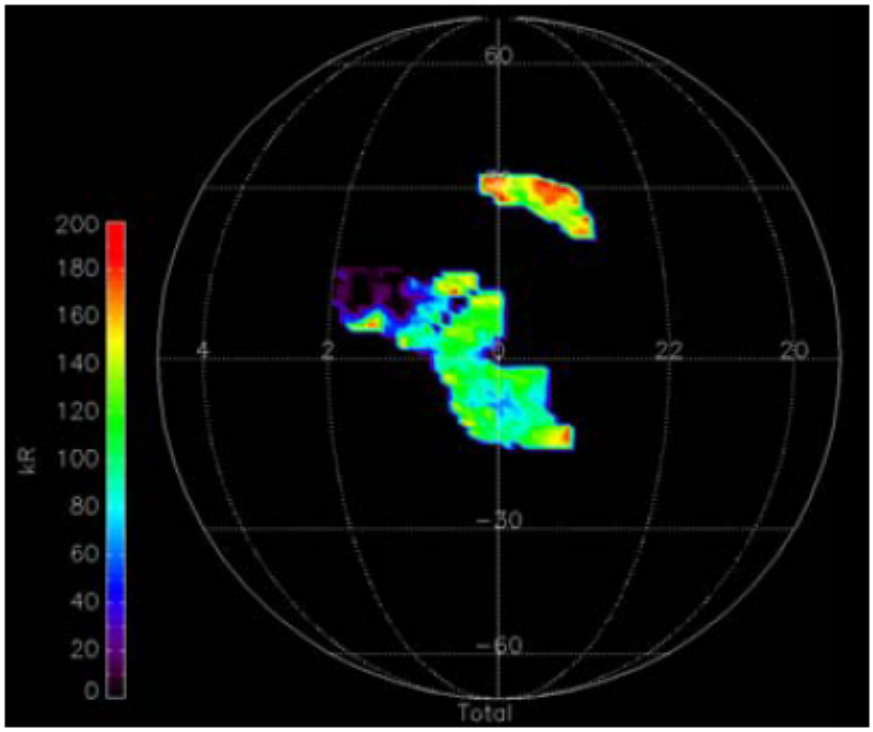

Figure 7.4: Global distribution of the O_2 Herzberg II airglow intensity (in kR) as measured by VIRTIS. Figure taken from Migliorini et al. (2011b).

The (0-v'') progressions of the O_2 Chamberlain band ($A'^3\Delta_u \rightarrow X^3\Sigma_g^-$) is also present but with a weaker intensity (Slanger and Black, 1978; Krasnopolsky and Tomashova, 1980; Slanger et al., 2001; García Muñoz et al., 2009b; Migliorini et al., 2011c). Slanger

et al. (2001) estimated the total intensity of the band to be 700 R, which is five to seven times weaker than the total intensity for the Herzberg II band. The vertical profiles analyzed by Migliorini et al. (2011c) show that this emission peaks between 102 and 104 km, a somewhat slightly higher altitude than for the Herzberg II emission.

The O_2 Herzberg I band ($A^3\Sigma_u^+ \rightarrow X^3\Sigma_g^-$) was reported with an intensity of 140 R, and the observed spectra show emission out of the v'=0 level (Krasnopolsky and Tomashova, 1980). The spectra were recorded between 19 and 05 LT and latitudes of $\pm 30^\circ$ using the spectrometer on board the Russian spacecraft Mars 5. To our knowledge, the detection of this band in a CO_2 atmosphere has never been repeated, which limits the extent of the comparison with our calculations. Lastly, another oxygen band system is also present in the Venusian airglow: the Slanger system ($c^1\Sigma_u^- \rightarrow a^1\Delta_g$) (Krasnopolsky and Tomashova, 1980).

Again, Table 7.1 provides a summary of the average intensity of the measured O_2 nightglow emissions in the planetary atmospheres of Earth, Venus, and Mars.

7.2 NO airglow

7.2.1 Mars atmosphere

The SPICAM instrument on board Mars Express confirmed the presence of nightglow as a feature of the Martian atmosphere through a clear detection of the hydrogen Lyman-α and the NO δ and γ bands ($C^2\Pi$, $A^2\Sigma^+ \rightarrow X^2\Pi$) (Bertaux et al., 2005). Then, Krasnopolsky (2006b) performed a sensitive search of the nighttime spectrum of Mars from a Earth-based observatory to detect the NO emission, but the detection limit of the instrument was above that of the expected brightness of the emission.

Cox et al. (2008) later analyzed 21 orbits of SPICAM containing limb observations of the NO UV emissions: the maximum brightness of these observations is in the range 0.2 to 10.5 kR, with a mean value of 1.2$\pm$1.5 kR, and it peaks between 55 and 92 km

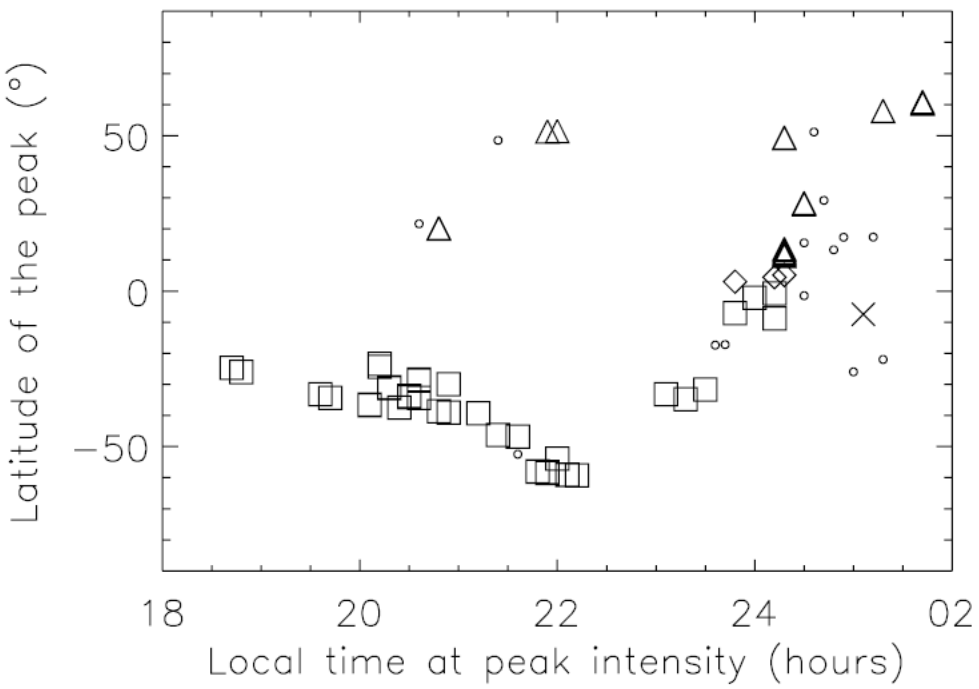

Figure 7.5: Latitude vs. local time distribution of the NO airglow data for Mars as measured by SPICAM. The diamonds represent data from the spring season in the Northern hemisphere (L_S=0-90°), the triangles are fall data in the Northern hemisphere (L_S=180-270°), the squares are spring observations in the Southern hemisphere (L_S=180-270°), and the crosses correspond to winter measurements in the Southern hemisphere (L_S=90-180°). Finally, the small circles correspond to data presenting no peak, typically below 0.5 kR, whatever the season. Figure taken from Cox et al. (2008).

in altitude, with a mean value of 73.0±8.2 km. The average vertical brightness of the emission from this dataset is 36±52 R and the observed topside scale height has a mean value of 6±1.7 kR and ranges between 3.8 and 11 km. Cox et al. (2008) concluded from their analysis that the higher the latitude of the measurements, the lower is the altitude of the peak, which they linked to the behaviour of constant pressure surfaces that are higher close to the equator. Also, they found that the highest intensities are generally associated with low altitudes but there is no real systematic dependence between the peak altitude and the peak brightness. Figure 7.5 shows the spatial distribution of the NO

nightglow as a function of the local time. This distribution seems to support the global transport mechanism generating a downward flux of N and O atoms on the nightside that recombine to produce the NO emissions (Bertaux et al., 2005).

7.2.2 Venus atmosphere

The first detection of NO nightglow in the Venus atmosphere was made by Stewart and Barth (1979) but the features were incorrectly attributed to another airglow emission, the CO Cameron bands. The first identification of the NO δ band emission was made by Feldman et al. (1979) with spectra measured from Earth with the International Ultraviolet Explorer (IUE) observatory. Attributing this emission to recombination of O and N atoms, Feldman et al. concluded from their measurements that the presence of this airglow feature is an indicator of efficient transport of these species from the dayside where they are produced.

The NO $\delta(0,v'')$ and $\gamma(0,v'')$ band emissions were later observed using the PVO UV spectrometer (Stewart and Barth, 1979; Stewart et al., 1980; Gérard et al., 1981). The observations revealed the tendency for the emission to be brighter at equatorial latitudes and eastward of the antisolar point, i.e., displayed from midnight towards the morning terminator, although the brightness and location of the maximum were found to be variable. The altitude of the peak emission was located at 111±7 km in the dataset of Stewart et al. (1980), while Gérard et al. (1981) reevaluated it at 115±2 km with a topside scale height of 3.2 km. These measurements were later reanalyzed in Bougher et al. (1990), who concluded that the dark-disk average brightness should be 400±120 R and the maximum vertical brightness 1.9±0.6 kR.

With the VEx orbiter monitoring the Venus atmosphere since 2005, extensive observations of NO nightglow by the SPICAV and VIRTIS instruments have been made in recent years (Gérard et al., 2008a, 2009a; García Muñoz et al., 2009a; Royer et al., 2010). The mean limb brightness of the emission is 32 kR and varies between 5 kR at

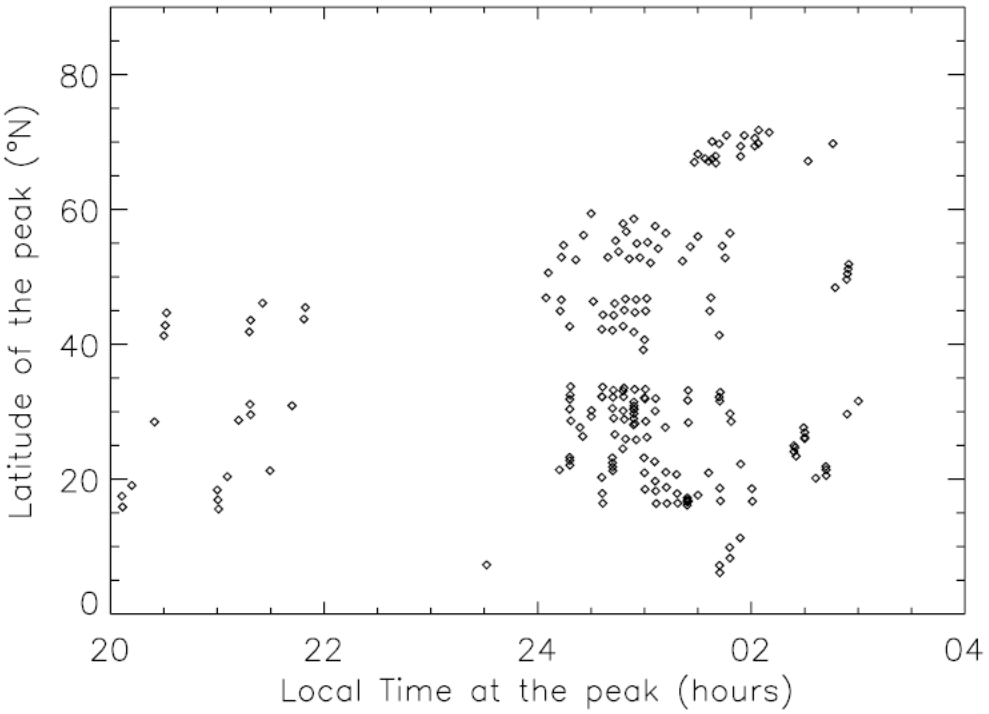

Figure 7.6: Latitude vs. local time distribution of the NO airglow data for Venus as measured by SPICAV. Figure taken from Gérard et al. (2008a).

Northern latitudes and 440 kR at low latitudes, while the mean altitude of the emission layer is at 113 km, with measurements ranging from 95 to 132 km. Royer et al. (2010) used a forward model to reproduce the observations of the NO emission by SPICAV and concluded that the layer is found at 113.5±6 km, has a scale height of 3.4±1 km, and the brightness varies between 19 and 540 kR. The SPICAV observations are compatible with a downward flow of O and N atoms on the nightside at the antisolar point, i.e., around midnight, as can be seen in Figure 7.6, which displays the latitude versus local time distribution of the O_2 IR nightglow. This transport mechanism is a consequence of the strong SSAS circulation (Bougher et al., 1990; Gérard et al., 2008a, 2009a).

Part II

Modeling of O_2 airglow emissions

This part of the thesis presents the results from simulations of the airglow emissions of selected molecular oxygen transitions in the Martian and Venusian atmospheres. Chapter 8 provides a description of the Venus and Mars atmospheric models. Using atmospheric conditions provided by these three-dimensional atmospheric models in combination with the airglow model described in Chapter 9, the simulations yield calculations for the Herzberg I & II, the Chamberlain, and the Infrared Atmospheric band emissions of O_2 for both Mars (Chapter 10) and Venus (Chapter 11) atmospheres. The results emphasize the advantage of using 3-D GCMs for the diagnosis of oxygen-related photochemistry in CO_2-dominated atmospheres.

Chapter 8

Atmospheric models

A GCM is a mathematical model of the general circulation of a planetary atmosphere based on the Navier-Stokes equations on a rotating sphere with thermodynamic terms for various energy sources, e.g., radiation, latent heat, etc. These equations are the basis for complex computer programs commonly used for simulating the atmosphere of the Earth. These computationally intensive numerical models are based on the integration of a variety of fluid dynamical, chemical, and sometimes biological equations. GCMs are widely applied for weather forecasting, understanding the climate, and projecting climate change.

GCMs for other planets than for Earth are commonly derived from Earth GCMs, which are robust in their interpretation of the atmospheric phenomena due to the availability of more observational datasets. Mars climate simulation models date as far back as the Viking missions to Mars in the late 1970s, and for Venus it started with the PVO era also in the late 70s. For this thesis, we were fortunate to work with two different teams that provided us with a Mars GCM, and one for Venus. This chapter gives a description of the LMD-MGCM and of the VTGCM that will be used for the airglow simulations.

8.1 Mars model

The LMD-MGCM is a GCM for Mars that solves the primitive equations of hydrodynamics on a sphere by means of a grid-point discretization. The first version of this model extended from the ground up to about 80 km above the surface, and included the radiative effects of CO_2 and suspended dust, a realistic CO_2 condensation scheme, and a number of subgrid-scale processes (Forget et al., 1999). Parametrizations to account for the water cycle (Montmessin et al., 2004) and for the photochemistry of the lower atmosphere (Lefèvre et al., 2004) were later added to the model. The LMD-MGCM has been extended up to the thermosphere, so that its vertical range is now from the surface up to about 250 km. Parametrizations to account for the physical processes important in this atmospheric region, such as the CO_2 radiative balance under non-local thermodynamic equilibrium (LTE) conditions, heating due to the absorption of UV solar radiation, molecular diffusion, the photochemistry of the rarefied upper atmosphere, and a number of other processes, have been included in the LMD-MGCM (Angelats i Coll et al., 2005; González-Galindo et al., 2005; González-Galindo et al., 2009). Although the photochemical scheme initially accounted only for species of the C, O and H families, it has been recently extended to include nitrogen chemistry (González-Galindo et al., 2008).

The airglow calculations shown in this work have used as inputs the simulation of one Martian year simulation performed with the LMD-MGCM, including the photochemical packages described by Lefèvre et al. (2004) and González-Galindo et al. (2005), with updated kinetics data. The ozone columns calculated by the LMD-MGCM have been shown to be in good agreement with the ultraviolet measurements of SPICAM (Lefèvre et al., 2008), which is important for our discussion of the emission initiated by the ozone photolysis. Model data have been provided on a 3-D grid with a resolution of 3.75° latitude × 5.6° longitude, on 50 vertical levels extending from the surface up to 150 or 250 km, depending on the version used. Results span the entire Martian year and have been extracted at 00 LT and 12 LT for each L_S.

In Section 10.2 where the sensitivity of airglow to dust and water loads is discussed, we will refer to three different simulations performed with the LMD-MGCM, called "runs". The model run described in the previous paragraph will be referred as run 3, which has been shown to represent satisfactorily the water distribution observed on Mars by MGS-TES (Lefèvre et al., 2008). This means that the ozone distribution in the model also agrees with the ozone measurements (Lefèvre et al., 2008), since the local amount of ozone on Mars is controlled by the abundance of odd hydrogen species produced by the photolysis of water vapour and its reaction with $O(^1D)$ (Lefèvre et al., 2004). For simulation run 1 and run 2, two different chemical schemes have been used: the Lefèvre et al. (2004) scheme for the lower layers (pressure larger than 1 Pa) and the González-Galindo et al. (2005) (extended to include N chemistry and ionosphere as in González-Galindo et al. (2008)) above this pressure level. Both photochemical models have been tested and provide similar results in the transition region. While both simulations use a solar flux appropriate for solar average conditions, they differ in the dust load in the lower atmosphere: while for run 1 a constant dust optical depth throughout the year is fixed, in run 2 a variable optical depth as observed by TES during MY 24 is used (Clancy et al., 2000). In summary, for run 1 the dust and water cycles have not been optimized, run 2 has a dust cycle matching MGS-TES MY24 measurements, but the same water cycle as run 1, and run 3 has the same dust cycle as run 2 and a water cycle matching the MGS-TES measurements (see Table 8.1). We use these three different runs, from which we obtain different atmospheric conditions, to perform a sensitivity study of the impact of water and dust loads on the airglow distribution.

For the simulations of airglow emissions in the Mars atmosphere, the density profiles of $O(^3P)$, O_3, and CO_2 are given by this atmospheric model, as are the temperature profiles (since the three-body reaction rates used in the airglow model are temperature-dependent). The temperature and density profiles at specific locations and seasons are shown in Figures 8.1 and 8.2 for 00 LT and 12 LT, respectively, for all three LMD-MGCM

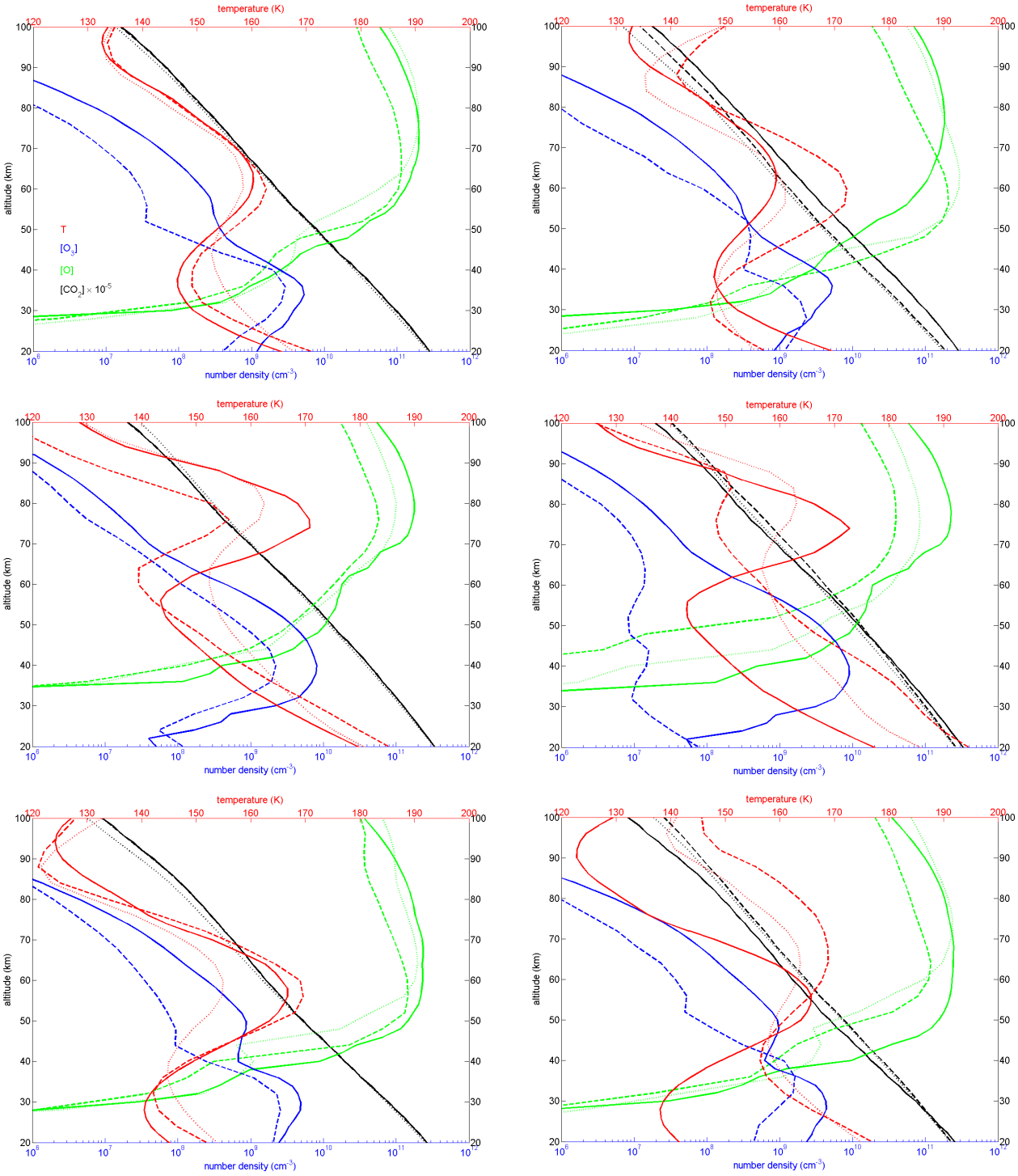

Figure 8.1: 00 LT profiles of CO_2 ($\times^{-4}$, black), O (green), and O_3 (blue) density (cm^{-3}), and of temperature (K) (red) at L_S=0° (left column) and L_S=180° (right column) for latitudes 67.5°N (upper row), 0° (middle row), and 67.5°S (lower row). The dashed line corresponds to LMD-MGCM run 1, the dotted line is LMD-MGCM run 2, and LMD-MGCM run 3 is the solid line.

Table 8.1: Difference between the three LMG-MCGM runs used in the calculations of the VER for the O_2 band emissions.

runs	1	2	3
water	moderate	moderate	TES MY 24
dust	moderate	TES MY 24	TES MY 24

runs described in the previous paragraph. All simulations shown in this work, except for the ones in Section 10.2, were performed with the dataset from run 3.

It is obvious from Figures 8.1 and 8.2 that differences in the dust and water schemes induce variations in the temperature, atomic oxygen density, and ozone density profiles. The CO_2 profile is least affected. The vertical distribution of temperature shows greater variations between run 1 and run 2, than between run 2 and run 3, indicating that changes in the dust load have the greater impact on the temperature profile. As for the atomic oxygen and ozone density distributions, the vertical structure is more similar between runs 1 and 2 as compared to run 3, meaning that the water cycle has a stronger effect on the oxygen chemistry than the dust level. These behaviours are not surprising since recent observations from Mars-orbiting spacecraft revealed similar trends (e.g., McCleese et al., 2010).

8.2 Venus model

The VTGCM is a 3-D finite-difference hydrodynamic model of the Venus upper atmosphere (Bougher et al., 1988) which is based on the National Center for Atmospheric Research (NCAR) terrestrial Thermospheric Ionosphere General Circulation Model (TIGCM). The VTGCM has been documented in detail as revisions and improvements have been made over more than two decades (e.g. Bougher et al., 1988, 1990; Bougher et al., 1997; Bougher et al., 1999; Bougher et al., 2002; Bougher et al., 2008; Bougher and Borucki,

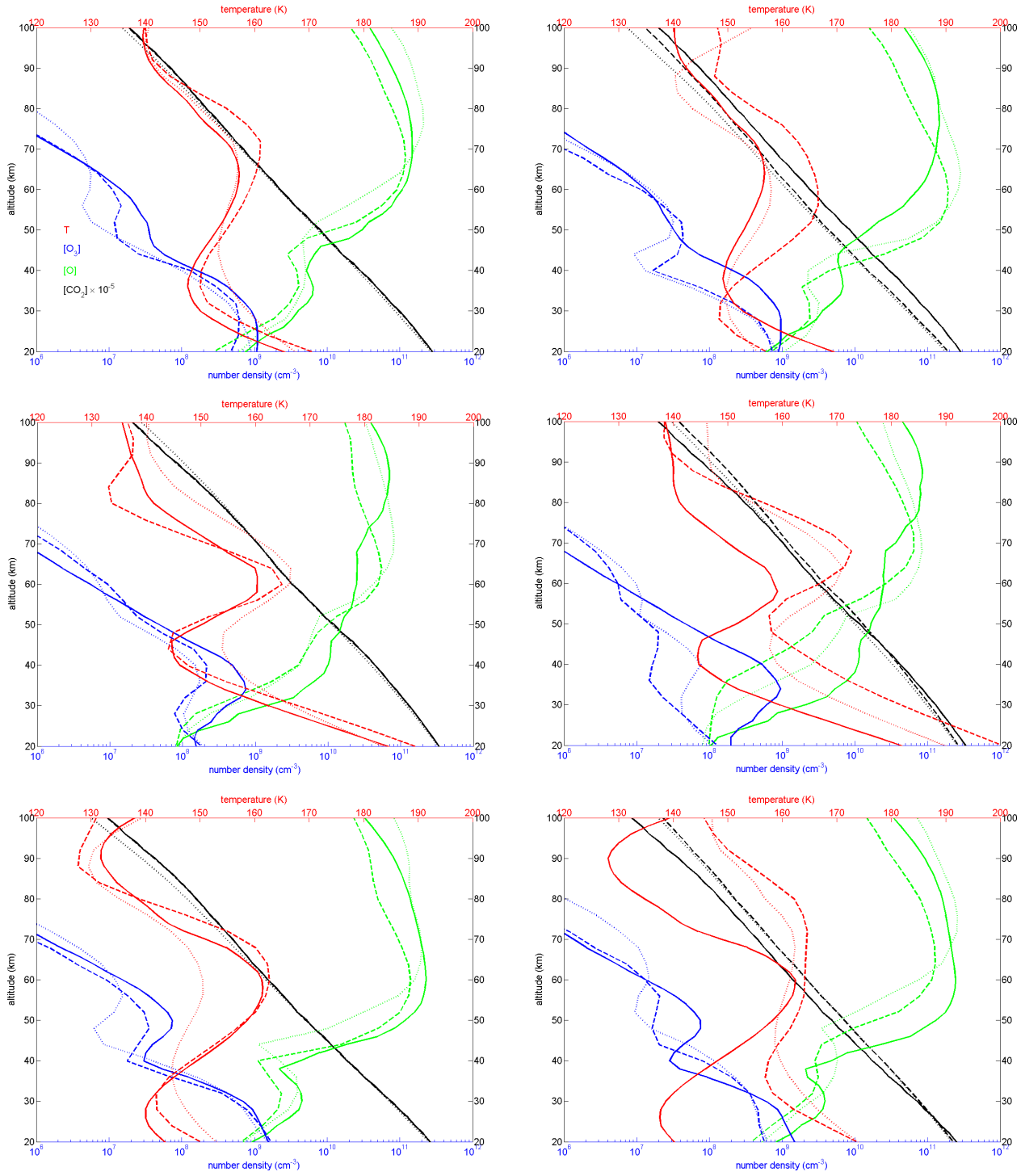

Figure 8.2: 12 LT profiles of CO_2 ($\times^{-4}$, black), O (green), and O_3 (blue) density (cm^{-3}), and of temperature (K) (red) at L_S=0° (left column) and L_S=180° (right column) for latitudes 67.5°N (upper row), 0° (middle row), and 67.5°S (lower row). The dashed line corresponds to LMD-MGCM run 1, the dotted line is LMD-MGCM run 2, and LMD-MGCM run 3 is the solid line.

1994; Zhang et al., 1996; Brecht et al., 2011).

Briefly, the 3-D hydrodynamic VTGCM solves the time-dependent primitive equations for the neutral upper atmosphere. The diagnostic equations (hydrostatic and continuity) provide geopotential and vertical motion fields. Additionally, the prognostic equations (thermodynamic, eastward momentum, northward momentum, and composition) are solved for steady-state solutions for the temperature, zonal (eastward) velocity, meridional (northward) velocity, and mass mixing ratios of specific species. The VTGCM includes major species (CO_2, CO, O, and N_2), minor species (O_2, $N(^4S)$, $N(^2D)$, and NO), and dayside photochemical ions (CO_2^+, O_2^+, O^+, and NO^+). In addition, the VTGCM incorporates nightside profiles of specific chemical trace species (Cl, Cl_2, ClCO, ClO, H_2, HCl, HO_2, O_3, OH) from an altitude of 80 km to 130 km (Krasnopolsky, 2010). The latest reaction rates being used in the VTGCM are shown in Tables 1 and 2 of Brecht et al. (2011).

Formulations for CO_2 15-μm cooling, wave drag, and eddy diffusion are parametrised within the VTGCM using standard aeronomical formulations. The evening terminator winds are faster than the morning terminator winds since the wave drag term, Rayleigh friction, is prescribed asymmetrically in local time in order to mimic the observed upper atmosphere retrograde superrotating zonal (RSZ) winds. The prescribed RSZ winds are very weak from ∼80 km to 110 km, and above 110 km the emergence of modest RSZ winds approach 60 m s^{-1} above ∼130 km (Brecht et al., 2011). The VTGCM can capture the full range of EUV-UV flux conditions (solar maximum to solar minimum).

Others adjustable parameters used in the VTGCM runs presented in this study that are of relevance are: solar minimum fluxes (F10.7 = 70), a maximum nightside eddy diffusion coefficient of 1.0×10^7 cm^2 s^{-1}, and a wave drag parameter of 0.5×10^{-4} s^{-1}. The model domain covers a 5° by 5° latitude-longitude grid, with 69 evenly-spaced log-pressure levels in the vertical, extending from approximately ∼70 to 200 km at midnight local time (00 LT).

The results used in the sensitivity study to the kinetic parameters are extracted from the VTGCM "mean" simulation, which represents mean conditions for Venus' upper atmosphere during the VEx sampling period (see Brecht et al., 2011). Figure 8.3 shows the temperature, CO_2 and atomic oxygen profiles at 00 LT.

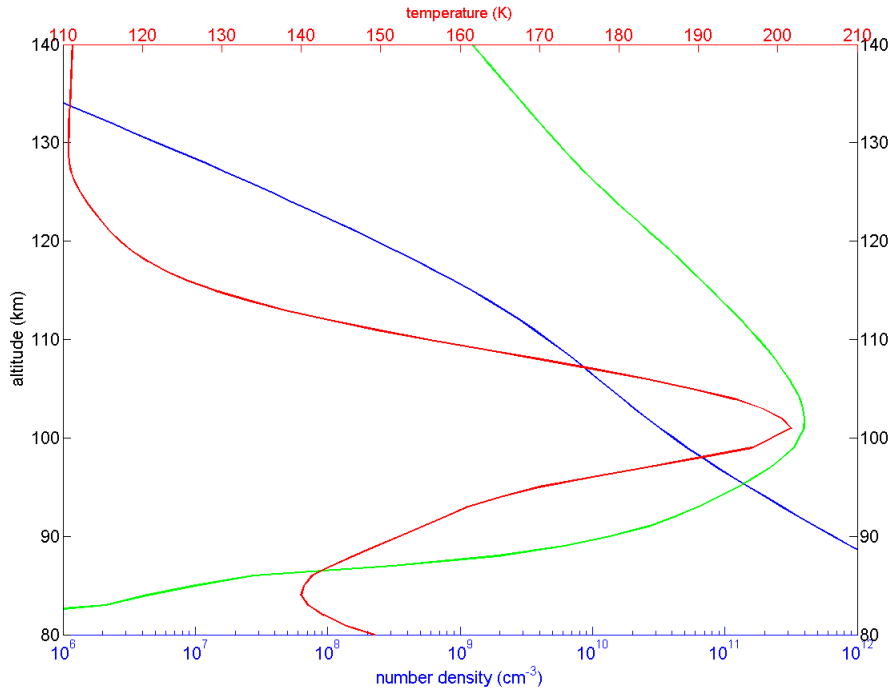

Figure 8.3: Profiles of atomic oxygen (green) and CO_2 ($\times^{-4}$, blue) number density (cm^{-3}) and temperature (K, red) for the VTGCM "mean" run at 00 LT and latitude 2.5°N (see text for details).

To investigate the impact of using consistent parameters in the offline airglow model and in the full GCM, two different runs of the VTGCM are used in this work. We use a VTGCM simulation that represents mean conditions for Venus' upper atmosphere during the Venus Express sampling period (Brecht et al., 2011, 2012), from which it was determined that with a $O_2(a^1\Delta_g)$ production yield of 0.75 (Crisp et al., 1996; Gérard et al., 2008c), the three-body recombination rate should be 2.75×10^{-32} cm^6 s^{-1} (value of Smith and Robertson (2008) multiplied by a factor of 2.5 as recommended by Nair et al. (1994)

for CO_2 as the third body), the lifetime 3800 s (rounded value of Badger et al. (1965)), and the CO_2 removal rate 2×10^{-20} cm^3 s^{-1} (value recommended in Sander et al. (2011)). This VTGCM simulation will be referred to as run 1. We also use a second VTGCM simulation, referred to as run 2, with the photochemical parameters used in Krasnopolsky (2011) and claimed to be the best combination to reproduce the airglow emission in the Mars atmosphere following the sensitivity study of Gagné et al. (2012a). These parameters are: 0.7 and $2.5 \cdot 3 \times 10^{-33} \cdot (300/T)^{3.25}$ cm^6 s^{-1} for the three-body recombination yield and rate coefficient (Krasnopolsky, 2010; Smith and Robertson, 2008), respectively, 4460 s for the lifetime (value of Lafferty et al. (1998) as used in Krasnopolsky (2011)), and 10^{-20} cm^3 s^{-1} for the quenching rate coefficient (Krasnopolsky, 2010). In both runs, we use the laboratory-determined removal rate coefficient by O of 2×10^{-16} cm^3 from Findlay and Snelling (1971) and Leiss et al. (1978) as recommended by (Sander et al., 2011). These parameters are listed in Table 8.2.

The difference between these two VTGCM runs resides in the recombination yield and rate coefficient, the radiative lifetime of the O_2 ($a^1\Delta_g$) state, and the CO_2 quenching rate coefficient used in the chemical scheme of the atmospheric model. These parameters directly affect the balance between the production and loss of $a^1\Delta_g$ in the atmosphere, and hence the overall distribution of the O_x species. In Figure 8.4, we show the global distribution, as a function of altitude versus latitude at 00 LT, of temperature and density of atomic oxygen from run 1 (see Figures 8.4a and 8.4c, respectively), as well as the difference in each field between run 1 and run 2 (see Figures 8.4b and 8.4d, respectively). We observed that both the temperature and atomic oxygen density fields have a local maximum slightly above 100 km over the equatorial region. We also notice the greatest difference in temperature between run 1 and run 2 is near 97 km in altitude. Another local maximum of temperature variation between these two runs is found over the mid-latitudes above 100 km. The density of atomic oxygen is larger in run 1 than in run 2 everywhere in the domain but the difference is more pronounced above 110 km for

Table 8.2: Kinetics parameters used in the calculations of the VER for the O_2 IR Atmospheric (0-0) emission in the different VTGCM runs.

	1	2
$\alpha(a^1\Delta_g)$	0.75 [1]	0.7 [2]
k_{O_2} ($cm^6\ s^{-1}$)	2.75×10^{-32} [3]	$2.5 \cdot 3 \times 10^{-33} \cdot (300/T)^{3.25}$ [4]
$\tau(a^1\Delta_g)$ (s)	3800 [5]	4460 [6]
Q_{CO_2} ($cm^3\ s^{-1}$)	2×10^{-20} [7]	10^{-20} [2]
Q_O ($cm^3\ s^{-1}$)	2×10^{-16} [7]	2×10^{-16} [7]

[1] Crisp et al. (1996); Gérard et al. (2008c)

[2] Krasnopolsky (2010)

[3] value of Campbell and Gray (1973) × 2.5 (Nair et al., 1994) used in Slanger et al. (2006)

[4] value of Smith and Robertson (2008) × 2.5 (Nair et al., 1994) used in Krasnopolsky (2011)

[5] Badger et al. (1965)

[6] interpretation of the value of Lafferty et al. (1998) by Krasnopolsky (2011)

[7] value recommended by Sander et al. (2011)

latitudes beyond 30°N.

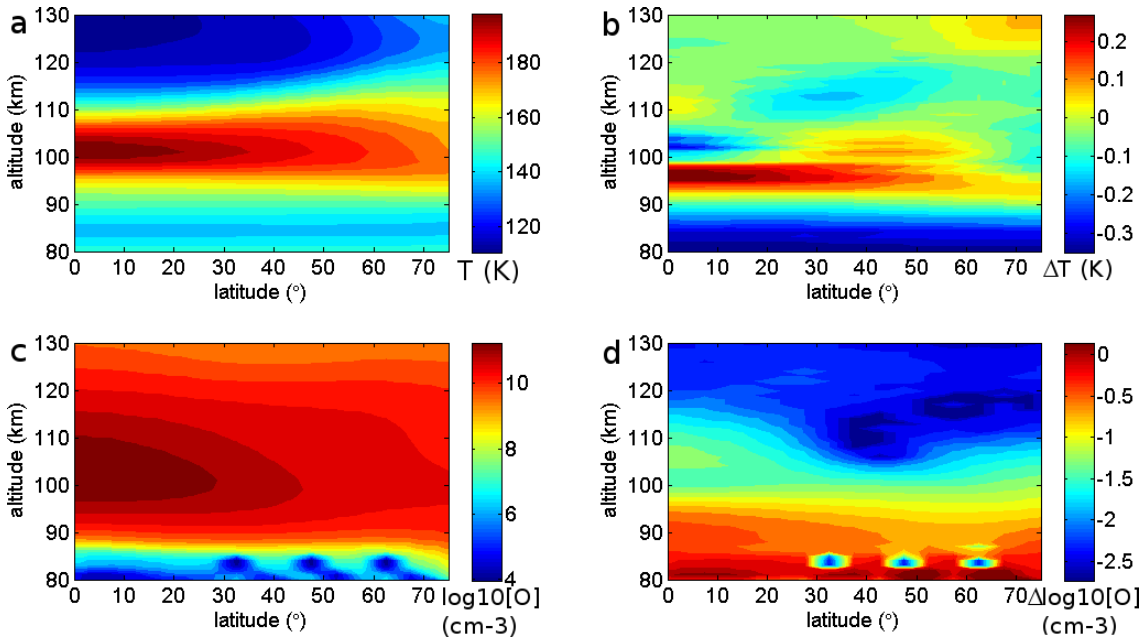

Figure 8.4: VTGCM results at 00:00 LT as a function of altitude and latitude of: a) temperature from run 1; b) absolute difference between run 1 and run 2 temperatures, i.e., $T_1 - T_2$; c) logarithm of atomic oxygen number density from run 1; d) relative difference between run 1 and run 2 logarithms of atomic oxygen, i.e., $([O]_1 - [O]_2)/\{([O]_1 + [O]_2)/2\}$.

Chapter 9

Airglow model

Airglow modeling assumes a steady state between the production and loss of the excited species. This assumption holds because chemical lifetimes are shorter than dynamical lifetimes in the neutral atmosphere. Hence, variations in the emission rates occur in response to diurnal, seasonal, and latitudinal changes in the dynamics and photochemistry of the atmosphere. Developing an airglow model is therefore a useful tool to make realistic predictions of the distribution of the emission features and it provides a way to test our understanding of the dynamics, composition, and energetics of an atmosphere.

An important aspect of airglow modeling is the proper choice of kinetic parameters to use in the calculations. This usually represents a major challenge since not all such parameters are known, sometimes due to lack of laboratory measurements or from difficulty in isolating the desired chemical reactions. On Earth, photometers on board rockets were used to measure the emission rates and derive empirically the kinetic constants, but such an approach is not currently feasible for other planets. Hence, several assumptions have to be taken in order to proceed with the airglow simulations, and these assumptions cause a limit on the accuracy of the method. For this reason, for each emission considered in this study, we use several sets of kinetic parameters, giving a range of possible values for characterizing the airglow features.

9.1 Description of the modeling approach

9.1.1 Volume emission rate

The volume emission rate (VER) is described as the ratio of the production to the loss of the excited species, weighted by its lifetime. It represents the number of photons emitted per unit time per unit volume from radiative relaxation out of the excited species $XY^\star$ state into all lower states. The VER for $XY^\star$ is expressed as follows:

$$\epsilon(XY^\star) = \frac{[XY^\star]}{\tau} \tag{9.1}$$

where τ is the lifetime by radiative relaxation of the specific excited state $XY^\star$.

Using the assumed production vs. loss steady-state concentration of $O_2^\star$, as given in Equation 5.5, Equation 9.1 becomes:

$$\epsilon(O_2^\star) = \frac{\alpha k_{O_2}[O]^2[CO_2]}{1 + \tau(Q_{CO_2}[CO_2] + Q_{O(^3P)}[O(^3P)])} \ . \tag{9.2}$$

Quenching coefficients of $O_2(c^1\Sigma_u^-)$ by N_2 and O_2 are of comparable magnitude to each other, at least at high vibrational levels (Copeland et al., 1996; Slanger et al., 2007), but no measurements of the collision rate of this state with N_2 have been made at low vibrational levels. However, the measured quenching coefficients for N_2 and O_2 are an order of magnitude smaller than for CO_2 at v'=9 (Slanger et al., 2007). Therefore, given the low abundance of N_2 (mixing ratios of 0.027 and 0.035) and O_2 (mixing ratios of 0.002 and 0.00009) in the Mars and Venus atmospheres, respectively, as compared to that of CO_2 (mixing ratios of 0.955 and 0.965), the quenching factors, i.e. $Q_Z[Z]$, by N_2 and O_2 are negligible. While quenching of the state $c^1\Sigma_u^-$ by N_2 and O_2 is less effective than by CO_2, given their low abundance in these CO_2-dominated atmospheres, Slanger et al. (2006) and Slanger et al. (2007) suggested that collisional removal by CO could be competing with that by CO_2. However, García Muñoz et al. (2009b) concluded that CO is not the major quencher throughout the airglow layer given the fact that it barely changes the airglow profile in simulations where its quenching efficiency is given a weight

equal to that of CO_2. Krasnopolsky (2011) also agrees that the branching ratio for the reaction with CO is minor in Mars and Venus. Therefore, we decided to neglect quenching by CO for the total quenching in our simulations.

For the daytime simulations, we use a different expression for the calculations of the VER to include the production from O_3 photodissociation:

$$\epsilon(O_2^\star) = \frac{\beta J[O_3] + \alpha k_{O_2}[O]^2[CO_2]}{1 + \tau(Q_{CO_2}[CO_2] + Q_{O(^3P)})} \tag{9.3}$$

where J is the rate of photodissociation of O_3 and β is the yield of $a^1\Delta_g$ from Reaction 5.4.

9.1.2 Vertically integrated intensity

For each emission band system, the airglow model also calculates the vertically integrated intensity over the course of a year covering the whole latitudinal range. The vertically integrated intensity from the ground to the top of the atmosphere (TOA) is expressed in our model by the following equation:

$$I(XY^\star) = \int_0^{TOA} \epsilon(XY^\star)dz \approx \sum_i^{n_z} \epsilon(XY^\star)_i \delta z_i \tag{9.4}$$

where n_z is the number of vertical levels in the model, $\epsilon(XY^\star)_i$ is the VER at the altitude corresponding to the layer i and δz_i is the width of each vertical layer. In our airglow model, the integration is performed from 0 to 100 km for Martian atmospheric conditions and from 80 to 140 km for Venusian atmospheric conditions.

For the airglow simulations, the density profiles of $O(^3P)$, O_3, and CO_2 are given by the atmospheric models described in Chapter 8, as is the temperature profile (since the recombination reaction rates used in our simulations are temperature-dependent).

9.1.3 Solar zenith angle

The position of the sun is defined by the solar zenith angle (SZA). It is the angle between the local vertical (Z), the planet center (O), and the sun (S) (Figure 9.1). We are

interested in knowing the SZA at a specific location, using latitude with ϕ=0° at the equator and 90° at the poles, and time, in terms of hour angle h. The hour angle is the angle between the location on the surface (P) and the point directly under the sun (D); at solar noon at any latitude, the hour angle is h=0. The local time corresponds to the hour angle expressed in hours and minutes with 12h local time (LT) referring to noon. Finally, we use the solar declination δ as the angular distance of the sun from the equator, where δ=0° at the equinoxes and δ=±23.5° at the solstices. With this information, we get the SZA (θ_0):

$$\cos\theta_0 = \sin\phi\sin\delta + \cos\phi\cos\delta\cos h. \tag{9.5}$$

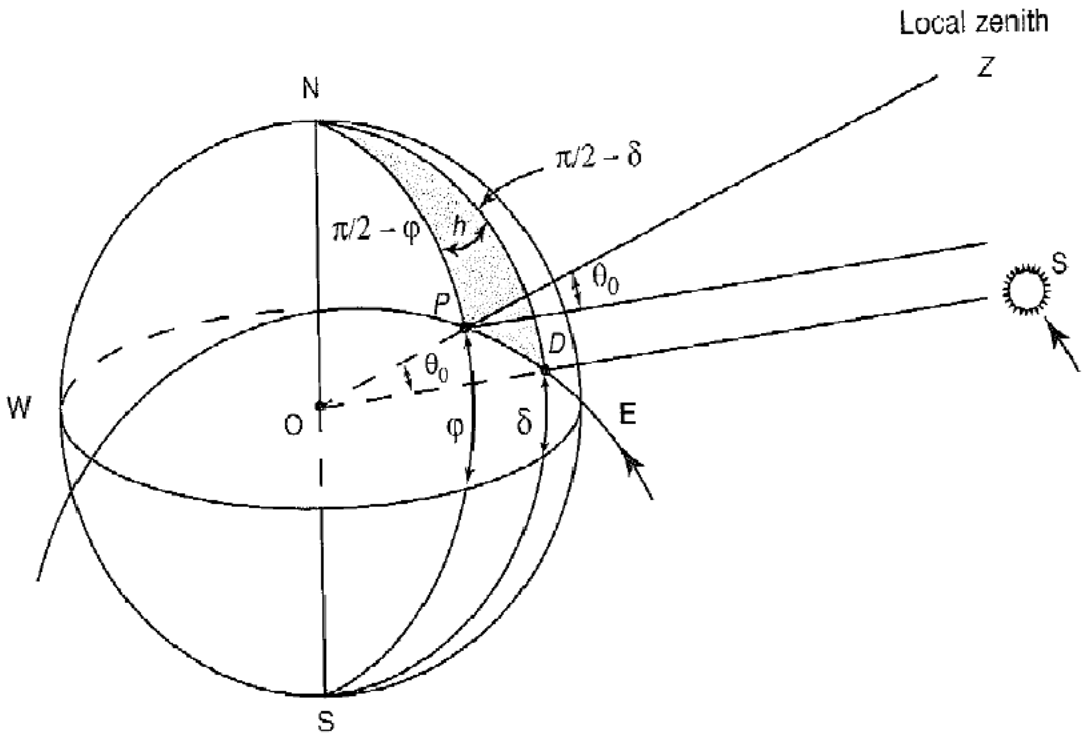

Figure 9.1: Relation of the solar zenith angle θ_0 to the latitude ϕ, the solar inclination angle δ, and the hour angle h. P and D are the point of observation and the point directly under the sun, respectively. Figure copied from Liou (2002).

9.1.4 Adopting a Chapman distribution for the airglow layer

In this model, the calculated VER is fitted to a Chapman distribution to illustrate some characteristics of the emission layer. Reed and Chandra (1975) proposed an equation analogous to the Chapman function after recognizing certain similarities between the distribution of atomic oxygen in the terrestrial mesosphere and the electron density in the ionospheric F region:

$$[O]_z = [O]_{max} \cdot \exp \frac{1}{2} \left[1 - \frac{z - z_{max}}{sH} - \exp \left(- \frac{z - z_{max}}{sH} \right) \right]. \tag{9.6}$$

In Equation 9.6, $[O]_{max}$ and z_{max} are the value and the altitude of the maximum density, respectively, in the profile, H is the scale height of the mixed atmosphere, and s is the scale factor. The scale factor s is a parameter reflecting the relative importance of mixing and diffusion in the lower thermosphere. If the atmosphere is completely mixed, then $2s \sim 1$. Reed and Chandra (1975) tested the validity of this equation by fitting it to several theoretical and measured profiles and concluded that it is a good approximation to relate the volume emission rate of oxygen-related airglow emissions to the atomic oxygen peak density. Later, Sharp and McDade (1996) suggested that the key parameters, $[O]_{max}$, z_{max}, and sH, could be obtained by simultaneously measuring airglow features from three oxygen-related emissions. The method was proven to be successful in deriving the atomic oxygen density distribution using airglow emissions from OH, atomic oxygen, and O_2 (Haley et al., 2000; Melo et al., 2001).

The expression of the Chapman distribution used in the airglow model follows the work of Cox et al. (2008, 2010) and Royer et al. (2010) to better capture the non-symmetry that is intrinsic to the loss and formation of the excited state:

$$\epsilon(XY^\star) = \epsilon_{max} \cdot \exp \left[1 - \frac{z - z_{max}}{H} - \exp \left(- \frac{z - z_{max}}{H} \right) \right] \tag{9.7}$$

where ϵ_{max} is the maximum value of the VER in the profile, in $cm^3\ s^{-1}$, z_{max} is the altitude in km at which this maximum occurs, and H is the e-folding depth in km of

the emission layer, or characteristic width of the airglow layer; that is the distance over which the VER decreases by a factor of e as compared to its maximum value ϵ_{max}. The parameters obtained from forcing the modeled VER to a fit with a Chapman function using a least-squares fitting method, i.e., ϵ_{max}, z_{max}, and H, along with the integrated intensity, I, allow quantitative comparisons with the available observations.

The motivation for choosing this approach is based on two major arguments: first, this parametrization represents the balance between production and loss of $XY^{\star}$; second, it provides a way to interpolate between the measured points, hence minimizing errors in the measurements as this interpolation is based on physical principles rather than mathematical. The limit of using a Chapman layer representation is that it does not capture dynamical features such as gravity waves. However, it is appropriate in this case since GCMs provide a climatological approach. The comparisons are made between modeled climate values and single-point observed profiles that are more susceptible to such events. This fact enables the investigation of local variations and therefore an improved understanding of the processed that control the composition and dynamics of the studied atmospheres.

9.2 Description of the kinetic parameters

9.2.1 The O_2 Herzberg I transition

Here, we assume that the three-body recombination Reaction 5.1 populates the lowest levels of $O_2(A^3\Sigma_u^+)$ (see Section 6 for a reason for this assumption). The calculations presented in this work have been performed using Equation 9.2; the kinetic parameters used in three different simulated scenarios are listed in Table 9.1. In case 1 of the Herzberg I simulations, we use the parameters derived empirically by Krasnopolsky (1986) following the Venus observations by Venera orbiters (Krasnopolsky and Tomashova, 1980), along with the quenching rate coefficients measured by Kenner and Ogryzlo (1983b, 1984)

that are also used in the former reference. The second simulated case combines the kinetic parameters measured in the laboratory at low vibrational levels by Kenner and Ogryzlo (1983b, 1984) with the yield inferred by Bates (1988). The last case for this emission is done with the best-fit set of parameters resulting from the model simulations of Krasnopolsky (2011) to match the Venus observations from the Venera era.

Table 9.1: Kinetics parameters used in the calculations of the VER of the O_2 Herzberg I band.

	Case 1	Case 2	Case 3
α	0.05 [1]	0.06 [2]	0.04 [3]
k_{O_2} ($cm^6\ s^{-1}$)	$2 \cdot 4.7 \times 10^{-33} \cdot (300/T)^2$ [4]	$2.5 \cdot 2.7 \times 10^{-33} \cdot (300/T)^2$ [5]	$2.5 \cdot 3 \times 10^{-33} \cdot (300/T)^{3.25}$ [6]
τ (s)	0.25 [1]	0.16 [7]	0.14 [3]
Q_{CO_2} ($cm^3\ s^{-1}$)	7×10^{-13} [8]	7×10^{-13} [8]	8×10^{-12} [3]
Q_O ($cm^3\ s^{-1}$)	1.3×10^{-11} [9]	1.3×10^{-11} [9]	1.3×10^{-11} [9]

[1] Krasnopolsky (1986)

[2] Bates (1988)

[3] Krasnopolsky (2011)

[4] value of Campbell and Gray (1973) × 2 (Krasnopolsky, 1986)

[5] value of Pejaković et al. (2008) × 2.5 (Nair et al., 1994)

[6] value of Smith and Robertson (2008) × 2.5 (Nair et al., 1994)

[7] Slanger and Copeland (2003)

[8] Kenner and Ogryzlo (1983b)

[9] Kenner and Ogryzlo (1984)

9.2.2 The O_2 Herzberg II transition

We consider three scenarios for the production of the Herzberg II emission in a CO_2 atmosphere. Table 9.2 lists the kinetic parameters used to calculate the VER from this emission following each scenario and using Equation 9.2. Case 1 is based on the recent observations of the Herzberg II transition by the VIRTIS instrument on Venus Express and the following analysis of the emission by García Muñoz et al. (2009b). The analysis

Table 9.2: Kinetics parameters used in the calculations of the VER of the O_2 Herzberg II band.

	Case 1	Case 2	Case 3
α	0.02 [1]	0.04 [2]	0.023 [3]
k_{O_2} (cm^6 s^{-1})	2.5×10^{-32} [4]	$2.5 \cdot 2.7 \times 10^{-33} \cdot (300/T)^2$ [5]	$2.5 \cdot 3 \times 10^{-33} \cdot (300/T)^{3.25}$ [6]
τ (s)	3.45 [7]	3.7 [8]	5-7 [3]
Q_{CO_2} (cm^3 s^{-1})	2.45×10^{-16} [1]	6×10^{-14} [9]	1.2×10^{-16} [3]
Q_O (cm^3 s^{-1})	5.9×10^{-12} [9]	5.9×10^{-12} [9]	8×10^{-12} [3]

[1] García Muñoz et al. (2009b)

[2] Bates (1988)

[3] Krasnopolsky (2011)

[4] Slanger et al. (2006)

[5] value of Pejaković et al. (2008) × 2.5 (Nair et al., 1994)

[6] value of Smith and Robertson (2008) × 2.5 (Nair et al., 1994)

[7] Bates (1989)

[8] Huestis et al. (1994)

[9] Kenner and Ogryzlo (1983a)

from García Muñoz et al. (2009b) resulted in a net production yield for the $O_2(c^1\Sigma_u^-, v{=}0)$ state of 0.01-0.02 and a rate coefficient for quenching by CO_2 of 2.45×10^{-16} cm^3 s^{-1}, when using the three-body recombination rate coefficient suggested by Slanger et al. (2006) and O quenching rate coefficient measured by Kenner and Ogryzlo (1983b). For case 2, we also calculate the emission from the $c^1\Sigma_u^-$ state using the laboratory measurements of the removal rate coefficients at small vibrational levels by Kenner and Ogryzlo (1983a; 1984) along with the recombination yield of Bates (1988). Case 3 uses the recommendations of Krasnopolsky (2011), which are a recombination yield of 0.023 and a removal rate coefficient by CO_2 of 1.2×10^{-16} cm^3 s^{-1}. These latter values were derived from reanalysis of the measurements of this emission on Venus by Venera 9 and 10 (Krasnopolsky and Tomashova, 1980; Krasnopolsky, 1981, 1986).

9.2.3 The O_2 Chamberlain transition

Krasnopolsky (2011) derived photochemical parameters for the production of the Chamberlain emission following assumptions based on observations of the band system. He used a production yield of 0.12 from theoretical calculations (Wraight, 1982; Smith, 1984), a three-body recombination rate of $3 \times 10^{-33} \cdot (300/T)^{3.25}$ cm^6 s^{-1} (value of Smith and Robertson (2008) scaled by a factor of 2.5), the same collisional removal rate by O as for the $A^3\Sigma_u^-$ state, which is 1.3×10^{-11} cm^3 s^{-1} (Kenner and Ogryzlo, 1984), and derived a quenching rate by CO_2 of 4.5×10^{-13} cm^3 s^{-1} to fit the observations of the emission on Venus.

9.2.4 The O_2 IR transition

In our airglow simulations, we use the product βJ (see Equation 9.3) as calculated by the LMD-MGCM. The kinetics parameters for Equation 9.1 for each of the simulated cases of the IR Atmospheric airglow intensity are shown in Table 9.3. In brief, case 1 corresponds to the best-fit parameters derived by Krasnopolsky (2010) from Earth-based observations of the O_2 IR emission in the Venus atmosphere, while case 2 uses the parameters that best match the VIRTIS observations of Venus nightglow (García Muñoz et al., 2009b), and the laboratory parameters for production and loss of $a^1\Delta_g$ define case 3. The parameters in this latter set are also used in the analysis of Krasnopolsky (2011) to reconcile the observations of the emission on both Earth and Venus.

Table 9.3: Kinetics parameters used in the calculations of the VER of the O_2 IR Atmospheric band.

	Case 1	Case 2	Case 3
α	0.67 [1]	0.5 [2]	0.7 [3]
k_{O_2} ($cm^6\ s^{-1}$)	$1.2 \times 10^{-32} \cdot (300/T)^2$ [4]	2.5×10^{-32} [5]	$2.5 \cdot 3 \times 10^{-33} \cdot (300/T)^{3.25}$ [6]
τ (s)	4470 [7]	4545 [8]	4460 [7]
Q_{CO_2} ($cm^3\ s^{-1}$)	5×10^{-21} [3]	2×10^{-20} [9]	10^{-20} [10]
Q_O ($cm^3\ s^{-1}$)		2×10^{-16} [9]	2×10^{-16} [9]

[1] Krasnopolsky (2003, 2006a)

[2] García Muñoz et al. (2009b)

[3] Krasnopolsky (2010)

[4] Krasnopolsky (1995)

[5] Slanger et al. (2006)

[6] value of Smith and Robertson (2008) × 2.5 (Nair et al., 1994)

[7] Lafferty et al. (1998)

[8] Newman et al. (1999)

[9] Sander et al. (2006)

[10] Krasnopolsky and Bjoraker (2000)

Chapter 10

Model simulations of O_2 airglow: Mars

In this chapter, we present the results of our simulations of the four O_2 airglow features considered in this study for the Martian atmosphere at nighttime using the atmospheric composition from a one-year simulation of the LMD-MGCM, as described in Section 8.1 in combination with the airglow model developed for this purpose (see Section 9.1). In Section 5.1, we discussed the specific mechanisms responsible for the production of each of the O_2 airglow emissions considered in this chapter, and in Section 9.2 we detailed the different kinetic parameters used in the airglow calculations to be presented here. The results from the simulations of the emission profiles performed for each of the sets of kinetic parameters will be analysed in Section 10.1. Water and dust can change the atmospheric conditions; the impact of these fields on the airglow intensities and the results are presented in Section 10.2. Finally, Section 10.3 summarises the outcomes of these O_2 airglow simulations.

The results presented in this chapter have been published in Gagné et al. (2012a).

10.1 Sensitivity to kinetic parameters

As discussed previously (see Section 6.1), the determination of the kinetic parameters needed to quantify the O_2 emissions from the proposed photochemical scheme (see Section 5.1) remains a challenge. The sensitivity of the airglow to this uncertainty is assessed in this section where we proceed with modeled simulations of each of the four O_2 band systems using three different sets of kinetic parameters for each system, which are explained and listed in Section 9.2.

10.1.1 The Herzberg I emission

Figure 10.1 shows the VER profiles for the O_2 emission resulting from the Herzberg I transition for each simulated case from Table 9.1 at latitudes 67.5°N, 0°, and 67.5°S for L_S=0 and 180°. Independently of the latitude and season, case 2 yields the strongest peak emission rate, with case 1 being slightly weaker. Case 3 is on average a factor of 1/3 to 1/4 the intensity of cases 1 and 2, respectively. The airglow layer peaks between 61 and 69 km over the polar regions, with case 3 peaking at a higher altitude than the other two cases, which is a consequence of stronger quenching by CO_2 in this latter case. The airglow layer has a mean topside scale height of 10 km. Over the equatorial region, the VER profile exhibits a double-layer profile with the upper layer, at 85 km on average, being the most intense. This upper layer is thinner than the lower one, with a mean scale height of 6.5 km. The temperature profile is also shifted upward by 10 km as compared to those in the polar regions (see Figure 8.1), and this directly increases the production of the excited state since, again, the recombination rates used here are temperature-dependent (see Table 9.1). The lower layer peaks at about the same altitude as the single-layer profile observed in the polar regions, which is near 65 km. The presence of this secondary peak is due to the maximum in O density that now occurs above 70 km.

According to our simulations, the maximum intensity reaches above 2 kR in case 3 over

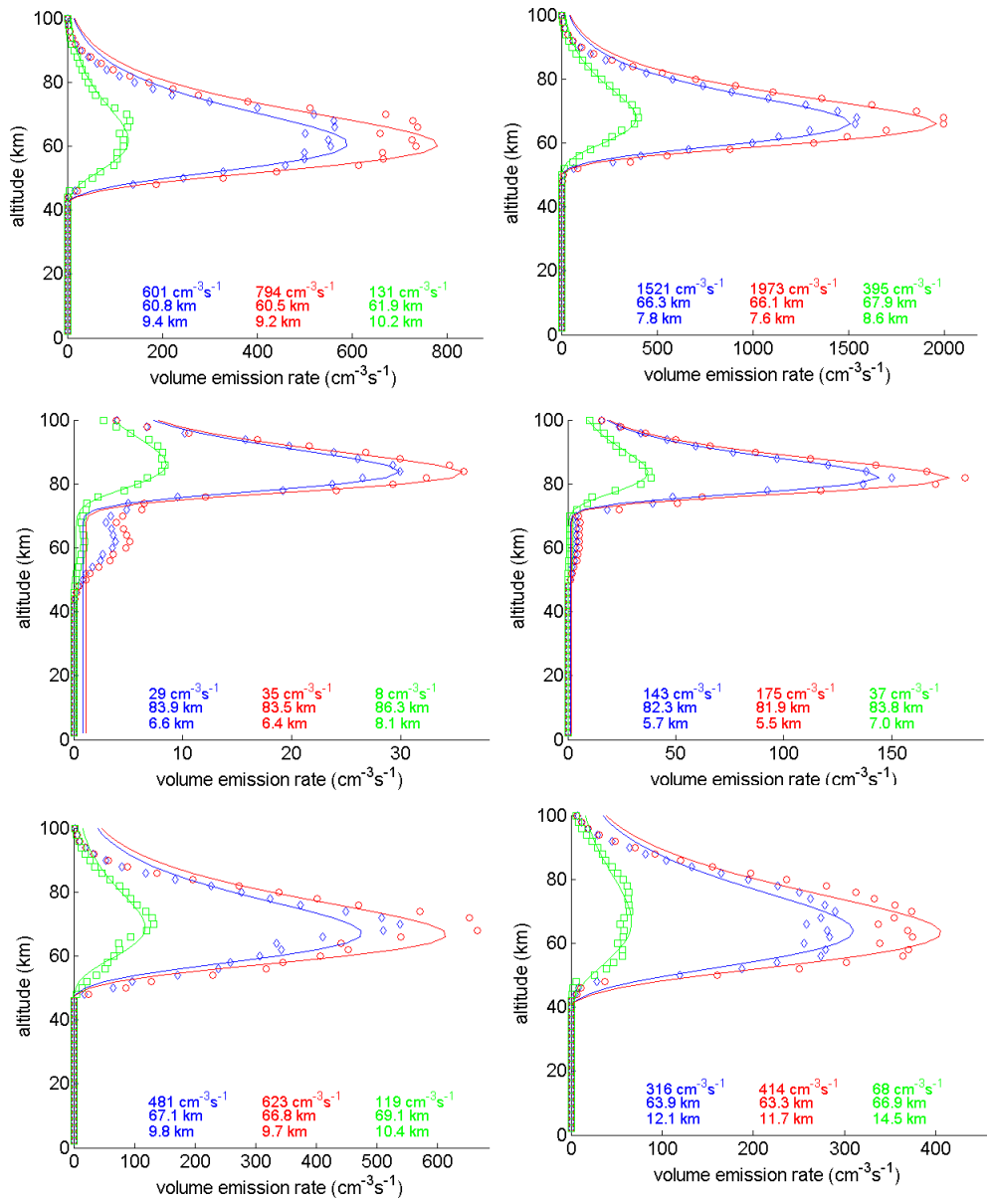

Figure 10.1: Simulated VER profiles for the O_2 Herzberg I emission at 00 LT at L_S=0° (left column) and L_S=180° (right column) for latitudes 67.5°N (upper row), 0° (middle row), and 67.5°S (lower row) for three sets of kinetic parameters called "cases" (see text for details). Blue features are used for case 1, red for case 2, and green for case 3. The symbols are the calculated VER at each altitude from the airglow model, while the line corresponds to the Chapman layer fit for each VER profile; the fitting parameters, ϵ_{max} (upper), z_{max} (middle), and H (lower), are given.

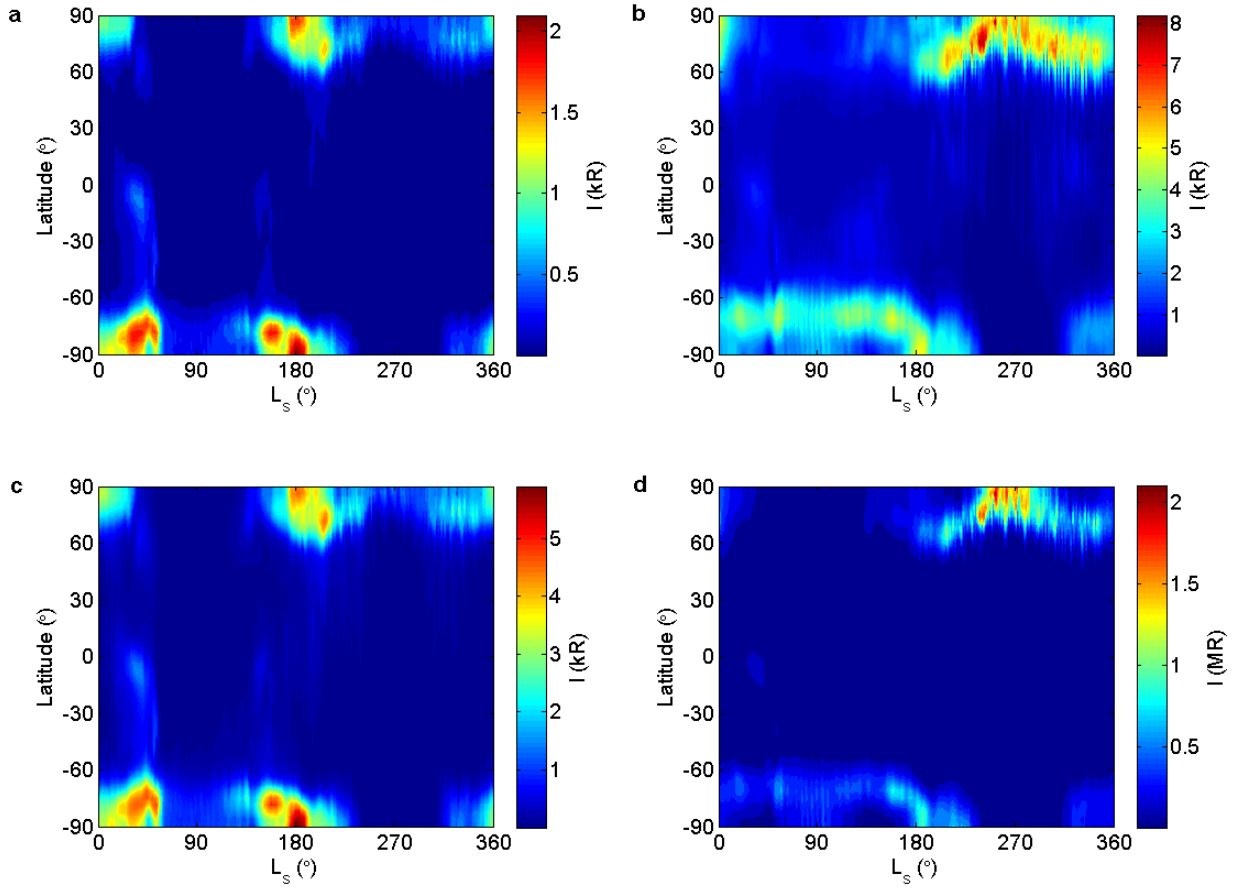

Figure 10.2: Simulations of the global distribution of intensity of the O_2 emission bands at 00 LT for: a) the Herzberg I emission; b) the Herzberg II emission; c) the Chamberlain emission; d) and the IR Atmospheric emission. The color bar is the intensity in kR and in MR for the IR emission.

the polar regions and the maxima are localised shortly before/after the vernal/automnal equinoxes. Over the equator, the maximum intensity drops by one to two orders of magnitude due mainly to the larger production of the excited state resulting from a larger atomic oxygen mixing ratio between 50 and 70 km in the polar regions. As for cases 1 and 2, the intensity range is larger by a factor of 3 to 4, respectively, as compared to simulated case 3. However, the structure of the annual distribution is similar, with a bimodal maximum in the polar regions during the polar nights. Figure 10.2a gives a representation of the global distribution of the emission following the case 3 scenario.

As discussed before (see Section 7.1.1), there is no observation of this emission in the Mars atmosphere to this date. From the discussion of Krasnopolsky (1986), the observed Venus intensity for the Herzberg I transition is 140 R for latitudes $\pm 30^\circ$ and the calculations reported in that study yield an expected intensity of 2 R for Mars, resulting in a Venus-to-Mars intensity ratio of 70. Case 3 of our simulations is the one that yields the lowest intensity values, with values as low as a few rayleighs up to around 200 R over the equatorial region. This simulation gives a maximum intensity of about 2 kR during the Southern hemisphere polar night and slightly lower values for the Northern hemisphere. The intensity range for cases 1 and 2 is typically an order of magnitude greater than for case 3. This latter case seems to be in better agreement with the expected intensity of Krasnopolsky (1986) and Krasnopolsky (2011). Therefore, it is our suggestion that the removal rate coefficient of the $A^3\Sigma_u^+$ state for quenching by CO_2 should be revised to account for greater loss of this excited state through this pathway. Slanger and Copeland (2003) also favour increasing the rate coefficient of Kenner and Ogryzlo (1983b) by one order of magnitude with the argument that "the trends of the higher levels suggests that [the latter] afterglow results underestimate the magnitude of the removal rate coefficients, a conclusion previously reached by aeronomic modellers."

We continue by exploring the relationship between the Herzberg I and Herberg II (further discussed below) emissions, to preserve the consistency between Mars and Venus

observations. If we apply the Venus-to-Mars ratio of intensity suggested by Krasnopolsky (1986) to case 1, i.e., 70, this would yield a maximum intensity of ∼14 kR on Venus in the tropics, which is larger than the maximum intensity of ∼5 kR observed on Venus from the Herzberg II band (Slanger et al., 2006). The laboratory results suggest that the Herzberg I system would be much weaker than the Herzberg II system in a CO_2 atmosphere. Two contributions could explain these discrepancies: extrapolation of the localised intensity maxima on Mars to the Venus atmosphere is not reasonable given the different dynamical processes responsible for the $O(^3P)$ distribution in each atmosphere, or the quenching of $A^3\Sigma_u^+$ is underestimated in our model, indicating that laboratory measurements for collisional removal of $A^3\Sigma_u^+$ are critically needed to properly quantify this emission. Nevertheless, we conclude from this exercise that the quenching rate by CO_2 measured in the laboratory for the upper state of the Herzberg I system should be increased by at least one order of magnitude. As for the three-body recombination yield, a relatively small value like the ones used in this study seems to give reasonable emission rates in conjunction with a proper quenching rate. These yields are close to the theoretically calculated ones (Wraight, 1982; Smith, 1984).

10.1.2 The Herzberg II emission

In Figure 10.3, which displays the results from the simulations of the O_2 Herzberg II emission, we observe that case 3 always yields the largest peak emission rate (ϵ_{max}) and case 2 the smallest. The variations in the CO_2 removal rate in the simulated cases are responsible for this observed difference: the weaker the quenching of the excited state by CO_2, the larger is the scale height (H) and the higher is the maximum of the emission (z_{max}). The peak emissivity occurs between 51 and 66 km for all latitudes. The profiles at 0° latitude show a double-layer structure, as for the Herzberg I band emission, with the secondary peak around 80 km. However, the lower layer is now the strongest for most of the profiles. The difference in the quenching factor for this emission as compared

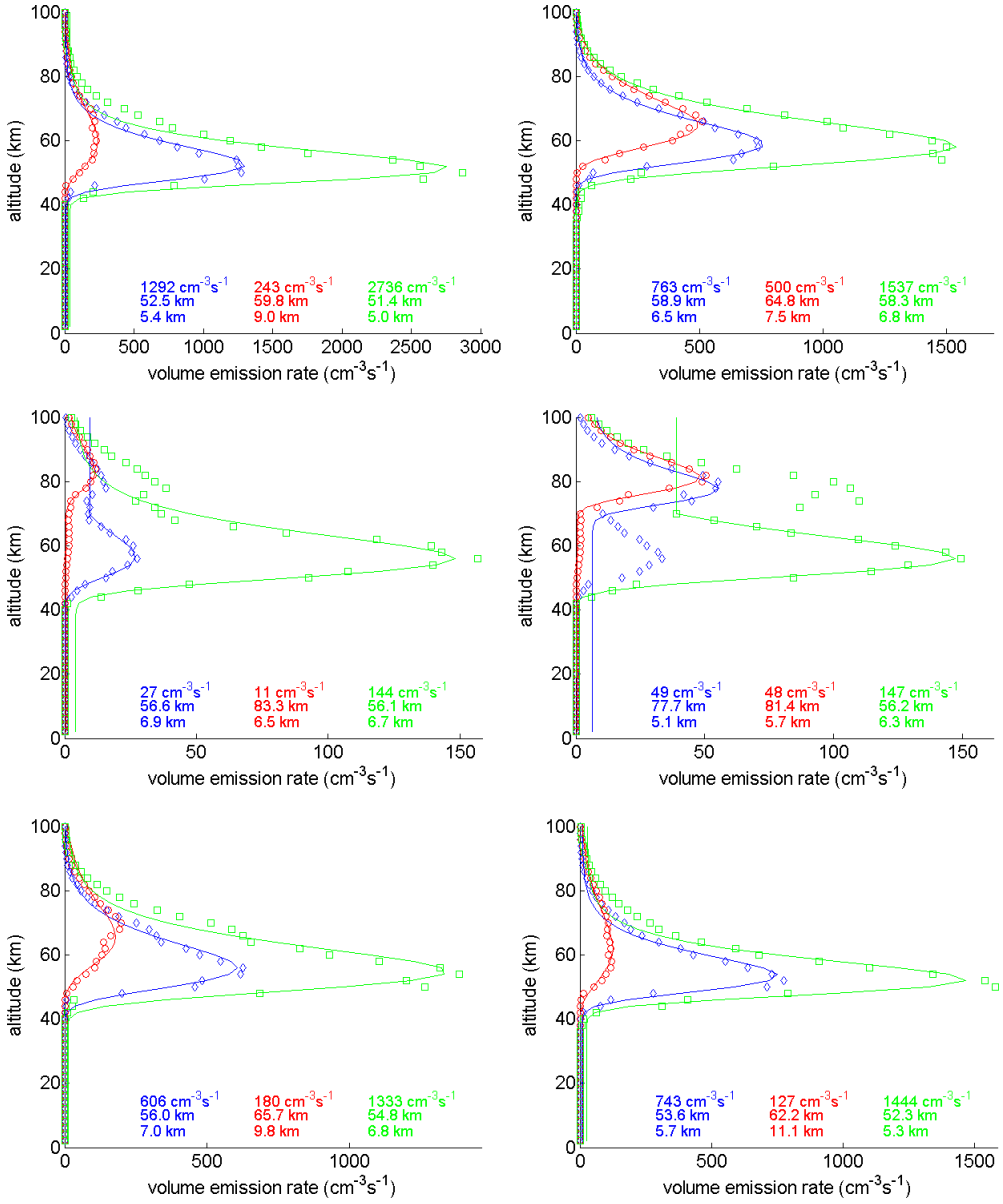

Figure 10.3: Simulated VER profiles for the O_2 Herzberg II emission at 00 LT at L_S=0° (left column) and L_S=180° (right column) for latitudes 67.5°N (upper row), 0° (middle row), and 67.5°S (lower row) for three sets of kinetic parameters called "cases" (see text for details). Blue features are used for case 1, red for case 2, and green for case 3. The symbols are the calculated VER at each altitude from the airglow model, while the line corresponds to the Chapman layer fit for each VER profile; the fitting parameters, ϵ_{max} (upper), z_{max} (middle), and H (lower), are given.

to that for the Herzberg I band is the reason for the predominance of the lower airglow layer observed here.

Again, we assume that the processes responsible for the O_2 photochemistry in Venus and Mars atmospheres are coherent because of the similarity in the temperature, and CO_2 and atomic oxygen density profiles (see Table 2.1). After analysis of the simulations performed for the same three cases using Venus nighttime conditions, as will be presented in Chapter 11, we concluded that the set of parameters used in cases 1 and 3 better reproduce the ϵ_{max} and z_{max} observed on Venus from VIRTIS (García Muñoz et al., 2009b; Migliorini et al., 2011b). The difference in peak VER of the simulated profiles is one order of magnitude between these cases and case 2. Between cases 1 and 3, there is a factor of two difference in VER, which results directly from the difference in the quenching rates between these two cases. Moreover, case 3 tends to produce a peak emission at a lower altitude, i.e., lower z_{max}, than case 1, which is in better agreement with the observations from VIRTIS (García Muñoz et al., 2009b). From the simulations presented here, we conclude that the quenching rate for the O_2 ($c^1\Sigma_u^-$) state by CO_2 should be revised to be about 2×10^{-16} cm^3 s^{-1}. A low production yield of 0.02 seems to be reasonable to produce the emission intensity that would be expected on Mars, based on the above-mentioned Venus simulations.

Given the fact that we argued previously that case 3 is the optimal set of kinetic parameters to represent the expected emission rate, according to comparison with Venus observations, we suggest that the airglow distribution for the Herzberg II band would resemble that of Figure 10.2b. The maximum intensity obtained for this case of the Herzberg II simulations is 8 kR before the North Pole winter solstice (L_S=240-270°) and 5 kR before the South Pole fall equinox (L_S=150-180°). Globally, the intensity distribution is more pronounced during the polar nights. The emission is weaker between latitudes ±50°, ranging from 20 to 700 R, and in the polar regions during spring and summer.

10.1.3 The Chamberlain emission

It is challenging to make any reasonable calculations for the VER profile of the Chamberlain transition, given the lack of measured rate coefficients for the $A'^3\Delta_u$ state, as discussed in Section 6.1.3.

We assume a ratio of intensity of the Chamberlain band to that of the Herzberg II band of about six according to the discussion of Slanger et al. (2001) based on the Venus observations of the Herzberg II band system. Assuming the same chemical mechanism for both Venus and Mars, a rough calculation of the expected intensity of this transition based on the intensity of the Herzberg II band from our simulations gives an expected intensity during the polar nights for the Chamberlain band of as much as 1.3 kR for case 3, and as little as 300 R when considering case 2.

When we use the parameters proposed by Krasnopolsky (2011) in our airglow model, i.e., α=0.12, k_{O_2}=$2.5 \cdot 3 \times 10^{-33} \cdot (300/T)^{3.25}$ cm^6 s^{-1}, Q_O=1.3×10^{-11} cm^3 s^{-1}, and Q_{CO_2}=4.5×10^{-13} cm^3 s^{-1}, we obtain a global distribution of the emission, as displayed in Figure 10.2c, that matches that of the Herzberg I band with slightly larger intensity values. This is reasonable since the yield used for the production of the $A'^3\Delta_u$ state is three times larger than that for the $A^3\Sigma_u^-$ state in case 3 of our simulations, while the quenching factor is about 20 times smaller for the Chamberlain band than for the Herzberg I band in case 3. The intensity resulting from the Chamberlain transition reaches values above 2 kR after/before the vernal/autumnal equinox and the maximum is found around L_S=180° in the Southern Hemisphere where the emission is larger than 5 kR. This maximum is greater than expected from the rough calculation inferred from the intensity ratio between the Herzberg II and the Chamberlain observations made in the Venus atmosphere as discussed above.

10.1.4 The IR Atmospheric emission

00 LT

We now present predictions for the nighttime O_2 1.27-μm emission following our airglow simulations. During the night, the main production mechanism for O_2 ($a^1\Delta_g$) is shut down, i.e., Reaction 5.4 is no longer active, so that the intensity is greatly reduced, except during the polar night, when the VER is increased by two orders of magnitude as compared to that over the equatorial regions. The increase in O_2 emission above the winter poles is due to downward transport of large amounts of O produced in the thermosphere (Gondet et al., 2010; Bertaux et al., 2011, 2012; Clancy et al., 2011a, 2012).

The VER profiles at 00 LT for this emission are more homogeneous from case to case as compared to the other band emissions as can be seen in Figure 10.4. The peak VER changes mostly in response to the production yield, with case 3 being the strongest and case 2 the weakest. The peak altitude, which is mostly determined from the collisional removal rate, is constant among the simulated cases for a given atmospheric background and varies between 53 and 61 km in the polar regions depending on the season. The scale height shows minimal variations across the simulations; the mean is 6 km with a standard deviation of 1 km.

In our simulations, the profiles at the equator show a double peak feature with the upper layer being weaker than the lower one for L_S=0° while the upper layer is the most intense at L_S=180°. The uppermost layer peaks at 80 km and the lower one reaches its maximum near 55 km. The vertical distribution of this emission is very similar to that for the Herzberg II emission, with peak VER located at about the same altitudes for these two transitions, while the profiles for the Herzberg I band peak at higher altitudes.

The intensity of the IR emission at 00 LT resulting from the simulations ranges from 1 to 2 MR, with a maximum located at winter solstice in the Northern hemisphere. The intensity maxima from case 1 are greater than for cases 2 and 3. Although by comparing

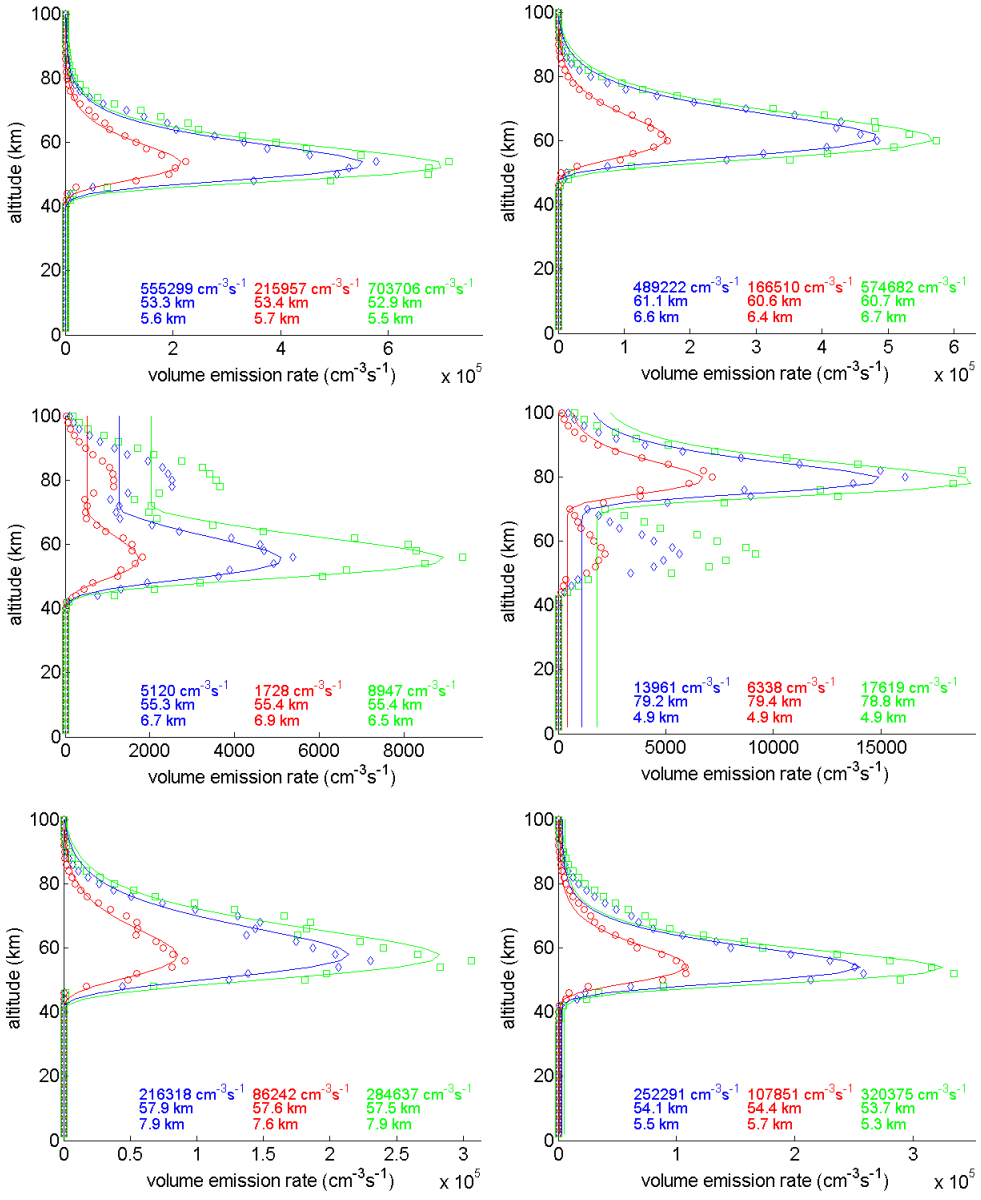

Figure 10.4: Simulated VER profiles for the O_2 IR emission at 00 LT at L_S=0° (left column) and L_S=180° (right column) for latitudes 67.5°N (upper row), 0° (middle row), and 67.5°S (lower row) for three sets of kinetic parameters called "cases" (see text for details). Blue features are used for case 1, red for case 2, and green for case 3. The symbols are the calculated VER at each altitude from the airglow model, while the line corresponds to the Chapman layer fit for each VER profile; the fitting parameters, ϵ_{max} (upper), z_{max} (middle), and H (lower), are given.

our results at 12 LT with SPICAM observations, as will be presented in the next section, we would be inclined to favour the parameters used in case 2; for 00 LT, it is more difficult to choose one case over the other. A seasonal map for this emission at 00 LT is shown in Figure 10.2d from simulations of the emission using the case 2 scenario. Our model results are in the same range of magnitude as the values from OMEGA.

Figure 10.5 reports on the individual measurements of the nighttime O_2 1.27-μm emission made with OMEGA (Bertaux et al., 2012) and also with SPICAM (Fedorova et al., 2011) along with our model results for the same location and season. To reduce the effect of local dynamical variations in the atmosphere, we also computed the average of the intensity over 5° of L_S centered around the season of the observation, i.e., average over L_S-2 to L_S+2. We notice from this figure that in most instances, the modeled intensity is smaller than the measured intensity. Also, the values are generally closer to the observed vertically integrated intensity for the period L_S=111-120°, while for the period L_S=152-164°, the model clearly underestimates the measured intensities. For the peak altitude, our model overestimates the altitude as compared to the OMEGA and SPICAM results. In general, we are satisfied with the realistic representation of the measurements from the simulations with our airglow model. We advise the reader to take into consideration that our model is used for a climatological study of the airglow distribution, while the observations represent single-point measurements that are subject to short time-scale variations due to the, e.g., solar activity, meteorological conditions, etc. We therefore do not expect a perfect match between the model results and the measurements. Moreover, without errors on the observed quantities from the OMEGA and SPICAM instruments, since they were not provided, we cannot quantify the accuracy of our model simulations.

From our simulations, we observe day-to-night variations over the polar regions that do not exceed more than one order of magnitude difference for all cases. This is a consequence of the constant solar illumination at high latitudes in summertime. In the regions of permanent day, i.e., summer poles, the O_2 emission includes a contribution

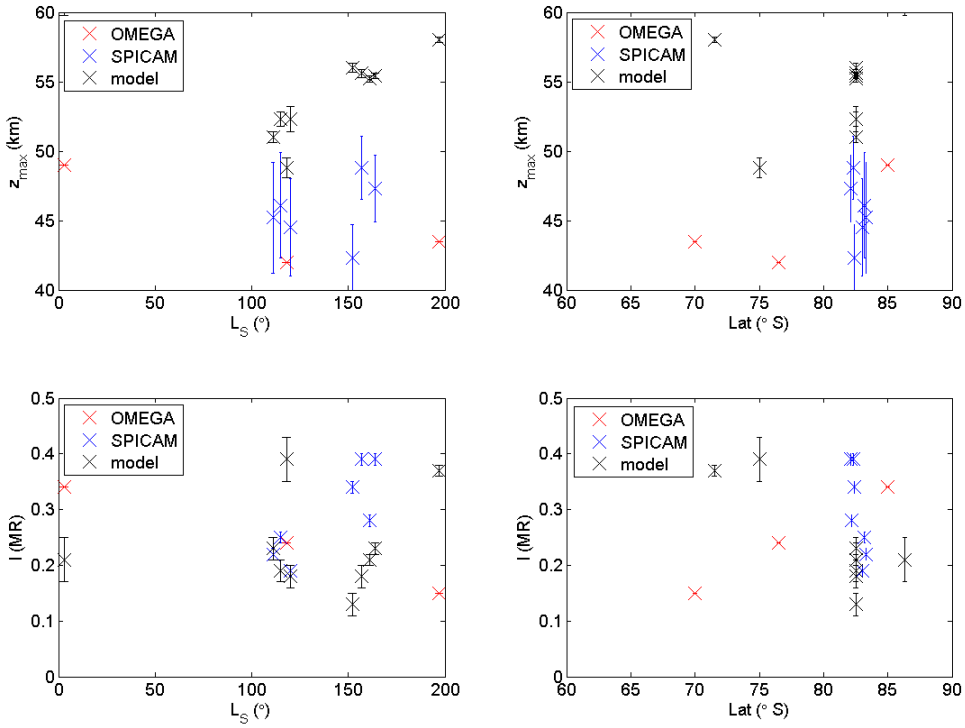

Figure 10.5: Comparison of measurements of O_2 1.27-μm nightglow with OMEGA (red, Bertaux et al. (2012)) and SPICAM (blue, Fedorova et al. (2011)) with modeling results (black). The model results are given for the same latitude and season as of the observations; these values are averages over 5° of L_S centered around the season of the observation.

from O_3 photolysis, which is not visible in Figure 10.2 since the O_3 photolysis was shut down for this simulation to avoid contamination from dayside $O_2(a^1\Delta_g)$ production by O_3 photolysis. By contrast, in the latitudinal band ±50°, the intensity ranges from 1 to 100 kR at 00 LT, much weaker than the simulated intensities at 12 LT (0.5-2 MR). This temporal variation is a consequence of the increased production of $a^1\Delta_g$ at 12 LT from the photolysis of O_3.

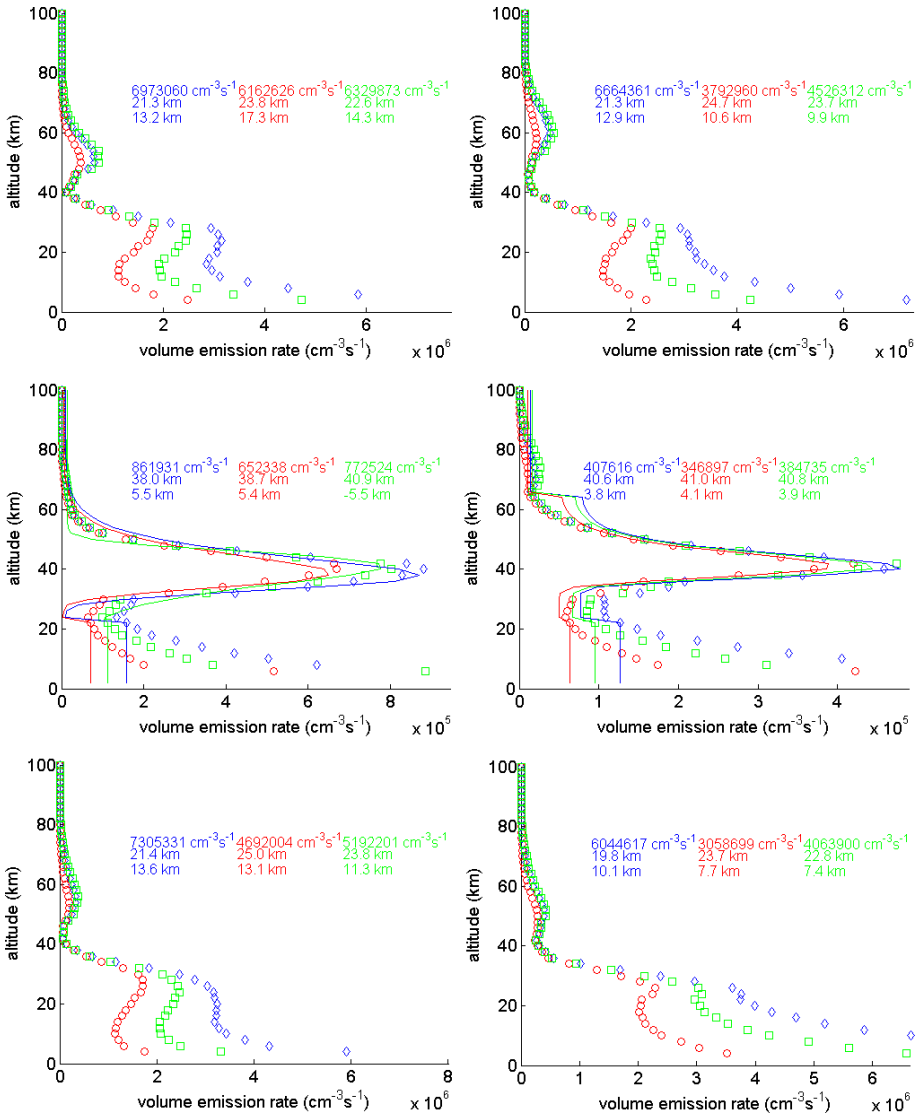

Figure 10.6: Simulated VER profiles for the O_2 IR emission at 12 LT at L_S=0° (left column) and L_S=180° (right column) for latitudes 67.5°N (upper row), 0° (middle row), and 67.5°S (lower row) for three sets of kinetic parameters called "cases" (see text for details). Blue features are used for case 1, red for case 2, and green for case 3. The symbols are the calculated VER at each altitude from the airglow model, while the line corresponds to the Chapman layer fit for each VER profile; the fitting parameters, ϵ_{max} (upper), z_{max} (middle), and H (lower), are given.

12 LT

To verify the internal consistency of our airglow model, we simulate emissions from the O_2 IR emission at 12 LT for comparison with the available observations. The VER profiles calculated for the three different cases at several latitudes and seasons are shown in Figure 10.6. The daytime airglow emissions mimic the ozone concentration throughout the vertical range, since it originates mainly from the production of the $a^1\Delta_g$ state through photodissociation of ozone (compare the density profile of O and O_3 in Figure 8.2). The contribution from O-O recombination is then negligible. The profiles all have a double-layer structure, except for L_S=0° at latitude 0° (see Figure 10.6). The lower layer is mainly due to $O_2(a^1\Delta_g)$ that is quenched at larger pressures, combined with the emission rate decreasing with increasing height. Contrary to the 00 LT profiles previously discussed for the other transitions, the layer close to the ground is the more intense during the day and has itself a double peak, although not properly defined. Over the equator, the double-peak feature of the lower airglow layer is better defined. Over the poles, the emission rate within this lower layer reaches a maximum below 30 km, then decreases with decreasing altitude, and increases again down to the surface. At these latitudes, the availability of O_3 results in an emission at 1.27 μm down to the surface, even in the presence of quenching. The uppermost layer peaks between 50 and 60 km in the polar regions, while the peak VER of the upper layer is shifted upward by about 10 km over the equator.

The simulations of the variations in latitudes and seasons of the intensity from the IR band at 12 LT give similar results for all cases regarding the structure of the airglow distribution. Figure 10.7a shows the global distribution of the daytime IR emission of O_2 following our scenario case 2, which gives smaller intensity maxima, in better agreement with the measurements of the emission on Mars. The major difference between the scenarios simulated here is the range of magnitude of the calculated intensity: case 1 maximum intensity reaches 50 MR, while cases 2 and 3 do not produce intensities

exceeding 40 MR, with case 2 producing slightly lower values.

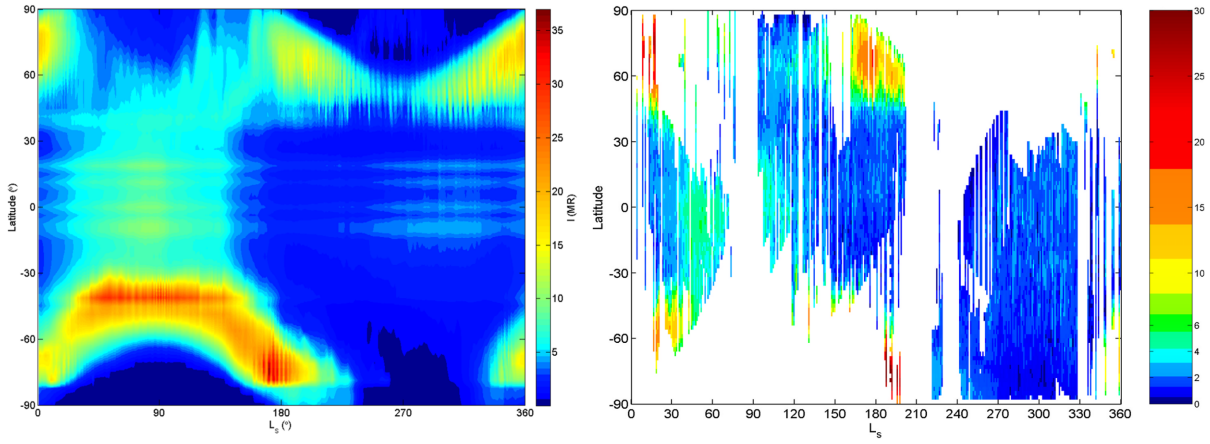

Figure 10.7: Simulated global distribution of intensity of the O_2 IR Atmospheric emission at 12 LT from: a) the model simulations using case 2 and b) the SPICAM measurements (figure copied from Fedorova et al. (2006a)). The color bar is the intensity in MR for the IR emission.

The structure of the seasonal and latitudinal distribution of O_2 emissions reflects the ozone distribution and variations. The intensity maxima are located around the polar night terminator on the dayside. The increase in intensity at the terminator encircling the polar winter is a direct consequence of the chemistry that occurs between the HO_x and O_x species: at high latitudes between 65° to 85° during wintertime, most of the water is condensed on the polar caps, which reduces the destruction of O_x through reactions with HO_x (Lefèvre et al., 2004).

We compare our global annual distribution of the daytime IR Atmospheric band for Mars with the Earth-based observations made with the IRTF/CSHELL long-slit spectrograph (Krasnopolsky, 2003, 2007), the model results of Krasnopolsky (2006a) and Krasnopolsky (2009), and the SPICAM observations (Fedorova et al., 2006a,b). The structure of the airglow distribution from our simulations is similar to the observations. Overall, our model captures well the seasonal and latitudinal variations of the observed O_2 IR emission. However, coverage of the polar regions, i.e., poleward of ±65°, by obser-

vations is sparse. As an example, we provide a visual comparison between the modeled IR distribution (Figure 10.7a) with the observations (Figure 10.7b) of this emission from SPICAM.

As for seasonal trends in our model predictions as shown in Figure 10.7a, the intensity increases shortly after winter solstice in the South polar region, i.e., beyond 65°, to reach a maximum intensity above 25 MR around the fall equinox and then decreases until shortly after the summer solstice. Then, the intensity remains low and constant during the polar winter night until it rises before the spring equinox when it reaches another maximum around L_S=0°. In the Northern hemisphere, a similar pattern is observed, but here the maximum at L_S=0° is stronger than at L_S=180°. Moreover, the intensity during the summer season does not reach as low values as in its Southern counterpart. Over the equatorial region, the increase in intensity seen in the observations between L_S=40–140° is also represented in our model.

For the latitudinal variations of the airglow at different seasons, the pattern seen in our model simulations agree well with the available data sets (Krasnopolsky, 2003, 2006a, 2007, 2009; Fedorova et al., 2006a,b; Altieri et al., 2009), with case 2 scenario in better agreement for the intensity range. From Figure 10.7a, the average intensity between latitudes ±30° varies from 5 to 10 MR for L_S=40–140° and is below 5 MR for the rest of the year. In the subpolar regions, i.e., between latitudes ±30–65°, all cases seem to overestimate the increase toward the polar terminator. However, Krasnopolsky (2003) notes that the airglow intensities observed at these dates for latitudes 50-70°S are unexpectedly low and this could be due to unfavourable observation geometries at the observation dates for the subpolar regions. As for the observations by SPICAM, the coverage was limited in this latitudinal band.

Current nightglow studies favour the use of a relatively high production yield (of 0.7 or larger) for the $a^1\Delta_g$ state in a CO_2 atmosphere (Crisp et al., 1996; Gérard et al., 2008c; Krasnopolsky, 2011). Therefore, a quenching rate close to the laboratory upper value of

2×10^{-20} cm^3 s^{-1} (Sander et al., 2006) is needed in order to be in agreement with the available observations of the IR Atmospheric emission on Mars.

10.2 Sensitivity to atmospheric conditions

Dust and water can vary strongly in the Mars atmosphere. As shown by the continuous measurements of temperature, dust, and water from the Mars Climate Sounder on MRO (McCleese et al., 2010), the main effect of dust is to warm the atmosphere, allowing more H_2O to be transported upwards. This is the reason O_3 disappears almost completely during the perihelion season, and hence the O_2 emission caused by photolysis also vanishes (Lefèvre et al., 2004). The effect of dust on photolysis rates is therefore expected to be negligible compared to the change in H_2O that occurs at the same time.

As mentioned in Section 8.1, simulations of the O_2 airglow emissions for the IR Atmospheric emission were performed with three different runs of the LMD-MGCM using the set of kinetic parameters case 2. As a reminder, in run 1, the dust and water cycles have not been optimised with any observations. However, in run 2, the dust cycle matches the MGS-TES MY24 measurements, but has the same water cycle as run 1, and run 3 has the same dust cycle as run 2 but a water cycle that reproduces the MGS-TES measurements. The goal of this exercise is to study the response of the airglow emissions to changes in the dust and water load. Given the impact of the water and dust content on the atmospheric composition and temperature structure, we would expect to see variations in the vertical structure of the airglow emissions. As for the VER profiles, shown in Figure 10.8, there is more similarity between the profiles performed with runs 1 and 2 above 50 km in altitude at latitude $\pm 67.5°$. Above this altitude, the emission rate from run 3 is typically stronger and peaks at lower altitudes than for the two other runs. This pattern illustrates the impact of the water cycle on the oxygen chemistry, which directly affects the emission profile. Below 50 km, the profiles from runs 2 and 3 have

a similar structure, although the emission rate from run 3 is greater than for run 2; the profile from run 1 does not follow the structure of the two other cases. This behaviour would be due to changes in dust levels affecting mostly the lower atmosphere.

Over the equator, the emission rate from run 3 is much larger than for the two other cases above 30 km. The profiles from runs 1 and 2 have a similar behaviour below 30 km, as compared to that from run 3. Dust load would be responsible for the observed difference: dust has a strong impact on daytime surface heating such that the more photons with short wavelengths, i.e., wavelengths in the UV range, reaching the lower atmosphere, the more atomic oxygen is produced due to ozone photodissociation. In contrast, the water cycle has a direct impact on the oxygen species, particularly over the polar regions where most of the cycling between the HO_x radicals and reservoir species come into play (Lefèvre et al., 2004). We would expect very subtle variations from the dust cycle beyond the subtropics because of the longer mean free path, which reduces the solar flux at the surface.

10.3 Summary

In this chapter, we have investigated the global distribution of the emission profile and integrated intensity of four emissions of O_2 airglow in a CO_2 atmosphere: the Herzberg I and II, the Chamberlain, and the IR Atmospheric occurring from the UV to the IR spectral region. Although none of the O_2 visible emissions have been observed on Mars at night, most probably because of the inadequate S/N of the previous instruments, the observations of the Herzberg II and Chamberlain band systems in the Venus atmosphere motivate this study. The O_2 Herzberg and Chamberlain estimations represent, to the best of our knowledge, the first attempt to simulate these emissions for Mars using a 3-D model as inputs for atmospheric conditions. Our simulations agree with previous studies that have suggested that the Herzberg II band emission is the most promising candidate

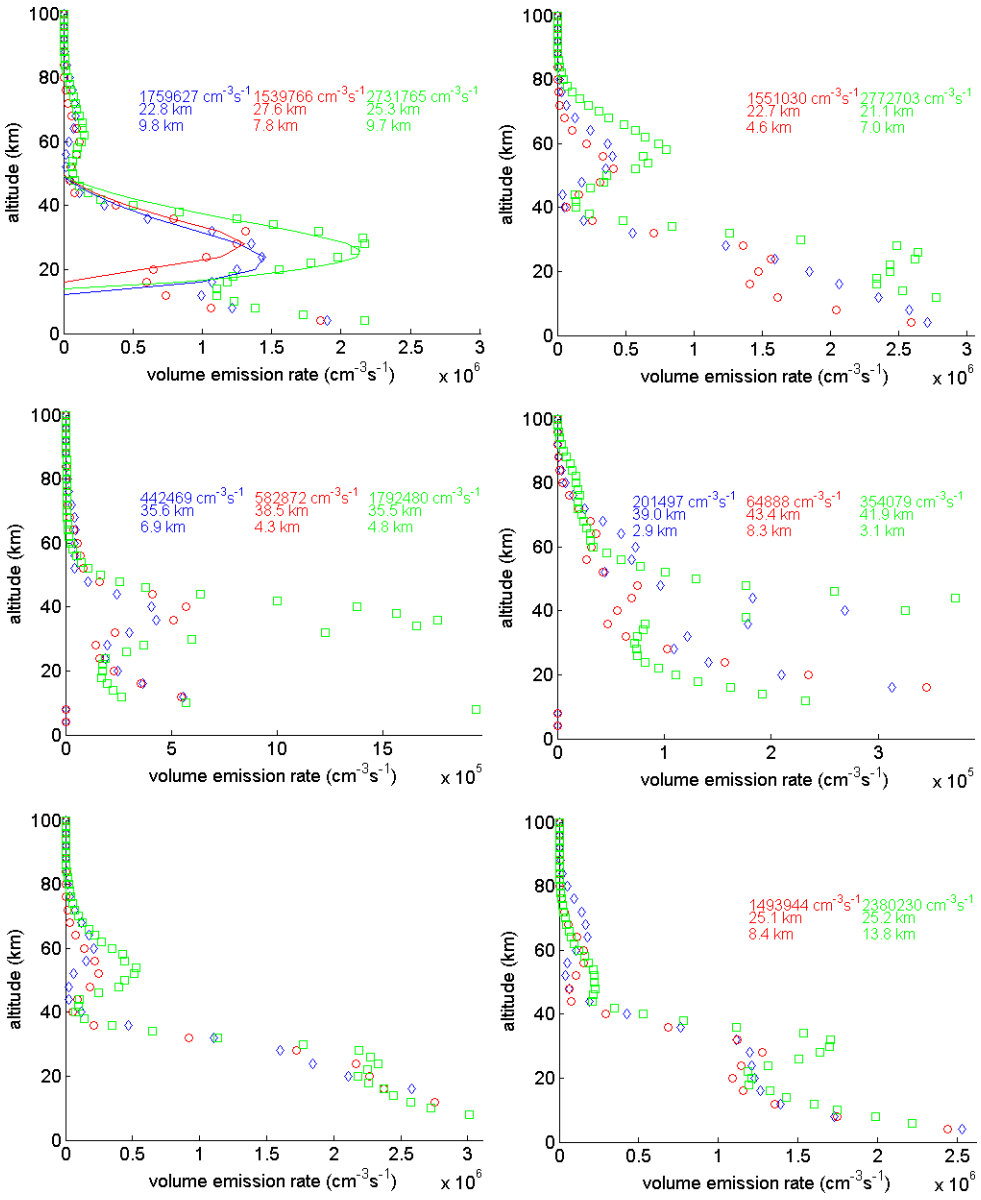

Figure 10.8: Simulated VER profiles for the O_2 IR Atmospheric emission at 12 LT at L_S=0° (left column) and L_S=180° (right column) for latitudes 67.5°N (upper row), 0° (middle row), and 67.5°S (lower row) for three GCM data sets called "runs" and the case 2 of kinetic parameters sets (see text for details). Blue features are used for run 1, red for run 2, and green for run 3. The symbols are the calculated VER at each altitude from the airglow model, while the line corresponds to the Chapman layer fit for each VER profile; the fitting parameters, ϵ_{max} (upper), z_{max} (middle), and H (lower), are given.

for a successful detection in the visible spectral range (Mullen et al., 2006; Krasnopolsky, 2011). Additionally, estimates for the O_2 IR emission were compared to the observations from SPICAM, CRISM, OMEGA, and ground-based instruments on Earth as a means of checking the consistency of the airglow model. The agreement between our model simulations and the SPICAM measurements of the daytime O_2 IR emission is sufficient to validate the O_2 photochemical scheme used in the airglow model. Furthermore, the limited dataset of nighttime observations of this emission provided more constraints on the airglow model simulations and the consistency is encouraging.

Strong latitudinal and seasonal differences in the O_2 airglow emissions were highlighted in this work, with stronger emissions occurring at the poles along the terminator. Another feature of our model simulations is the frequent occurrence of structures in the vertical distribution of the emissions studied here. On Earth, frequent occurrences of double-layer structures in airglow have been reported by Melo et al. (2000) and further studied in models. Double-peaked vertical profiles of airglow emissions have been observed on Mars by CRISM (Clancy et al., 2011b, 2012) and on Venus by VIRTIS (Piccioni et al., 2009).

As expected, the molecular oxygen emissions are directly affected by variations in the vertical structure of the temperature and O_x species concentration. Our sensitivity study highlights the response of the airglow emissions to different levels of water vapour and dust content. The airglow layer at low altitudes, a typical feature of daytime equatorial emissions, responds directly to variations in dust levels, while the emissions observed during the polar nights are modulated by the water vapour distribution, which is anti-correlated with the ozone concentration. Thus, airglow provides a useful tool for characterizing the actual state of the atmosphere.

Chapter 11

Model simulations of O_2 airglow: Venus

Similarly to the previous chapter, we here present the results of our simulations of the four O_2 airglow features considered in this study for the Venusian atmosphere at nighttime using the atmospheric composition from a one-year simulation of the VTGCM, as described in Section 8.2, in combination with the airglow model developed for this purpose (see Chapter 9.1). In Section 5.1, we discussed the specific mechanisms responsible for the production of each of the O_2 airglow emissions considered in this chapter, and in Section 9.2 we detailed the different kinetic parameters used in the airglow calculations to be presented here. The results from the simulations of the emission profiles performed for each of the sets of kinetic parameters will be analysed in Section 11.1. The impact of thetemperature and atomic oxygen density fields on the airglow intensities and the results are presented in Section 11.2. Finally, Section 11.3 summarises the outcomes of these O_2 airglow simulations.

The results presented in this chapter have been published in Gagné et al. (2012b).

11.1 Sensitivity to kinetic parameters

As discussed previously (see Section 6.1), the determination of the kinetic parameters needed to quantify the O_2 emissions from the proposed photochemical scheme (see Section 5.1) remains a challenge. The sensitivity of the airglow to this uncertainty is assessed in this section where we proceed with modeled simulations of each of the four O_2 band systems using three different sets of kinetic parameters for each system, which are explained and listed in Section 9.2. This approach mimics the sensitivity study to the kinetic parameters with the Mars atmospheric conditions found the previous chapter (see Section 10.1). In this section, we use as input to the airglow model the Venus atmospheric conditions from the VTGCM run 1 as described in Section 8.2.

11.1.1 The Herzberg I emission

The specific values used in the three cases for the simulations of the Herzberg I emission are listed in Table 9.1. Figure 11.1 shows the VER and integrated intensity for Venus atmospheric conditions. The peak altitude is the same for the three cases, as seen in Figure 11.1a, but the maximum emission rate is much smaller in case 3 than in cases 1 and 2, and correspondingly so is the emission intensity shown in Figure 11.1b. This is partly explained by the order of magnitude difference in the quenching rates between cases 1 and 2 compared to case 3. The difference between the yields from each case is not sufficient to compensate for the reduction in intensity in case 3 as compared to cases 1 and 2. The maximum intensity of 200 R from case 3 is in better agreement with the measured intensity of this band from the Venera era, which is 140 R for the latitudinal band $\pm 30^\circ$ (Krasnopolsky et al., 1976). The intensity in the two other cases is a few times larger than this measurement. We conclude that the quenching rate as measured in the laboratory should be increased by one order of magnitude to reproduce the range of intensity observed previously on Venus. Unfortunately, only one data set of observations

for this emission on Venus is available, which restricts our analysis.

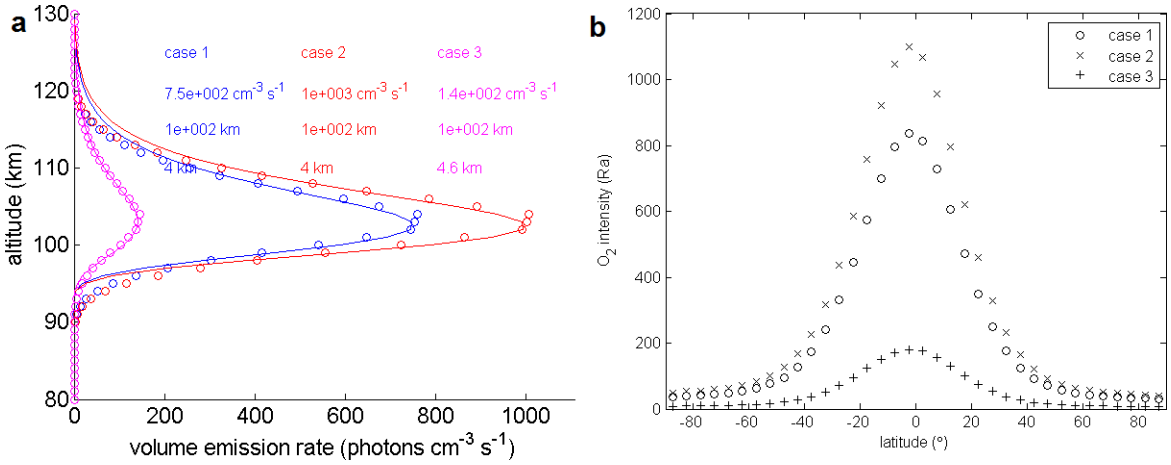

Figure 11.1: Simulated a) VER (cm^{-3} s^{-1}) profiles at latitude 2.5°N and b) latitudinal variations of vertically integrated intensity (R) for the O_2 Herzberg I emission at 00 LT for three different cases of kinetic parameters with Venus atmospheric conditions from run 1.

11.1.2 The Herzberg II emission

Table 9.2 lists the values for each case of the simulations of the emission resulting from the Herzberg II transition of O_2. The altitude of the maximum emission varies from 96 to 102 km from our simulations, as can be seen in Figure 11.2a. The observations of the emission on Venus places the peak altitude between 95 km and 100 km (García Muñoz et al., 2009b). In our simulations, case 2 puts the emission at an altitude above this range, while cases 1 and 3 fall within the range observed. As for the intensity of the emission, as displayed in Figure 11.2b, the maximum in case 2 is lower than 500 R, where the intensity from cases 1 and 3 reaches 2 and 4 kR, respectively, at 2.5°N, which is in better agreement with the observed range of 3–6 kR (Slanger et al., 2006; García Muñoz et al., 2009b). We then favour a rate coefficient of the order of 10^{-16} cm^3 s^{-1}, and a yield in the range of 0.02 to match our simulations with the past observations. We

note that the laboratory measurement of the rate coefficient for quenching of $c^1\Sigma_u^-$ by CO_2 was reported as an upper limit (Kenner and Ogryzlo, 1983a).

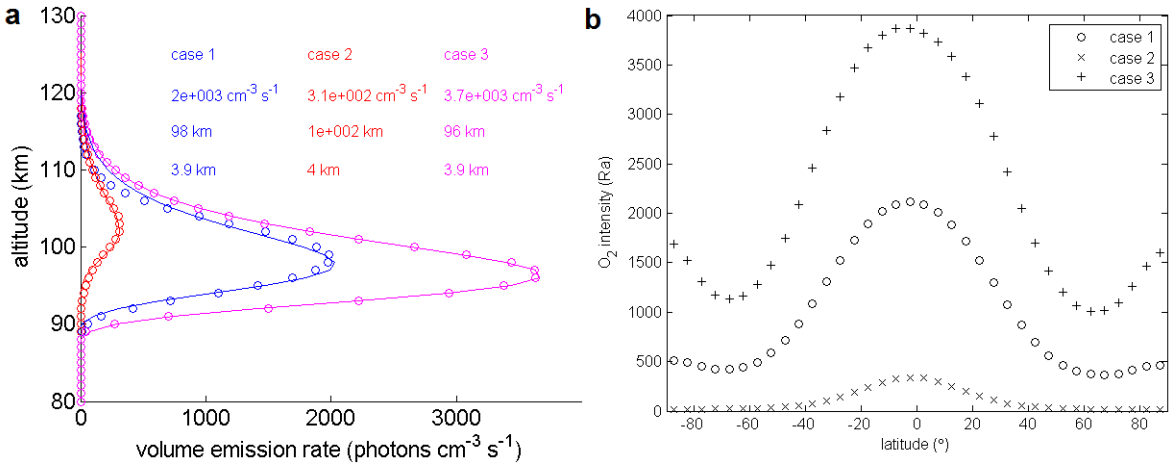

Figure 11.2: Simulated a) VER (cm^{-3} s^{-1}) profiles at latitude 2.5°N and b) latitudinal variations of vertically integrated intensity (R) for the O_2 Herzberg I emission at 00 LT for three different cases of kinetic parameters with Venus atmospheric conditions from run 1.

11.1.3 The IR emission

We now present our predictions for the nighttime O_2 1.27-μm emission following three cases of airglow simulations. The reader is referred to Table 9.3 for the specific values for each case. Figure 11.3a displays the simulated VER profiles for the three cases mentioned above. The variation in peak altitude among the cases is minimal: 99 km for cases 1 and 2, and 98 km for case 3. The three cases show profiles with total intensities that differ within a factor of two to three, from 0.4 for case 2 to 0.9 and 1.1 MR for cases 1 and 3, respectively, (Figure 11.3b). Cases 1 and 3 are in better agreement with the average of peak emission altitude and maximum intensity of the Venus observations (Piccioni et al., 2009; Gérard et al., 2010), but all cases are within the range of the observations. It is therefore not possible to draw further conclusions from these simulations than to say that

we would favour a high yield of ∼0.7 to match the average maximum intensity observed of 1 MR (Slanger et al., 2008; García Muñoz et al., 2009b; Piccioni et al., 2009).

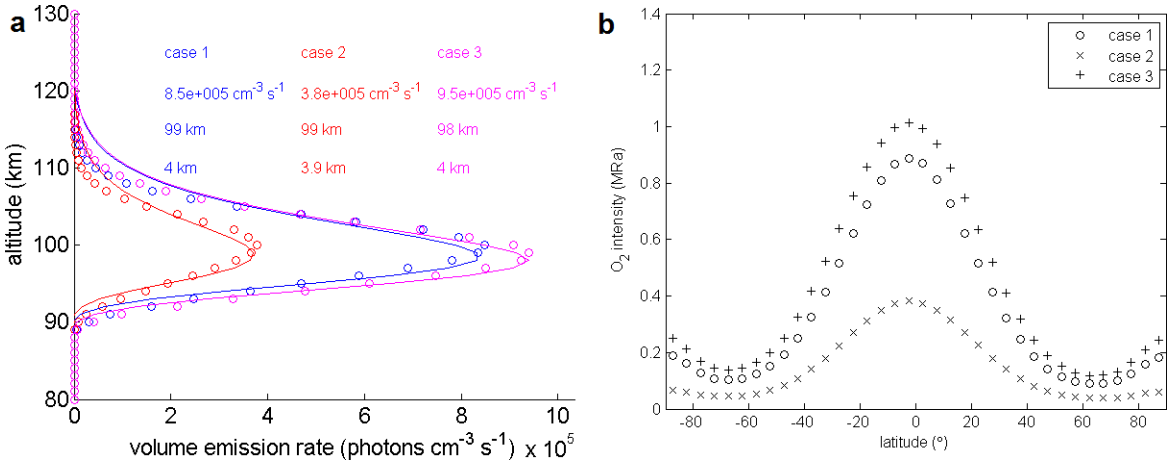

Figure 11.3: Simulated a) VER (cm^{-3} s^{-1}) profiles at latitude 2.5°N and b) latitudinal variations of vertically integrated intensity (R) for the O_2 Herzberg I emission at 00 LT for three different cases of kinetic parameters with Venus atmospheric conditions from run 1.

11.2 Sensitivity to atmospheric conditions

11.2.1 Comparisons between two VTGCM runs

We now present our results for the nighttime O_2 1.27-μm emission using two VTGCM runs: run 1 and run 2 for the background atmosphere, as described in Section 8.2. Briefly, run 1 represents mean conditions for Venus' upper atmosphere during the Venus Express sampling period (Brecht et al., 2011, 2012). Run 2 was obtained using the photochemical parameters used in case 2 of the Mars O_2 IR airglow simulations, which case was claimed to be the best combination to reproduce O_2 IR airglow in the Mars atmosphere following the sensitivity study of Section 10.1.4. Figure 11.4 gives an example of VER profiles with a fitted Chapman layer for 2.5°N and 00 LT using both VTGCM runs. This time and

location correspond to the antisolar point where we would expect the strongest emission, as will be explained in below. We notice that the peak VER (ϵ_{max}), is larger in run 2, which is a consequence of the larger atomic oxygen density in this run, as compared to run 1.

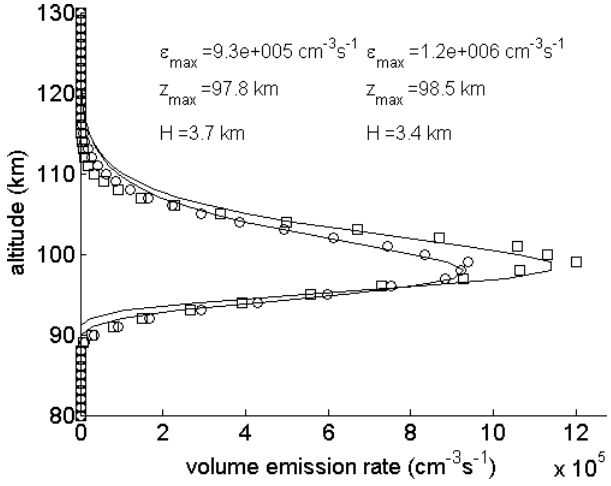

Figure 11.4: Simulated VER (cm^{-3} s^{-1}) profiles for the O_2 IR Atmospheric emission with Venus atmospheric conditions from the VTGCM run 1 (squares) and run 2 (circles) at 00 LT for latitude 2.5°N as a function of altitude (km). The symbols are the model-calculated values and the lines are the fitted Chapman layer. The parameters of the Chapman fit, i.e., ϵ_{max}, z_{max}, and H, for each case are given.

The latitudinal vs. local time distribution of the total integrated intensity from both runs are shown in Figure 11.5. The maximum integrated intensity is ∼1 MR between 00:00 and 01:00 LT around latitude 0°, with the values obtained from the run 2 being slightly larger. The maximum intensity obtained from our calculations is lower than the average maximum brightness of 1.2 MR obtained from observations, as discussed in Section 7.1.2. The bright spot location is consistent with the VIRTIS measurements, where it is centered around midnight. In some reports of VIRTIS data, secondary maxima were observed slightly before 00:00 LT or after midnight (Gérard et al., 2008b; Hueso et al., 2008; Piccioni et al., 2009; Shakun et al., 2010; Migliorini et al., 2011a; Soret et al.,

2012). The calculated location of the maximum 1.27-μm emission is shifted from midnight as a consequence of relatively weak RSZ winds over the altitude range of the airglow layer in the VTGCM (Brecht et al., 2011), in combination with the relatively long lifetime of $a^1\Delta_g$ at this altitude range, i.e., longer than one hour. Since this emission originates from the three-body recombination of oxygen atoms, it is expected to be maximised near the antisolar point where the oxygen atoms tend to accumulate due to zonal transport caused by the SSAS circulation followed by vertical transport in the downwelling branch (Bougher and Borucki, 1994; Gérard et al., 2009a; Brecht et al., 2011). The intensity of O_2 in Figure 11.5 decreases away from the antisolar point, which is consistent with the analyses of Gérard et al. (2010) and Soret et al. (2011), which show a linear decrease of the limb peak brightness from the antisolar point, i.e., 00 LT, to the terminators, i.e., towards dawn of dusk. Overall, the structure mimics the distribution maps produced with the observations by VIRTIS (Gérard et al., 2008c; Hueso et al., 2008; Piccioni et al., 2009; Shakun et al., 2010; Soret et al., 2011; Migliorini et al., 2011a), as well as the atomic oxygen density map near 103 km derived from VIRTIS measurements (Soret et al., 2011) and simulated by the VTGCM (Brecht et al., 2011, 2012).

The vertical cross sections of the emission rate, i.e., $\epsilon_{max_i} \cdot \Delta z_i$, as calculated by our model using the atmospheric conditions from the two VTGCM runs are seen in Figure 11.5. We observe that the airglow layer is maximised at lower latitudes near 97 km for the results from run 1 (see Figure 11.5c) and 98 km for the results from run 2 (see Figure 11.5d), with an nighttime average above 0.5 MR between 0 and 20°N in latitude and between 95 and 102 km in altitude. The emission rate decreases towards the North Pole and the altitude of the layer also show a decreasing trend, which is in agreement with the analysis of Piccioni et al. (2009) and Gérard et al. (2009b). We reiterate that this distribution is consistent with the hypothesis for the source of the nighttime O_2 1.27-μm being the recombination of oxygen atoms produced on the dayside and carried to the nightside by the SSAS circulation followed by a downward transport at the antisolar point

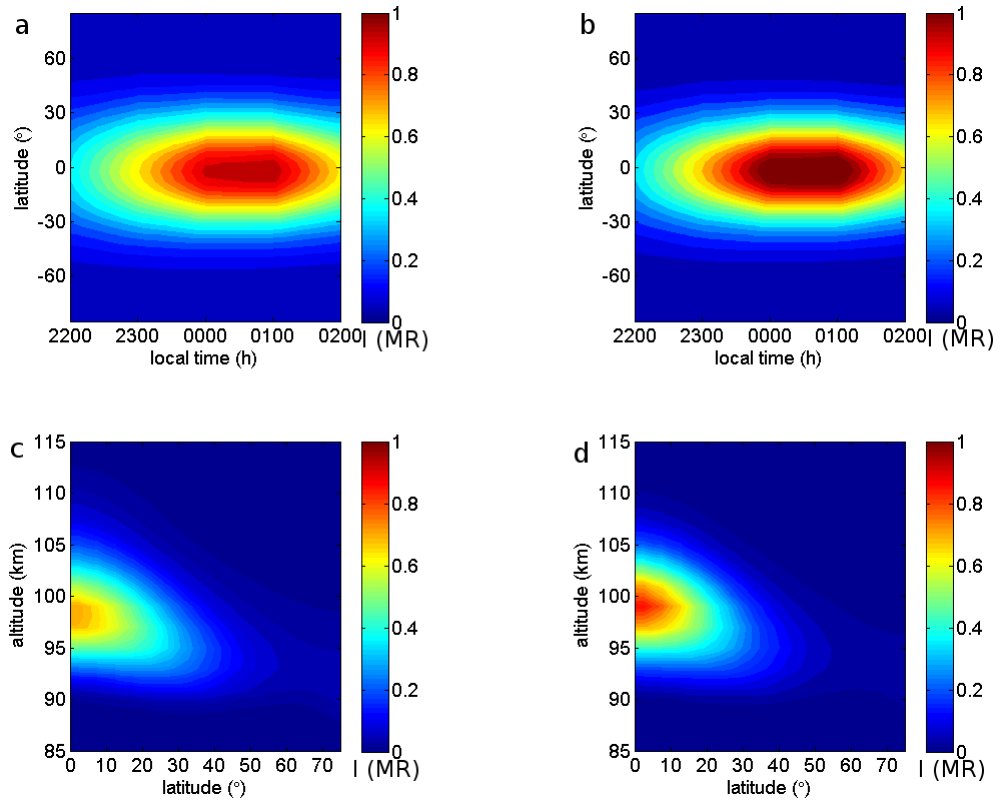

Figure 11.5: Simulated contours of total integrated intensity (MR) as a function of latitude (°) vs. local time (hr) for the O_2 IR Atmospheric emission with the Venus atmospheric conditions from the VTGCM a) run 1 and b) run 2. Contours of total emission rate (MR) averaged between 22:00 LT and 02:00 LT as a function of altitude (km) vs. latitude (°) with the VTGCM c) run 1 and d) run 2.

(Hueso et al., 2008; Gérard et al., 2008c, 2009a, 2010; Piccioni et al., 2009). The airglow layer characterizes the altitude where there is an equilibrium between the production and loss of the excited state molecule. However, in Gérard et al. (2012) some individual measurement sequences from VIRTIS show a second localised maximum near 50°N which is not reproduced in our model. Similarly, some single-orbit observations from Gérard et al. (2009b), Gérard et al. (2012), Piccioni et al. (2009) and Soret et al. (2011) show maxima of intensity around 30°N. This dynamically-induced variability is not reproduced in our simulations, which rely on climatologically-averaged atmospheric conditions.

11.2.2 Comparisons with observations from VIRTIS

Figure 11.6 presents the latitudinal variations of the peak VER, integrated intensity, peak altitude, and characteristic width averaged over the local time range of our simulations, from 22:00 to 02:00 LT. The model results are compared with observations from VIRTIS, i.e., mean values with 1σ standard deviation error bars, as reported in Piccioni et al. (2009), which were gathered mainly in the Northern hemisphere. We observe that in both modeled cases, the peak VER, i.e., ϵ_{max}, is less than 1×10^6 cm^{-3} s^{-1} at 0° and decreases to less than 1×10^5 cm^{-3} s^{-1} at 50°, where it remains constant poleward (Figure 11.6a). The behaviour of the model results of ϵ_{max} is consistent with the trend in the observations from Piccioni et al. (2009) for latitudes <25°, with run 2 calculations being closer to the mean values from the measurements in this latitude range. Over the whole latitude range, the model results show a steeper decrease in ϵ_{max} towards the poles than the VIRTIS data set.

For the integrated intensity in Figure 11.6b, the agreement between the model results and the observations from VIRTIS at low latitudes is satisfying in terms of latitudinal dependence. When looking at the actual values, we notice that the model results are offset from the observations by about 30%. Beyond 25°, the model results are diverging from the measurements. Moreover, the latitudinal trend of integrated intensity from VIRTIS measurements in singular orbits as reported by Gérard et al. (2009a) is sometimes increasing poleward unlike the model results, which consistently decrease poleward.

The peak altitude decreases from 98 km to 94 km between 0° and ∼50° in our simulations using atmospheric conditions from run 2 (Figure 11.6c), while in Piccioni et al. (2009) it oscillates between 97 and 98 km over this latitude range. The peak altitude values of our model are in agreement with the VIRTIS observations, within the error bars for lower latitudes. In Gérard et al. (2008c), the peak altitude remains close to 96 km between 17-32°N, in agreement with our calculations. Conversely, the measurements reported from the VIRTIS limb observations by Gérard et al. (2010) show a slight increase

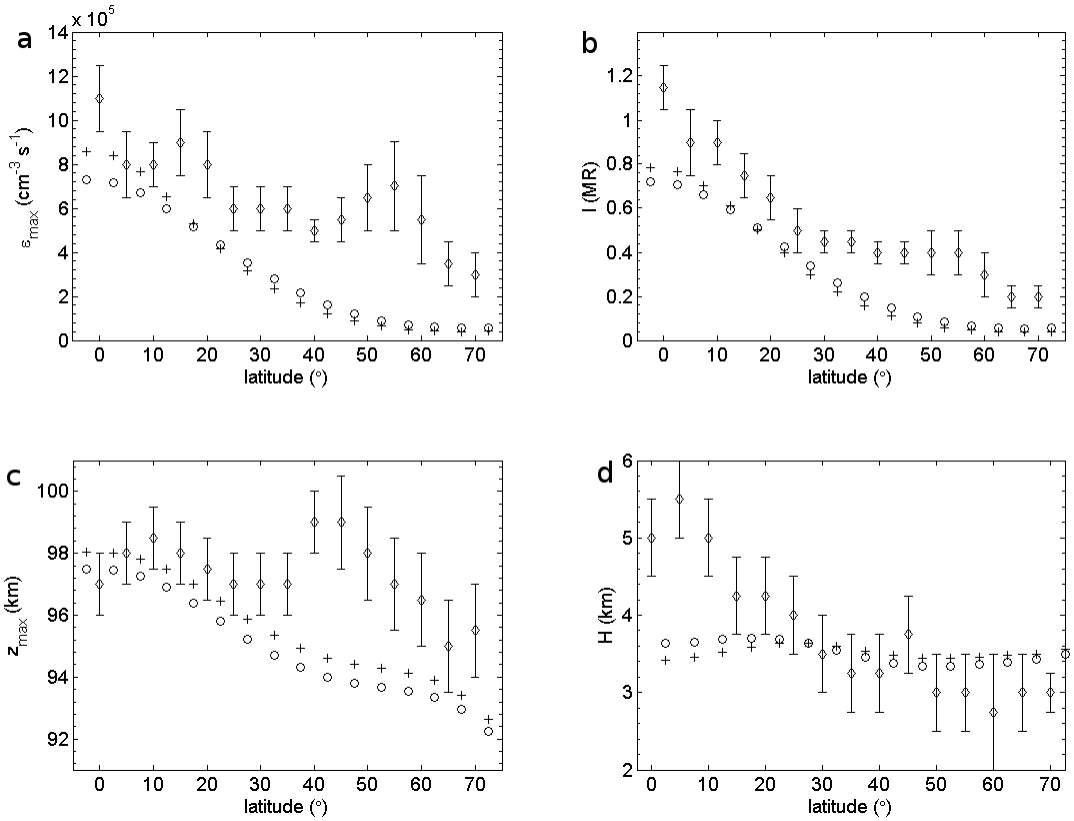

Figure 11.6: Variations of a) peak VER (cm^{-3} s^{-1}), b) intensity (MR), c) peak altitude (km), and d) characteristic width (km) for the O_2 IR Atmospheric emission with the atmospheric conditions from the VTGCM run 1 (circles) and run 2 (pluses) averaged between 22:00 and 02:00 LT as a function of latitude (°). The model results are compared with the observations (diamonds with 1σ error bars) of Piccioni et al. (2009) displayed in Figure 6 of that reference. Note that the latter measurements are restricted to the Northern hemisphere, hence, for consistency, only the results from our model simulations in the Northern hemisphere are displayed.

in peak altitude with latitude by about 2-3 km from 0° to 80°N.

As for the characteristic width (see Figure 11.6d), in our simulations it is more or less constant throughout the Northern hemisphere, while Piccioni et al. (2009) reported a decreasing trend toward the North pole for the full width at half maximum (FWHM) of the emission layer, with a steeper rate of decrease between latitudes 0-30°N. The FWHM values from Piccioni et al. (2009) have been divided by a factor of 2, i.e., half width at half maximum (HWHM) since HWHM=$z(\epsilon_{max}) - z(\epsilon_{max}/2)$, while the characteristic width is calculated as $H = z(\epsilon_{max}) - z(\epsilon \cdot e^{-1})$, in Figure 11.6d to provide a more direct comparison with the depth of the airglow layer parameter used in our model. Unlike the previous parameters, the agreement between the modeled H and the measured HWHM, within 1σ standard deviation, is only achieved for latitudes northward of 20°N.

In general, we conclude that with the exception of the characteristic width, the model results from both runs are in agreement with the observations from Piccioni et al. (2009) for lower latitudes. For latitudes greater than ∼25°, the simulations results diverge from the mean of the measurements. This behaviour is also observed when comparing VTGCM results with O density maps from VIRTIS (Brecht et al., 2012). Nevertheless, it is important to consider that models yield climatological results from average conditions at specific times and locations while the observations used for comparison in this study are averages of single-point measurements that vary in time and location and can be subject to local variations; variability in the Venus atmosphere is expected.

The agreement in behaviour between the airglow simulations using the VTGCM data set representing the VEx-era mean atmospheric conditions, i.e., run 1, and the VEx observations in the equatorial region is encouraging and gives confidence in the distributions of the species (especially O) and dynamics in the VTGCM. The disagreement at higher latitudes (for peak VER and intensity) is consistent with the findings of Brecht et al. (2012), for which the VTGCM-simulated O densities decrease faster with increasing latitude (poleward of 30°) than VEx-extracted O densities (Soret et al., 2011). The

O_2 airglow and atomic O disagreement may come mainly from two sources. First, the VTGCM is designed to produce climatological fields, i.e., mean conditions produced from the tuning of several input parameters as described in Section 8.2, while most of the O_2 IR airglow studies to date use statistically-averaged maps of instantaneous emissions and atmospheric conditions from several measurement sequences. Secondly, the transport of O_x species from the equator to the poles may be less efficient, i.e., slower meridional winds, in the VTGCM than actual conditions during the VIRTIS sampling period, as also reported in Brecht et al. (2012). The authors attributed the difference between observed and simulated O density at higher latitudes to the slower wind speeds in the VTGCM at latitudes polewards of 30°, but also to cooler temperatures between 80 km and 90 km. As stated in Brecht et al. (2012), Pioneer Venus Orbiter Infrared Radiometer (PVO IR) measurements at 90 km and Venus Express Radio Science (VeRa) occultations show the temperatures increasing from 175 to 180 K from the antisolar point to 60° along the midnight meridian (Schofield and Taylor, 1983; Pätzold et al., 2007; Tellmann et al., 2009). However, in Figure 8.4a, the temperature is 135–145 K between 80–90 km. The cooler temperatures between 80 km and 90 km represent smaller scale heights in this region. From Figure 11.6d, we can see that indeed the scale heights near the equator are smaller in the model simulations. Also, the scale height is nearly consistent for all latitudes, which is representative of the temperature distribution. Near the equator, the dynamics contribute to the oxygen supply, but farther from the equator, the dynamics are not converging and the temperature structure below is more evident.

11.2.3 Discussion about the sensitivity study

Sensitivity tests have been done by gradually increasing the O density from the equator to the poles, which results in a decrease of the absolute difference between the modeled and observed intensities and VER, but not for the peak altitude and the characteristic width of the airglow layer. The sensitivity to temperature was also assessed with tests done by

changing the temperature field in the same way. Figure 11.7 demonstrates the results from the sensitivity tests on the intensity distribution. We notice that by increasing gradually the oxygen density towards the pole by 2.5%, i.e., $[O] = [O] \cdot (1 + 0.025 \cdot lat)$, the offset between the observed and modeled intensities is minimised (see Figure 11.7a). However, increasing the temperature did not make the observed and modeled values converge (see Figure 11.7b). These sensitivity tests therefore strengthen the argument that the O distribution beyond $> 30°$ is underestimated in the VTGCM. It is possible that the modeled vertical transport over the polar regions is not as efficient as in the actual Venusian atmosphere, since the difference between the modeled and the measured peak altitudes of the airglow layer were not improved in these tests (not shown). Following the comparison of the VTGCM representation of the O density field with values derived from O_2 IR nightglow measurements by VIRTIS, Brecht et al. (2012) concluded that there is a need to improve the local time variations of the wind patterns in the VTGCM.

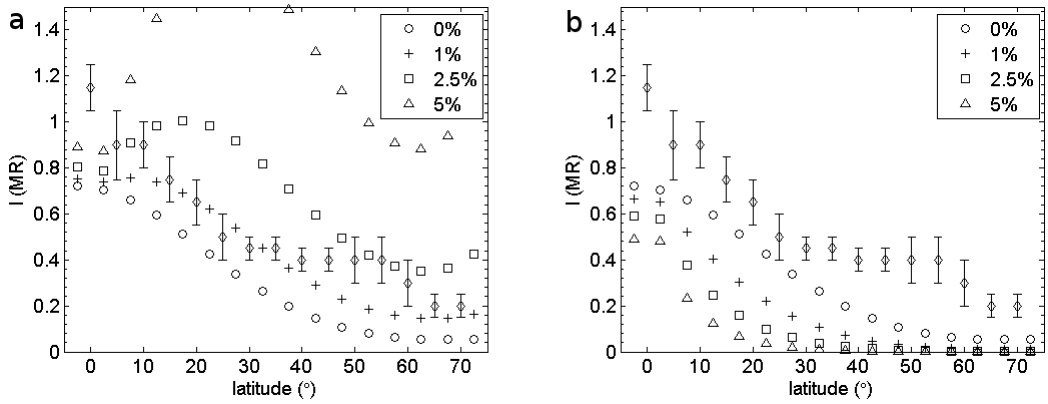

Figure 11.7: a) Variations of intensity (MR) as a function of latitude using the atmospheric conditions from the VTGCM run 1 averaged between 22:00 and 02:00 LT with an increase in O density as a percentage of increasing latitude by 0% (circles), 1% (pluses), 2.5 (squares), and 5% (triangles). The model results are compared with the observations (diamonds with 1σ error bars) of Piccioni et al. (2009) displayed in Figure 6 of that reference. b) Same as in a) but for an increase in temperature as a percentage of increasing latitude.

The airglow simulation using atmospheric conditions from the VTGCM run 2 is only slightly different from the one performed with the VTGCM run 1. The differences in the intensity distribution of the airglow emission from the $a^1\Delta_g$ state between these two sets of simulations (Figure 11.5), as will be described below, reflect the dependence of the airglow model on the background atmosphere. From simulations of the VER profiles using different atmospheric conditions and several combinations of kinetic parameters (not shown here), we observed that the profiles converge toward a similar airglow profile when the background state of the atmosphere is chosen to match the conditions at the time of the airglow observations, as can be seen from the example given in Figure 11.4.

The changes in the kinetic parameters between VTGCM runs 1 and 2 affect the lifetime of atomic oxygen in the middle atmosphere, and therefore induce variations in the atomic oxygen density profile, as shown in Figure 8.4d. In fact, the effect of dynamics, i.e., vertical velocity distribution, on O_x distributions has been explained in the literature (Gérard et al., 2010; Brecht et al., 2011, 2012). Our results confirm that the structure of the airglow layer depends significantly on the background atmosphere, most importantly on the O density profiles, and that the set of kinetic parameters chosen to reproduce the observations is not the only factor to be taken into account. Indeed, we obtain converging results from the two simulations by using atmospheric conditions from two different VTGCM runs and adjusting the photochemical parameters in the airglow model. This convergence of the simulated O_2 airglow profiles is evident when examining the latitudinal variations of the peak VER, integrated intensity, peak altitude, and e-folding depth in Figure 11.6. Hence, using a 1-D photochemical model to produce a background atmosphere for airglow studies is only a limited approach.

This conclusion strengthens the argument that dynamics play a significant role in the Venus atmosphere. For example, it was shown from modeling studies and observations that gravity waves affect the background atmosphere and therefore are reflected in the airglow fields (e.g., Melo et al., 2006; Piccioni et al., 2009). Brecht et al. (2011) studied

the sensitivity of the Venusian oxygen density distribution to winds by changing the wave-drag timescale and concluded that the peak density is controlled by this parameter, i.e., stronger winds provide more oxygen atoms on the nightside, resulting in an increased concentration. Moreover, Hoshino et al. (2012) advanced the argument that temporal variations of the intensity and distribution in the observations of the O_2 IR emission could be a consequence of Kelvin wave propagation, according to simulations with different planetary wave schemes in their Venus GCM. These dynamical variations cannot be provided by 1-D photochemical models. Lastly, it is well-known that brighter regions of O_2 IR nightglow are correlated with stronger downwelling motion, very often collocated with the antisolar point, i.e. 00 LT and latitude 0° (Hueso et al., 2008; Gérard et al., 2008b, 2009b, 2010; Shakun et al., 2010; Piccioni et al., 2009).

11.3 Summary

In this chapter, we studied the nightglow emissions from molecular oxygen in the Venusian atmosphere. We estimated the global distribution of four band emissions from different sets of kinetic parameters available in the literature, similar to the procedure used in Chapter 10. The distribution of the O_2 emissions at 00 local time has maxima located over the equator at the antisolar point, when the atomic oxygen mixing ratio is highest due to downward vertical transport in the descending branch of the dominant SSAS circulation. The Infrared Atmospheric emission is the strongest, as expected, and has maximum intensity above about one MR close to the equator, and the intensity gradually decreases towards the poles.

In particular, we put the emphasis on the global distribution of the O_2 emission at 1.27 μm because of the availability of observations for comparison. We obtained emission rate profiles and airglow intensities that generally match the VIRTIS observations within the range of uncertainty of the measurements. The difference in O distribution between

the two VTGCM runs, the results of changing the kinetic parameters in the atmospheric model itself, is sufficient to reproduce the range of airglow observations from VIRTIS. This confirms the fact that O_x distribution relates to both the background atmospheric conditions and the photochemistry.

We showed that using GCM initial conditions that differ in the kinetic parameters used in the oxygen photochemical scheme of the VTGCM, i.e., the three-body rate coefficient and yield, the lifetime, and the CO_2 quenching rate, leads to variations in the atomic oxygen distribution, as expected. Given that the variations in atomic oxygen density directly impact the values of the O_2 airglow peak altitude and emission rate, we adjusted the photochemical parameters in the airglow model to obtain results that were consistent between the two simulations. Hence, this sensitivity study illustrates that differences in the airglow morphology are reduced when we use atmospheric conditions consistent with the observations conditions, hence the choice of photochemical parameters for the airglow structure is not the only determining factor.

Our model study describes the behaviour of the peak intensity, peak altitude, and characteristic width of the airglow layer. The model results are in agreement with observations at low latitudes. However, the model forecasts a faster decrease of these parameters towards the poles as compared to the measurements. This model tendency is explained by the O distribution over the poles being under-estimated in the VTGCM, which correlates with colder temperature and a steeper decreasing latitudinal trend, as compared to the VEx-era mean conditions. The weaker meridional transport towards the poles, the result of the use of Rayleigh friction in the VTGCM, is thought to be the cause of this misrepresentation of the atomic oxygen density (Brecht et al., 2012).

Part III

Retrievals of NO airglow emissions

This part of the thesis concerns observations of NO airglow in the Martian atmosphere. Chapter 12 provides a description of the SPICAM instrument, including the characteristics of the detector that need to be understood prior to using the raw signal recorded in the datasets. Then, Chapter 13 explains how to treat the raw signal to extract the NO emission, and then how to proceed with a inversion of the signal from the NO airglow to obtain the absolute brightness and vertical distribution of the airglow layer. The method is tested with the first year of SPICAM observations, and the results from this experiment are presented in Chapter 14.

Chapter 12

The SPICAM experiment on board Mars Express

Mars Express is a mission of the European Space Agency dedicated to the orbital study of the interior, subsurface, surface, atmosphere, and environment of the planet Mars. It was launched in June 2003 and started orbiting Mars in December 2003, and is still conducting science operations to this date. The current elliptical orbit is characterized by a pericenter altitude of 298 km and an apocenter altitude of 10,107 km; the period is 6.7 h. On its payload, the Spectroscopy for the Investigation of the Characteristics of the Atmosphere of Mars (SPICAM) instrument is a spectrometer dedicated to the study of the atmosphere of Mars from the surface to the exosphere in a variety of observing modes. The description of SPICAM and the major results from the first few years of observations are discussed at length in Bertaux et al. (2006).

In this chapter, a description of the characteristics of SPICAM that will enable an understanding of the retrieval technique to be explained in Chapter 13 is provided. Specifically, the optical design of the instrument for spectroscopic measurements, as well as the specifications of the detector that enables the recording of these measurements, are described. Also presented are the different modes of observation, as well as a detailed

explanation of the stellar occultation technique.

12.1 Description of SPICAM

The SPICAM instrument is comprised of two spectrometers: one focused on the UV part of the spectrum (110 to 310 nm), and the second one observing in the near-IR (1.0 to 1.7 μm). These two channels are managed by one data processing unit (DPU), providing the interface with the spacecraft. Only observations from the UV channel of SPICAM are used in this work, such that the following description of the optical design and the detector unit refers strictly to this spectrometer.

12.1.1 The optical component

Figure 12.1 shows the optical scheme of SPICAM. The UV spectrometer is comprised of two reflective surfaces that provide a high efficiency. The off-axis parabolic mirror collects the incoming light and reflects it towards the entrance of the spectrometer. At the focal point, f=120 mm behind the mirror, a mechanical slit with variable width (50 μm at one end and 500 μm at the opposite end) is placed to be used for observations of extended sources, but not in the case of stellar occultations. When the slit is not in place, the total useful field-of-view (FOV) is $2^\circ \times 3.16^\circ$ because it is limited by a diaphragm in front of the focal plane to avoid the contribution from reflected stray light. The pointing accuracy is better than 0.2°. After passing through the slit, the light is dispersed by a grating before entering the detector. The image ratio is $\sim$1 such that an image at the entrance of the spectrometer is conserved in the plane of the detector.

12.1.2 The detector

At each occultation, 288 spectra are recorded along the 2.88°-long slit on the rows of the CCD, and each spectrum is spread over 384 of the 408 pixels in a row. Figure 12.2 is a

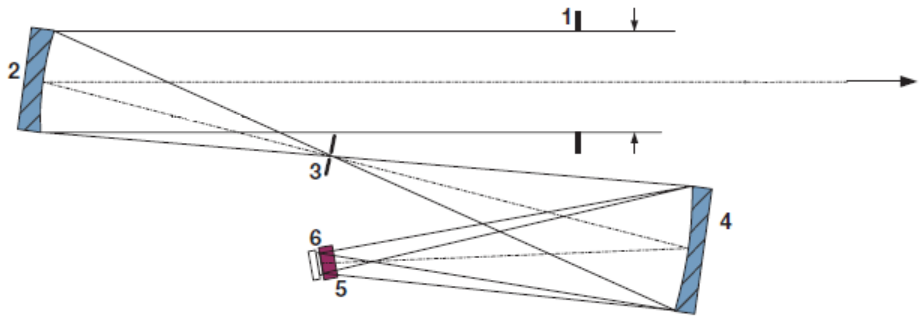

Figure 12.1: Optical scheme of the UV channel of SPICAM. 1, aperture of the UV channel; 2, off-axis parabolic mirror; 3, slit (can be changed from wide to narrow by a mechanical actuator or completely removed); 4, concave UV grating; 5, intensifier; 6, CCD. Figure modified from Bertaux et al. (2006).

representation of the CCD design. However, for each occultation in a sequence, only five spectra are transmitted to Earth. Hence, to increase the S/N, the spectra are summed over several rows, and this sum is performed according to different schemes. Figure 12.3 shows the possible configurations. In the case of the stellar occultation observations studied in this work, we are interested in the binning mode that uses a defined number of spectra to be summed (Figure 12.3b). Starting at any row on the CCD, spectra are summed over 2, 4, 8, 16, or 32 rows depending on the chosen binning number. Hence, for each occultation sequence containing n occultations, we obtain n spectra from five different bands b of a signal spread over a wavelength range defined by the pixel numbers p: $S(n, b, p)$.

Now, each pixel of the CCD has a size of 0.23 μm $\times$ 0.23 μm, which covers a FOV of 0.01° $\times$ 0.01°. The total FOV of the CCD when the slit is not in place is 2° $\times$ 3.16°. Since the magnifying value of the spectrometer is 1, we can define the FOV in the focal plane with "virtual" pixels of the same dimension of the "real" pixels of the CCD.

Actually, there are 408 pixels along a CCD row, but some pixels are not used when

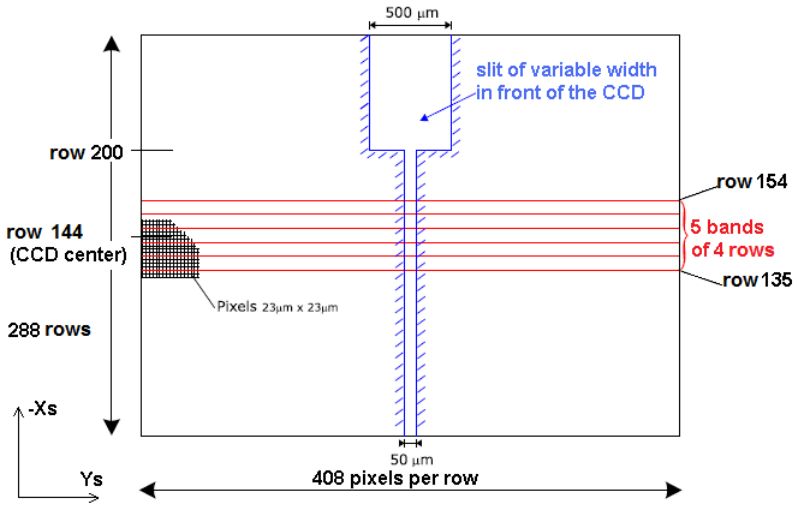

Figure 12.2: Schematic of the CCD. The pixel numbers are on the horizontal axis, which corresponds to the wavelength axis, while the row numbers are on the vertical axis. The slit (blue line), with variable width, is perpendicular to the rows. The red lines show the binning mode of five bands each of four rows. Figure modified from Perrier (2006).

analysing a signal. Table 12.1 lists the function of each pixel, with the 384 pixels at the center of the CCD used for the observed spectra, while the remaining ones serve to calibrate the measured signal. Section 13.1 will describe the calibration method. Moreover, the efficiency of each pixel with respect to an incoming light source is variable. A calibration of this efficiency, referred to the effective area[1], S_{eff}, was assessed prior to the mission, and it is regularly re-evaluated during the mission. Figure 12.4 shows the efficiency of the CCD to an distant light source.

The incoming photons do not get directly from the spectrometer to the CCD to get recorded. Each incoming photon that reaches the entrance of the detector creates a photo-electron; this is a photo-event. The photo-electron creates a pulse of light that gets intensified by the intensifier before it gets distributed over a few pixels of the CCD. The light pulse is read on the CCD as a number of Analog-to-Digital Units (ADUs), provided

[1]The effective area is defined as the ratio of the number of detected photons (photo-events) to the flux of photons entering the instrument (photons cm^{-2}). It is expressed in cm^2.

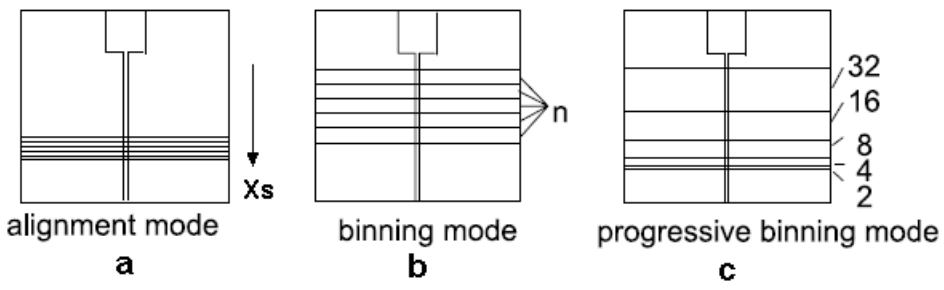

Figure 12.3: The various modes of SPICAM CCD reading. a) The alignment mode (used very rarely): a complete image of the CCD is obtained by groups of 5 lines (with 1 line overlap), in order to find the spectrum of the star. b) The binning mode (most often used), when 5 bins of 2, or 4, 8, 16, 32 rows are grouped together. The first row may be selected anywhere. c) The progressive binning mode (used at the beginning of the mission): 32 rows for a weak signal, 2 rows for a strong signal. Figure taken from Bertaux et al. (2006).

by the Analog-to-Digital converter (A/D). The intensifier is set to a high voltage level from 500 to 900 V that is remotely commanded by setting a digital level value of HT (for the French translation "haute tension") between 0 and 255; at HT=20, 1.5 ADU are created by photo-event. The gain, G, gives the relationship between the high voltage and the number of ADUs created:

$$G = \exp\left[7.46113 \cdot \ln\left(500 + 1.57 \cdot HT - 46.3864\right)\right] \tag{12.1}$$

(Perrier, 2006). The gain was determined prior to launch for various levels of HT, and it varies between 1 to 79 over the whole range of possible HT values.

12.2 Description of the observational geometry

The attitude of the spacecraft is constant in inertial space. The optical axis of SPICAM is aligned with the $+\vec{Z}_s$ axis of the spacecraft, which is the optical axis of all instruments, within alignment errors. The spacecraft was designed with two basic modes of orientation,

pixel #	
1	buffer
2–8	offset
9–392	normal
393	buffer
394–407	masked
408	buffer

Table 12.1: Purpose of the different pixels on a given row of the SPICAM CCD.

nadir or limb, that enable different configurations of observations.

12.2.1 Observations modes

Figure 12.5 shows the different modes of observation for SPICAM. When the $+\vec{Z}_s$ axis is directed towards the center of Mars, SPICAM is making observations in the nadir mode. This mode does not provide any vertical resolution since it yields measurements over the whole atmospheric column.

In the limb-viewing mode, the $+\vec{Z}_s$ axis is oriented in a pre-calculated direction to provide scans of the planet's limb while the spacecraft is at the pericenter of its orbits around the planet. The advantages of this method compared to the nadir-viewing mode are that it increases the intensity of the signal by looking through a longer atmospheric path and it provides a knowledge of the altitude dependence of the measured quantity.

During the emission phase function mode, SPICAM observes a particular geographical area from various emission angles, to discriminate the emission from the ground and from the airborne dust scattering. It is rarely used.

In the solar and stellar occultation modes, the $+\vec{Z}_s$ axis is oriented to the direction of the Sun or a star, respectively. While scanning the limb during the spacecraft's orbital motion, the Sun, or the star, slowly disappears behind the planet. The technique of stellar occultation will be described at length in the next section, since it is the mode

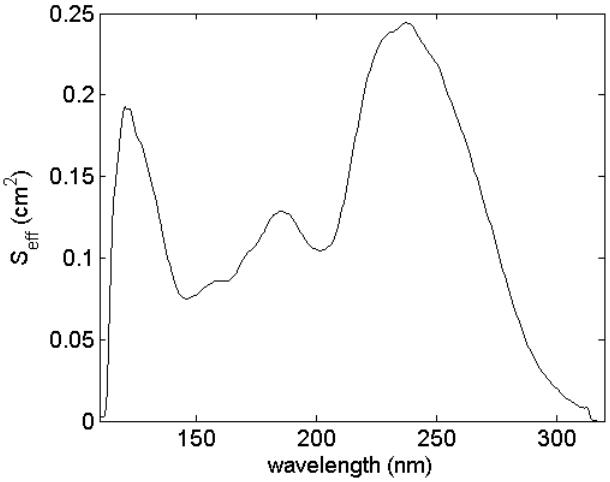

Figure 12.4: Effective area (cm^2) of the CCD as a function of wavelength (nm). It was determined with a star signal recorded on the CCD row and obtained by integrating over 8 spectra centered on row 144. This determination is version"v6" dated 22/02/2012 obtained by Aurélie Rébérac from LATMOS/CNRS (France).

that is used in the datasets that we analysed.

12.2.2 Stellar occultation technique

In the absence of emission by gases and aerosols, the intensity of the incoming solar radiation at a given wavelength λ is given by the Beer-Bougher-Lambert law. To simplify the notation, we use the slant path s for referring to a distance, which is a function of the altitude, z, the angle of incidence with respect to the upward normal, θ, and ϕ, the azimuthal angle. Hence, the Beer-Bougher-Lambert law is expressed as:

$$I_\lambda(s) = I_\lambda(0)e^{-\tau_\lambda} \tag{12.2}$$

where $I(0)$ is the intensity at s=0; for this case it is the top of the atmosphere. τ is the optical depth that depends on the density, ρ, and the cross section, σ_λ, of the absorbing

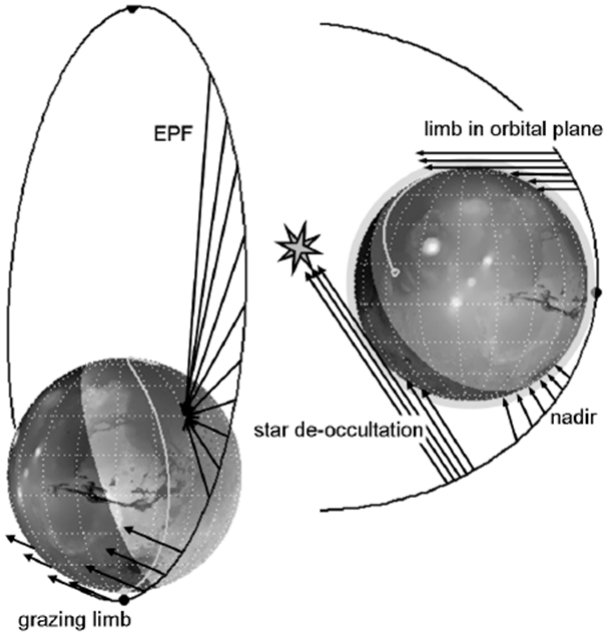

Figure 12.5: Schematic of various modes of observation for SPICAM. In all cases, the black line indicates the LOS of SPICAM to the target. Except for the usual nadir orientation and the special case of EPF (Emission Phase Function), the spacecraft is moving along the orbit, keeping a constant celestial orientation, which allows SPICAM to scan across the target (limb) or to perform an occultation of star or Sun. Figure taken from Bertaux et al. (2006).

molecules[2]:

$$\tau_\lambda = \int_s^0 \rho\sigma_\lambda \cdot ds \tag{12.3}$$

where ds is the slant path increment. The transmission is given by the ratio between the incident intensity at s=0 and that at s:

$$T_\lambda(s) = \frac{I_\lambda(s)}{I_\lambda(0)} = e^{-\tau_\lambda}. \tag{12.4}$$

Quémerais et al. (2006) reviewed the principles of the stellar occultation technique and described the general algorithm developed to use these types of observations with SPICAM. In this work, the transmission from each occultation, i.e., the proportion of the

[2]We can combine both quantities as the mass absorption coefficient $\kappa_\lambda = \rho\sigma_\lambda$

signal coming from a star passing through the atmosphere, is used to extract the atmospheric signal coming by subtracting the contribution from the pointed star using a reference signal acquired outside the atmosphere. This concept will be further elaborated in the next chapter in Section 13.1.

Figure 12.6 illustrates the principle behind a stellar occultation. As Mars Express orbits around Mars, it scans the limb of the atmosphere by continuously having the line-of-sight (LOS) pointing towards a reference star. The spectra recorded by SPICAM at the two different times, i.e., I_λ vs. wavelength at t_0 for outside the atmosphere (black curve) and at $t_0 + \Delta t$ through the atmosphere (red curve), are depicted in the left-hand-side plot. The plot on the right-hand-side shows the transmission T_λ, that is the ratio between the spectrum measured outside the atmosphere and one spectrum measured through the atmosphere. We note that the transmission is severely attenuated at wavelengths smaller than 150 nm due to CO_2 absorption at these wavelengths.

The main advantage of the stellar occultation technique is that the altitude determination is possible since the instrument is pointing towards a specific star, which is a point source with a well-defined geophysical location, and the position of the satellite in its orbit is also known (Bertaux et al., 2006). The vertical resolution is also excellent, whatever is the distance of the spacecraft to the planet, because the star is a point source. Moreover, by taking the ratio between measured spectra, i.e., one outside the atmosphere and one through, which is a relative quantity, we derive an absolute quantity, a calibrated spectrum of the atmospheric signal, without relying on the radiometric calibration of the instrument. This auto-calibration of the signal is another advantage of using the stellar occultation technique. The vertical resolution depends on the integration time (dt=0.64 s) of the detector, the sampling rate (1 Hz), and the vertical velocity (a few km/s depending on the geometry of observation) of the tangent point, which gives typical values of the order of a few km.

Some limitations of the stellar occultation observational mode include a low S/N due

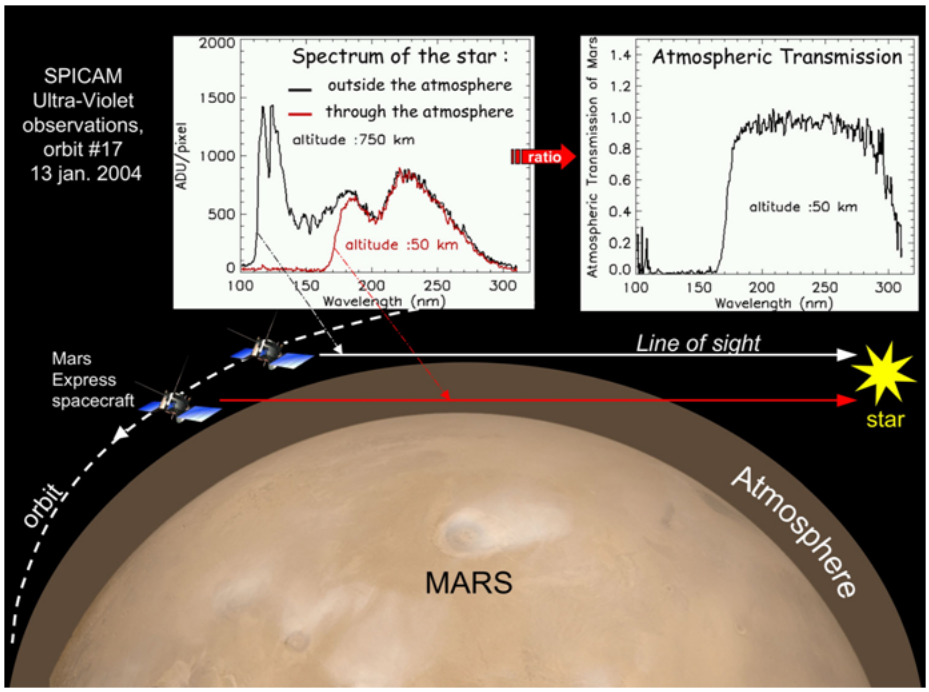

Figure 12.6: Schematic of a stellar occultation. From the two spectra obtained outside and through the atmosphere (left plot), an atmospheric transmission can be derived (right plot). Shortward of 150 nm, the signal is completely attenuated by CO_2. Figure taken from Bertaux et al. (2006).

to the weak brightness of the observed stars and an exclusivity of nightside observations since the dayside emissions from the bright limb are more difficult to differentiate from the stellar flux (Bertaux et al., 2006). Also, because different stars are used at different times depending on the location of MEx in its orbit, the difference in spectral features and intensities of the pointed stars may induce variations in the transmission accuracy. Nevertheless, the advantages of this method enable the extraction of useful information to build the first climatology of the NO emission in the Martian atmosphere, which enables an assessment of the behaviour of global circulations models, e.g., composition and dynamics.

12.2.3 Measurements without slit

When the slit is in place at the focal plane f (see point 3 on Figure 12.1), a point along the slit will have its spectrum displayed on the corresponding row on the CCD detector. The pointing vector of the spacecraft is fixed in the coordinate system $\vec{X}_s$, $\vec{Y}_s$, $\vec{Z}_s$, such that the focal plane is determined by the components X_s^f in the $\vec{X}_s$ direction and Y_s^f=0 in the $\vec{Y}_s$ direction. Note that the CCD axes ($\vec{X}$ and $\vec{Y}$) are aligned with the spacecraft ($\vec{X}_s$ and $\vec{Y}_s$), assuming no mechanical offsets due to a misalignment of the telescope (see Figure 12.2). The spectrum will be focused on a specific line of the CCD detector with a nominal wavelength assignment, i.e., λ=F(pixel #), which will be explained in Section 13.1.4. Each row of the CCD corresponds to a certain point along the slit, and is referred to by the row number and the value of $\vec{X}_s$.

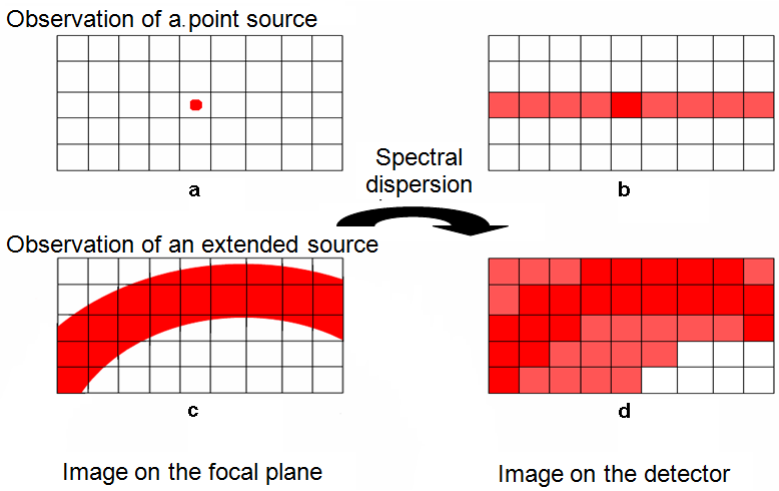

Figure 12.7: Schematic of the image recorded on the CCD when: a) a point source is seen in the FOV of SPICAM such that b) the spectrum from this light source is spread over the corresponding row of the CCD; c) an extended source is seen in the FOV such that d) each pixel has its spectrum spread over the corresponding row of the CCD causing a superposition of spectra. Figure taken from Royer (2011).

When the slit is removed, all points of the focal plane (characterized by the X_s^f and

Y_s^f components along the $\vec{X_s}$ and $\vec{Y_s}$), where the image of the observed scene was formed, will produce a spectrum on the detector, on the row corresponding to X_s^f but shifted with respect to the nominal wavelength assignment by a value corresponding to Y_s^f. Figure 12.7 illustrates how the spectra recorded from a point source and an extended source are recorded on the CCD. If the coordinate of one direction has $Y_s > 0$, then the spectrum will be moved to higher pixel numbers along the CCD row. Hence, the distribution of the NO emission along the FOV defined by the observation band will be recorded as a superposition of identical spectra, similar to the one measured when the slit is in place, called the reference spectrum (S_{ref} and displayed in Figure 12.8a), but shifted in pixel position by a value corresponding to Y_s^f, as shown in Figure 12.8b.

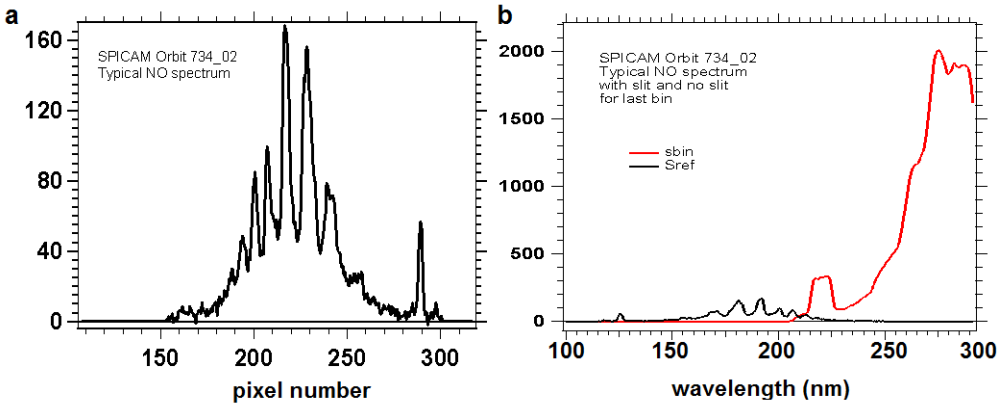

Figure 12.8: a) Reference spectrum of the NO emission as observed by SPICAM in the Martian atmosphere obtained from retrieving the NO signal from one occultation with the limb-viewing mode (orbit 734); b) Simulated spectrum in the case of only the last 20 pixels being completely and uniformly illuminated by the NO emission (red line) as comparison with the reference spectrum (black line). In both cases, the signal is given in arbitrary units (ADU per pixel). Courtesy of Dr. J.-L. Bertaux.

Figure 12.9 shows different times during a stellar occultation when the slit is not in place. The projection of the image of the CCD onto the limb is illustrated with a transparent rectangle, while the atmosphere of Mars is represented in yellow around the

planet, with the NO airglow layer highlighted by the red circle. The spectrum obtained from each occultation is shown on the upper panel, with the intensity given in ADU and the pixel numbers along the CCD row instead of the wavelength number assignment. At the beginning, (left, t_0), the FOV of SPICAM scans the high altitudes, the spectrum is centered over the low pixel numbers, which is reflected by the red annulus behind the lower portion of the CCD. The CCD is inclined with respect to the limb, such that the movement of the spectra towards higher pixel numbers as time elapses is noticeable (at $t_0+\Delta t$ and $t_0+2\Delta t$).

This chapter has provided a general description of the SPICAM instrument, describing how it observes the atmosphere of Mars as well as how the signal gets recorded on the detector. These details are necessary to understand the treatment of the raw signal and the retrieval algorithm developed to extract the NO airglow signal that will be explained in the following chapter.

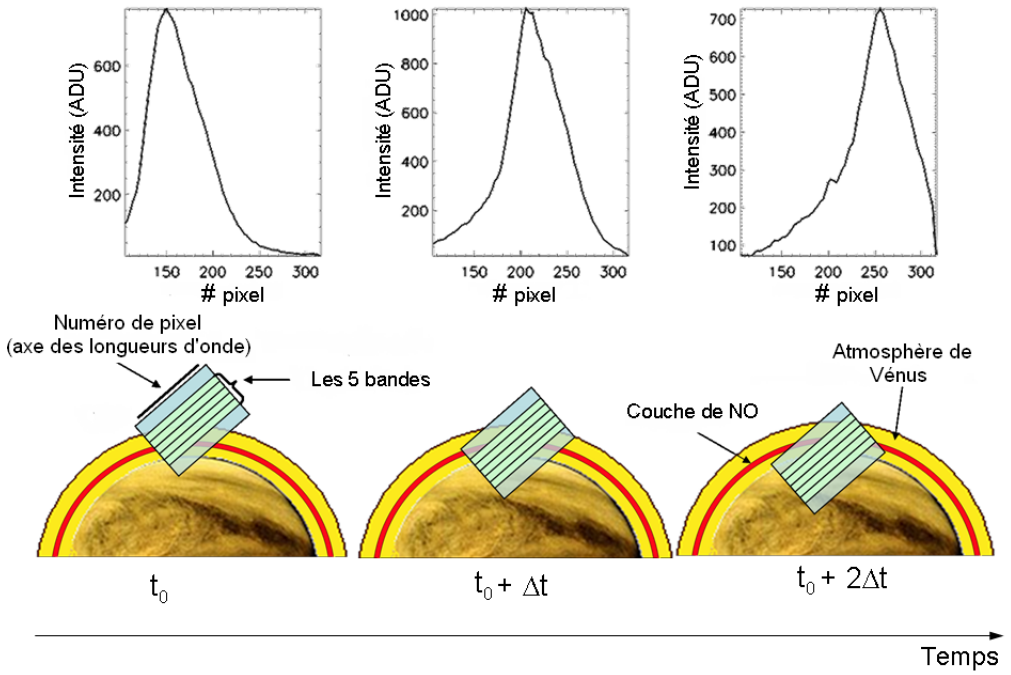

Figure 12.9: Schematic of the shift in the NO spectrum along the wavelength axis. During a stellar occultation sequence when the CCD is inclined with respect to the limb, a band on the CCD will probe a different altitude range, and since the slit in not in place, the observed spectrum will no longer be correlated with the nominal wavelength assignment. The red circle around the planet is the NO airglow layer; the FOV of the CCD is represented by an image of the CCD scanning the limb. The corresponding spectrum on one line of the CCD recorded at the corresponding time is shown above in the plot. Figure taken from Royer (2011).

Chapter 13

Retrieval technique

This chapter describes the algorithm developed to retrieve the brightness of the NO emission from observations made with the SPICAM instrument. The goal of this inversion is to construct a brightness map of the NO emission projected onto a plane passing through the center of Mars. There are two points to consider: (1) We want to reconstruct the FOV of each band onto this plane during the occultation sequence. We therefore need to consider the trajectory of the spacecraft and project it onto this plane; (2) For each band and each occultation, we want to do the inversion of the observed spectrum to determine the distribution of brightness from the NO emission along the band.

The data files from the SPICAM measurements contain the raw signal and therefore some processing is required to separate the signal from the NO emission to that of the reference star. These steps are explained in Section 13.1. Then, Section 13.2 shows how the geographical information is recovered during the observation sequence. In Section 13.3, the procedure developed for a inversion of the signal recorded by the SPICAM detector when the instrument is in stellar occulation mode with the slit removed is described. The objective is to reconstitute the 2-D distribution of the NO nightglow emission at the limb from a given observation.

13.1 Preliminary treatment of the signal

In the SPICAM data archive, we search for the occultation sequence names containing the tag "E", standing for stellar occultation ("étoile" in French for "star"). Figure 13.1 is a time-series of spectra, i.e., spectrum number n corresponding to time on the vertical axis vs. pixel number p corresponding to wavelength on the horizontal axis, of one occultation sequence (orbit # 588), displaying the recorded signal (in ADU) on the five bands of the CCD.

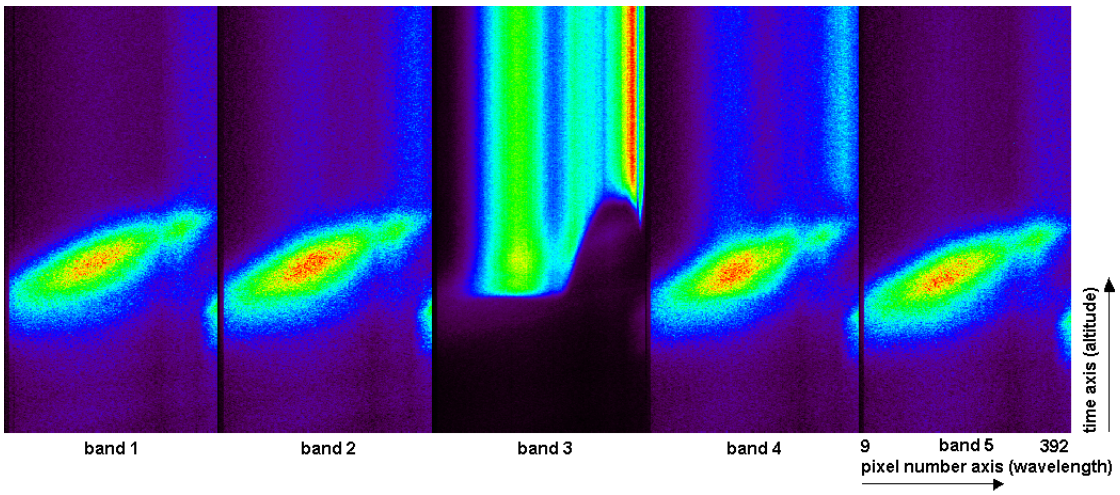

Figure 13.1: Time variation of the spectra measured by SPICAM for the five bands during orbit # 588 before processing of the raw signal to extract the signal from the NO airglow emission. The signal is color-coded in ADU with lower values in purple and higher values in red. The oval-shaped emission on bands 1, 2, 4, and 5 is due to the presence of an airglow layer, while the central band is saturated with the star signal (upper-half of plot) until the LOS is through the atmosphere (lower-half).

We then process each data file to retrieve the signal from the NO airglow emission. This first level of data processing involves removing the electronic offset, the dark current (DC) and the reference star signal, and calibrating the CCD in wavelength as described below. The observed signal, S_{obs}, is described as a combination of the star signal, $S_\lambda(z)$,

the airglow signal, $S_{airglow}$, the signal from the offset, S_{offset}, and the DC signal, S_{DC}:

$$S_{obs} = S_{\lambda}(z) + S_{airglow} + S_{offset} + S_{DC}. \tag{13.1}$$

Hence, to recover the airglow signal, $S_{airglow}$, we need to remove all the other components that make up the observed signal.

Now, some of these stellar occultation sequences are not usable, in most cases because it is a technological sequence, i.e., an occultation sequence to recalibrate the instrument such that there is no spectrum within the atmosphere, or usable but they do not contain a signal from NO. The former occultations were rejected, while the latter occultations that did not contain the NO signal were not processed, but their geometrical information was saved for statistical purposes, e.g., occurrence of emission.

13.1.1 Electronic offset correction

An electronic offset is applied to the detector to avoid negative values at the entrance of the A/D converter. The goal is simply to avoid statistical biases in the case of weak signals, since the negative values are assigned a value of zero. This electronic offset is applied to the raw data before digitisation. It is defined on pixels numbered 1 to 7 (see Table 12.1) by taking their mean, therefore, there is a specific offset for each of the five bands. The offset is subtracted from the signal of the remaining pixels at the same time as the DC, which will be detailed in the next section.

13.1.2 Dark current correction

The dark current corresponds to the recorded signal when no light source is illuminating the CCD. On the CCD, the accumulation of electrons on the pixels is not only caused by the generations of electrons by photons: a current is generated by thermal energy that produces parasite electrons that accumulate on the pixels. DC increases with increasing temperature and exposure time of the CCD. Hence, a cooling system is required for

limiting the DC effect. On SPICAM, a Peltier cooler enables the CCD to be cooled down to its working temperature, between -20 and 40($°C$), when activated. However, it was observed that once activated, the cooler reduces the DC, but after a certain time, the temperature rises again, which is thought to be due to a possible vacuum leak in the cooler (Bertaux et al., 2006).

As shown in Table 12.1, some pixels of the CCD are masked and are supposedly sensitive to the DC and the electronic offset. The offset is assumed to be constant, while the DC is expected to vary as a function of temperature of the detector, from pixel to pixel. In-flight measurements have been made without the intensifier and the Peltier cooler, which is called a technological sequence, to characterize the output from the CCD. It was verified that the signal (DC + offset) from the pixels exposed to a light source is a linear function of the signal from the masked pixels (see Table 12.1), but the rate is different from pixel to pixel (Bertaux et al., 2006). We refer to this linear function as the Dark Current Non Uniformity (DCNU). Figure 13.2a gives three examples of the DCNU for three different CCD temperatures. We notice that the linear relationship between the DC + offset of each pixel and the masked pixels may be determined from such observations, allowing corrections of normal observations.

The DCNU may vary with time, such that technological sequences as described above are repeated on a regular basis. From these calibrations, a new DCNU correction curve is extracted for each of the five bands:

$$DC(n,p) = E(p) \cdot m(n) - F(p) \tag{13.2}$$

where E and F are the coefficients of the linear variation for each pixel p, and m is the mean of the DC on the masked pixel for each occultation n (Royer, 2011). The DCNU correction for each band is shown in Figure 13.2b. Corrections are then made to the raw signal by subtracting the DCNU signal for each pixel on each band.

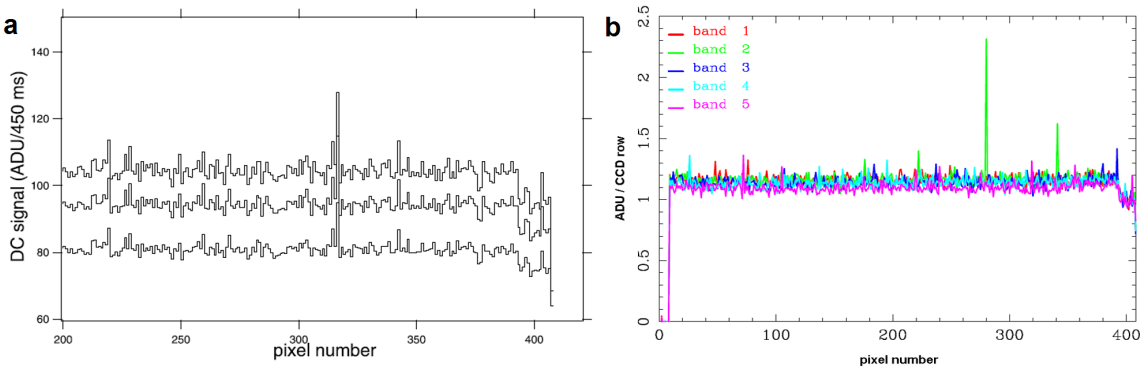

Figure 13.2: a) DC and offset on the CCD (in ADU) as a function of the pixel number, taken during orbit # 1789 with the intensifier and Peltier cooler off. The three curves are for three temperatures; the trends are identical, but the signal increases with increasing temperature. Figure taken from Bertaux et al. (2006). b) Model of the DCNU signal (in ADU) for each band as a function of the pixel number. Figure taken from Perrier (2006).

13.1.3 Removal of the star signal

As explained in Section 12.2.1, during a stellar occultation, SPICAM points towards a star while it scans the atmospheric limb. Outside the atmosphere, only the star signal is recorded, $S_\lambda(0)$, an example of which is shown in Figure 13.3. Then, when the LOS of the instrument descends through the atmosphere, the star signal is attenuated by absorption features in the atmosphere, $S_\lambda(s)$. Using Equation 12.4, we replace $S_\lambda(s)$ by $\alpha_b \cdot S_\lambda(0) \cdot T_\lambda(s)$, where α_b is a coefficient that indicates the percentage of the star signal incident on band b (Royer, 2011). For a binning of 16, which is the most common binning value for the stellar occultation observations to be treated in this work, the spread of stellar flux is as follows: α_b varies from 3-5% for the bands on both sides of the central band, b_2 and b_4, such that α_3 ~90%; b_1 and b_5 gets about 0.01% of the signal (Quémerais et al., 2006).

From Equation 13.1, we now have that the corrected signal, $S_{corr} = S_{obs} - S_{offset} -$

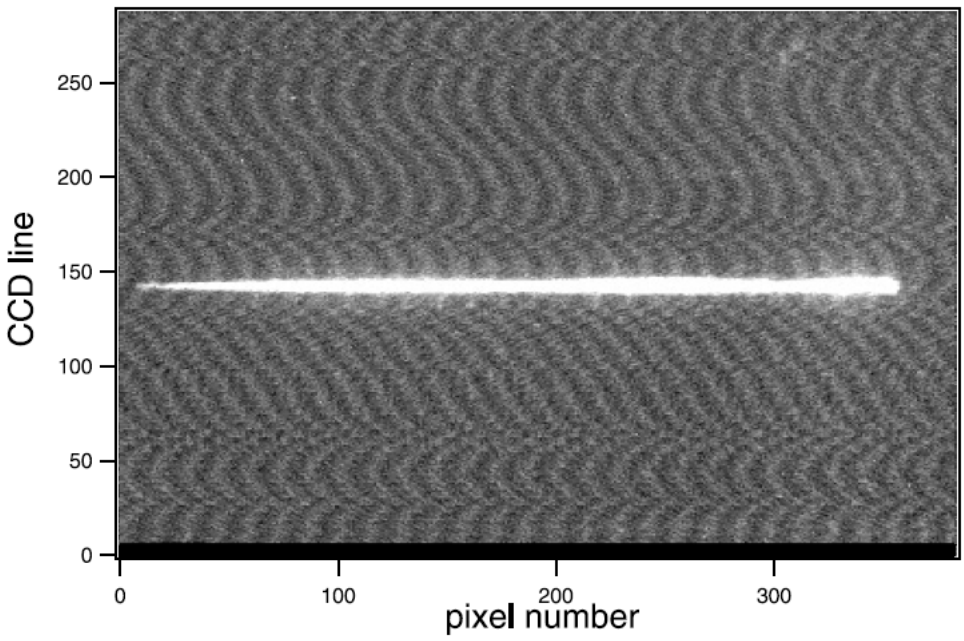

Figure 13.3: Distribution of light over the whole detector when a star (in this case Delta Scorpii) is observed without the slit. The log of intensity in ADU is gray-coded, and the contrast is enhanced to emphasize low signals. The spectrum is horizontal, along the CCD rows, parallel to the $\vec{Y_s}$ axis of the spacecraft. Because of optical aberrations, the spectrum is spread over several rows of the CCD. The slit orientation is parallel to the $\vec{X_s}$ axis, along the column axis of the CCD (vertically in this figure). The "tapestry" effect is residual electronic noise, after subtraction of offset and DC. Figure taken from Bertaux et al. (2006).

S_{DC}, is a combination of the star signal and the airglow signal:

$$S_{corr} = S_\lambda(s) + S_{airglow}, \tag{13.3}$$

such that:

$$S_{corr} = \alpha_b \cdot S_\lambda(0) \cdot T_\lambda(s) + S_{airglow} \tag{13.4}$$

(Royer, 2011). However, there are two unknown quantities, $T_\lambda(s)$ and $S_{airglow}$, that need to be deduced from a single observation. To overcome this problem, we determine a typical transmission profile from another observation that does not contain contamination

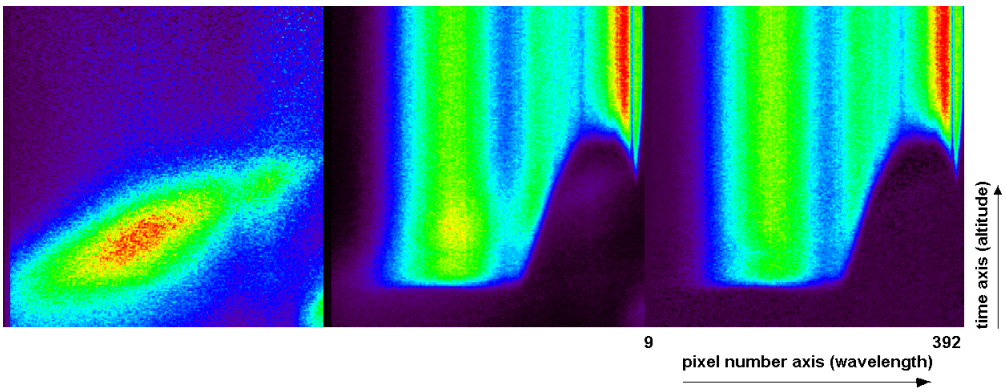

Figure 13.4: Time variation of the spectra for the central band, band 3, in orbit # 588 before processing of the raw signal (central panel) to extract the signal from NO airglow emission (left panel) from the star signal (right panel). The signal is color-coded in ADU with lower values in purple and higher values in red.

from an airglow signal. Furthermore, we use all the spectra in the given occultation sequence that were measured outside of the atmosphere to calculate the values of α_b and $S_\lambda(0)$, which are not contaminated by any airglow emission or affected by atmospheric absorption. Hence, by calculating the contribution on the adjacent bands, α_b, we can determine the contribution from the star signal, which will enable us to isolate the airglow signal that dominates on these bands (see Figure 13.1). Now, this problem:

$$S_{airglow} = S_{corr} - \alpha_b \cdot S_\lambda(0) \cdot T_\lambda(s) \tag{13.5}$$

can be solved. Figure 13.4 shows the time-series of spectra from the band 3 (central panel), after removing the star signal (right panel), and hence recovering the airglow signal (left panel).

13.1.4 Wavelength assignment

The wavelength assignment of the SPICAM detector was made prior to launch. It is regularly calibrated in-flight during technological sequences. Figure 13.5 shows the wavelength as a function of pixel number as it is used for this work.

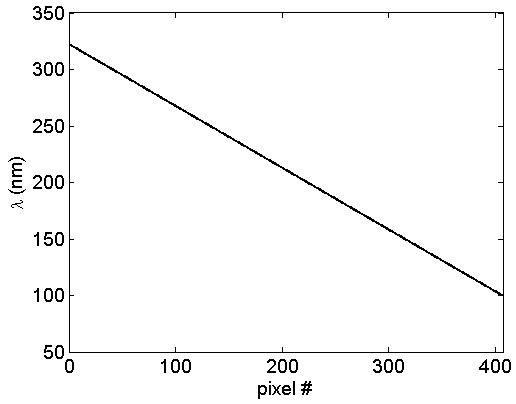

Figure 13.5: Wavelength (nm) assignment of the CCD as a function of the pixel number.

13.2 Determination of the observational geometry

We need to reconstruct the geometry of the orbital configuration at the time of the observation. For each occultation sequence in the SPICAM data, also referred as orbits, there is a file containing the nominal geometry data corresponding to this occultation sequence. These "GEOM" files are intended to describe what is seen at each second. However, the information provided is not suitable to link observations together during an occultation sequence, or a so-called orbit, because the reference frame moves with the spacecraft. We therefore need to choose a plane of observation that will contain the image from the intensity distribution of the NO emission across the limb. During a stellar occultation, each band on the CCD, which subtends a solid angle of $0.16° \times 1°$, is projected onto the plane in a different location.

We define a plane E that is perpendicular to the direction of the star and passes through the center of the planet. Since the spacecraft is in a fixed inertial attitude throughout the occultation, it is natural to take the image plane, i.e., the plane that is parallel to the $\vec{X_s}$ and $\vec{Y_s}$ axes of the spacecraft, and therefore perpendicular to the $\vec{Z_s}$ axis that passes through the center of Mars, O. Figure 13.6 illustrates this geometry. We need to determine where the axis $\vec{Z_s}$ crosses plane E. For this, we have to find the position of the spacecraft, P, in the system $\vec{X_s}'$, $\vec{Y_s}'$, $\vec{Z_s}'$ that passes through the center

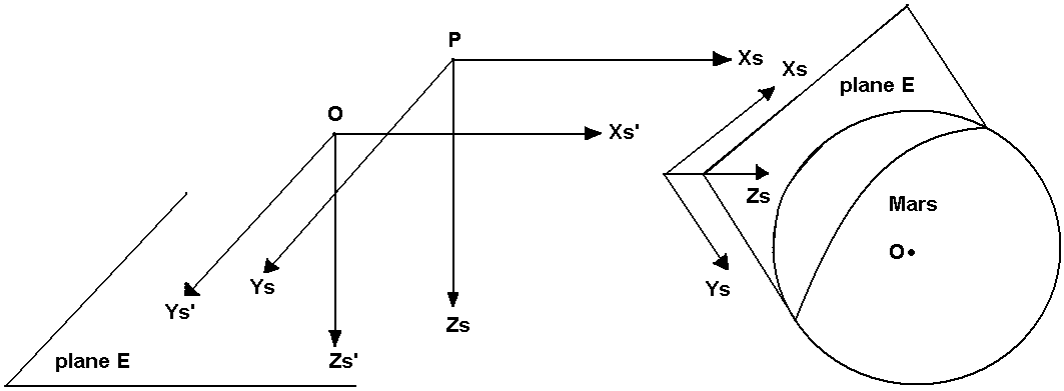

Figure 13.6: The position of the spacecraft, P, is projected along the axis $\vec{Z}_s$ towards the footprint of the projection of the trajectory onto the observation plane E, which passes through the center O of Mars and parallel to the axis $P\vec{X}_s$, $P\vec{Y}_s$.

of Mars, O.

The optical axis of the instrument is defined by the center of the slit, and by the footprint of row 144 of the CCD along the slit (see Figure 12.2). It is close to the $\vec{Z}_s$ axis of the spacecraft; the separation is of small angles that we call "mechanical offsets", which are known. For the moment, we can neglect these and assume that the optical axis is the $\vec{Z}_s$ axis.

As stated above, there is a problem with the arbitrary choice of the reference frame in the "GEOM" files when we want to link the many occultations in a given sequence. To overcome this problem, we will choose a common frame of reference, the coordinate system EMEJ2000, or J2000 for short, which is defined as follows: $\vec{Z}$ axis points towards Earth's North pole and $\vec{X}$ is along the crossing of the terrestrial equator with the ecliptic plane on January 1^{st}, 2000.

We know the position of P in a reference system determined by the International Astronomical Union (IAU) that is attached to Mars, and hence rotating. This reference frame will be referred to the IAU_{Mars} system. Therefore, the position P, in terms of longitude (θ), latitude (ϕ), and distance (R) from the Mars Nearest Point (MNP) in the

IAU_{Mars} system is:

$$\begin{aligned} X_P &= R \cdot \cos(\phi) \cdot \cos(\theta) \\ Y_P &= R \cdot \cos(\phi) \cdot \sin(\theta) \\ Z_P &= R \cdot \sin(\phi). \end{aligned} \tag{13.6}$$

The X_P, Y_P, and Z_P are the components of the vector $\vec{OP}$ that determines the position of the spacecraft in the IAU_{Mars} system.

We also know the right ascension (α) and the declination (δ) in the J2000 system, which defines the IAU_{Mars} system. We calculate the correspondence of the IAU_{Mars} axes in the J2000 system:

$$\begin{aligned} X_x^{J2000} &= \cos(\delta_x) \cdot \cos(\alpha_x) \\ X_y^{J2000} &= \cos(\delta_x) \cdot \sin(\alpha_x) \\ X_z^{J2000} &= \sin(\delta_x) \end{aligned} \tag{13.7}$$

and similarly for the $\vec{Y}$ and $\vec{Z}$ axes, giving the vectors $\vec{X}^{J2000}$, $\vec{Y}^{J2000}$, and $\vec{Z}^{J2000}$. We can then calculate the components of $\vec{OP}$ in the J2000 reference frame (Equation 13.7) by successively taking the scalar products of each axis with $\vec{OP}$ (Equation 13.6):

$$\vec{OP}^{J2000} = X_P \cdot \vec{X}^{J2000} + Y_P \cdot \vec{Y}^{J2000} + Z_P \cdot \vec{Z}^{J2000}. \tag{13.8}$$

To switch from the IAU_{Mars} system to the J2000 system, we need the $\vec{X}$, $\vec{Y}$, and $\vec{Z}$ components of the Mars Mean Equator (MME) of date J2000. It is defined as this: the $\vec{Z}$ axis is pointing towards the Mars North Pole, the $\vec{X}$ is pointing towards the IAU_{Mars} vector of date J2000. The IAU_{Mars} vector of date J2000 is defined as the intersection of the Mars equator and the J2000 equator. The $\vec{Y}$ axis completes the right-hand frame. The origin of this frame is the centre of Mars O. The components of the MME are obtained

from the Spice Library (http://naif.jpl.nasa.gov/pub/naif/MEX/kernels/fk/RSSD0002.TF):

$$\mathbf{MME} = \begin{pmatrix} 0.67325 & 0.73941 & 0.00000 \\ -0.58963 & 0.53687 & 0.60339 \\ 0.446158 & -0.40623 & 0.79744 \end{pmatrix}. \tag{13.9}$$

We can then calculate the components of the vectors $\vec{X_s}$, $\vec{Y_s}$, and $\vec{Z_s}$ in the J2000 system. We multiply each vector by the transpose matrix of **MME** (Equation 13.9):

$$\vec{X_s}^{J2000} = \mathbf{MME}^t \cdot \vec{X_s} \tag{13.10}$$

and similarly for the $\vec{Y_s}^{J2000}$ and $\vec{Z_s}^{J2000}$ vectors. The pointing vectors with respect to the spacecraft position in the IAU$_{Mars}$ system, $\vec{X_s}$, $\vec{Y_s}$, and $\vec{Z_s}$, are contained in the "GEOM" files.

We finally obtain the components of $\vec{OP}$ in the system parallel to the spacecraft axes, by computing the scalar product of $\vec{OP}$ (Equation 13.8) with each axis $\vec{X_s}$, $\vec{Y_s}$, and $\vec{Z_s}$ of the spacecraft (Equation 13.10) in the J2000 system:

$$OP_{s_x}^{J2000} = \vec{X_s}^{J2000} \cdot \vec{OP}^{J2000} \tag{13.11}$$

and similarly for $OP_{s_y}^{J2000}$ and $OP_{s_z}^{J2000}$, which constitute the vector $\vec{OP_s}$. Figure 13.7a shows the footprint of the pointing vector of the spacecraft, i.e., $\vec{Z_s}$, that crosses plane E, as well as the FOV of the central band, i.e., the 3^{rd} band. Figure 13.7b is a close-up of Figure 13.7a that better displays the FOV of the third band.

Finally, from Equation 13.11, we obtain the altitude between the surface of the planet and the projection of the 3^{rd} band in the FOV:

$$z = \sqrt{(OP_{s_x}^{J2000})^2 + (OP_{s_y}^{J2000})^2} - R_{Mars} \tag{13.12}$$

where R_{Mars} is the radius of Mars. And lastly, we also know the angle between the local vertical and the $\vec{X_s}$ axis of the spacecraft:

$$\theta = \arctan\left(\frac{OP_{s_y}^{J2000}}{OP_{s_x}^{J2000}}\right). \tag{13.13}$$

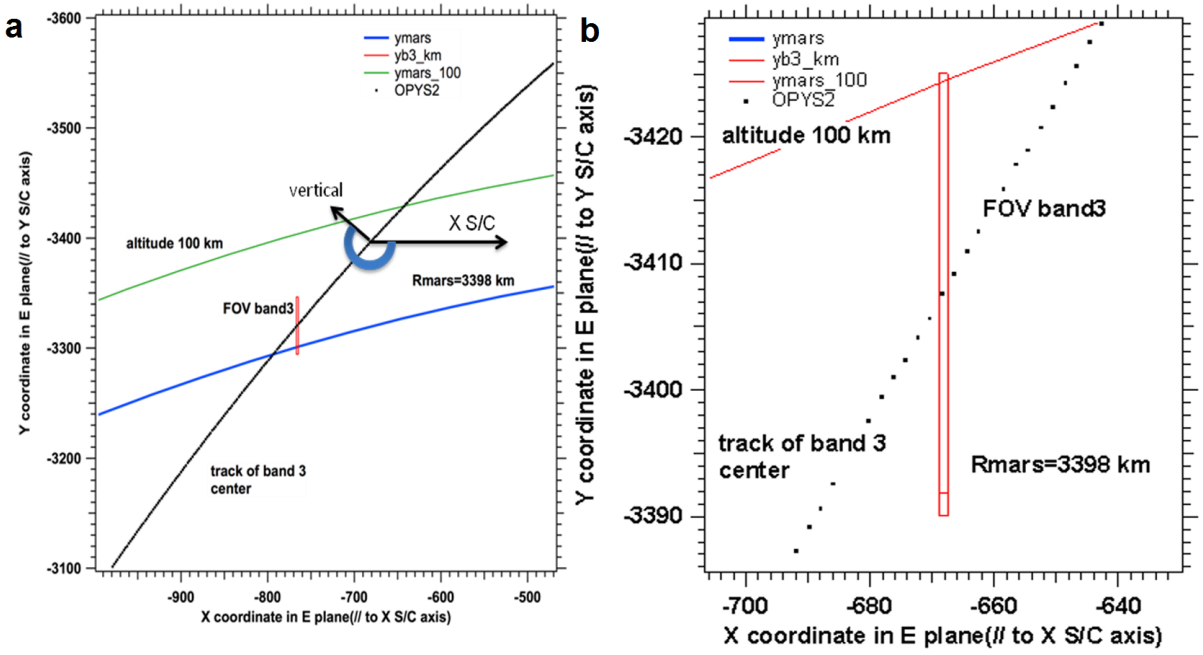

Figure 13.7: a) Footprint of $\vec{Z}_s$ in the observation plane E (black dotted line) representing one occultation per second. The FOV is the central band (red rectangle), parallel to the $\vec{Y}_s$ axis, and perpendicular to the slit, which is parallel to the $\vec{X}_s$ axis. The surface of the planet is indicated by the blue line, and the altitude of 100 km above the planet's surface with a green line. Courtesy of Dr. J.-L. Bertaux. b) Expanded view of a. The central band (red rectangle) contains a smaller section at one end representing the direction of $+\vec{Y}_s$, which enables the direction between the virtual pixels in the FOV and the real pixels on the CCD to be verified. Here, in the case of a de-occultation, the emission is first seen on the opposite end of the small rectangle, and it will be last seen on the side of the small rectangle. Courtesy of Dr. J.-L. Bertaux.

The final step is to correct for the "mechanical offsets", the small angle difference between the direction of the central band, or 3^{rd} band, and the $\vec{Z_s}$ in both directions $\vec{X_s}$ and $\vec{Y_s}$. In the reference frame J2000, with the declination (δ) and the right ascension (α), we obtain the vector $\vec{Q}_{s,3^{rd}}$:

$$\begin{aligned} X_{s,3^{rd}} &= \cos(\delta) \cdot \cos(\alpha) \\ Y_{s,3^{rd}} &= \cos(\delta) \cdot \sin(\alpha) \\ Z_{s,3^{rd}} &= \sin(\delta) \end{aligned} \tag{13.14}$$

such that the offsets are:

$$\begin{aligned} OFF_x &= \arccos(\vec{Q}_{s,3^{rd}} \cdot \vec{X_s}^{J2000}) \\ OFF_y &= \arccos(\vec{Q}_{s,3^{rd}} \cdot \vec{Y_s}^{J2000}). \end{aligned} \tag{13.15}$$

13.3 Inversion of the signal

For a given occultation, the direct calculation of the signal in ADUs on each pixel, p, is obtained from the reference spectrum S_{ref}, and the distribution of brightness $B(Y_s)$ along the CCD row:

$$S^{ADU}(p) = \sum_i B(i) \cdot S_{ref}(p-i). \tag{13.16}$$

From the spectral distribution of the emission on one band, we have to find the distribution of the emission along the $\vec{Y_s}$ in the focal plane, at each second. To achieve this, we have to invert the matrix containing the signal. First, we consider 19 bins of $0.2°$ (corresponding to 20 pixels), $B_1, B_2, ..., B_{19}$, in each of the five bands:

$b_1 = Y_s^f\{0°, 0.2°\}$

$b_2 = Y_s^f\{0.2°, 0.4°\}$

...

$b_5 = Y_s^f\{0.8°, 1.0°\}$

and the signal recorded by each pixel in ADU: $S_1, S_2, ..., S_{384}$. Now we have:

$$\begin{pmatrix} S_1 \\ S_2 \\ ... \\ S_{384} \end{pmatrix} = \begin{pmatrix} a_1^1 & a_1^2 & ... & a_1^{19} \\ a_2^1 & a_2^2 & ... & a_2^{19} \\ ... & & & \\ a_{384}^1 & a_{384}^2 & ... & a_{384}^{19} \end{pmatrix} \begin{pmatrix} B_1 \\ B_2 \\ ... \\ B_{19} \end{pmatrix}$$

such that: $S_i = a_i^1 \cdot B_1 + a_i^2 \cdot B_2 + ... + a_i^{384} \cdot B_{19}$ or in a matrix form:

$$\mathbf{S} = \mathbf{AB}. \tag{13.17}$$

The inverse problem consists in determining the 19 unknown brightness values, B_1, B_2, ..., B_{19}, from a spectrum measured without a slit, and spread across the 384 pixels of the CCD. All of the 288 rows of the CCD are filled this way simultaneously. A common approach to such a problem is to reduce the number of variables that we are trying to find using the least squares method. In the linear case, this is provided by the *normal equations*:

$$\mathbf{D} = (\mathbf{A^t})\mathbf{A}, \tag{13.18}$$

which implies that by taking the transpose of the matrix $\mathbf{A}$, we get a square matrix, $\mathbf{D}$.

Now, if we multiply both sides of Equation 13.17 with $\mathbf{A^t}$, we get $(\mathbf{A^t})\mathbf{S} = (\mathbf{A^t})\mathbf{AB}$. By substituting the square matrix, $\mathbf{D} = (\mathbf{A^t})\mathbf{A}$, we obtain a system of 19 equations containing 19 unknowns:

$$\mathbf{B} = (\mathbf{D^{-1}})(\mathbf{A^t})\mathbf{S}. \tag{13.19}$$

13.3.1 The normalized spectrum of NO

The reference spectrum is obtained from a stellar occulation of the atmosphere of Mars by SPICAM with the slit in place during orbit # 716, as displayed in Figure 13.8. We calibrate this spectrum in intensity to find the correspondence between the absolute intensity in ADU to that in kR. To obtain the number of photo-events per pixel, S_{ref}^{pe},

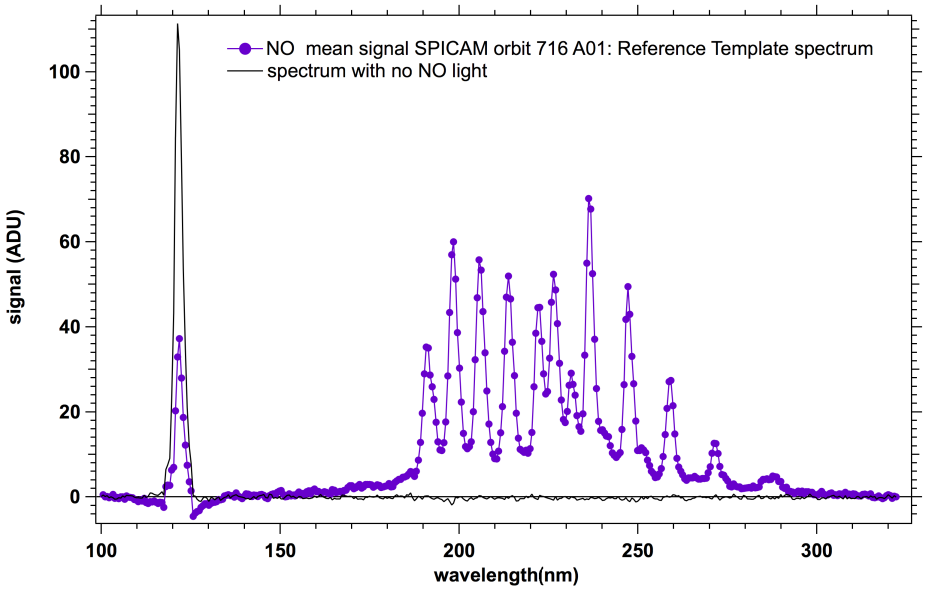

Figure 13.8: Reference spectrum of the NO emission as measured by SPICAM in the stellar occultation mode with the slit in place during orbit # 716. The signal is given in ADU as a function of wavelength (nm). At 120 nm, the signal is due to the hydrogen Lyman-α emission. Courtesy of Dr. J.-L. Bertaux.

we divide the reference signal by the nominal gain, g_0=37.9473 ADU/photo-event:

$$S_{ref}^{pe} = \frac{S_{ref}^{ADU}}{g_0}. \tag{13.20}$$

Then, to get the flux of photons per nm, S_{ref}^{flux}, on each pixel, we divide by the effective area, S_{eff} (see Section 12.1.2), the integration time, dt, and the width of one pixel, $d\lambda$:

$$S_{ref}^{flux} = \frac{S_{ref}^{pe}}{S_{eff} \cdot dt \cdot d\lambda}. \tag{13.21}$$

Now, to convert to kR, we find the solid angle in the case of a stellar occultation with the slit in place, $d\omega$:

$$d\omega = \frac{50\mu m \cdot 23\mu m \cdot 32}{(120mm)^2} \times 10^{-6} \tag{13.22}$$

where the width of the slit is 50 μm, multiplied by the size of one pixel 23 μm $\times$ 32 pixels, i.e., binning of 32 rows, and the focal length is f=120 mm. Then, we obtain the

calibration of the reference signal in kR/nm:

$$S_{ref}^{kR/nm} = \frac{S_{ref}^{flux}}{d\omega} \cdot 4\pi \times 10^{-9}. \tag{13.23}$$

Finally, we normalise the reference spectrum to a brightness of 1 kR coming from one pixel:

$$S_{ref}^{1kR} = \frac{23\mu m}{50\mu m} \cdot \frac{S_{ref}^{ADU}}{\sum S_{ref}^{kR/nm}}. \tag{13.24}$$

Figure 13.9 shows this normalised spectrum.

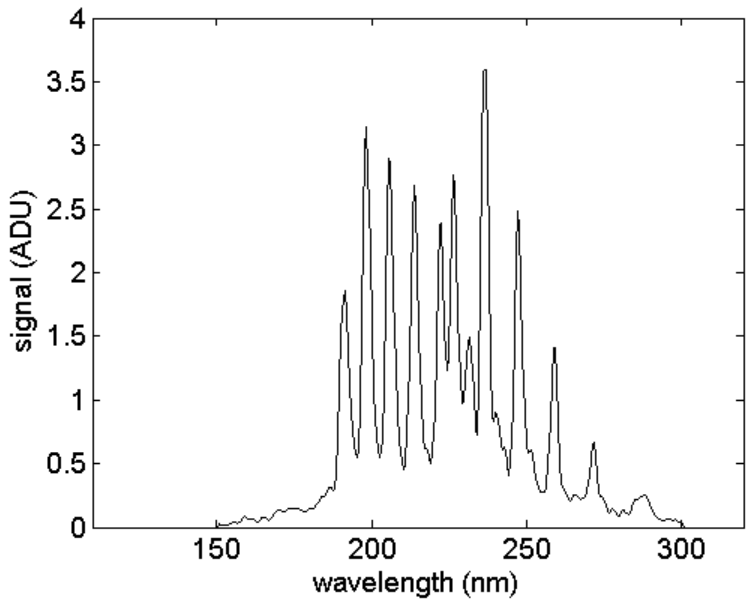

Figure 13.9: Reference spectrum of the NO emission in ADUs as measured by SPICAM in the stellar occultation mode with the slit in place during orbit # 716 normalised to a total brightness of 1 kR. Courtesy of Dr. J.-L. Bertaux.

13.3.2 The inverse matrix

From the normalised reference spectrum obtained from Equation 13.24 and shown in Figure 13.9, we construct the coefficients of the matrix that will pass the raw signal of a measured spectrum in ADU as input through the 19 bins of 20 virtual pixels, which

yields the distribution of brightness along a band as measured by the detector. We need to shift the reference spectrum by the corresponding distance in Y_s^f, with Y_s^f=0 corresponding to the 10^{th} bin, and with one virtual pixel equivalent to one real pixel. In concrete terms, at each pixel p, we have to shift the reference spectrum by $i\times20$ pixels, i corresponding to the bin number, such that $S^{ADU}(p) = S_{ref}(p) \cdot B_{tot}$ with $S^{ADU}(p,i) = S_{ref}(p-20\times(i-10)-20)$. Finally, we integrate from $\vec{Y_s}$=0 to $\vec{Y_s}$=20×pixel size=20×0.0109° to obtain the total brightness in each bin. We repeat these steps for each bin. This matrix, **A**, shown in Figure 13.10a, is applicable to any observational geometry. Then, we operate the theorem in Equation 13.18 on **A** to get the square matrix **D**, shown in Figure 13.10b, and finally we take its inverse to obtain $\mathbf{D}^{-1}$, as displayed in Figure 13.10c.

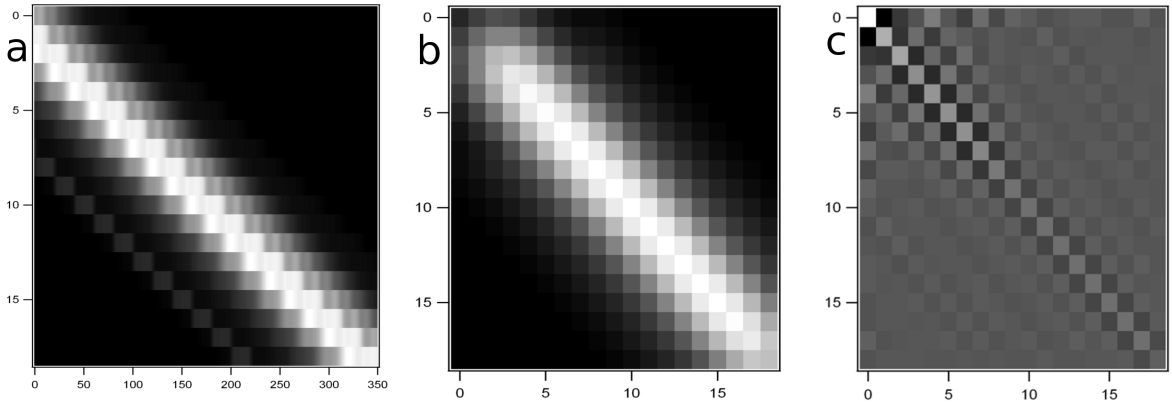

Figure 13.10: a) Matrix of the reference signal **A** with on the horizontal axis the pixel number assignment p and on the vertical axis the bin number assignment i; b) Square matrix **D** with the bin number assignment i on both axis; c) Inverse matrix $\mathbf{D}^{-1}$ of the square matrix. Courtesy of Dr. J.-L. Bertaux.

The inversion described above applies to one spectrum from one occultation sequence. From Equation 13.19, we solve for the brightness value $B(i)$ for each of the 19 bins of 20 pixels in one band from a given spectrum. However, from each occultation, the signal is recorded on the five bands, b=1,...,5, of the CCD, and each occultation sequence contains

many occultations, n. Therefore, we are interested in finding the brightness values for all of the i bins, b bands, and n spectra: $B(b, n, i)$. By doing so, we obtain a brightness map similar to the one in Figure 13.11 that shows the distribution of the NO emission during one occultation sequence.

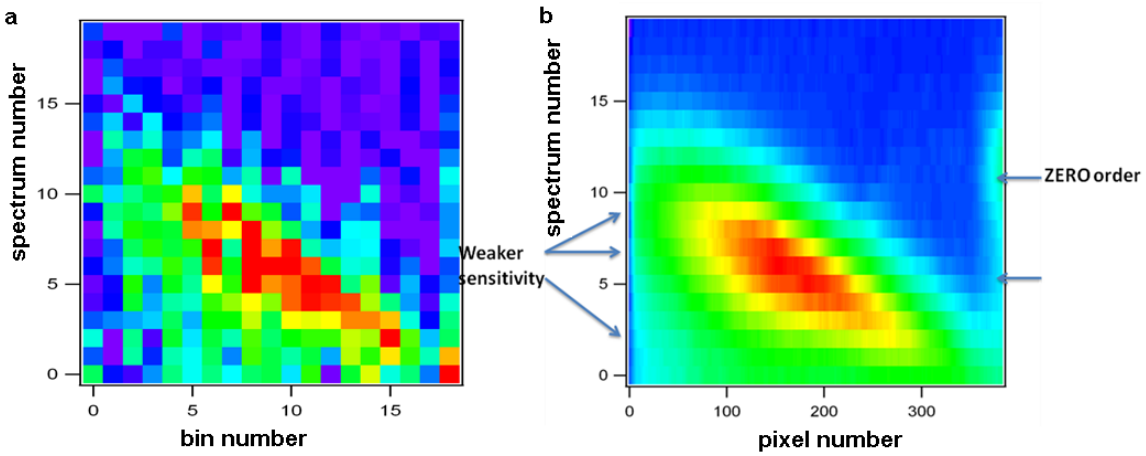

Figure 13.11: Time-series of spectra of the NO brightness distribution from one band in the stellar occultation mode gathered during the occultation from orbit # 102. The brightness is represented by the color-coded contours: purple is the least intense and red is the most intense. a) Result from the inversion of 20 spectra. b) Raw signal from the same 20 spectra before any treatment. Courtesy of Dr. J.-L. Bertaux.

13.4 Output from the retrieval algorithm

In summary, we start by preprocessing the raw signal to remove the noise and extracting the signal from the NO emission. Then, to recover the geometrical information at the time of the observation. We then invert the signal from the NO emission to retrieve the spatial distribution of the absolute brightness in ADU during an occultation sequence. Finally, we need to convert this brightness value to kR. For that, we compute the solid

angle, $d\omega$, seen by one pixel:

$$d\omega = \frac{23\mu m \cdot 23\mu m}{(120mm)^2} \times 10^{-6}$$

where the size of one pixel is 23 μm $\times$ 23 μm, and the focal length f is 120 mm. The gain is given by Equation 12.1. Hence, the conversion from a signal in ADU, N_{ADU}, to a brightness, B, in kilorayleigh (kR) is obtained from:

$$B = \frac{N_{ADU}}{G \cdot d\omega \cdot dt} \cdot 4\pi \times 10^{-6}. \tag{13.25}$$

An example of such an inversion is shown in Figure 13.12 from a particular occultation made with SPICAV on Venus Express, that was used to test the method since the signal is stronger in the Venusian atmosphere. The figure shows the brightness values (color-coded dots) for each of the bins (see red rectangle with black dots in the lower-left portion of the plot that represents the FOV from band 3), for many spectra (along-track illustrated by the red line). The axes are the X_s and Y_s components of plane E (see Figure 13.6). We notice that the emission is seen at an altitude of $\sim$100 km (red line) above the surface of Venus (blue line).

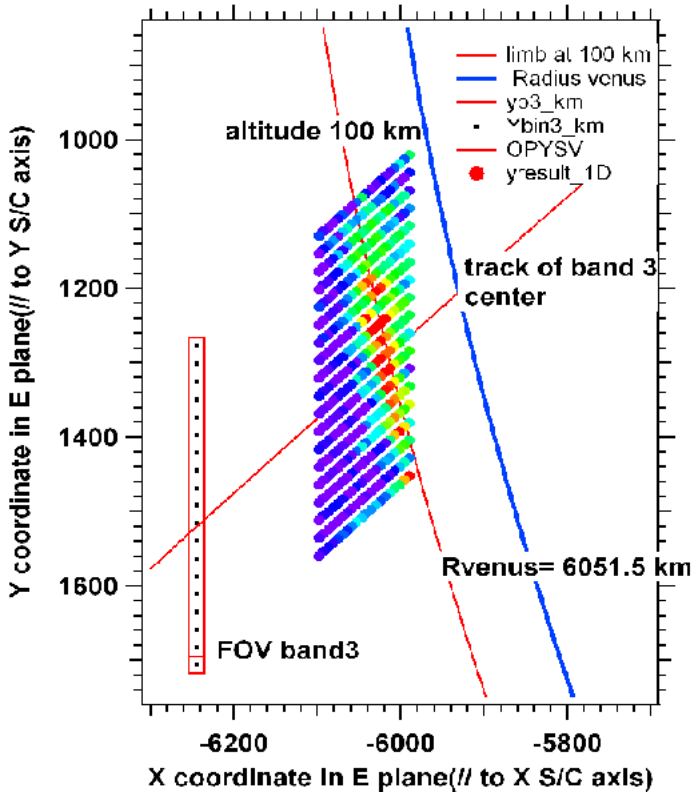

Figure 13.12: Example of the brightness of the NO emission in the FOV of SPICAV from orbit # 514. The brightness is color-coded with red corresponding to the brightest regions; each color dot represents the brightness of one bin B_i (following the orientation of the slit shown by the red rectangle) from one occultation n_i (along the track of the spacecraft represented by the black line). The emission is seen between the surface of the planet (blue line) and 100 km in altitude above the planet's surface (red line). Courtesy of Dr. J.-L. Bertaux.

Chapter 14

Retrievals of NO airglow

In this chapter, we present the results from our retrieval methodology applied to NO airglow in the SPICAM dataset of stellar occultations. The technique described in Chapter 13 is used to infer the brightness of the airglow layer in kilorayleigh, as well as allowing the extraction of a 3-D snapshot of the airglow layer within one occultation. We present the preliminary analysis of one year of SPICAM observations to test the validity of the methodology.

The results are then compared with the analysis of the SPICAM limb observations of the NO emission by Cox et al. (2008), which is the only observational dataset for this emission in the Mars atmosphere available in the literature. The observations of the emission are further compared with airglow model simulations to verify our understanding of the photochemical mechanism producing this feature in the Mars atmosphere.

14.1 Observations

Stellar occultation sequences from orbits 485 to 2994, which roughly correspond to one Martian year of observations, or two Earth years, have been considered. In this dataset, 108 occultation sequences did contain useful nightglow information corresponding to the NO emission. Table B.1 in Appendix B gives some details regarding the location and time

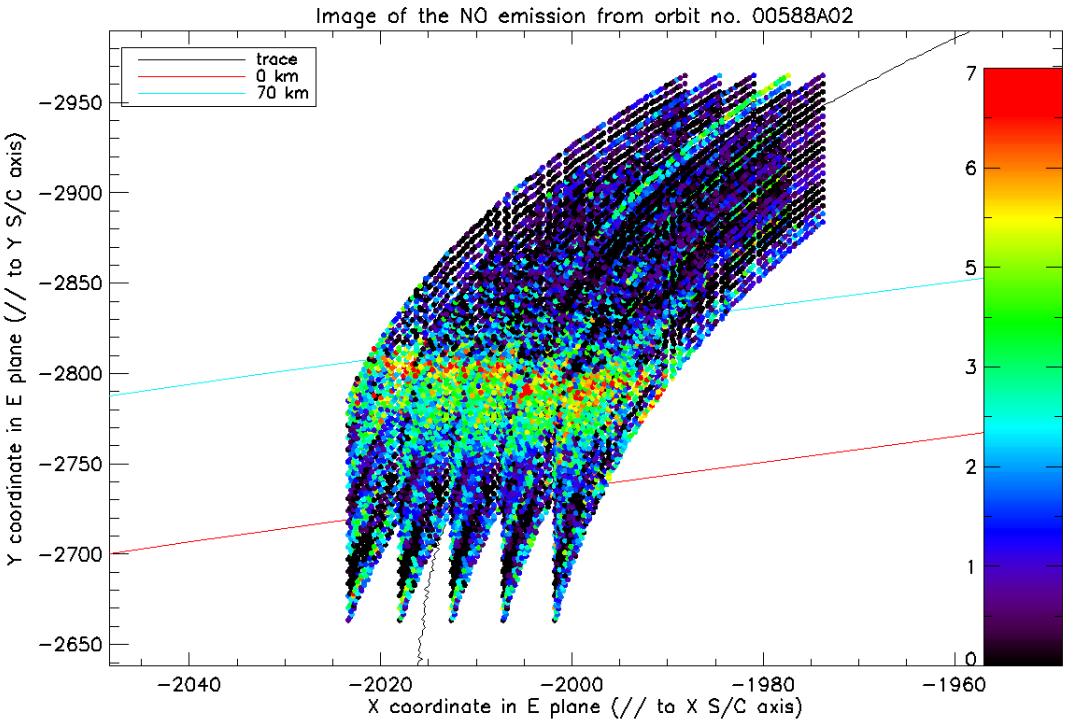

Figure 14.1: Intensity of the NO emission (colorbar, in kR) for several spectra as recorded with the five bands of the SPICAM detector. The intensity is plotted as a function of its position with respect to the planet, where the origin of this coordinate system is the center of Mars and the horizontal and vertical axes are parallel (//) to the $\vec{X}_s$ and $\vec{Y}_s$ axes of the spacecraft. See Section 13.3 for more details on how to interpret this type of plot.

of these observations. For each of these occultations, we proceeded with the inversion technique described in the previous chapter, Chapter 13. As an example, the result of this inversion for the first occultation of Table B.1 is shown in Figure 14.1. The brightness from the NO airglow is displayed in a spatial perspective corresponding to the instrument FOV during its occultation sequence with respect to the center of Mars (black line). The surface of Mars (red line) and the altitude mark of 70 km (blue line) are also shown. We notice that during this sequence, an NO airglow layer was observed slightly below 70 km.

Figure 14.2 shows the peak brightness as a function of latitude and season, as ex-

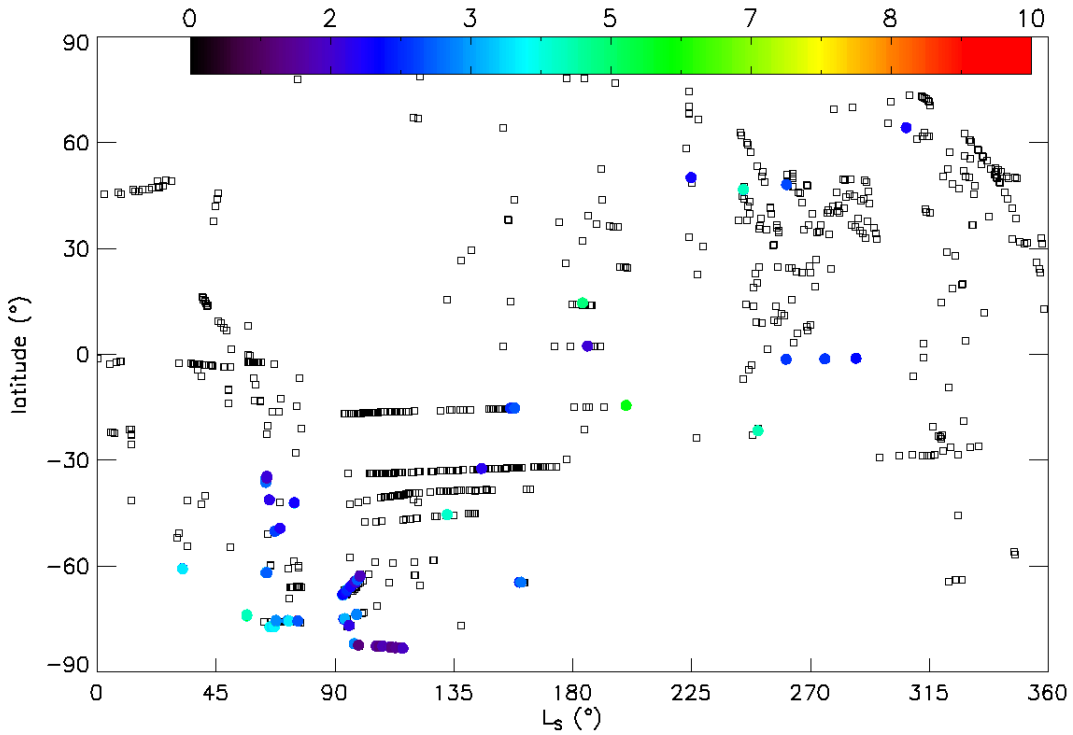

Figure 14.2: Latitude vs. areocentric longitude distribution of the peak brightness from the NO emission. The color bar is the brightness in kR. The brightness of the NO emission is represented by color-coded circles with red corresponding to the brightest values. The black empty squares correspond to orbits with no detectable NO airglow signal.

tracted from the inversion algorithm (color dots). Also displayed on the figure are the locations of all 108 occultations, even those that do not contain a detectable airglow signal (empty squares). We notice that although the measurements cover a large latitudinal and seasonal range, there is a localised airglow maximum in the Southern hemisphere around the winter solstice, i.e., for latitudes above 30°S and for L_S=50–120°. The mean brightness of the occultations with detectable NO airglow in this dataset is 3.0±1.9(1σ) kR, which is higher than the mean brightness of 1.2±1.5 kR from the work of Cox et al. (2008), but these values are compatible within their combined range of uncertainty.

Similarly, Figure 14.3 displays the peak altitude of the NO emission as a function of

latitude and season (color dots), as also obtained from the partial inversion algorithm. The lowest altitudes are found in the Southern hemisphere close to the winter pole with values below 100 km, while higher values are observed at all latitudes. The mean altitude of the peak from our dataset is 80.5±24.0(1σ) km in agreement with the calculated mean of Cox et al. (2008), which is 73.0±8.2 km. We note that our dataset presents values that extend above 60° latitude, which is not the case for the work of Cox et al. (2008), and therefore we are expanding the coverage of the measurements.

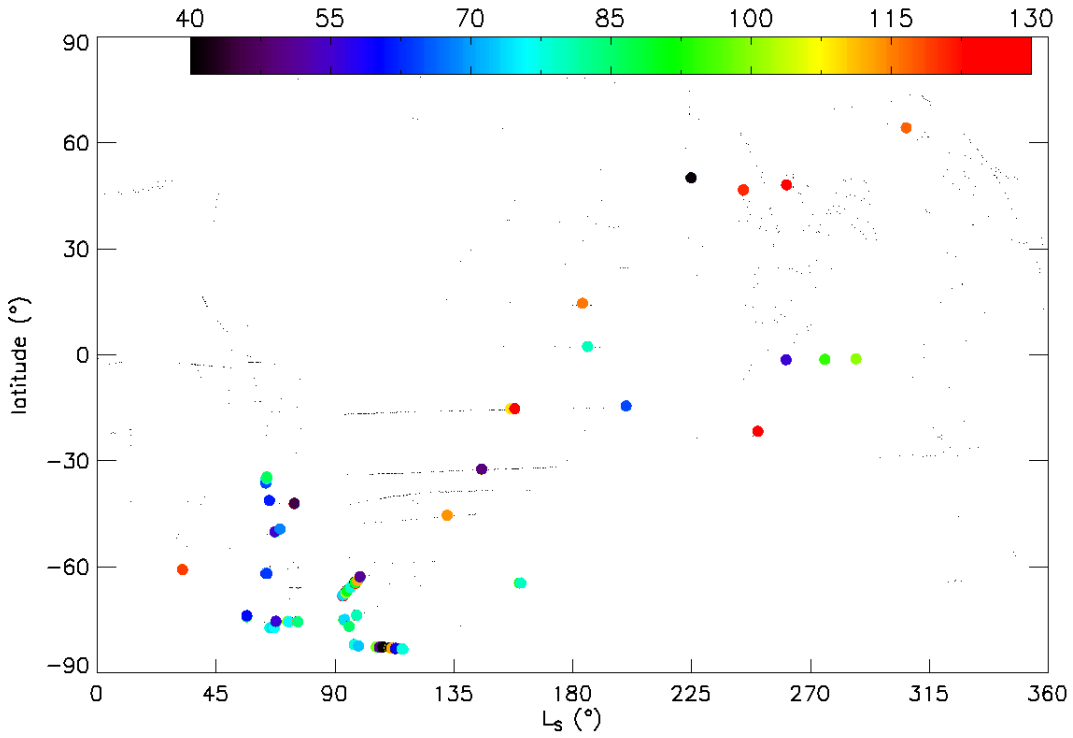

Figure 14.3: Latitude vs. areocentric longitude distribution of the peak altitude from the SPICAM NO emission. The color bar is the altitude in km. The peak altitude of the NO emissions is represented by color-coded circles with red corresponding to the largest values. The black dots correspond to orbits with no detectable NO airglow signal.

As is a common practice when analysing the distribution of an airglow feature, we plotted the peak altitude versus the peak brightness of the observations containing a signal from NO airglow (Figure 14.4). There seems to be no correlation between these

two parameters, and the spread of the values is large as in Cox et al. (2008). This apparent lack of correlation is compatible with the short lifetime of the excited species, i.e., 3.2×10^{-8} s (Sun and Dalgarno, 1996): we expect the NO airglow to be localised and strongly linked to the downward transport of N and O atoms. Those are subject to dynamical variations, as originally proposed by Bertaux et al. (2005). Such dependency induces significant variability in the altitude of the recombination and hence of the brightness.

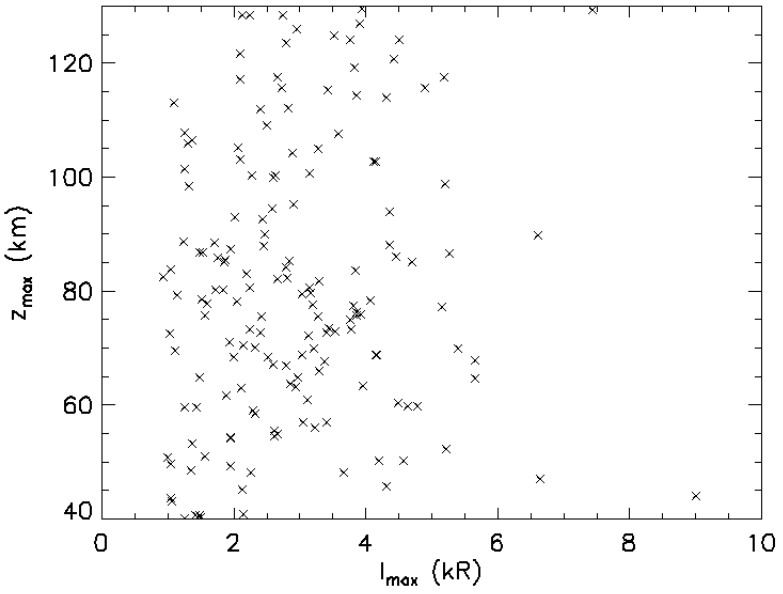

Figure 14.4: Peak altitude (km) vs. brightness of the peak (kR) of the NO airglow from SPICAM.

14.2 Comparison with model simulations

We compare the retrieved NO airglow profiles with model simulations. To perform the model calculations, we used the same atmospheric model described in Section 8.1 to provide the atmospheric conditions for the airglow calculations. Figure 14.5 shows the density profiles of the nitrogen atoms, N(^{4}S), in the Mars atmosphere obtained with run 2 of the LMD-MGCM.

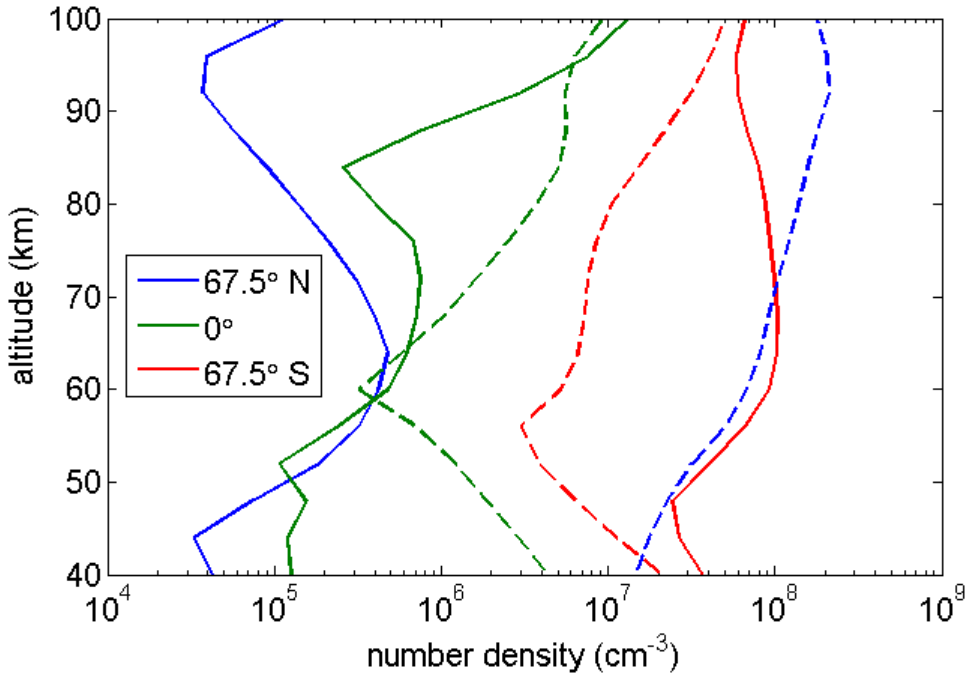

Figure 14.5: 00 LT profiles of N_2 at L_S=90° (solid lines) and L_S=180° (dashed lines) for latitudes 67.5°N (blue), 0° (green), and 67.5°S (red) from the LMDMGCM run 2.

We then compute the volume emission rate of NO from Equation 9.1:

$$\epsilon(NO^\star) = \frac{[NO^\star]}{\tau} \tag{14.1}$$

where τ is the lifetime by radiative relaxation of excited NO species. From Section 5.2, we know how to calculate the density of $NO^\star$ (see Equation 5.10):

$$[NO^\star] = \frac{k_{NO}[N][O]}{1/\tau_{NO}}. \tag{14.2}$$

The rate coefficient k_{NO} for the recombination reaction of O and N atoms, Reaction 5.6, is $1.92 \cdot (300/T)^{1/2} \cdot (1 - 0.57/(T^{1/2})) \times 10^{-17}$ cm^3 s^{-1} (Dalgarno et al., 1992), and the lifetime, τ_{NO}, is taken to be 3.2×10^{-8} s (Sun and Dalgarno, 1996). Figure 14.6 displays the latitudinal vs. areocentric longitude distribution of intensity (Figure 14.6a) and of the peak altitude (Figure 14.6b) from the calculations of the NO emission in the Mars atmosphere at 00 LT. The coarse resolution of this model simulation (due to averaging

over 30° L_S) causes abrupt changes in the peak altitudes of Figure 14.6b. We observe that the NO emission is strongest over the autumn/winter poles in each hemisphere within the latitude band 60–90°. There, the intensity ranges from a few kR to above 10 kR around the equinoxes, i.e., L_S=0 and 180°. This distribution is consistent with the variations in atomic oxygen density (see Section 8.1). Elsewhere, the emission is at least one order of magnitude weaker.

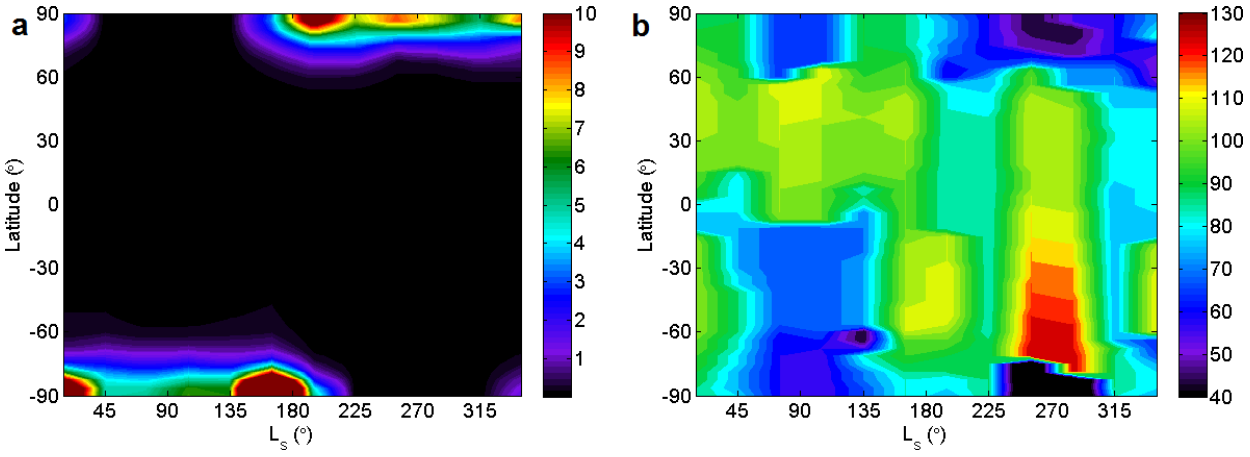

Figure 14.6: a) Simulated global distribution of intensity of the NO airglow at 00 LT using the atmospheric conditions from run 2 of the LMD-MGCM. The color bar is the intensity in kR. b) Global distribution of the peak altitude of the NO airglow at 00 LT. The color bar is the peak altitude in km.

The distribution of the peak altitude demonstrates a strong variability, with values ranging from 40 to 130 km. From Figure 14.6b, we observe that within the latitudinal band 60–90°, the lowest altitudes of the peak brightness are localised around the solstices, i.e., L_S=90 and 270°, contrary to the peak brightness that is found around the equinoxes. The peak altitude increases from a solstice to the next equinox, and then decreases toward the following solstice. The highest peak altitudes are found in the summer hemispheres over mid-latitudes, with the maximum values during the southern summer.

Detections of NO airglow signal with the SPICAM instrument are biased towards the winter night in the Southern hemisphere. Given the model simulations, we expect more

intense emission in this region during the polar winter, so that may explain the higher density of observations. The emission intensity in the observations at these latitudes and this time is a few kR, which is consistent with the model predictions. However, the SPICAM measurements over the tropical region, i.e., latitudes -30° to 30°, gives larger intensity values than predicted by the model by about one order of magnitude (see Figure 14.2). Since measurements are subject to localised dynamical variations, strong horizontal transport at the time of these observations would enhance the abundance of N and O atoms in this region. As for the peak altitude, the observational values are lower, between 50 and 100 km, over the South polar region around the winter night, while they are higher, between 90 and 130 km, in the tropical region, i.e., -30° to 30° (see Figure 14.3). This tendency is consistent with the model predictions. However, the derived peak altitudes from the measurements seem to generally be higher than in the model, especially over the equatorial region by 10 to 20 km.

The difference between the retrieval results and the model simulations could either be due to the accuracy of the calibration of the raw signal or could be linked to the circulation regime in the model, if it diverges from that of the conditions during which the measurements were taken. Some assumptions are made in the method presented here that could affect the quality of NO signal retrieval:

- there are no other emissions than that of NO present;
- the ratio of intensities between NO($C^2\Pi$) and NO($A^2\Sigma$) does not change with temperature;
- the reference spectrum used was extracted from a selected limb observation from SPICAM, another one could be produced that might show variations in the spectral features;
- after the preliminary filtering of the raw signal to extract the DC and the star signal, no other source of contaminations or errors are considered, like the scintillation of

the star in the LOS;

- the CCD sensitivity, or efficient area, and the DC are expected to vary slightly with time.

We reiterate that GCMs provide a climatological average of atmospheric conditions while observations are singular values subject to localised spatial and temporal variations. Larger intensities suggest a greater density of the emitting constituents, for instance atomic oxygen and atomic nitrogen. Higher altitudes of the maximum emission could be an indication of a weaker downward vertical transport over this region than in the model, hence the recombination occurs higher in the atmosphere.

14.3 Summary

The preliminary results of retrieving the NO airglow from the first year of SPICAM stellar occultations are consistent with the available measurements and with simulations using a 3-D model. In general, we find consistency between the results from the processing of the SPICAM stellar occultations presented in this thesis and the analysis of the SPICAM limb observations by Cox et al. (2008). We emphasize that our dataset contains three times as many observations as the latter work, and our measurements extend above 60° latitude, as well as covering a much broader seasonal range. Overall, this analysis of the first year of SPICAM observations of NO airglow expands the existing observations from Cox et al. (2008).

Similarly, the comparison of the observations with the LMD-MGCM model predictions is encouraging. There is a coherence between the time and location of the presence of NO airglow in both datasets, and the range of peak brightness and peak altitude values are consistent. The number of measurements used to validate the method may be insufficient to verify that the model is behaving optimally. Hence, we plan to process the remaining dataset of SPICAM observations, up to orbit # 10,000, in the stellar oc-

cultation mode to achieve a more complete climatology of the NO emission in the Mars atmosphere. It would provide a more robust dataset for model simulation comparisons.

Our retrievals of the NO emission yield higher peak brightness and peak altitude values in the equatorial region than obtained from LMD-MGCM simulations. This problem could be solved by re-evaluating the accuracy of the calibration of the raw signal, by improving the retrieval algorithm, and by obtaining realistic atmospheric conditions, e.g., meteorological phenomena, winds, etc., to use in the airglow model, i.e., data assimilation, which is not currently implementable given the small number of data available. Another possible cause for these differences could be that the source of the NO emission is particle precipitation, which is absent from the model. This effect could be studied by investigating the correlation between the solar flux and the intensity of the NO airglow, since there are more O and N atoms produced on the dayside when the solar activity is more intense. The frequency of observations with respect to the solar flux variations is a good indicator of the dependence of an emission on particle precipitation events. This analysis is beyond the scope of this thesis but remains a potential topic for future work.

Chapter 15

Conclusions

The dependence of spectral features on temperature is due to molecular properties. From a molecular spectroscopy perspective, vibrations and rotations of molecules yield a rotational and vibrational temperature when the system is in thermal equilibrium. In a gas medium, if enough collisions occur, the temperature of the gas would be equal to the temperature of the rotational and/or vibrational temperature, we say that such molecules are thermalised. This concept can be applied to a planetary atmosphere at an altitude region where metastable excited molecules are present and would have sufficient time to vibrate or rotate at the atmospheric temperature before de-excitation occurs. In the atmosphere of Mars and Venus, the temperature throughout the aerobraking region is strongly affected by the atomic oxygen density distribution. Conveniently, airglow from O_2 emissions dominates at these altitudes and can therefore be monitored to derive the temperature. Additionally, knowledge of the photochemical mechanism producing these emissions enables the retrieval of the vertical distribution of atomic oxygen.

Modeling of airglow features has proven to be a clever approach to test the temperature effect on spectral features. In the atmospheres of Mars and Venus, the nighttime visible spectrum is dominated by signatures from O_2 and NO emissions. Studying these two emissions using a modeling approach, combined with measurements from the Mars and

Venus atmospheres, was a means to better understanding the temperature and atomic oxygen distributions that characterize both atmospheres. By investigating more than one emission, we covered a greater altitude range, providing better constraints on the atomic oxygen density distribution. Ultimately, this should yield a deeper understanding of the thermal structure in these CO_2-dominated atmospheres by improving the oxygen photochemistry in GCMs.

This chapter is a general conclusion to the work presented in this thesis. Section 15.1 gives a summary of the results from the O_2 airglow simulations in both Mars and Venus atmospheres and discusses the similarities and differences between these. Section 15.2 discusses the importance of the results from the NO airglow retrievals of the SPICAM stellar occultation dataset, as well as the importance of the method for building a climatology of the NO airglow in the Mars atmosphere. Then, Sections 15.3 and 15.4 conclude the thesis with a discussion about the perspective of this research and suggestions for future work.

15.1 Summary of O_2 airglow model simulations

In Part II, we have investigated the global distribution of the emission profile and integrated intensity of four emissions of O_2 airglow in CO_2-dominated atmospheres: the Herzberg I and II, the Chamberlain, and the IR Atmospheric occurring from the UV to the IR spectral region. This comparative study between O_2 airglow in the Mars and Venus atmospheres is important as it adds to the consistency of the oxygen photochemical scheme proposed for CO_2-dominated atmospheres.

15.1.1 Major results

From the results presented for the Herzberg I band emission in the atmospheres of Mars and Venus, we concluded that using the quenching rate by CO_2 measured in the lab-

oratory by Kenner and Ogryzlo (1983b) would yield an overestimation of the emission from the Herzberg I band and this rate coefficient should be reduced by one order of magnitude to match the observations.

In the simulations of the Herzberg II transition, a rate coefficient for quenching by CO_2 that is two orders of magnitude smaller than the one measured in the laboratory by Kenner and Ogryzlo (1983a) produces a profile with a peak emission altitude that best reproduces the observations in both planets' atmospheres, that is between 95 to 100 km. Moreover, even with a relatively small yield of 0.02, the production of the excited state from the three-body recombination is sufficient to yield the expected emission intensity of a few kR.

As for the Chamberlain band emission, only a rough estimate of the integrated intensity could be calculated because of the lack of knowledge of the kinetics parameters related to the upper state of this transition, $A'^3\Delta_u$. The obtained intensity distribution is similar to that of the Herzberg II band, but with weaker intensity values.

For the IR Atmospheric nightglow emission, the analysis of the different quenching rate coefficients by CO_2 is less conclusive because of the high radiative efficiency of the excited state. In fact, in the Venus atmosphere at the altitude of the O_2 airglow layer, the loss of the excited state through radiative decay dominates over its collisional removal by CO_2. However, we share the opinion of the cited authors, in using a high recombination yield for the production of the excited following the recombination reaction (Gérard et al., 2008b; Krasnopolsky, 2011), to reproduce the intensity observed.

A feature of our model simulations is the frequent occurrence of structures in the vertical distribution of the emissions studied here. On Earth, frequent occurrences of double-layer structures in airglow have been reported by Melo et al. (2000) and further studied in models. Double-peaked vertical profiles of airglow emissions have been observed on Mars by CRISM (Clancy et al., 2011a,b, 2012) and on Venus by VIRTIS (Piccioni et al., 2009). This model study strengthens the argument for using 3-D mod-

els to provide dynamical variations for representing realistic simulations of the vertical structure and global distribution of airglow features.

15.1.2 Outcomes

Our study demonstrates that the set of kinetic parameters chosen to reproduce the observations is not the only factor to be taken into account when comparing simulations with measurements. The characteristics of the airglow layer depend quite significantly on the background atmosphere and therefore meaningful comparisons require a 3-D model that accounts for dynamical variations. As expected, the molecular oxygen emissions are directly affected by variations in the vertical structure of the temperature and O_x species concentration. In general, current GCMs have deficiencies due to a misrepresentation of the atomic oxygen distribution.

To improve airglow modeling, and therefore to improve the reliability of using airglow as a proxy for atomic oxygen density and temperature profiles, laboratory measurements are required to quantify the kinetics of the reaction chain that produces the O_2 airglow. Alternatively, an instrument that could measure the VER of these emissions simultaneously with some precision, i.e., within an error margin of 10%, could allow for a clear identification of the physical chemistry processes. In particular, knowledge of the quenching rates of the excited states of O_2 by CO_2 is needed. Further, we need a better description of the recombination reaction of O in a CO_2 atmosphere at low temperatures and the determination of the pathways from collisional removal of the excited O_2 molecules with CO_2 and CO.

Much information has been gained about oxygen photochemistry in a CO_2-dominated atmosphere by the recent availability of airglow measurements for both Mars and Venus. We believe that more precision on the intensity and VER estimates can be gained by absolutely calibrated measurements of oxygen airglow covering both the visible and IR spectral regions on Mars and Venus for nighttime conditions.

In conclusion, we advise that in order to use airglow measurements together with models to constrain any given value of the kinetic constants for the reactions, and in an effort to overcome the lack of laboratory measurements, we need a 3-D representation of the atmosphere to provide dynamics and global patterns. Although photochemical models are useful for local in-depth studies, relying on this type of model to reproduce airglow observations is not recommended since these models limit the dynamical variations and may not capture the actual distribution of constituents. Indeed, 3-D models provide dynamical variations for representing realistic simulations of the vertical structure and global distribution of airglow features. Furthermore, another modeling improvement would be to combine kinetic and/or fluid approaches, as is done in 1-D photochemical modeling studies, with 3-D GCMs as inputs, hence bridging the gap between these two methods.

15.2 Summary of NO airglow retrievals

Part III presented a new methodology for studying the NO airglow measurements in the Mars atmosphere provided by the SPICAM instrument on board MEx. The stellar occultation technique provides many advantages; among the most important are an absolute calibration of the signal and resolution of the vertical information. Another important aspect of this method that is different from the retrieval algorithms previously used for this type of measurement is that it does not require any assumption about the vertical structure while still enables to extract the vertical distribution. This new technique yields an image that is the brightness of the NO layer in its spatial perspective at the time of observation.

15.2.1 Major Results

To test the validity of the algorithm developed to retrieve useful NO airglow information, we processed the first year of SPICAM observations. The results obtained are promising and indicate an acceptable level of reliability of the method and its usefulness in providing meaningful information about the nighttime photochemistry in the Mars atmosphere. Hence, the study of NO emissions in the Martian atmosphere provides one more source of information into the links between Martian photochemical processes and dynamics.

The average peak brightness of the detected NO emissions and the corresponding average peak altitude is in agreement with previous measurements. Our results were also compared with model simulations to assess the distribution of the nitrogen (N) and oxygen (O) atoms in the model. We attributed the discrepancy between the observations and the model simulations to the short lifetime of the NO emission that renders it susceptible to localised variations in N and O amounts.

15.2.2 Outcomes

The NO emissions serve to trace the descending branch of the circulation in the Mars and Venus atmospheres. NO airglow is particularly valuable for constraining the Venus thermospheric circulation in the absence of direct wind measurements (Gérard et al., 2008a, 2009a). The intensity of the NO brightness is proportional to the dayside column of N atoms. The average distribution map of NO nightglow can be viewed as an approximate map of the downward flux of N atoms being supplied from the dayside.

Since the NO emissions occur well below the nightside homopause, processes other than molecular diffusion, e.g., large scale winds and/or eddy mixing, must play a role in the vertical transport (Gérard et al., 1981; Bougher et al., 1990). Indeed, the strength of vertical mixing affects the altitude at which the O and N density profiles have their maxima and the altitude of the maximum VER. The resulting NO nightglow depends

on the accuracy and stability of the parametrized net dayside production of O(^{3}P) and N(^{4}S), the strength and distribution of the global circulation, and the nightside chemical sinks and eddy mixing. The observed nightglow places constraints on the thermospheric global circulation and eddy mixing, the mean state of the densities and the temperature, and the dayside production of atomic nitrogen and oxygen available for transport.

15.3 Perspective

The perspective that this thesis aimed to bring was a better understanding of the oxygen-related emissions in CO_2-dominated atmospheres. To achieve this task, we considered two avenues: (1) 3-D model simulations of airglow emissions in two CO_2-dominated atmospheres: Mars and Venus, and (2) development of a data processing methodology to recover 3-D airglow fields from the SPICAM instrument on board the Mars Express mission.

Part II treated the development of an airglow model for O_2 transitions that input atmospheric conditions to perform simulations of the volume emission rate and integrated intensity. A sensitivity study of the photochemical parameters was performed to improve the photochemical scheme currently assumed to produce these transitions. Moreover, 3-D GCMs of the Mars and Venus atmospheres were used to provide composition fields as inputs to the airglow model, which brought dynamical variations into the airglow results. The impacts of changes induced by dynamics on the temperature, dust, and water distributions on the airglow characteristics were investigated.

In part III, we described a newly-developed method to retrieve the observations of NO nightglow with SPICAM-UV in the stellar occultation mode without slit. We showed results from one year of NO retrievals to demonstrate the usefulness of the method developed. These results show some agreement with the limited dataset of previous observations. By processing one year of SPICAM observations with this algorithm, we

were able to characterize the latitudinal and seasonal tendencies of the NO emissions in the Mars atmosphere.

Overall, this work has improved the representation of oxygen photochemistry in CO_2-dominated atmospheres, thereby contributing to more reliable measurements and model forecasts of temperature in the future.

15.4 Outlook

The airglow model developed in this work could potentially provide the basis for the development of an instrument that would measure the desired O_2 and NO emissions and from which temperature and atomic oxygen density profiles could be derived. For example, we could exploit the temperature dependence of the rotational structure of the O_2 emissions and hence use the rotational temperature as a diagnostic for the atmospheric temperatures. Similarly, we could use the airglow model to calibrate a spectrum with a pre-defined temperature and compare with measurements to infer the temperature distribution at the altitude of the airglow layer. Using airglow to infer atmospheric properties is a cost-effective technique, since relatively simple photometers could be used to measure the selected emission rates. Therefore, the use of airglow to derive a temperature profile is attractive for a planetary mission. The focus of the airglow investigation presented in this work is the UV and visible spectral region because of an instrumental advantage: this spectral region requires a simpler optical design of the instrument, reducing cost and weight and hence making it easier to accommodate to any payload. However, the use of the visible spectral region has not been exploited yet.

The inversion algorithm developed to retrieve NO airglow from the SPICAM stellar occultation dataset could be used to process the remaining dataset, up to orbit # 10,000, to achieve a more complete climatology of the NO emission in the Mars atmosphere. Alternatively, this NO data processing technique developed for the SPICAM instrument

could be used in the same way with SPICAV data to build a climatology of the NO emission in the Venus atmosphere.

Appendix A

Abbreviations used in the thesis

ADU	Analog-to-Digital Unit
A/D	Analog-to-Digital converter
AU	Astronomical Unit
CCD	Charged Coupled Device
CNRS	Centre National de la Recherche Scientifique
CRISM	Compact Reconnaissance Imaging Spectrometer for Mars
DC	Dark Current
DCNU	Dark Current Non Uniformity
DPU	Data Processing Unit
EPF	Emission Phase Function
EUV	Extreme Ultraviolet
FOV	Field Of View
FWHM	Full Width at Half Maximum
G	Gain
GCM	Global Circulation Model
HT	Haute Tension
HWHM	Half Width at Half Maximum
IAU	International Astronomical Union
IR	Infrared
IUE	International Ultraviolet Explorer
L_S	Areocentric Longitude

LATMOS	Laboratoire Atmosphères, Milieux, Observations Spatiales
LMD	Laboratoire de Météorologie Dynamique
LT	Local Time
LTE	Local Thermodynamic Equilibrium
LOS	Line Of Sight
MCS	Mars Climate Sounder
MEx	Mars Express
MGCM	Mars Global Circulation Model
MGS	Mars Global Surveyor
MME	Mars Mean Equator
MNP	Mars Nearest Point
MOLA	Mars Orbiter Laser Altimeter
MRO	Mars Reconnaissance Orbiter
MY	Martial Year
OMEGA	Observatoire pour la Minéralogie, l'Eau, les Glaces et l'Activité
PVO	Pioneer Venus Orbiter
R	Rayleigh
REMPI	Resonance Enhanced Multi-Photon Ionization
RSZ	Retrograde Superrotating Zonal
SPICAM	Spectroscopy for the Investigation of the Characteristics of the Atmosphere of Mars
SPICAV	Spectroscopy for the Investigation of the Characteristics of the Atmosphere of Venus
S/N	Signal-to-Noise ratio
SSAS	SubSolar to AntiSolar
SZA	Solar Zenith Angle
TES	Thermal Emission Spectrometer
UV	Ultraviolet
VER	Volume Emission Rate
VeRa	Venus Express Radio Science
VEx	Venus Express
VIRTIS	Visible and InfraRed Thermal Imaging Spectrometer
VTGCM	Venus Thermospheric Global Circulation Model

Appendix B

Table of retrieved NO airglow detection from the SPICAM stellar occultation dataset

Table B.1: Characteristics of the SPICAM stellar occultation sequences with detected NO airglow

orbit #	band #	L_S (°)	lat (°)	LT (hr)	I (kR)	z_{peak}(km)
0588A02	1	56.8	-74.3	22.2	4.4	88.1
0588A02	2	56.8	-74.1	22.2	4.2	68.8
0588A02	3	56.8	-74.1	22.2	4.2	68.8
0588A02	4	56.8	-74.0	22.2	5.7	67.8
0588A02	5	56.8	-74.0	22.3	4.5	60.4
0647A02	1	64.0	-35.3	21.4	2.2	83.0
0647A02	2	64.0	-35.3	21.4	2.8	82.4
0647A02	4	64.0	-35.5	21.4	3.2	79.7
0647A02	5	64.0	-36.4	21.4	3.0	64.8
0647A03	1	64.0	-62.0	2.2	2.9	63.2
0647A03	2	64.0	-62.0	2.2	3.3	66.0
0647A03	3	64.0	-62.1	2.0	4.2	50.1

Table B.1:

orbit #	band #	L_S (°)	lat (°)	LT (hr)	I (kR)	z_{peak}(km)
0647A03	4	64.0	-62.1	2.0	4.6	50.1
0647A03	5	64.0	-62.0	2.1	3.1	60.9
0650A01	1	64.4	-35.2	21.3	1.5	78.6
0650A01	2	64.4	-34.7	21.3	1.8	85.8
0650A02	1	64.4	-62.1	2.0	2.6	54.5
0650A02	2	64.4	-62.0	2.2	3.5	72.9
0650A02	3	64.4	-62.1	2.0	3.0	56.9
0650A02	4	64.4	-62.1	2.0	3.4	56.9
0650A02	5	64.4	-62.0	2.1	2.9	63.7
0658A01	1	65.4	-41.4	20.0	1.9	61.7
0659A03	2	65.5	-77.4	6.4	9.0	44.1
0659A03	4	65.5	-77.4	6.4	4.7	85.1
0659A03	5	65.5	-77.4	6.4	4.1	78.3
0666A01	1	66.3	-77.3	6.3	5.2	52.3
0666A01	4	66.3	-77.3	6.3	3.8	83.6
0666A01	5	66.3	-77.3	6.3	3.8	73.3
0673A03	1	67.2	-77.3	6.2	3.3	105.0
0673A03	2	67.2	-77.3	6.2	6.6	47.0
0673A03	4	67.2	-77.3	6.2	3.8	77.5
0673A03	5	67.2	-77.3	6.2	3.9	76.0
0675A01	1	67.4	-50.2	19.8	3.0	68.8
0675A01	2	67.4	-50.3	19.8	2.8	85.2
0675A01	3	67.4	-50.3	19.8	2.4	75.5
0675A01	4	67.4	-50.3	19.8	3.3	75.5
0675A01	5	67.4	-50.2	19.8	2.7	55.0
0678A01	1	67.8	-75.6	21.0	3.4	67.6
0678A01	2	67.8	-75.7	21.0	3.3	81.7
0678A01	3	67.8	-75.6	21.0	4.6	59.8
0678A01	4	67.8	-75.6	21.0	4.8	59.8
0678A01	5	67.8	-75.6	21.1	3.2	56.0

Table B.1:

orbit #	band #	L_S (°)	lat (°)	LT (hr)	I (kR)	z_{peak}(km)
0691A01	1	69.4	-49.4	19.3	2.0	92.9
0691A01	2	69.4	-49.4	19.3	2.5	68.3
0691A01	3	69.4	-49.4	19.3	2.4	72.6
0691A01	4	69.4	-49.4	19.3	3.4	72.6
0691A01	5	69.4	-49.4	19.3	2.0	68.3
0714A01	2	72.2	-75.6	7.3	4.1	102.8
0714A01	3	72.2	-75.6	7.3	4.1	102.8
0714A01	4	72.2	-75.6	7.3	5.2	98.8
0714A01	5	72.2	-75.6	7.3	3.2	100.6
0718A01	2	72.7	-75.7	7.3	4.5	86.1
0718A01	3	72.7	-75.7	7.3	3.7	48.1
0718A01	4	72.7	-75.7	7.3	4.4	93.9
0718A01	5	72.7	-75.7	7.3	3.9	75.7
0735A01	1	74.8	-42.2	18.9	1.8	85.1
0735A01	2	74.8	-42.2	19.0	2.1	63.0
0735A01	3	74.8	-42.3	18.9	3.9	126.9
0735A01	4	74.8	-42.2	18.9	2.8	67.0
0735A01	5	74.8	-42.1	19.0	2.1	45.2
0745A03	1	76.0	-75.7	6.9	19.5	47.3
0745A03	2	76.0	-75.7	6.9	3.9	114.3
0746A01	4	76.1	-75.7	6.8	5.2	117.5
0746A01	5	76.1	-75.7	6.9	2.8	84.2
0884A01	1	93.1	-68.4	1.6	3.5	124.8
0884A01	5	93.1	-68.2	1.5	2.2	73.2
0887A02	2	93.5	-75.1	3.8	3.0	125.9
0887A02	4	93.5	-75.1	3.8	3.4	115.3
0887A02	5	93.5	-75.1	3.8	2.5	88.0
0890A01	2	93.9	-75.0	3.7	3.6	107.7
0890A01	3	93.9	-75.0	3.7	7.4	129.3
0890A01	4	93.9	-75.0	3.7	3.4	73.5

Table B.1:

orbit #	band #	L_S (°)	lat (°)	LT (hr)	I (kR)	z_{peak}(km)
0893A01	1	94.2	-67.3	1.3	1.9	54.3
0893A01	4	94.2	-67.3	1.3	2.3	59.1
0893A01	5	94.2	-67.5	1.4	2.1	103.2
0897A02	1	94.7	-66.9	1.3	2.3	58.5
0897A02	2	94.7	-66.8	1.2	4.3	45.7
0897A02	4	94.7	-67.0	1.3	2.5	89.9
0904A01	1	95.6	-76.9	18.5	1.3	48.4
0904A01	2	95.6	-77.0	18.4	2.2	80.5
0904A01	3	95.6	-77.0	18.4	1.9	85.4
0908A02	1	96.1	-65.9	1.0	2.6	67.1
0908A02	4	96.1	-66.0	1.1	2.6	100.0
0908A02	5	96.1	-65.9	1.0	2.0	78.2
0919A01	1	97.5	-82.2	0.2	3.8	74.9
0919A01	2	97.5	-82.1	0.2	4.0	63.4
0919A01	5	97.5	-82.2	0.2	3.2	77.6
0921A01	5	97.7	-64.4	0.8	1.4	40.7
0922A01	2	97.9	-64.5	0.8	3.9	76.3
0922A01	4	97.9	-64.8	0.8	2.1	121.7
0922A01	5	97.9	-64.6	0.8	1.7	88.5
0926A02	1	98.4	-73.8	2.7	2.3	48.1
0926A02	3	98.4	-73.9	2.7	3.9	129.6
0926A02	4	98.4	-73.8	2.7	3.1	80.6
0929A01	4	98.7	-63.9	0.7	2.0	87.4
0929A01	5	98.7	-64.0	0.7	2.8	112.2
0932A01	2	99.1	-82.6	0.2	1.1	69.6
0932A01	3	99.1	-82.6	0.2	1.0	72.6
0936A01	1	99.6	-62.9	0.5	1.9	54.2
0936A01	4	99.6	-63.0	0.5	2.1	70.5
0936A01	5	99.6	-62.9	0.5	1.6	51.0
0985A02	1	105.7	-82.8	23.9	1.2	88.7

Table B.1:

orbit #	band #	L_S (°)	lat (°)	LT (hr)	I (kR)	z_{peak}(km)
0985A02	2	105.7	-82.8	23.9	1.2	101.5
0985A02	3	105.7	-82.7	23.9	1.1	79.2
0985A02	4	105.7	-82.8	23.9	1.3	98.4
0985A02	1	105.7	-82.8	23.9	1.3	98.4
0995A01	1	107.0	-83.0	23.8	0.9	82.5
0995A01	5	107.0	-82.9	23.8	1.0	50.8
1005A02	1	108.3	-82.8	23.7	1.5	40.7
1005A02	1	108.3	-82.8	23.7	1.5	40.7
1025A02	3	110.8	-83.1	23.6	1.3	106.0
1027A02	1	111.1	-83.0	23.6	1.1	43.2
1027A02	2	111.1	-83.0	23.6	1.5	40.3
1031A02	2	111.6	-83.1	23.6	1.5	64.8
1031A02	4	111.6	-83.2	23.6	1.4	106.6
1031A02	5	111.6	-83.2	23.6	1.1	113.0
1042A02	1	113.0	-83.3	23.5	1.3	40.0
1042A02	4	113.0	-83.3	23.5	1.4	53.3
1042A02	5	113.0	-83.3	23.5	1.0	43.7
1044A01	1	113.3	-83.2	23.5	1.0	49.6
1044A01	2	113.3	-83.2	23.5	1.4	59.6
1044A01	3	113.3	-83.2	23.5	1.2	59.6
1061A01	2	115.5	-83.3	23.4	1.5	86.8
1061A01	3	115.5	-83.3	23.4	1.5	86.8
1061A01	5	115.5	-83.3	23.4	1.0	83.8
1064A02	1	115.9	-83.4	23.4	1.3	107.8
1064A02	4	115.9	-83.4	23.4	1.6	77.9
1191A01	1	132.7	-45.5	0.8	2.6	100.3
1191A01	2	132.7	-45.5	0.8	4.3	113.9
1285A01	1	145.7	-32.5	0.2	2.1	105.1
1285A01	5	145.7	-32.5	0.2	1.9	49.2
1361A01	1	156.6	-15.4	23.6	2.5	109.1

Table B.1:

orbit #	band #	L_S (°)	lat (°)	LT (hr)	I (kR)	z_{peak}(km)
1372A01	1	158.2	-15.3	23.4	2.8	123.6
1384A01	2	160.0	-64.7	23.3	2.9	95.2
1384A01	3	160.0	-64.7	23.3	2.4	92.7
1388A02	2	160.6	-64.7	23.2	3.0	79.5
1539A01	5	183.9	14.5	22.6	4.9	115.7
1551A01	1	185.8	2.2	22.1	1.8	80.2
1551A01	3	185.8	2.2	22.1	1.9	70.9
1551A01	5	185.8	2.2	22.1	1.7	80.2
1640A01	1	200.4	-14.6	20.5	6.6	89.8
1640A01	2	200.4	-14.6	20.5	5.3	86.5
1640A01	3	200.4	-14.6	20.5	5.2	77.2
1640A01	5	200.4	-14.6	20.5	5.7	64.7
1784A01	1	225.0	50.0	20.3	2.3	70.1
1784A01	5	225.0	50.0	20.4	2.1	40.8
1896A02	2	244.8	46.5	23.6	2.7	115.7
1896A02	3	244.8	46.6	23.6	4.4	120.8
1927A02	3	250.3	-21.8	2.5	3.8	124.1
1927A02	4	250.3	-21.8	2.5	4.5	124.1
1987A02	2	260.9	-1.5	3.6	2.6	55.5
1988A02	1	261.1	48.0	19.4	2.7	128.5
2070A02	1	275.6	-1.4	2.3	2.2	128.5
2070A02	2	275.6	-1.4	2.3	2.7	82.1
2070A02	4	275.6	-1.4	2.3	2.9	104.3
2070A02	5	275.6	-1.4	2.3	2.6	94.4
2138A02	2	287.4	-1.3	1.2	2.1	128.5
2138A02	4	287.4	-1.2	1.2	2.7	117.5
2138A02	5	287.4	-1.2	1.2	2.3	100.3
2251A02	1	306.4	64.1	2.8	1.6	75.7
2251A02	2	306.4	64.1	2.8	3.1	72.2
2251A02	3	306.4	64.1	2.8	5.4	69.9

Table B.1:

orbit #	band #	L_S (°)	lat (°)	LT (hr)	I (kR)	z_{peak}(km)
2251A02	4	306.4	64.1	2.8	3.2	69.9
2251A02	5	306.4	64.2	2.8	2.1	117.1
2847A01	1	32.4	-60.9	2.9	2.4	111.9
2847A01	5	32.4	-60.9	2.9	3.8	119.2

Bibliography

F. Altieri, L. Zasova, E. D'Aversa, G. Bellucci, F.G. Carrozzo, B. Gondet, and J.-P. Bibring. O_2 1.27-μm emission maps as derived from OMEGA/MEx data. *Icarus*, 204(2):499 – 511, 2009.

F. Altieri, A. Spiga, L. Zasova, G. Bellucci, and J-P. Bibring. Martian O_2 dayglow at 1.27 μm and atmospheric waves. volume 6, Nantes, France, 2011. EPSC-DPS Joint Meeting 2011.

M. Angelats i Coll, F. Forget, M. A. López-Valverde, and F. González-Galindo. The first Mars thermospheric general circulation model: The Martian atmosphere from the ground to 240 km. *Geophysical Research Letters*, 32(4):L04201, 2005. doi: 10.1029/2004GL021368.

R. M. Badger, A. C. Wright, and R. F. Whitlock. Absolute intensities of discrete and continuous absorption bands of oxygen gas at 1.26 and 1.065 μm and radiative lifetime of $^1\Delta_g$ state of oxygen. *Journal of Chemical Physics*, 43(12):4345–4350, 1965. ISSN 0021-9606.

J. Bailey, V. S. Meadows, S. Chamberlain, and D. Crisp. The temperature of the Venus mesosphere from O_2 ($a^1\Delta_g$) airglow observations. *Icarus*, 197(1):247–259, 2008.

P. M. Banks and G. Kockarts. *Aeronomy: Part A*. Academic Press Inc., 1973.

C. A. Barth and A. F. Hildebrandt. The 5577 Å airglow emission mechanism. *Journal of Geophysical Research*, 66(3):985–986, 1961.

C. A. Barth, J. B. Pearce, K. K. Kelly, L. Wallace, and W. G. Fastie. Ultraviolet emissions observed near Venus from Mariner V. *Science*, 158(3809):1675–1678, 1967.

C. A. Barth, C. W. Hord, J. B. Pearce, K. K. Kelly, G. P. Anderson, and A. I. Stewart. Mariner-6 and Mariner-7 Ultraviolet spectrometer experiment - Upper atmosphere data. *Journal of Geophysical Research*, 76(10):2213–2217, 1971.

C. A. Barth, A. L. Lane, A. I. Stewart, and C. W. Hord. Mariner-9 Ultraviolet experiment - Mars airglow spectroscopy and variations in Lyman alpha. *Icarus*, 17(2):457–468, 1972.

D. R. Bates. Excitation and quenching of the oxygen bands in the nightglow. *Planetary and Space Science*, 36(9):875–881, 1988.

D. R. Bates. Oxygen band system transition arrays. *Planetary and Space Science*, 37(7):881–887, 1989.

D. L. Baulch, D. D. Drysdale, J. Duxbury, and S. J. Grant. Evaluated kinetic data for high temperature reactions vol. 3: Homogeneous gas phase reactions of the O_2-O_3 system, the CO-O_2-H_2 system, and of sulfur-containing species. Technical report, 1976.

P. F. Bernath. *Spectra of atoms and molecules*. Oxford University Press, Inc., New York, NY, 2nd edition, 2005.

J.-L. Bertaux, F. Leblanc, S. V. Perrier, E. Quémerais, O. Korablev, E. Dimarellis, A. Reberac, F. Forget, P. C. Simon, S. A. Stern, B. Sandel, and SPICAM Team. Nightglow in the upper atmosphere of Mars and implications for atmospheric transport. *Science*, 307(5709):566–569, 2005.

J.-L. Bertaux, O. Korablev, S. Perrier, E. Quémerais, F. Montmessin, F. Leblanc, S. Lebonnois, P. Rannou, F. Lefèvre, F. Forget, A. Fedorova, E. Dimarellis, A. Reberac, D. Fonteyn, J.-Y. Chaufray, and S. Guibert. SPICAM on Mars Express: Observing modes and overview of UV spectrometer data and scientific results. *Journal of Geophysical Research-Planets*, 111:E10S90, 2006. doi: 10.1029/2006JE002690.

J.-L. Bertaux, B. Gondet, J.-P. Bibring, F. Montmessin, and F. Lefèvre. First detection of O_2 recombination nightglow emission at 1.27 μm in the atmosphere of Mars with OMEGA/MEX and comparison with model. Paris, France, 2011. Fourth International Mars Atmosphere Workshop: Modelling and Observations.

J.-L. Bertaux, B. Gondet, F. Lefèvre, J.-P. Bibring, and F. Montmessin. First detection of O_2 1.27 μm nightglow emission at Mars with OMEGA/MEX and comparison with general circulation model predictions. *Journal of Geophysical Research-Planets*, 117:E00J04, 2012. doi: 10.1029/2011JE003890.

S. W. Bougher and W. J. Borucki. Venus O_2 visible and IR nightglow - Implications for lower thermosphere dynamics and chemistry. *Journal of Geophysical Research-Planets*, 99(E2):3759–3776, 1994.

S. W. Bougher, R. E. Dickinson, E. C. Ridley, and R. G. Roble. Venus mesosphere and thermosphere .3. Three-dimensional general-circulation with coupled dynamics and composition. *Icarus*, 73(3):545–573, 1988.

S. W. Bougher, J. C. Gérard, A. I. F. Stewart, and C. G. Fesen. The Venus nitric oxide night airglow: Model calculations based on the Venus Thermospheric General Circulation Model. *Journal of Geophysical Research-Space Physics*, 95(A5):6271–6284, 1990.

S. W. Bougher, M. J. Alexander, and H. G. Mayr. *Venus II: Geology, geophysics, atmosphere, and solar wind environment*, chapter Upper atmosphere dynamics: Global circulation and gravity waves, pages 259–291. 1997.

S. W. Bougher, S. Engel, R. G. Roble, and B. Foster. Comparative terrestrial planet thermospheres 2. Solar cycle variation of global structure and winds at equinox. *Journal of Geophysical Research-Planets*, 104(E7):16591–16611, 1999.

S. W. Bougher, R. G. Roble, and T. Fuller-Rowell. Simulations of the upper atmospheres of the terrestrial planets. In Mendillo, M., Nagy, A., & Waite, J. H., editor, *Atmospheres in the solar system: Comparative aeronomy*, volume 130 of *Geophysical Monogragh*, pages 261–288. AGU, 2002.

S. W. Bougher, P.-L. Blelly, M. Combi, J. L. Fox, I. Mueller-Wodarg, A. Ridley, and R. G. Roble. Neutral upper atmosphere and ionosphere modeling. *Space Science Reviews*, 139(1-4):107–141, 2008. doi: 10.1007/s11214-008-9401-9.

A. S. Brecht, S. W. Bougher, J. C. Gerard, C. D. Parkinson, S. Rafkin, and B. Foster. Understanding the variability of nightside temperatures, NO UV and O_2 IR nightglow emissions in the Venus upper atmosphere. *Journal of Geophysical Research-Planets*, 116:E08004, 2011. doi: 10.1029/2010JE003770.

A.S. Brecht, S.W. Bougher, J.-C. Gérard, and L. Soret. Atomic oxygen distributions in the Venus thermosphere: Comparisons between Venus Express observations and global model simulations. *Icarus*, 217(2):759–766, 2012.

I. M. Campbell and C. N. Gray. Rate constants for $O(^3P)$ recombination and association with $N(^4S)$. *Chemical Physics Letters*, 18(4):607–609, 1973.

I. M. Campbell and B. A. Thrush. The association of oxygen atoms and their combination with nitrogen atoms. *Proceedings of the Royal Society of London Series A-Mathematical and Physical Sciences*, 296 (1445):222–232, 1967.

R. T. Clancy, B. J. Sandor, M. J. Wolff, P. R. Christensen, M. D. Smith, J. C. Pearl, B. J. Conrath, and R. J. Wilson. An intercomparison of ground-based millimeter, MGS TES, and Viking atmospheric temperature measurements: Seasonal and interannual variability of temperatures and dust loading in the global Mars atmosphere. *Journal of Geophysical Research-Planets*, 105(E4):9553–9571, 2000.

R. T. Clancy, M. Wolff, M. Smith, B. Cantor, and F. Lefèvre. MRO CRISM and MARCI observations of Mars ozone. Paris, France, 2011a. Fourth International Mars Atmosphere Workshop: Modelling and Observations.

R. T. Clancy, B. J. Sandor, M. Wolff, M. Smith, F. Lefèvre , J.-B. Madeleine, F. Forget, S. Murchie, F. Seelos, K. Seelos, H. Nair, A. Toigo, D. Humm, D. Kass, A. Kleinböhl, and N. Heavens. Extensive MRO CRISM observations of 1.27 μm O_2 singlet delta airglow in Mars polar night and their comparison to MRO MCS temperature profiles and LMD GCM simulations. *Journal of Geophysical Research-Planets*, 117:E00J10, 2012. doi: 10.1029/2011JE004018.

R.T. Clancy, M. Wolff, M. Smith, T. McConnochie, F. Lefèvre, Scott Murchie, and CRISM Operations Team. CRISM limb observations of Mars dayside O_2 singlet delta emission during 2010-2011. volume 6, Nantes, France, 2011b. EPSC-DPS Joint Meeting 2011.

P. Connes, J. F. Noxon, W. A. Traub, and N. P. Carleton. $O_2(^1\Delta)$ emission in the day and night airglow of Venus. *Astrophysical Journal*, 233(1):L29–L32, 1979.

B. J. Conrath, J. C. Pearl, M. D. Smith, W. C. Maguire, P. R. Christensen, S. Dason, and M. S. Kaelberer. Mars Global Surveyor Thermal Emission Spectrometer (TES) observations: Atmospheric temperatures during aerobraking and science phasing. *Journal of Geophysical Research-Planets*, 105 (E4):9509–9519, 2000.

R. A. Copeland. Laser double-resonance study of the collisional removal of $O_2(A^3\Sigma_u^+, v{=}7)$ with O_2. *Journal of Chemical Physics*, 100(1):744–745, 1994.

R. A. Copeland, K. Knutsen, M. E. Onishi, and T. Yalcin. Collisional removal of $O_2(c^1\Sigma_u^-, v{=}9)$ by O_2, N_2, and He. *Journal of Chemical Physics*, 105(23):10349–10355, 1996.

C. Cox, A. Saglam, J.-C. Gérard, J.-L. Bertaux, F. González-Galindo, F. Leblanc, and A. Reberac. Distribution of the ultraviolet nitric oxide Martian night airglow: Observations from Mars Express and comparisons with a one-dimensional model. *Journal of Geophysical Research-Planets*, 113(E8): E08012, 2008. doi: 10.1029/2007JE003037.

C. Cox, J.-C. Gérard, B. Hubert, J.-L. Bertaux, and S. W. Bougher. Mars ultraviolet dayglow variability: SPICAM observations and comparison with airglow model. *Journal of Geophysical Research-Planets*, 115:E04010, 2010. doi: 10.1029/2009JE003504.

D. Crisp, V. S. Meadows, B. Bézard, C. deBergh, J. P. Maillard, and F. P. Mills. Ground-based near-infrared observations of the Venus nightside: 1.27-μm $O_2(a^1\Delta_g)$ airglow from the upper atmosphere. *Journal of Geophysical Research-Planets*, 101(E2):4577–4593, 1996.

A. Dalgarno, J. F. Babb, and Y. Sun. Radiative association in planetary-atmospheres. *Planetary and Space Science*, 40(2-3):243–246, 1992. doi: 10.1016/0032-0633(92)90062-S.

A. Farrel, T. Dunne, R. Novak, Y. Cabral, M. J. Mumma, and B. Bonev. Seasonal mapping of ozone in the middle atmosphere of Mars. *Bulletin of the American Astronomical Society*, 36:15, 2005.

A. A. Fedorova, O. I. Korablev, S. Perrier, J.-L. Bertaux, F. Lefèvre, and A. Rodin. Observation of O_2 1.27-μm dayglow by SPICAM IR: Seasonal distribution for the first Martian year of Mars Express. *Journal of Geophysical Research-Planets*, 111(E09S07):E09S07, 2006a. doi: 10.1029/2006JE002694.

A. A. Fedorova, O. I. Korablev, S. Perrier, J. L. Bertaux, F. Lefèvre, A. Rodin, and A. Kiselev. Exploration of Mars in the SPICAM-IR experiment onboard the Mars-Express spacecraft: 2. Nadir observations: Simultaneous observations of water vapor and O_2 glow in the Martian atmosphere. *Cosmic Research*, 44(4):294–304, 2006b.

A.A. Fedorova, S. Guslyakova, F.Lefèvre, J.-L. Bertaux, O. Korablev, F. Montmessin, A. Reberac, and B. Gondet. The O_2 nightglow in the Martian atmosphere by SPICAM onboard of Mars-Express. volume 6, Nantes, France, 2011. EPSC-DPS Joint Meeting 2011.

A.A. Fedorova, F. Lefèvre, S. Guslyakova, O. Korablev, J.-L. Bertaux, F. Montmessin, A. Reberac, and B. Gondet. The O_2 nightglow in the martian atmosphere by SPICAM onboard of Mars-Express. *Icarus*, 219(2):596–608, 2012.

P. D. Feldman, H. W. Moos, and J. T. Clarke. Identification of the UV nightglow from venus. *Nature*, 279(5710):221–222, 1979.

Paul D. Feldman and Peter Z. Takacs. Nitric oxide gamma and delta band emission at twilight. *Geophys Research Letters*, 1(4):169–171, 1974. doi: 10.1029/GL001i004p00169.

F. D. Findlay and D. R. Snelling. Collisional deactivation of $O_2(^1\Delta_g)$. *Journal of Chemical Physics*, 55 (2):545–551, 1971.

F. Forget, F. Hourdin, R. Fournier, C. Hourdin, O. Talagrand, M. Collins, S. R. Lewis, P. L. Read, and J. P. Huot. Improved general circulation models of the Martian atmosphere from the surface to above 80 km. *Journal of Geophysical Research-Planets*, 104(E10):24155–24175, 1999.

F. Forget, F. Montmessin, J. L. Bertaux, F. González-Galindo, B. Lebonnois, E. Quémerais, A. Reberac, E. Dimarellis, and M. A. López-Valverde. Density and temperatures of the upper Martian atmosphere measured by stellar occultations with Mars Express SPICAM. *Journal of Geophysical Research-Planets*, 114:E01004, 2009. doi: 10.1029/2008JE003086.

M.-E. Gagné, S. M. L. Melo, F. Lefèvre, F. González-Galindo, and K. Strong. Modeled O_2 airglow distribution in the Martian atmosphere. *Journal of Geophysical Research-Planets*, 117:E06005, 2012a. doi: 10.1029/2011JE003901.

M.-E. Gagné, S. M. L. Melo, S. W. Bougher, A. S. Brecht, and K. Strong. Modeled O_2 airglow distribution in the Venusian atmosphere. *Journal of Geophysical Research-Planets, in press*, 2012b. doi: 10.1029/2012JE004102.

M.-E. Gagné, S. M. L. Melo, J.-L. Bertaux, F. Montmessin, and K. Strong. Observations of NO nightglow with SPICAM in the stellar occultation mode without slit. *Geophysical Research Letters, in preparation*, 2012c.

A. García Muñoz, F. P. Mills, G. Piccioni, and P. Drossart. The near-infrared nitric oxide nightglow in the upper atmosphere of Venus. *Proceedings of the National Academy of Sciences of the United States of America*, 106(4):985–988, 2009a.

A. García Muñoz, F. P. Mills, T. G. Slanger, G. Piccioni, and P. Drossart. Visible and near-infrared nightglow of molecular oxygen in the atmosphere of Venus. *Journal of Geophysical Research-Planets*, 114:E12002, 2009b. doi: 10.1029/2009JE003447.

J.-C. Gérard, A. I. F. Stewart, and S. W. Bougher. The altitude distribution of the Venus ultraviolet nightglow and implications on vertical transport. *Geophysical Research Letters*, 8(6):633–636, 1981.

J.-C. Gérard, C. Cox, A. Saglam, J.-L. Bertaux, E. Villard, and C. Nehme. Limb observations of the ultraviolet nitric oxide nightglow with SPICAV on board Venus Express. *Journal of Geophysical Research-Planets*, 113:E00B03, 2008a. doi: 10.1029/2008JE003078.

J.-C. Gérard, B. Hubert, V. I. Shematovich, D. V. Bisikalo, and G. R. Gladstone. The Venus ultraviolet oxygen dayglow and aurora: Model comparison with observations. *Planetary and Space Science*, 56 (3-4):542–552, 2008b.

J.-C. Gérard, A. Saglam, G. Piccioni, P. Drossart, C. Cox, S. Erard, R. Hueso, and A. Sanchez-Lavega. Distribution of the O_2 infrared nightglow observed with VIRTIS on board Venus Express. *Geophysical Research Letters*, 35(2):L02207, 2008c. doi: 10.1029/2007GL032021.

J.-C. Gérard, C. Cox, L. Soret, A. Saglam, G. Piccioni, J.-L. Bertaux, and P. Drossart. Concurrent observations of the ultraviolet nitric oxide and infrared O_2 nightglow emissions with Venus Express. *Journal of Geophysical Research-Planets*, 114:E00B44, 2009a. doi: 10.1029/2009JE003371.

J.-C. Gérard, A. Saglam, G. Piccioni, P. Drossart, F. Montmessin, and J.-L. Bertaux. Atomic oxygen distribution in the Venus mesosphere from observations of O_2 infrared airglow by VIRTIS-Venus Express. *Icarus*, 199(2):264–272, 2009b.

J.-C. Gérard, L. Soret, A. Saglam, G. Piccioni, and P. Drossart. The distributions of the OH Meinel and $O_2(a^1\Delta\text{-}X^3\Sigma)$ nightglow emissions in the Venus mesosphere based on VIRTIS observations. *Advances in Space Research*, 45(10):1268–1275, 2010. doi: 10.1016/j.asr.2010.01.022.

J.-C. Gérard, L. Soret, G. Piccioni, and P. Drossart. Spatial correlation of OH Meinel and O_2 infrared atmospheric nightglow emissions observed with VIRTIS-M on board Venus Express. *Icarus*, 217(2): 813–817, 2012.

T. I. Gombosi. *Physics of the space environment*. Cambridge Atmospheric and Space Science Series. Cambridge University Press, Cambridge, UK, first paperback 2004 edition, 1998.

B. Gondet, J.-P. Bibring, J.-L. Bertaux, and F. Montmessin. O_2 nightglow emission detection in the atmosphere of Mars, identified by the OMEGA/MEx investigation. volume 12. EGU General Assembly 2010, 2010.

F. González-Galindo, M. A. López-Valverde, M. Angelats i Coll, and F. Forget. Extension of a Martian general circulation model to thermospheric altitudes: UV heating and photochemical models. *Journal of Geophysical Research-Planets*, 110:E09008, 2005. doi: 10.1029/2004JE002312.

F. González-Galindo, G. Gilli, M.A. López-Valverde, F. Forget, and F. Leblanc. Nitrogen and ionospheric chemistry in the thermospheric LMD-MGCM. Williamsburg, Virginia, 2008. Third International Workshop on The Mars Atmosphere: Modelling and Observations.

F. González-Galindo, F. Forget, M. A. López-Valverde, M. Angelats i Coll, and E. Millour. A ground-to-exosphere Martian general circulation model: 1. Seasonal, diurnal, and solar cycle variation of thermospheric temperatures. *Journal of Geophysical Research-Planets*, 114:E04001, 2009. doi: 10.1029/2008JE003277.

C. S. Haley, I. C. McDade, and S. M. L. Melo. An assessment of a method for recovering atomic oxygen density profiles from column integrated nightglow intensity measurements. pages 1147–1152, Warsaw, Poland, 2000. COSPAR 33^{rd} Scientific Assembly.

G. Herzberg. *Spectra of diatomic molecules*, volume I of *Molecular spectra and molecular structure*. D. Van Nostrand Company, Inc., 2nd edition, 1950.

J. M. Hollas. *Modern Spectroscopy*. John Wiley & Sons, Ltd, West Sussex, England, 2^{nd} edition, 1992.

N. Hoshino, H. Fujiwara, M. Takagi, Y. Takahashi, and Y. Kasaba. Characteristics of planetary-scale waves simulated by a new venusian mesosphere and thermosphere general circulation model. *Icarus*, 217(2):818–830, 2012.

R. Hueso, A. Sanchez-Lavega, G. Piccioni, P. Drossart, J.-C. Gérard, I. Khatuntsev, L. Zasova, and A. Migliorini. Morphology and dynamics of Venus oxygen airglow from Venus Express/Visible and Infrared Thermal Imaging Spectrometer observations. *Journal of Geophysical Research-Planets*, 113: E00B02, 2008. doi: 10.1029/2008JE003081.

D. L. Huestis, R. A. Copeland, K. Knutsen, T. G. Slanger, R. T. Jongma, M. G. H. Boogaarts, and G. Meijer. Branch intensities and oscillator-strengths for the Herzberg absorption systems in oxygen. *Canadian Journal of Physics*, 72(11-12):1109–1121, 1994.

D. L. Huestis, R. A. Copeland, and T. G. Slanger. Yields of O_2 electronic states in oxygen atom recombination. In *Fall Meet. Suppl.*, volume 81. EOS Trans. AGU, 2000. SA52A-09.

D. L. Huestis, S. W. Bougher, J. L. Fox, M. Galand, R. E. Johnson, J. I. Moses, and J. C. Pickering. Cross sections and reaction rates for comparative planetary aeronomy. In *Workshop on Comparative Aeronomy*, pages 63–105, Bern, Switzerland, 2007.

E. S. Hwang and R. A. Copeland. Temperature dependence of the collisional removal of $O_2(A^3\Sigma_u^+, v{=}9)$ with O_2 and N_2. *Geophysical Research Letters*, 24(6):643–646, 1997.

C. S. Jamieson, R. M. García, C. S. Jamieson, D. Pejaković, and K. Kalogerakis. The kinetics of oxygen atom recombination in the presence of carbon dioxide. In *Fall Meeting Suppl.*, volume 90. EOS Trans. AGU, 2009. P51D-1156.

R. D. Kenner and E. A. Ogryzlo. Deactivation of $O_2(A^3\Sigma_u^+)$ by O_2, O, and Ar. *International Journal of Chemical Kinetics*, 12(7):501–508, 1980.

R. D. Kenner and E. A. Ogryzlo. Quenching of $O_2(c^1\Sigma_u^-, v{=}0)$ by $O(^3P)$, $O_2(A^1\Delta_g)$, and other gases. *Canadian Journal of Chemistry*, 61(5):921–926, 1983a.

R. D. Kenner and E. A. Ogryzlo. Rate constant for the deactivation of $O_2(A^3\Sigma_u^+)$ by N_2. *Chemical Physics Letters*, 103(3):209–212, 1983b.

R. D. Kenner and E. A. Ogryzlo. Quenching of the $O_2(A, v{=}2\text{-}X, v{=}5)$ Herzberg-I band by $O_2(A)$ and O. *Canadian Journal of Physics*, 62(12):1599–1602, 1984.

R. D. Kenner, E. A. Ogryzlo, and S. Turley. Excitation of the night airglow of Earth, Venus and Mars. *Journal of Photochemistry*, 10(2):199–204, 1979.

K. Knutsen, M. J. Dyer, and R. A. Copeland. Laser double-resonance study of the collisional removal of $O_2(A^3\Sigma_u^+)$ v=6,7, and 9 with O_2, N_2, CO_2, Ar and He. *Journal of Chemical Physics*, 101(9): 7415–7422, 1994.

V. A. Krasnopolsky. Excitation of oxygen emissions in the night airglow of the terrestrial planets. *Planetary and Space Science*, 29(9):925–929, 1981.

V. A. Krasnopolsky. Oxygen emissions in the night airglow of the Earth, Venus and Mars. *Planetary and Space Science*, 34(6):511–518, 1986.

V. A. Krasnopolsky. Uniqueness of a solution of a steady-state photochemical problem - Applications to Mars. *Journal of Geophysical Research-Planets*, 100(E2):3263–3276, 1995.

V. A. Krasnopolsky. Mapping of Mars O_2 1.27-μm dayglow at four seasonal points. *Icarus*, 165(2): 315–325, 2003.

V. A. Krasnopolsky. Photochemistry of the Martian atmosphere: Seasonal, latitudinal, and diurnal variations. *Icarus*, 185(1):153–170, 2006a.

V. A. Krasnopolsky. A sensitive search for nitric oxide in the lower atmospheres of Venus and Mars: Detection on Venus and upper limit for Mars. *Icarus*, 182(1):80–91, 2006b.

V. A. Krasnopolsky. Long-term spectroscopic observations of Mars using IRTF/CSHELL: Mapping of O_2 dayglow, CO, and search for CH_4. *Icarus*, 190(1):93–102, 2007.

V. A. Krasnopolsky. Seasonal variations of photochemical tracers at low and middle latitudes on Mars: Observations and models. *Icarus*, 201(2):564–569, 2009.

V. A. Krasnopolsky. Venus night airglow: Ground-based detection of OH, observations of O_2 emissions, and photochemical model. *Icarus*, 207(1):17–27, 2010.

V. A. Krasnopolsky. Excitation of the oxygen nightglow on the terrestrial planets. *Planetary and Space Science*, 59(8):754–766, 2011.

V. A. Krasnopolsky and G. L. Bjoraker. Mapping of Mars $O_2(^1\Delta)$ dayglow. *Journal of Geophysical Research-Planets*, 105(E8):20179–20188, 2000.

V. A. Krasnopolsky and A. A. Krysko. On the night airglow of the Martian atmosphere. *Space Research*, 16:1005–1008, 1976.

V. A. Krasnopolsky and V. A. Parshev. *Photochemistry of the Venus atmosphere*. University of Arizona Press, 1983.

V. A. Krasnopolsky and G. V. Tomashova. Venus nightglow variations. *Cosmic Research*, 18:766, 1980.

V. A. Krasnopolsky, A. A. Krysko, V. N. Rogachev, and V. A. Parshev. Spectroscopy of the Venus night airglow from the Venera 9 and 10 orbiters. *Cosmic Research*, 14(5):789–795, 1976.

W. J. Lafferty, A. M. Solodov, C. L. Lugez, and G. T. Fraser. Rotational line strengths and self-pressure-broadening coefficients for the 1.27-μm, $a^1\Delta_g$-$X^3\Sigma_g^-$, v=0-0 band of O_2. *Applied Optics*, 37 (12):2264–2270, 1998.

G. M. Lawrence, C. A. Barth, and V. Argabright. Excitation of Venus night airglow. *Science*, 195(4278): 573–574, 1977.

F. Leblanc, J. Y. Chaufray, J. Lilensten, O. Witasse, and J. L. Bertaux. Martian dayglow as seen by the SPICAM UV spectrograph on Mars Express. *Journal of Geophysical Research-Planets*, 111(E9): E09S11, 2006. doi: 10.1029/2005JE002664.

F. Lefèvre, S. Lebonnois, F. Montmessin, and F. Forget. Three-dimensional modeling of ozone on Mars. *Journal of Geophysical Research-Planets*, 109(E7):E07004, 2004. doi: 10.1029/2004JE002268.

F. Lefèvre, J. L. Bertaux, R. T. Clancy, T. Encrenaz, K. Fast, F. Forget, S. Lebonnois, F. Montmessin, and S. Perrier. Heterogeneous chemistry in the atmosphere of Mars. *Nature*, 454(7207):971–975, 2008.

A. Leiss, U. Schurath, K. H. Becker, and E. H. Fink. Revised quenching rate constants for metastable oxygen molecules $O_2(a^1\Delta_g)$. *Journal of Photochemistry*, 8(3):211–214, 1978. doi: 10.1016/0047-2670(78)80021-5.

K. N. Liou. *An introduction to atmospheric radiation*, volume 84 of *International Geophysics Series*. Academic Press, San Diego, CA, 2^{nd} edition, 2002.

M. López-Puertas and M. A. López-Valverde. Radiative energy-balance of CO_2 non-LTE infrared emissions in the Martian atmosphere. *Icarus*, 114(1):113–129, 1995.

J. A. Magalhaes, J. T. Schofield, and A. Seiff. Results of the Mars Pathfinder atmospheric structure investigation. *Journal of Geophysical Research-Planets*, 104(E4):8943–8955, 1999.

D. McCleese and D. M. Kass. Results of the Mars climate investigations on the Mars Reconnaissance Orbiter. Number C31-0014-10, Bremen, Germany, 2010. 38^{th} COSPAR Scientific Assembly 2010, COSPAR.

D. J. McCleese, N. G. Heavens, J. T. Schofield, W. A. Abdou, J. L. Bandfield, S. B. Calcutt, P. G. J. Irwin, D. M. Kass, A. Kleinböhl, S. R. Lewis, D. A. Paige, P. L. Read, M. I. Richardson, J. H. Shirley, F. W. Taylor, N. Teanby, and R. W. Zurek. Structure and dynamics of the Martian lower and middle atmosphere as observed by the Mars Climate Sounder: Seasonal variations in zonal mean temperature, dust, and water ice aerosols. *Journal of Geophysical Research-Planets*, 115(E12):E12016, 2010. doi: 10.1029/2010JE003677.

T.L. McDunn, S.W. Bougher, J. Murphy, M.D. Smith, F. Forget, J.-L. Bertaux, and F. Montmessin. Simulating the density and thermal structure of the middle atmosphere (∼80-130 km) of Mars using the MGCM-MTGCM: A comparison with MEX/SPICAM observations. *Icarus*, 206(1):5–17, 2010.

A. B. Meinel. The spectrum of the airglow and the aurora. *Reports on Progress in Physics*, 14:121–146, 1951.

S. M. L. Melo, R. P. Lowe, and J. P. Russell. Double-peaked hydroxyl airglow profiles observed from WINDII/UARS. *Journal of Geophysical Research-Atmospheres*, 105(D10):12397–12403, 2000.

S. M. L. Melo, I. C. McDade, and H. Takahashi. Atomic oxygen density profiles from ground-based nightglow measurements at 23 degrees S. *Journal of Geophysical Research-Atmospheres*, 106(D14): 15377–15384, 2001.

Stella M. L. Melo, O. Chiu, A. García Muñoz, K. Strong, J. C. McConnell, T. G. Slanger, M. J. Taylor, R. P. Lowe, I. C. McDade, and D. L. Huestis. Using airglow measurements to observe gravity waves in the Martian atmosphere. *Advances in Space Research*, 38(4):730–738, 2006.

A. Migliorini, F. Altieri, L. Zasova, G. Piccioni, G. Bellucci, A. Cardesin Moinelo, P. Drossart, E. D'Aversa, F. G. Carrozzo, B. Gondet, and J.-P. Bibring. Oxygen airglow emission on Venus and Mars as seen by VIRTIS/VEX and OMEGA/MEX imaging spectrometers. *Planetary and Space Science*, 59(10, SI):981–987, 2011a. doi: 10.1016/j.pss.2010.05.019.

A. Migliorini, G. Piccioni, J.-C. Gérard, P. Drossart, and VIRTIS/Venus Express Team. The Venus visible oxygen nightglow with VIRTIS on board Venus Express. volume 6, Nantes, France, 2011b. EPSC-DPS Joint Meeting 2011.

A. Migliorini, T. G. Slanger, D. Saran, G. Piccioni, J.-C. Gérard, M. Snels, R. Politi, and P. Drossart. Nightglow investigation in the Visible Range with the VIRTIS/Venus-Express instrument. Number P13A-1648, San Francisco, USA, 2011c. AGU Fall Meeting 2011.

F. Montmessin, F. Forget, P. Rannou, M. Cabane, and R. M. Haberle. Origin and role of water ice clouds in the Martian water cycle as inferred from a general circulation model. *Journal of Geophysical Research-Planets*, 109(E10):E10004, 2004. doi: 10.1029/2004JE002284.

C. Mullen, E. Bolin, R. A. Copeland, and T. G. Slanger. Collisional removal of highly vibrational excited oxygen in the c state. In *Fall Meeting Suppl.*, volume 87. EOS Trans. AGU, 2006.

H. Nair, M. Allen, A. D. Anbar, Y. L. Yung, and R. T. Clancy. A photochemical model of the Martian atmosphere. *Icarus*, 111(1):124–150, 1994.

S. M. Newman, I. C. Lane, A. J. Orr-Ewing, D. A. Newnham, and J. Ballard. Integrated absorption intensity and Einstein coefficients for the O_2 $a^1\Delta_g$-$X^3\Sigma_g^-$ (0,0) transition: A comparison of cavity ringdown and high resolution Fourier transform spectroscopy with a long-path absorption cell. *Journal of Chemical Physics*, 110(22):10749–10757, 1999.

A. O. Nier and M. B. McElroy. Composition and strucutre of Mars upper atmosphere: Results from neutral mass spectrometers on Vikings 1 and 2. *Journal of Geophysical Research*, 82(28):4341–4349, 1977.

R. E. Novak, M. J. Mumma, M. A. DiSanti, N. Dello Russo, and K. Magee-Sauer. Mapping of ozone and water in the atmosphere of Mars near the 1997 aphelion. *Icarus*, 158(1):14–23, 2002.

R. E. Novak, M. J. Mumma, S. Lee, L. Ivanov, B. Bonev, and G. Villanueva. Mapping of D/H ratio in the Martian atmosphere near the perihelion. *Bulletin of the American Astronomical Society*, 37:669, 2005.

J. F. Noxon, W. A. Traub, N. P. Carleton, and P. Connes. Detection of O_2 dayglow emissions from Mars and Martian ozone abundance. *Astrophysical Journal*, 207(3):1025–1035, 1976.

S. Ohtsuki, N. Iwagami, H. Sagawa, Y. Kasaba, M. Ueno, and T. Imamura. Ground-based observation of the Venus 1.27-μm O_2 airglow. *Planetary Atmospheres, Ionospheres, and Magnetospheres*, 36(11): 2038–2042, 2005.

S. Ohtsuki, N. Iwagami, H. Sagawa, M. Ueno, Y. Kasaba, T. Imamura, K. Yanagisawa, and E. Nishihara. Distributions of the Venus 1.27-μm O_2 airglow and rotational temperature. *Planetary and Space Science*, 56(10):1391–1398, 2008.

M. Pätzold, B Häusler, M. K. Bird, S. Tellmann, R. Mattei, S. W. Asmar, V Dehant, W. Eidel, T. Imamura, R. A. Simpson, and G. L. Tyler. The structure of Venus' middle atmosphere and ionosphere. *Nature*, 450:657–660, 2007.

D. A. Pejaković, K. S. Kalogerakis, R. A. Copeland, and D. L. Huestis. Laboratory determination of the rate coefficient for three-body recombination of oxygen atoms in nitrogen. *Journal of Geophysical Research-Space Physics*, 113(A4):A04303, 2008. doi: 10.1029/2007JA012694.

S. Perrier. *Climatologie de l'ozone, des poussières et des nuages dans l'atmosphére martienne d'après les mesures de l'instrument SPICAM sur Mars Express.* PhD thesis, Université Paris VI, 2006.

G. Piccioni, L. Zasova, A. Migliorini, P. Drossart, A. Shakun, A. García Muñoz, F. P. Mills, and A. Cardesin-Moinelo. Near-IR oxygen nightglow observed by VIRTIS in the Venus upper atmosphere. *Journal of Geophysical Research-Planets*, 114:E00B38, 2009. doi: 10.1029/2008JE003133.

E. Quémerais, J.-L. Bertaux, O. Korablev, E. Dimarellis, C. Cot, B. R. Sandel, and D. Fussen. Stellar occultations observed by SPICAM on Mars express. *Journal of Geophysical Research-Planets*, 111: E09S04, 2006. doi: 10.1029/2005JE002604.

E. I. Reed and S. Chandra. Global characteristics of atmospheric emissions in lower thermosphere and their aeronomic implications. *Journal of Geophysical Research-Space Physics*, 80(22):3053–3062, 1975.

E. Royer. *Étude des émissions de monoxyde d'azote (NO), observées en ultraviolet par SPICAM/Venus Express, en mode d'occultation stellaire*. PhD thesis, Université Paris VI Pierre et Marie Curie, 2011.

E. Royer, F. Montmessin, and J.-L. Bertaux. NO emissions as observed by SPICAV during stellar occultations. *Planetary and Space Science*, 58(10):1314–1326, 2010.

S. P. Sander, R. R. Friedl, J. Abbatt, J. R. Barker, J. B. Burkholder, D. M. Golden, C. E. Kolb, M. J. Kurylo, G. K. Moortgat, P. H. Wine, and R. E. Huie. Chemical kinetics and photochemical data for use in atmospheric studies. Technical Report 15, Jet Propulsion Laboratory, Pasadena, 2006. JPL Publication 06-2.

S. P. Sander, R. R. Friedl, J. Abbatt, J. R. Barker, J. B. Burkholder, D. M. Golden, C. E. Kolb, M. J. Kurylo, G. K. Moortgat, P. H. Wine, and R. E. Huie. Chemical kinetics and photochemical data for use in atmospheric studies. Technical Report 15, Jet Propulsion Laboratory, Pasadena, 2011. JPL Publication 10-6.

J. T. Schofield and F. W. Taylor. Measurements of the mean, solar-fixed temperature and cloud structure of the middle atmosphere of Venus. *Quarterly Journal of the Royal Meteorological Society*, 109(459): 57–80, 1983.

A. Seiff and D. B. Kirk. Structure of the atmosphere of Mars in summer at mid-latitudes. *Journal of Geophysical Research*, 82(28):4364–4378, 1977.

A. V. Shakun, L. V. Zasova, G. Piccioni, P. Drossart, and A. Migliorini. Investigation of oxygen $O_2(a^1\Delta_g)$ emission on the nightside of Venus: Nadir data of the VIRTIS-M experiment of the Venus Express mission. *Cosmic Research*, 48(3):232–239, 2010.

W. E. Sharp and I. C. McDade. Peak height and density of the mesospheric oxygen layer from ground based airglow measurements. In *Fall Meeting Suppl.*, volume 77. EOS Trans. AGU, 1996. F547.

C. Y. She and R. P. Lowe. Seasonal temperature variations in the mesopause region at mid-latitude: Comparison of lidar and hydroxyl rotational temperatures using WINDII/UARS OH height profiles. *Journal of Atmospheric and Solar-Terrestrial Physics*, 60(16):1573–1583, 1998.

T. G. Slanger. Generation of $O_2(c^1\Sigma_u^-, C^3\Delta_u, A^3\Sigma_u^+)$ from oxygen atom recombination. *Journal of Chemical Physics*, 69(11):4779–4791, 1978. doi: 10.1063/1.436504.

T. G. Slanger and G. Black. $O_2(C^3\Delta_u \rightarrow a^1\Delta_g)$ bands in nightglow spectrum of Venus. *Geophysical Research Letters*, 5(11):947–948, 1978.

T. G. Slanger and R. A. Copeland. Energetic oxygen in the upper atmosphere and the laboratory. *Chemical Reviews*, 103(12):4731–4765, 2003.

T. G. Slanger, P. C. Cosby, D. L. Huestis, and T. A. Bida. Discovery of the atomic oxygen green line in the Venus night airglow. *Science*, 291(5503):463–465, 2001.

T. G. Slanger, D. L. Huestis, P. C. Cosby, N. J. Chanover, and T. A. Bida. The Venus nightglow: Ground-based observations and chemical mechanisms. *Icarus*, 182(1):1–9, 2006.

T. G. Slanger, C. Mullen, E. Bolin, and R. A. Copeland. Venus photochemistry and ground-based observations. Number 9007, Maryland, USA, 2007. Workshop on Planetary Atmospheres, LPI, NASA.

T. G. Slanger, T. E. Cravens, J. Crovisier, S. Miller, and D. F. Strobel. Photoemission phenomena in the solar system. *Space Science Reviews*, 139:267–310, 2008.

G. P. Smith and R. Robertson. Temperature dependence of oxygen atom recombination in nitrogen after ozone photolysis. *Chemical Physics Letters*, 458(1-3):6–10, 2008.

I. W. M. Smith. The role of electronically excited-states in recombination reactions. *International Journal of Chemical Kinetics*, 16(4):423–443, 1984.

M. D. Smith. Interannual variability in TES atmospheric observations of Mars during 1999-2003. *Icarus*, 167(1):148–165, 2004.

L. Soret, J.-C. Gérard, G. Piccioni, and P. Drossart. The OH Venus nightglow: morphology and relation to ozone in the upper atmosphere. volume 6, Nantes, France, 2011. EPSC-DPS Joint Meeting 2011.

L. Soret, J.-C. Gérard, F. Montmessin, G. Piccioni, P. Drossart, and J.-L. Bertaux. Atomic oxygen on the Venus nightside: Global distribution deduced from airglow mapping. *Icarus*, 217(2):849–855, 2012.

J. A. Steadman and B. A. Thrush. A laboratory study of the mechanism of the oxygen airglow. *Journal of Atmospheric Chemistry*, 18(4):301–317, 1994.

A. I. Stewart. Mariner 6 And 7 ultraviolet spectrometer experiment: Implications of CO_2^+, CO, and O airglow. *Journal of Geophysical Research*, 77(1):54–68, 1972.

A. I. Stewart and C. A. Barth. ultraviolet night airglow of Venus. *Science*, 205(4401):59–62, 1979.

A. I. Stewart, D. E. Anderson, L. W. Esposito, and C. A. Barth. Ultraviolet spectroscopy of Venus: Initial results from the Pioneer Venus Orbiter. *Science*, 203(4382):777–779, 1979.

A. I. F. Stewart, J. C. Gérard, I. D. W. Rusch, and S. W. Bougher. Morphology of the Venus ultraviolet night airglow. *Journal of Geophysical Research*, 85(A13):7861–7870, 1980.

I. P. Stott and B. A. Thrush. Laboratory studies of the mechanism of the oxygen nightglow. *Proceedings of the Royal Society of London Series A-Mathematical Physical and Engineering Sciences*, 424(1866): 1–17, 1989.

Y. Sun and A. Dalgarno. Radiative association of N-atoms and O-atoms at low-temperatures. *Journal of Geophysical Research-Space Physics*, 97(A5):6537–6539, 1992.

Y Sun and A Dalgarno. Infrared emission spectra of nitric oxide following the radiative association of nitrogen atoms and oxygen atoms. *Journal of Quantitative Spectroscopy & Radiative Transfer*, 55(2): 245–249, 1996.

H. Svedhem, D. V. Titov, F. W. Taylor, and O. Witasse. Venus as a more Earth-like planet. *Nature*, 450(7170):629–632, 2007.

S. Tellmann, M. Päetzold, B. Häeusler, M. K. Bird, and G. L. Tyler. Structure of the Venus neutral atmosphere as observed by the Radio Science experiment VeRa on Venus Express. *Journal of Geophysical Research-Planets*, 114:E00B36, 2009. doi: 10.1029/2008JE003204.

P. D. Tennyson, P. D. Feldman, G. F. Hartig, and R. C. Henry. Near-midnight observations of nitric oxide δ- and γ-band chemiluminescence. *Journal of Geophysical Research*, 91(A9):10141–10146, 1986.

W. A. Traub, N. P. Carleton, P. Connes, and J. F. Noxon. Latitude variation of O_2 dayglow and O_3 abundance on Mars. *Astrophysical Journal*, 229(2):846–850, 1979.

P. C. Wraight. Association of atomic oxygen and airglow excitation mechanisms. *Planetary and Space Science*, 30(3):251–259, 1982.

S. Zhang, S. W. Bougher, and M. J. Alexander. The impact of gravity waves on the Venus thermosphere and O_2 IR nightglow. *Journal of Geophysical Research-Planets*, 101(E10):23195–23205, 1996.